J. Mech. Phys. Solids 160 (2022) 104754

Contents lists available at ScienceDirect

Journal of the Mechanics and Physics of Solids

journal homepage: www.elsevier.com/locate/jmps

Three-dimensional fluid-driven stable frictional ruptures

Alexis Sáez [a], Brice Lecampion [a,*], Pathikrit Bhattacharya [b], Robert C. Viesca [c]

[a] Geo-Energy Laboratory-Gaznat Chair on Geo-Energy, Ecole Polytechnique Fédérale de Lausanne, EPFL-ENAC-IIC-GEL, Lausanne CH 1015, Switzerland
[b] School of Earth and Planetary Sciences, National Institute of Science Education and Research, Bhubaneswar, Odisha 752050, India
[c] Department of Civil and Environmental Engineering, Tufts University, Medford, MA 02155, USA

ARTICLE INFO

Keywords:
Fracture (A)
Friction (B)
Geological material (B)
Boundary integral equation (C)
Injection induced slip

ABSTRACT

We investigate the quasi-static growth of a fluid-driven frictional shear crack that propagates in mixed mode (II+III) on a planar fault interface that separates two identical half-spaces of a three-dimensional solid. The fault interface is characterized by a shear strength equal to the product of a constant friction coefficient and the local effective normal stress. Fluid is injected into the fault interface and two different injection scenarios are considered: injection at constant volume rate and injection at constant pressure. We derive analytical solutions for circular ruptures which occur in the limit of a Poisson's ratio $\nu = 0$ and solve numerically for the more general case in which the rupture shape is unknown ($\nu \neq 0$). For an injection at constant volume rate, the fault slip growth is self-similar. The rupture radius ($\nu = 0$) expands as $R(t) = \lambda L(t)$, where $L(t)$ is the nominal position of the fluid pressure front and λ is an amplification factor that is a known function of a unique dimensionless parameter T. The latter is defined as the ratio between the distance to failure under ambient conditions and the strength of the injection. Whenever $\lambda > 1$, the rupture front outpaces the fluid pressure front. For $\nu \neq 0$, the rupture shape is quasi-elliptical. The aspect ratio is upper and lower bounded by $1/(1-\nu)$ and $(3-\nu)/(3-2\nu)$, for the limiting cases of critically stressed faults ($\lambda \gg 1$, $T \ll 1$) and marginally pressurized faults ($\lambda \ll 1$, $T \gg 1$), respectively. Moreover, the evolution of the rupture area is independent of the Poisson's ratio and grows simply as $A_r(t) = 4\pi\alpha\lambda^2 t$, where α is the fault hydraulic diffusivity. For injection at constant pressure, the fault slip growth is not self-similar: the rupture front evolves at large times as $\propto (\alpha t)^{(1-T)/2}$ with T between 0 and 1. The frictional rupture moves at most diffusively ($\propto \sqrt{\alpha t}$) when the fault is critically stressed, but in general propagates slower than the fluid pressure front. Yet in some conditions, the rupture front outpaces the fluid pressure front. The latter will eventually catch the former if injection is sustained for sufficient time. Our findings provide a basic understanding on how stable (aseismic) ruptures propagate in response to fluid injection in 3-D. Notably, since aseismic ruptures driven by injection at constant rate expand proportionally to the squared root of time, seismicity clouds that are commonly interpreted to be controlled by the direct effect of fluid pressure increase might be controlled by the stress transfer of a propagating aseismic rupture instead. We also demonstrate that the aseismic moment M_0 scales to the injected fluid volume V as $M_0 \propto V^{3/2}$.

* Corresponding author.
E-mail addresses: alexis.saez@epfl.ch (A. Sáez), brice.lecampion@epfl.ch (B. Lecampion), pathikritb@niser.ac.in (P. Bhattacharya), robert.viesca@tufts.edu (R.C. Viesca).

https://doi.org/10.1016/j.jmps.2021.104754
Received 9 September 2021; Received in revised form 15 December 2021; Accepted 15 December 2021
Available online 5 January 2022

1. Introduction

Fluid-driven frictional ruptures play an important role in earthquake and fault mechanics and can occur either as a natural process or be induced by human activities. Some examples of the natural source are related to fault valving behavior (Sibson, 1992; Zhu et al., 2020) and metamorphic dehydration reactions (Wong et al., 1997; Hacker et al., 2003; Kato et al., 2010) in fault systems, whereas seismic swarms (Parotidis et al., 2005; Chen et al., 2012; Ross et al., 2020; Hatch et al., 2020) and aftershock sequences (Bosl and Nur, 2002; Miller et al., 2004; Hainzl et al., 2016; Ross et al., 2017; Miller, 2020) are other natural phenomena commonly attributed to the migration of fluids in fault zones. On the other hand, anthropogenic fluid injections associated with hydrocarbon and geothermal operations routinely produce microseismicity and have been extensively linked to the reactivation of faults (Healy et al., 1968; Deichmann and Giardini, 2009; Keranen et al., 2013; Eyre et al., 2019; Ellsworth et al., 2019).

Evidence for fluid-driven frictional ruptures is generally inferred from the observation of seismicity spreading away from natural or human-related fluid injections in the Earth's crust (Shapiro et al., 1997; Parotidis et al., 2005; Hainzl et al., 2016; Ross et al., 2017; Goebel and Brodsky, 2018; Ross et al., 2020). Observed seismicity is the result of unstable (seismic) frictional sliding that radiates detectable seismic waves. Nevertheless, seismic slip is not the only possible result of fluid injection. In fact, stable (aseismic) slip, which is more difficult to detect due to the virtual absence of elastodynamic waves, is a likely frequent result of the injection of fluids as demonstrated by past large-scale fluid injections in the field (Hamilton and Meehan, 1971; Scotti and Cornet, 1994; Bourouis and Bernard, 2007), recent laboratory and in-situ experiments (Guglielmi et al., 2015; Scuderi and Collettini, 2016; Cappa et al., 2019; Passelègue et al., 2020), and recent cases of injection-induced seismicity (Wei et al., 2015; Chen et al., 2017; Eyre et al., 2019).

As suggested by a number of recent experimental and observational studies (Wei et al., 2015; Guglielmi et al., 2015; Duboeuf et al., 2017; Eyre et al., 2019; Cappa et al., 2019; Bhattacharya and Viesca, 2019), injection-induced aseismic slip may trigger seismicity by the transfer of solid stresses to unstable patches in pre-existing structural discontinuities, such as fractures and faults. Such spatio-temporal perturbation of the stress field is due to a quasi-statically expanding fluid-driven slipping patch that propagates along an initially locked and predominantly frictionally-stable pre-existing discontinuity. In this view and in the framework of this model, seismicity can be conceptually understood as the result of instabilities triggered by perturbating the pre-injection stress state of frictionally-unstable patches present either in the same pre-existing discontinuity (due to heterogeneities in rock frictional properties) or in others nearby the propagating rupture. The potential prominence of this triggering mechanism has increased in recent times since new investigations have suggested that fluid-induced aseismic slip can outpace the diffusion of fluid pressure (Eyre et al., 2019; Bhattacharya and Viesca, 2019) and may be in fact the primary cause of observed seismicity during in-situ experiments (Guglielmi et al., 2015; Duboeuf et al., 2017) and responsible for the triggering of hydraulic fracturing-induced earthquakes (Eyre et al., 2019).

Recent efforts for understanding injection-induced aseismic slip have been motivated mostly by the sudden increase of seismicity due to anthropogenic fluid injection (Keranen et al., 2014; Bao and Eaton, 2016; Goebel and Brodsky, 2018). Nevertheless, understanding the mechanics of fluid-driven aseismic slip is indeed relevant to any phenomenon that is predominantly characterized by stable frictional sliding and the pressurization of interfacial fluids. This might be the case of, for instance, some seismic swarms (Chen et al., 2012; Hatch et al., 2020), aftershock sequences (Ross et al., 2017), and slow slip transients near the base of the seismogenic zone due to fault valving (Zhu et al., 2020) or metamorphic dehydration reactions (Kato et al., 2010).

Despite the apparent relevance of fluid-driven aseismic ruptures in a wide variety of natural and anthropogenic phenomena, the spatio-temporal evolution of aseismic slip in response to fluid injection remains poorly constrained in 3-D. This is, in part, due to the challenge of solving such a moving boundary value problem in which both fault slip and rupture shape are unknown. In this article, we investigate the mechanics of injection-induced fault slip by solving the problem of a fluid-driven frictional shear crack that propagates in mixed mode (II+III) on a planar fault that separates two identical half-spaces of a three-dimensional, linear elastic, and impermeable solid. The fault interface is saturated by pressurized fluid and it is characterized by a constant hydraulic transmissivity and a shear strength that is determined by the product of a constant friction coefficient and the local effective normal stress. We consider that fluid is injected into the fault interface under two injection scenarios: injection at constant volume rate and injection at constant pressure. The model is an extension to 3-D of a previous 2-D model presented by Bhattacharya and Viesca (2019) and more recently by Viesca (2021). In the process, we also investigate the fundamental problem of crack-shape selection of a frictional shear crack under localized (point-force-like) and distributed effective shear loadings, including its dependence on the Poisson's ratio of the bulk.

This paper is organized as follows. In Section 2, we present the mathematical formulation of the problem and the chosen numerical methods. In Section 3, we solve the problem of a stable rupture driven by injection at constant volume rate, for which we first derive an exact analytical solution in the case of axisymmetric circular ruptures, and then solve numerically for the more general case in which the rupture shape is part of the solution. Following a similar approach, we solve in Section 4 the problem of a stable rupture driven by injection at constant pressure. Finally, Section 5 discusses our findings and its possible implications to a number of fluid-driven earthquake-related phenomena such as injection-induced seismicity, seismic swarms and aftershock sequences.

2. Problem formulation and numerical methods

2.1. Problem formulation

We consider a fault plane Γ located along $z = 0$ that separates two semi-infinite, homogeneous, isotropic and linear elastic solids (see Fig. 1). The fault interface is governed by Coulomb's friction with a constant friction coefficient. The initial stress tensor is

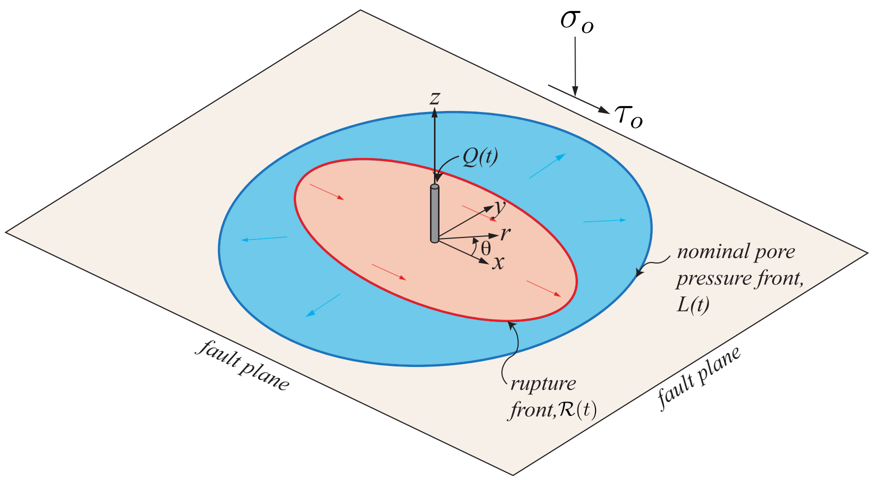

Fig. 1. Model schematic. A planar fault separates two semi-infinite linear elastic, homogeneous, and isotropic solids. The fault is characterized by a constant friction coefficient and is embedded in uniform initial fluid pressure and stress fields. Fluid is injected right into the fault through a wellbore located along the z axis. Fluid flow is confined within the fault plane and is fault-parallel and axisymmetric with regard to the z-axis. A quasi-static rupture of front $\mathcal{R}(t)$ whose shape is unknown is driven by axisymmetric fluid pressure diffusion that is characterized by a nominal fluid pressure front $L(t)$.

uniform and is characterized by a shear stress τ_o resolved on the fault plane that acts along the x direction, and a total normal stress σ_o to the fault plane (that acts along the z direction). We assume that fluid is injected into the fault plane through, for instance, a wellbore, that is located along the z axis. We also assume that the solid is impermeable and the fault interface has a uniform and constant hydraulic transmissivity; fluid flow thus occurs only within the fault plane and is fault-parallel and axisymmetric with regard to the z axis. Owing to the planarity of the fault and the uniform direction of the initial shear stress τ_o, fluid flow induces fault slip δ and changes in the shear stress τ resolved on the fault plane that are both characterized by a uniform direction along the x axis. The magnitude of the fault slip δ is maximum at the origin (the injection point) and vanishes along the rupture front $\mathcal{R}(t) = \{(x, y) : \delta(x, y, t) = 0\}$. The rupture front $\mathcal{R}(t)$ is unknown a priori and is to be determined as part of the solution.

The quasi-static elastic equilibrium that relates the fault slip δ to the shear stress τ on the fault plane Γ can be written as the following boundary integral equation (Hills et al., 1996)

$$\tau(x, y, t) = \tau_o + \int_{\Gamma} K(x - \xi, y - \zeta; \mu, \nu)\delta(\xi, \zeta, t)\mathrm{d}\xi\mathrm{d}\zeta, \tag{1}$$

where τ_o is the initial shear stress, μ is the shear modulus of the solid, ν is the Poisson's ratio, and K is the hypersingular (of order $1/r^3$) elastostatic traction kernel (Hills et al., 1996). We adopt the convention of slip positive in clockwise rotation, $\delta(x, y, t) = u_x(x, y, z = 0^+, t) - u_x(x, y, z = 0^-, t)$, where u_x is the displacement component in the x direction. We also adopt the convention of normal stress positive in compression.

The fault is assumed to obey a Mohr–Coulomb shear failure criterion without any cohesion:

$$|\tau(x, y, t)| \leq f\left(\sigma_o - p(r, t)\right), \tag{2}$$

where f is the constant friction coefficient, $\sigma_o - p(r, t)$ denotes Terzaghi's effective stress normal to the fault plane with $p(r, t)$ being the spatiotemporally evolving fluid pressure, which is axisymmetric about the point of injection $\{O; r, \theta, z\}$ (see Fig. 1). We further assume that fault slip occurs without any normal displacement discontinuity, neither dilatant nor contractant, and that fault slip does not impact fluid flow.

We make the assumption that the surrounding rock can be considered impermeable compared to the fault itself at the scale of the injection duration. Single phase porous media flow (Bear, 1972) in the fault thus reduces (after width averaging across the fault thickness w_h) to the following two-dimensional pressure-diffusion equation on the fault plane

$$S\frac{\partial p}{\partial t} - \frac{k}{\eta}\nabla^2 p = 0, \tag{3}$$

where S is a storage coefficient combining the effect of both fluid and pore compressibilities, k is the constant and uniform fault permeability, and η the fluid dynamic viscosity.

The fault is initially fully locked (zero slip rate) and the uniform initial fluid pressure field is equal to p_o. We investigate sustained fluid injection for $t > 0$ under two different scenarios: either at constant volume rate or at constant overpressure. The solutions of both boundary value problems for the two-dimensional diffusion equation are well-known (Carslaw and Jaeger, 1959) and can be written in the following functional form

$$p(r, t) = p_o + \Delta p_* \Pi(r, \alpha t), \tag{4}$$

where Δp_* is a characteristic pressure and Π is the dimensionless injection-induced overpressure. These solutions of the diffusion equation (3) notably depend on the fault hydraulic diffusivity $\alpha = k/S\eta$ $[L^2/T]$ via the well-known diffusion characteristic length $\sqrt{\alpha t}$.

For a constant volume rate injection from a point source, the two-dimensional flow solution is given in polar coordinates by (section 10.4, eq. 5, Carslaw and Jaeger, 1959):

$$\Delta p_* = \frac{Q_w \eta}{4\pi k w_h}, \quad \Pi(r,t) = E_1\left(\frac{r^2}{4\alpha t}\right), \tag{5}$$

where Q_w is the constant injection volume rate $[L^3/T]$, w_h is the fault thickness $[L]$, and E_1 is the exponential integral function. Note that the product kw_h is often denoted as the fault hydraulic transmissivity $[L^3]$.

For the case of an injection from a finite wellbore at constant overpressure, the solution reads (section 13.5, Eq. (6), Carslaw and Jaeger, 1959):

$$\Delta p_* = \Delta p_w, \quad \Pi(r,t) = 1 + \frac{2}{\pi}\int_0^\infty e^{-\xi^2 \alpha t/r_w^2} \frac{J_0(\xi r/r_w)Y_0(\xi) - Y_0(\xi r/r_w)J_0(\xi)}{\xi\left(J_0^2(\xi) + Y_0^2(\xi)\right)} \mathrm{d}\xi, \tag{6}$$

where Δp_w is the applied constant overpressure at the wellbore of radius r_w, and J_0 and Y_0 are the zero-order Bessel functions of the first and second kind, respectively.

The uniform initial fluid pressure and stress fields must satisfy the condition $|\tau_o| < f\sigma_o'$ on the fault plane, where $\sigma_o' = \sigma_o - p_o$ is the initial effective normal stress. This condition means no activation of fault slip prior to the start of the injection. Fault slip starts when the fluid pressure increase is sufficient to reach the Mohr–Coulomb shear failure criterion. The ensuing aseismic rupture grows due to the direct effect of the fluid pressure that reduces locally the fault strength in Eq. (2), and due to the quasi-static nonlocal elastic integral operator in Eq. (1) that operates over the fault slip distribution δ and determines the local shear stress change consistent with the Mohr–Coulomb strength condition.

2.2. Numerical methods

We developed a fully implicit boundary-element-based solver with an elasto-plastic-like constitutive interfacial law to solve simultaneously the quasi-static elastic equilibrium (1) and the activation criterion (2) knowing the semi-analytical fluid pressure evolution on the fault (either Eq. (5) or (6) depending on the injection scenario). The main features of our numerical solver are briefly described below.

2.2.1. Spatial discretization

We discretize the fault plane Γ using an unstructured Delaunay triangulation $\Gamma = \cup_{k=1}^{N_E}\Gamma_k$, where Γ_k is the kth triangular element and N_E is the total number of elements in the mesh (see Fig. 5a–b for examples of the unstructured meshes used). We use the displacement discontinuity method (Crouch and Starfield, 1983) to solve the quasi-static elastic equilibrium and employ piecewise quadratic triangular boundary elements (Nikolskiy et al., 2013). The analytical integration of the traction kernel for a generic triangle with quadratic shape functions was obtained by Nikolskiy et al. (2013) for the three components of the displacement discontinuity. Our implementation considers boundary elements with six collocation points such that $N_C = 6N_E$ is the total number of collocation points in the mesh, and $N = 3N_C$ is the total number of degrees of freedom.

In the configuration investigated here where the principal shear direction is known and does not change, the quasi-static elastic equilibrium, Eq. (1), can be written in the x-direction of the global reference system only. Nevertheless, we use a fully 3D collocation displacement discontinuity method and instead expressed it in the local reference system $\{\boldsymbol{x}^k; \boldsymbol{e}_1^k, \boldsymbol{e}_2^k, \boldsymbol{e}_3^k\}$ of each kth boundary element, where $\boldsymbol{e}_1^k$ and $\boldsymbol{e}_2^k$ are two unit vectors tangent to Γ_k (and mutually orthogonal) and $\boldsymbol{e}_3^k$ is a unit vector normal to Γ_k such that $\boldsymbol{n}^+ = -\boldsymbol{n}^- = -\boldsymbol{e}_3$ where "+" and "−" refer to the upper and bottom fault faces. The spatially discretized form of the quasi-static elastic equilibrium in the local reference system of the boundary elements is

$$\boldsymbol{t} = \boldsymbol{t}^o + \mathbf{E}\boldsymbol{d}, \tag{7}$$

where $\boldsymbol{t} \in \mathbb{R}^N$ is the total traction vector, $\boldsymbol{t}^o \in \mathbb{R}^N$ is the initial total traction vector, $\boldsymbol{d} \in \mathbb{R}^N$ is the displacement discontinuity vector, and $\mathbf{E} \in \mathbb{R}^{N\times N}$ is the collocation boundary element matrix which is dense and non-symmetric. We approximate this dense boundary element matrix $\mathbf{E}$ using a hierarchical matrix $\mathbf{E}_{\mathcal{H}}$ representation. Using a hierarchical matrix approximation allows to significantly reduce the memory requirements and speed up algebraic operations for an otherwise computationally expensive matrix (see Ciardo et al., 2020, and references therein for further details).

The system of Eqs. (7) is arranged in order that $\boldsymbol{t} = t_i^m = (t_1^1, t_2^1, t_3^1, t_1^2 \dots, t_3^{N_C})$, where the index $i = 1,2,3$ denotes the local components with regard to the local reference systems of the boundary elements, and the index $m = 1,\dots,N_C$ denotes the collocation points.

Finally, the spatially discretized form of the Mohr–Coulomb shear failure criterion is solved locally (at the collocation point level) and is written as

$$\|\boldsymbol{\tau}^m\| \le f t_3^{\prime,m}, \tag{8}$$

where $\boldsymbol{\tau}^m = \left(t_1^m, t_2^m\right)$ is the local shear traction vector at the mth collocation point, and $t_3^{\prime,m} = t_3^m - p^m$ is the normal component of the local effective traction vector at the mth collocation point.

2.2.2. Time integration

We use a backward Euler time integration scheme. Let $\Delta X = X^{n+1} - X^n$ be the increment of a generic variable X from the time t^n to the time t^{n+1} with $\Delta t = t^{n+1} - t^n$ being the time step. Taking the time derivative of Eq. (7) and using the definition of Terzaghi's effective stress such that $\boldsymbol{t} = \boldsymbol{t}' + \boldsymbol{p}$, where $\boldsymbol{t}' \in \mathbb{R}^N$ is the effective traction vector and $\boldsymbol{p} \in \mathbb{R}^N$ is the fluid pressure vector, we arrive to the following fully discretized incremental form of the quasi-static elastic equilibrium

$$\Delta \boldsymbol{t}'(\Delta \boldsymbol{d}) = -\Delta \boldsymbol{p} + \mathbf{E}_{\mathcal{H}} \Delta \boldsymbol{d}. \tag{9}$$

Note that $\Delta \boldsymbol{p} = (0, 0, \Delta p^1, 0, \dots, \Delta p^{N_C})$ as the fluid pressure affects only the normal components of the effective traction vector.

Eq. (9) is a nonlinear system of N equations for $\Delta \boldsymbol{d}$ that is solved via a Newton–Raphson scheme. Note that $\Delta \boldsymbol{t}'$ depends nonlinearly on $\Delta \boldsymbol{d}$ due to the Mohr–Coulomb shear failure criterion on the fault interface (8).

2.2.3. Integration of the constitutive interfacial law

The Mohr–Coulomb criterion (8) defines two different modes of contact at every collocation point which are either locked or in frictional sliding. On the contrary to the rigid-plastic approach developed in Ciardo et al. (2020), we solve here for $\Delta \boldsymbol{t}'(\Delta \boldsymbol{d})$ using an elasto-plastic constitutive interface relation between the local effective traction $\boldsymbol{t}'$ and displacement discontinuity $\boldsymbol{d}$. In other words, we regularize the fault frictional contact behavior by allowing a degree of elastic displacement discontinuity and write the increment of displacement discontinuity vector as the sum of an elastic part $\Delta \boldsymbol{d}^e$ and a plastic part $\Delta \boldsymbol{d}^p$,

$$\Delta \boldsymbol{d} = \Delta \boldsymbol{d}^e + \Delta \boldsymbol{d}^p. \tag{10}$$

We introduce a linear elastic relation between the increment of effective tractions $\Delta \boldsymbol{t}'$ and the elastic part of the displacement discontinuity,

$$\Delta \boldsymbol{t}' = -\boldsymbol{D} \Delta \boldsymbol{d}^e, \tag{11}$$

where $\boldsymbol{D} \in \mathbb{R}^{3\times3}$ is a diagonal elastic stiffness matrix containing the shear and normal stiffness components of the local elastic springs (of dimension F/L^3) modeling the fault elastic response. Numerically, we consider sufficiently large values of the elastic stiffness components such that $\|\Delta \boldsymbol{d}^p\| \gg \Delta \boldsymbol{d}^e$, whenever plastic flow occurs. Note that the minus sign in the above directly comes from our convention of signs for tractions (positive in compression) and displacement discontinuities (positive in opening).

The Mohr–Coulomb yield function in the local reference frame of a triangular displacement discontinuity element can be rewritten as

$$\mathcal{F}(\boldsymbol{t}') = \|\boldsymbol{\tau}\| - f t'_3. \tag{12}$$

If $\mathcal{F} < 0$, the mode of contact is *elastic* and no frictional sliding occurs $\Delta \boldsymbol{d}^p = \boldsymbol{0}$, whereas if $\mathcal{F} = 0$, *plastic* frictional contact occurs and thus frictional sliding $\Delta \boldsymbol{d}^p \neq \boldsymbol{0}$.

We use a non-associated Mohr–Coulomb flow rule with zero dilatancy to describe the evolution of the plastic part of the displacement discontinuity:

$$\Delta \boldsymbol{d}^p = -\Delta\gamma \frac{\partial G}{\partial \boldsymbol{t}'}, \quad G(\boldsymbol{t}') = \|\boldsymbol{\tau}\|, \tag{13}$$

where $\Delta\gamma \geq 0$ is the plastic multiplier increment and G is the plastic flow potential.

The previously mentioned inequalities for the yield function and plastic flow can be re-written as the Karush–Kuhn–Tucker conditions of elastoplasticity:

$$\Delta\gamma \geq 0, \ \mathcal{F}(\boldsymbol{t}') \leq 0, \ \Delta\gamma \mathcal{F}(\boldsymbol{t}') = 0. \tag{14}$$

For a given increment of the total displacement discontinuity vector $\Delta \boldsymbol{d}$, the system of Eqs. (10) to (14) has to be solved in order to obtain the plastic multiplier increment $\Delta\gamma$, and consequently the increment of plastic fault slip $\Delta \boldsymbol{d}^p$ and the incremental change of effective tractions $\Delta \boldsymbol{t}'$. We use a classical elastic predictor–plastic corrector algorithm to solve this system of equations. The elastic predictor–plastic corrector algorithm is a two-step procedure in which the two possible modes of contact, elastic and plastic, are solved sequentially and the final solution is chosen as the only one satisfying the yield inequality (see for example de Souza Neto et al., 2008 for details). Note that this algorithm is executed locally at every collocation point for every Newton–Raphson iteration for a given increment of time. As usual in elastoplasticity, it is critical to use the consistent tangent operator during the Newton–Raphson iterations in order to achieve quadratic convergence. We recall the expression of this consistent tangent operator in Appendix A.

2.2.4. Implementation details

Since we do not consider fluid flow being affected by mechanical deformation, the numerical time-stepping scheme consists only of solving a Newton–Raphson scheme for the mechanical equilibrium and the local elasto-plastic relation at time t^{n+1} knowing the fluid pressure increment given by the semi-analytical solutions (Eqs. (5) or (6)). Convergence of the non-linear Newton–Raphson solver is reached when the relative increment of the L^2 norm of the displacement discontinuity vector between two consecutive iterations falls below 10^{-4}. The linear tangent mechanical system at each Newton step is solved using a biconjugate gradient stabilized iterative solver (BiCGSTAB) with a tolerance set to 10^{-4}.

It is worth noting that the exponential integral function in Eq. (5) is log singular at the injection point $r = 0$. Hence, for the case of injection at constant volume rate, the fluid pressure is actually unbounded right at the origin. There is thus an evolving but rather small (comparing to the rupture size) circular region in the neighborhood of the injection point where the fluid pressure p is larger than the initial effective normal stress σ'_o. Even though our model does not account for fault opening, the effect of this singularity is negligible in our numerical solutions, since, even for relatively high resolution, $p < \sigma'_o$ at every single discrete (collocation) point of the simulations.

3. Self-similar rupture growth due to injection at constant volume rate

3.1. Scaling and similarity

We first investigate the case of a constant volume rate injection, where the fluid pressure evolution driving the rupture is given by Eq. (5). Such a diffusion solution is self-similar: the pressure is only function of the self-similar variable $r/\sqrt{4\alpha t}$, where $L(t) = \sqrt{4\alpha t}$ is the characteristic diffusion lengthscale which corresponds to the evolution of the fluid pressure front disturbance. Because no other time or length scales enter the problem, the quasi-static rupture will also evolve in a self-similar fashion. This result is essential for the problem addressed in this section. We denote the a priori unknown rupture shape as $\mathcal{R}(t) = \{(x, y) : \delta(x, y, t) = 0\}$ and scale it as

$$\mathcal{R}(t) = R(t)\mathcal{S}, \tag{15}$$

where $\mathcal{S}$ is the dimensionless rupture front and $R(t)$ the characteristic rupture lengthscale. Moreover, we define the amplification factor λ that relates the instantaneous rupture characteristic scale $R(t)$ to the nominal location of the fluid pressure front $L(t)$, such that $R(t) = \lambda L(t)$. A value of $\lambda > 1$ indicates that the rupture lengthscale is greater than the fluid pressure front radius, whereas a value of $\lambda < 1$ indicates the opposite.

We can scale the spatial variables (x, y) with the diffusion lengthscale $L(t)$ (or alternatively with the characteristic rupture scale $R(t)$) while the characteristic fluid pressure scale is directly given by Δp^* in Eq. (5). Introducing these characteristic scales in the Mohr–Coulomb and elasticity equations allows to close the scaling of the problem as:

$$\frac{\vec{x}}{L(t)} \to \vec{x},\ \frac{\tau - f\sigma'_o}{f\Delta p_*} \to \tau,\ \frac{\delta}{\delta_c(t)} \to \delta,\ \frac{p - p_0}{\Delta p_*} \to p, \tag{16}$$

where the characteristic slip is given by $\delta_c(t) = f\Delta p_* L(t)/\mu$ (or alternatively by $f\Delta p_* R(t)/\mu$ if $R(t)$ is used for the spatial scale). Using this scaling, the dimensionless form of the problem depends on only two dimensionless parameters:

$$T = \frac{1 - \tau_o/f\sigma'_o}{\Delta p_*/\sigma'_o}, \tag{17}$$

and the Poisson's ratio ν. The dimensionless rupture shape $\mathcal{S}$ thus depends on both ν and T. The parameter T is similar to the one found by Bhattacharya and Viesca (2019) in their 2D plane-strain model of a frictional shear crack driven by injection at constant pressure, whereas the second dimensionless parameter, the Poisson's ratio, arises from the three-dimensional nature of the problem considered here, in which the rupture propagates in mixed mode (II+III) with an a priori unknown shape.

The *stress-injection parameter* T is crucial in the present study. It encapsulates the information about the initial state of stress acting on the fault and the characteristic injection pressure. More specifically, the numerator of T, $1 - \tau_o/f\sigma'_o$, is a measurement of the "distance" to failure under pre-injection ambient conditions (close to zero for a critically stressed fault, and close to one for a fault initially far away from frictional failure), whereas the denominator $\Delta p^*/\sigma'_o$ is an overpressure ratio which measures the amount of pressurization due to injection with regard to the initial effective normal stress. Both numerator and denominator are indeed independent parameters of a more general model for a shear crack obeying slip-weakening friction in 2-D elastic media investigated by Garagash and Germanovich (2012).

The stress-injection parameter varies between 0 and $+\infty$. The limiting values of T are associated with end-member scenarios that are relatively similar to the ones identified by Garagash and Germanovich (2012), Bhattacharya and Viesca (2019) and Viesca (2021) for two-dimensional problems involving injections at constant pressure. For small values of T, the condition $1 - \tau_o/f\sigma'_o \ll \Delta p^*/\sigma'_o$ must be satisfied. This means that the fault is "critically stressed" with regard to the overpressure ratio. For large values of T, the condition $\Delta p^*/\sigma'_o \ll 1 - \tau_o/f\sigma'_o$ must be satisfied, so that the fault is "marginally pressurized" with regard to the level of stress criticality. Hence, following these prior studies, we denominate the corresponding end-member scenarios as a *critically stressed fault* ($T \ll 1$) and a *marginally pressurized fault* ($T \gg 1$).

It is worth noting that the characteristic pressure $\Delta p_* = Q_w\eta/4\pi k w_h$ increases (and therefore the stress-injection parameter T decreases) not only when the injection volume rate Q_w grows, but also when the fluid viscosity η increases or the fault hydraulic transmissivity kw_h decreases. On the other hand, large values of T might be eventually upper bounded if the fluid pressure near the injection point is high enough to make fault opening a significant mechanism driving the propagation of the rupture. Such a problem has been already addressed in 2-D (Azad et al., 2017).

3.2. Analytical solution for circular ruptures

We first consider the particular case where the Poisson's ratio ν is set to zero such that the solution of the problem only depends on the value of T. In this limit ($\nu = 0$), the rupture front $\mathcal{R}(t)$ is circular because the energy release rate for an axisymmetric shear load distributes uniformly along the circular crack front (see Appendix B). The dimensionless rupture shape $\mathcal{S}$ is thus the unit circle and $R(t)$ is simply the rupture radius. For such a frictional shear crack with a constant friction coefficient, there is no fracture energy spent during propagation. The condition for quasi-static crack propagation then reads (see Appendix B)

$$\int_0^{R(t)} \frac{\Delta\tau(r,t)}{\sqrt{R(t)^2 - r^2}} r\mathrm{d}r = 0, \tag{18}$$

where the axisymmetric shear stress drop is given by

$$\Delta\tau(r,t) = \tau_o - f\left(\sigma'_o - \Delta p_* \Pi(r,t)\right). \tag{19}$$

The stress drop can be viewed as the contribution of two terms: a constant, negative term $\tau_o - f\sigma'_o$ which is the difference between the initial shear stress τ_o and the initial fault strength $f\sigma'_o$, and an axisymmetric and positive term $f\Delta p_* \Pi(r,t)$ capturing the local reduction of fault strength due to fluid injection. After a change of variable $s = r/R$ and incorporating the previous definition of the amplification factor $\lambda = R(t)/L(t)$ into Eq. (18), the condition for quasi-static crack propagation can be rewritten in dimensionless form as

$$\int_0^1 \frac{sE_1(s^2\lambda^2)}{\sqrt{1-s^2}}\mathrm{d}s = T. \tag{20}$$

As expected from scaling analysis, T is the only governing dimensionless parameter and, as a result, there is a unique value of λ for each value of T. The integral in Eq. (20) can be evaluated analytically to obtain the following implicit equation for λ as function of T

$$2 - \gamma + \frac{2}{3}\lambda^2 {}_2F_2\left[\begin{matrix}1 & 1 \\ 2 & 5/2\end{matrix}; -\lambda^2\right] - \ln(4\lambda^2) = T, \tag{21}$$

where $\gamma = 0.577216...$ is the Euler–Mascheroni's constant and ${}_2F_2\,[\;]$ is the generalized hypergeometric function. The relation (21) is plotted in Fig. 2. This figure shows that a critically stressed fault ($T \ll 1$) is characterized by a rupture that largely outpaces the fluid pressure front ($\lambda \gg 1$). On the other hand, a marginally pressurized fault ($T \gg 1$) is characterized by a rupture that substantially lags the fluid pressure front ($\lambda \ll 1$).

The limiting behavior of Eq. (21) for small and large λ allows to obtain simple closed-form expressions for the corresponding end-member cases. In the limit of a critically stressed fault ($\lambda \gg 1$), Eq. (21) can be asymptotically expanded as $T \sim 1/(2\lambda^2) + O(1/\lambda^4)$, leading to the following asymptotic solution for the amplification factor

$$\lambda \sim \frac{1}{\sqrt{2T}}. \tag{22}$$

Likewise in the limit of a marginally pressurized fault ($\lambda \ll 1$), Eq. (21) follows the asymptotic expansion $T \sim 2 - \gamma - \ln(4\lambda^2) + O(\lambda^2)$, that can be inverted to obtain

$$\lambda \sim \frac{1}{2}e^{(2-\gamma-T)/2}. \tag{23}$$

Since in the critically stressed limit, the pressurized fault patch is small compared to the rupture area, the fluid pressure perturbation can be approximated by a monopole distribution. Such an approximation is, in terms of local reduction of fault strength, equal to a point force given by $f\Delta p_* \Pi(r,t) \approx f\Delta p_* \left(\int_0^{+\infty} \Pi(r,t) r\mathrm{d}r\right) \delta^{dirac}(r)/r = 2\alpha f \Delta p_* t \delta^{dirac}(r)/r$, where δ^{dirac} is the Dirac delta function in polar coordinates. Replacing this approximation in Eq. (19), and then evaluating the crack propagation condition, Eq. (18), leads equivalently to the asymptotic solution for λ in the critically stressed limit, Eq. (22).

On the other hand, in the marginally pressurized limit, where the crack size is small compared to the pressurized area, the fluid pressure perturbation within the crack can be approximated by considering the behavior of the exponential integral function in Eq. (5) for small values of its argument. Such approximate injection-induced local reduction of fault strength is $f\Delta p_* \Pi(r,t) \approx -f\Delta p_* \left(2\ln\left(r/\sqrt{4\alpha t}\right) + \gamma\right)$. Again, replacing this approximation in the crack propagation condition, Eq. (18), leads alternatively to the asymptotic solution for λ in the marginally pressurized limit, Eq. (23).

The purpose of the previous analysis is to highlight the asymptotic form of the driving forces related to the two end-member cases. As we will see later, both fault slip and rupture shape will also show well-defined asymptotic behaviors, and thus the results can be directly associated with the type of force that drives the crack growth in both limiting cases.

The asymptotic solutions (22) and (23) are shown in Fig. 2 together with the general solution given by Eq. (21). Note that the transition between both propagation regimes (defined as $\lambda = 1$) occurs at $T \approx 0.5915$.

Another interesting analytical result is the rupture speed V_r that decreases with the squared root of time and is simply given by

$$V_r = \lambda\sqrt{\frac{\alpha}{t}}. \tag{24}$$

The singularity of the rupture speed at $t = 0$ is a consequence of the self-similar diffusion lengthscale $\sqrt{4\alpha t}$ and the absence of inertia. In addition, the acceleration of the rupture front is equal to $-\lambda\sqrt{\alpha}/(2t^{3/2})$. This power-law deceleration is comparable to tensile hydraulic fracture propagation under a constant injection rate albeit at a different power-law of time (Detournay, 2016).

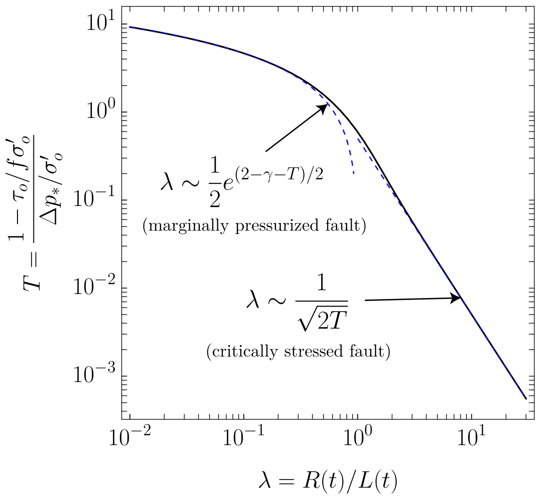

Fig. 2. Analytical solution for the amplification factor λ for circular ruptures ($\nu = 0$) driven by injection at constant volume rate. λ relates the rupture radius $R(t)$ to the nominal position of the fluid pressure front $L(t) = \sqrt{4\alpha t}$ as $R(t) = \lambda L(t)$. The amplification factor λ is a unique function of the stress-injection parameter $T = (1 - \tau_o/f\sigma_o')/(\Delta p_*/\sigma_o')$. The black curve corresponds to the analytical solution given by Eq. (21), the blue dashed curves represent the asymptotic solutions for a critically stressed fault ($T \ll 1$, $\lambda \gg 1$), Eq. (22), and a marginally pressurized fault ($T \gg 1$, $\lambda \ll 1$), Eq. (23).

3.3. Numerical solution for circular ruptures

The numerical solution for circular ruptures allows us to obtain the axisymmetric self-similar slip profiles and also to verify our numerical solver against the previously derived solution for the amplification factor $\lambda(T)$. We use the boundary-element-based solver previously described in Section 2.2 and run seven simulations for values of $T = 0.001$, 0.01, 0.1, 0.7, 2.0, 4.0 and 7.0 with $\nu = 0$. We perform 10 fully implicit time steps for each simulation.

3.3.1. Axisymmetric slip profiles and accumulated fault slip at the injection point

Fig. 3a displays typical slip and pore pressure spatial profiles at different times after the start of injection. The slip profiles correspond to the case $T = 0.1$ where the rupture front outpaces the fluid pressure front ($\lambda \approx 2.3$). Owing to the self-similarity of the problem, the slip profiles at different times collapse into one single curve under the scaling of Eq. (16). As a consequence, there is a unique dimensionless slip profile for a given value of the stress-injection parameter T. The unique self-similar slip profiles for the different values of T are shown in Fig. 3b and d for critically stressed and marginally pressurized cases, respectively. Moreover, in Appendix C, we derive closed-form analytical expressions for the self-similar slip profiles in the limiting cases of critically stressed ($\lambda \gg 1$) and marginally pressurized ($\lambda \ll 1$) faults, that are:

$$\frac{\delta(r,t)\mu}{f\Delta p_* R(t)} = \frac{8}{\pi}\left[\sqrt{1-\bar{r}^2} - |\bar{r}|\arccos(|\bar{r}|)\right] \tag{25}$$

in the marginally pressurized limit, and

$$\frac{\delta(r,t)\mu}{f\Delta p_* L(t)} = \frac{2\sqrt{2T}}{\pi}\left[\frac{\arccos(|\bar{r}|)}{|\bar{r}|} - \sqrt{1-\bar{r}^2}\right], \tag{26}$$

in the critically stressed limit, where $\bar{r} = r/R(t)$ is the self-similar radial coordinate. Eq. (26) is indeed valid for $r \gg L(t)$ and it corresponds to the "outer" solution in the critically stressed limit. Both analytical expressions are shown in Fig. 3b and d together with the numerical results.

The accumulated fault slip at the injection point, $\delta(r = 0, t)$, is plotted in Fig. 3c as a function of the stress-injection parameter T. Note that $\delta(r = 0, t)$ is normalized by the position of the fluid pressure front $L(t)$ on the left axis and by the rupture radius $R(t)$ on the right axis. $\delta(r = 0, t)$ is easily obtained from Eq. (25) in the marginally pressurized limit as

$$\delta(r=0,t) = \frac{8}{\pi}\frac{f\Delta p_*}{\mu}R(t), \tag{27}$$

whereas in the critically stressed limit,

$$\delta(r=0,t) \approx c\,\frac{f\Delta p_*}{\mu}L(t). \tag{28}$$

The prefactor c is obtained numerically and is approximately 3.5 (see Fig. 3c).

Eqs. (25) to (28) confirm that the relevant scale for the shear stress is $f\Delta p_*$, as chosen in the scaling analysis. Also, it becomes now clear that the relevant lengthscale in the problem depends on the limiting case under consideration; for marginally pressurized faults, the relevant lengthscale is the rupture radius $R(t)$, whereas for critically stressed faults, the proper lengthscale is the nominal radius of the pressurized fault patch $L(t)$.

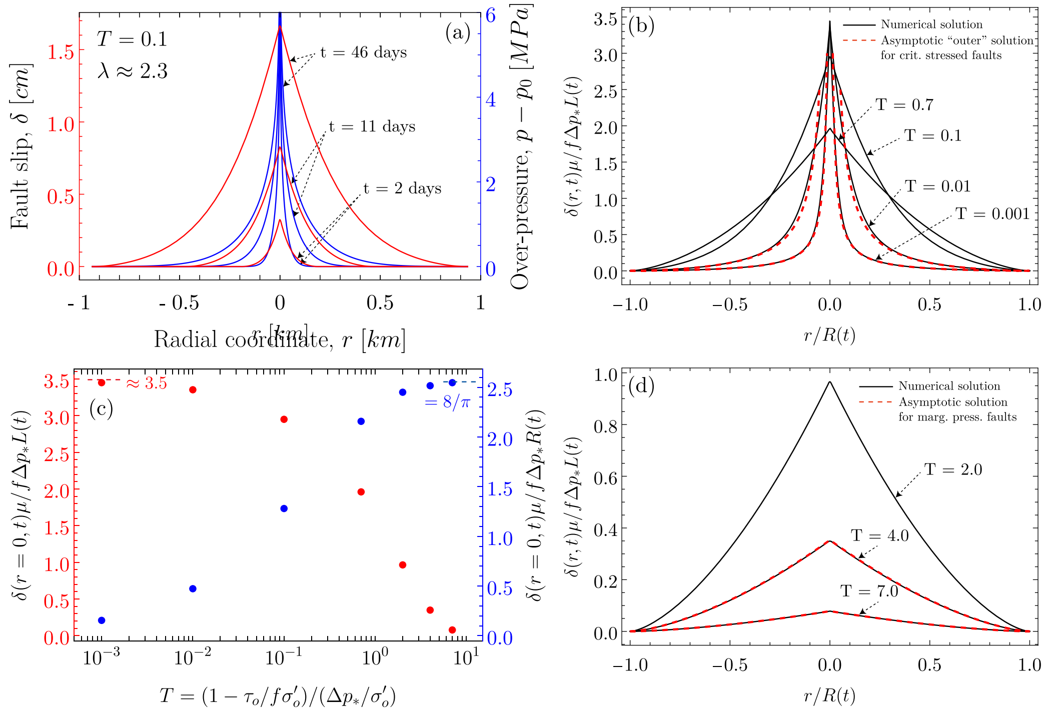

Fig. 3. (a) Axisymmetric spatial profile of slip (red) and fluid overpressure (blue) at three different times for a circular rupture driven by the injection of fluid at constant volume rate. The stress-injection parameter is $T = 0.1$ for the particular choice of simulation parameters: $\sigma_0 = 120$ [MPa], $\tau_0 = 47.958$ [MPa], $p_0 = 40$ [MPa], $f = 0.6$, $\mu = 30$ [GPa], $\nu = 0$, $\alpha = 0.01$ [m^2/s], $Q_w = 1.8$ [m^3/min], $kw_h = 3 \cdot 10^{-12}$ [m^3], $\eta = 8.9 \cdot 10^{-4}$ [Pa s]. (b) and (d) Self-similar slip profiles as a function of the self-similar radial coordinate $r/R(t)$ for different values of the stress-injection parameter T considering both numerical and asymptotic analytical solutions. (c) Normalized accumulated fault slip at the center of the rupture (the injection point) as a function of the stress-injection parameter T, including prefactors derived analytically ($8/\pi$) and numerically (3.5).

3.3.2. Rupture radius and solver verification

In order to determine numerically the instantaneous rupture radius $R(t)$ at every time step t_n and verify our numerical solver against the analytical solution, Eq. (21), we solve numerically for $R(t_n)$ by searching for the position of zero slip $\delta(R, t_n) = 0$. As the solution for slip is axisymmetric in the limit of $\nu = 0$, we search in fact for the zeros along the entire rupture front by taking 100 equally-spaced values of the angular cylindrical coordinate $\theta \in [0, 2\pi)$. In this way, we build the rupture front and compute finally the instantaneous rupture radius by fitting the equation of a circle centered at the origin to the zeros found for all the values of θ considered.

Fig. 4a shows the results for the rupture radius as a function of the nominal location of the fluid pressure front $L(t) = \sqrt{4\alpha t}$ for different values of the stress-injection parameter T. In such plot, self-similar solutions for the rupture growth in the form $R(t) = \lambda L(t)$ are represented by straight lines that cross the origin and have a slope equal to the amplification factor λ. We estimate numerically the amplification factor λ for each value of the stress-injection parameter T, by simply averaging the ratios $R(t^n)/L(t^n)$ over the different time steps of the simulation.

The numerical results for the amplification factor λ are displayed in Fig. 4b together with the analytical solution, Eq. (21). The numerical results are in excellent agreement with the theoretical predictions. This plus the previous comparison with the asymptotics of fault slip allows us to verify our numerical solver before exploring the case of non-circular ruptures, which is solved by numerical means only. The relative error between the numerical results and the exact analytical solution for the amplification factor λ is showed in the inset of Fig. 4b and is approximately below 1%.

3.4. Numerical solution for non-circular ruptures

We move now to the more general case where the Poisson's ratio is different than zero. It is important to recall that the rupture shape $\mathcal{R}(t)$ is not known a priori but, of course, remains self-similar. In order to cover the relevant parameter space, we run 21 simulations for the same seven values of the stress-injection parameter T considered in the previous section, 0.001, 0.01, 0.1, 0.7, 2.0, 4.0 and 7.0, for three values of the Poisson's ratio $\nu = 0.15$, 0.30, and 0.45.

3.4.1. Rupture shape

We quickly recognize in our simulations that the ruptures evolve systematically in a nearly elliptical shape. We also observe that the aspect ratio of the ruptures depends strongly not only on the Poisson's ratio but also on the stress-injection parameter T, i.e., on

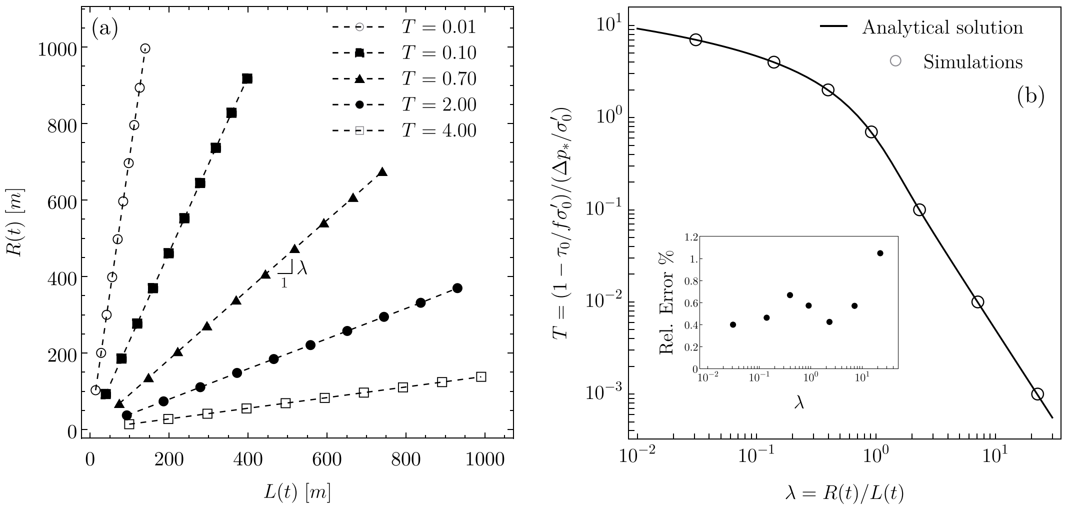

Fig. 4. (a) Simulation results for the rupture radius $R(t)$ as a function of the fluid pressure front location $L(t) = \sqrt{4\alpha t}$ for different values of the stress-injection parameter T. Self-similar solutions of the rupture growth in the form $R(t) = \lambda L(t)$ are represented by straight lines that cross the origin and have a slope equal to the amplification factor λ. (b) Comparison between the numerical results for the amplification factor λ and the exact value given by the analytical solution, Eq. (21). The relative error for λ as $(\lambda^{num} - \lambda^{exact})/\lambda^{exact}$ is displayed in the inset.

the initial stress state and the driving force itself. Snapshots of two rupture simulations having the same Poisson's ratio but different values of the stress-injection parameter are shown in Fig. 5a–b. It is clear that the aspect ratio for critically stressed faults (Fig. 5a, $T = 0.001$, $\lambda \gg 1$) is higher than the aspect ratio for marginally pressurized faults (Fig. 5b, $T = 7.0$, $\lambda \ll 1$).

In order to quantify the rupture shape, we perform a nonlinear regression of the rupture front at every time step assuming an elliptical shape:

$$\mathcal{R}(t) = \left\{ (x, y, z = 0) : \left(\frac{x}{a(t)}\right)^2 + \left(\frac{y}{b(t)}\right)^2 = 1 \right\}, \tag{29}$$

where a and b are the semi-major and semi-minor axes of the ellipse. We use the same procedure described previously to estimate the rupture front, with the only difference that now the spatiotemporal evolution of slip is no longer axisymmetric. Typical ellipsoidal fits of the rupture front are displayed in Fig. 5a–b. Further details of the computation of the rupture fronts can be found in Appendix E, in which an estimate of the misfit between the ellipsoidal fits and the actual numerical front is also provided.

The results for the aspect ratio a/b as a function of the stress-injection parameter T and the Poisson's ratio ν are summarized in Fig. 5c. Note that the aspect ratio is time-invariant due to the self-similarity of the problem, thus, we average the aspect ratio over the simulations' time steps for better accuracy. Fig. 5c displays clearly two asymptotic behaviors of the aspect ratio for the two end-member cases of a critically stressed fault and a marginally pressurized fault. Additional simulations were run to better explore the dependence on Poisson's ratio for $T = 0.001$ ($\lambda \approx 22.37$, critically stressed faults) and $T = 7.0$ ($\lambda \approx 0.03$, marginally pressurized faults). The results are shown in Fig. 5d. We notably found by numerical observation that the aspect ratio grows asymptotically with the Poisson's ratio as

$$\begin{cases} a/b \sim 1/(1-\nu) & \text{for critically stressed faults } (T \ll 1,\ \lambda \gg 1) \\ a/b \sim (3-\nu)/(3-2\nu) & \text{for marginally pressurized faults } (T \gg 1,\ \lambda \ll 1) \end{cases} \tag{30}$$

It is interesting to note that the aspect ratio for critically stressed faults, $a/b \sim 1/(1-\nu)$, is similar to the results obtained by Gao (1988) and Elie et al. (2006) for three dimensional planar shear-crack under uniform remote loading and a uniform energy release rate along the crack front.

3.4.2. Generalized amplification factor λ

Since the rupture front $\mathcal{R}(t)$ is self-similar and nearly elliptical, we can write $a(t) = \lambda_a L(t)$ and $b(t) = \lambda_b L(t)$, where λ_a and λ_b are the corresponding amplification factors for the semi-major and semi-minor axes of the rupture front, respectively. Note that λ_a and λ_b depend only on the stress-injection parameter T and the Poisson's ratio ν. The evolution of $a(t)$ and $b(t)$ as a function of the fluid pressure front location $L(t) = \sqrt{4\alpha t}$ is shown in Fig. 6a for different values of the stress-injection parameter T and the Poisson's ratio ν. In this figure, we also include the reference circular case $\nu = 0$, and indicate the meaning of λ_a, λ_b, and λ as the slopes of the straight lines for $a(t)$, $b(t)$, and $R(t)$ (of the reference circular case), respectively. Fig. 6a shows that the major and minor axes for the elliptic ruptures ($\nu \neq 0$) lie about the radius for the reference circular solution ($\nu = 0$). For a given value of T and any value of ν, we find that the geometric mean of $a(t)$ and $b(t)$, $\sqrt{a(t)b(t)}$, is equal to the radius $R(t)$ of the circular crack solution for the same

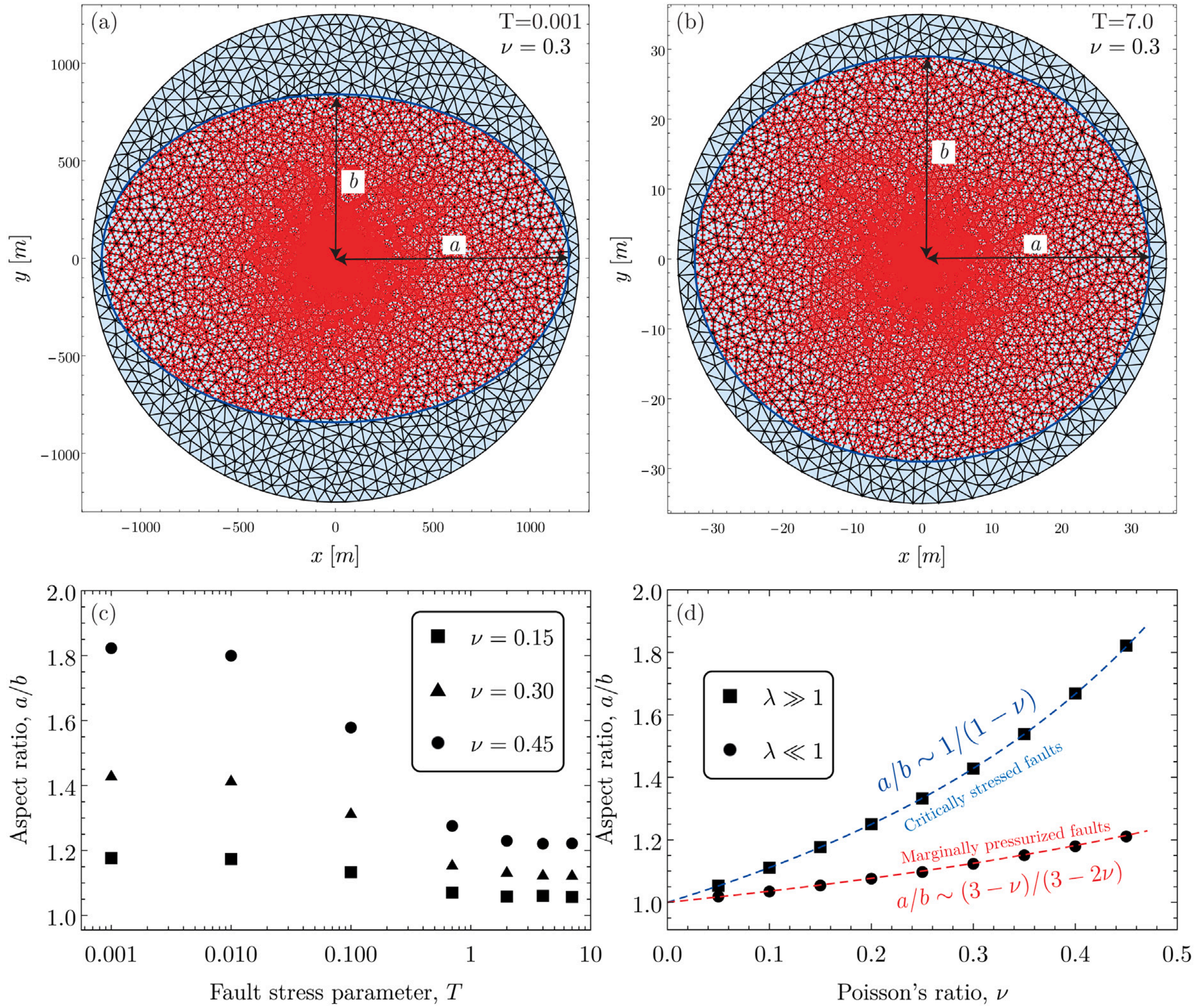

Fig. 5. Typical simulations' snapshots and ellipsoidal fits (blue curves) of the rupture front for $\nu = 0.3$ and (a) $T = 0.001$ ($\lambda \approx 22.37$, a critically stressed fault) and (b) $T = 7.0$ ($\lambda \approx 0.03$, a marginally pressurized fault). The red points indicate the collocation points that have slipped. In the background, the unstructured mesh made on triangular boundary elements with quadratic shape functions. (c) Aspect ratio a/b as a function of the stress-injection parameter T for different values of the Poisson's ratio ν. (d) Aspect ratio a/b with increased resolution for the Poisson's ratio ν for the two end-member cases, $T = 0.001$ ($\lambda \approx 22.37$, critically stressed faults) and $T = 7.0$ ($\lambda \approx 0.03$, marginally pressurized faults).

value of T (and $\nu = 0$). This equality is equivalent to the equality of amplification factors

$$\lambda = \sqrt{\lambda_a \lambda_b} = \frac{\sqrt{a(t)b(t)}}{L(t)} \tag{31}$$

This is demonstrated in the inset of Fig. 6a in which the numerical values of $\lambda^{num} = \sqrt{\lambda_a \lambda_b}$ for all values of T and ν are plotted against the exact solution for circular ruptures λ^{circ}.

The numerical results for Eq. (31) are plotted in Fig. 6b together with the analytical solution, Eq. (21), for all values of T and ν. In the inset, the relative difference between the numerical results and the analytical solution are also displayed. Fig. 6b thus demonstrates that Eq. (31) is a generalization of the amplification factor that is now valid for any value of the Poisson's ratio. In the particular case of $\nu = 0$, Eq. (31) reduces simply to $\lambda = R(t)/L(t)$, as originally defined when deriving the analytical solution for the circular rupture case.

3.4.3. Poisson's ratio-independent rupture area

The generalized amplification factor $\lambda = \sqrt{\lambda_a \lambda_b}$ has a clear physical meaning. Indeed, it is equivalent to the squared root of the ratio between the instantaneous elliptic rupture area $A_r(t) = \pi a(t)b(t)$ and the instantaneous pressurized area $\pi L^2(t)$: $\lambda = \sqrt{A_r(t)/(\pi L^2(t))}$ such that the evolution of the rupture area $A_r(t)$ is simply given by

$$A_r(t) = 4\pi\alpha\lambda^2 t \tag{32}$$

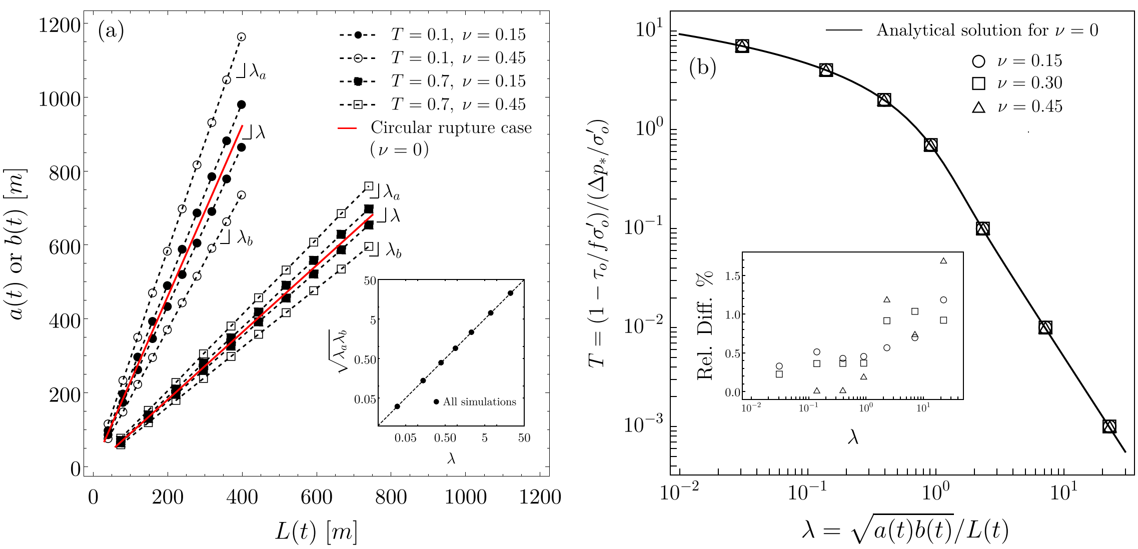

Fig. 6. (a) Evolution of the semi-major $a(t)$ and semi-minor $b(t)$ axes of quasi-elliptical ruptures as a function of the fluid pressure front location $L(t)$ for different values of the **stress-injection parameter** T and Poisson's ratio ν. Solid red lines correspond to the analytical solution for $\nu = 0$, Eq. (21). λ_a and λ_b are the slopes of the straight lines for $a(t)$ and $b(t)$, respectively. Inset: comparison between the numerical results for the geometric mean $\sqrt{\lambda_a \lambda_b}$ and the exact analytical solution for circular ruptures λ^{circ}. (b) Comparison between the numerical values of the generalized amplification factor $\lambda^{num} = \sqrt{\lambda_a \lambda_b} = \sqrt{a(t)b(t)}/L(t)$ (symbols) and λ^{circ} (solid line). Inset: the relative difference $(\lambda^{num} - \lambda^{circ})/\lambda^{circ}$ as a function of the amplification factor λ^{circ}.

and is thus independent of the value of the Poisson's ratio ν. The Poisson's ratio (together with the value of T) modifies the shape of the ruptures, which are more or less elongated, but it does not modify the rupture area, which solely depends on T. The rupture area A_r evolves linearly with time and proportionally to the injected volume ($\propto V$) for such a constant injection rate case.

Furthermore, for the two end-member cases of critically stressed and marginally pressurized faults, Eqs. (22) and (23) lead to simple closed-form expressions for the evolution of the rupture area as function of the stress-injection parameter T

$$\begin{cases} A_r(t) \sim 2\pi\alpha t/T & \text{for critically stressed faults } (\mathrm{T} \ll 1,\ \lambda \gg 1) \\ A_r(t) \sim \pi\alpha e^{2-\gamma-T} t & \text{for marginally pressurized faults } (T \gg 1,\ \lambda \ll 1) \end{cases} \tag{33}$$

It is worth noting that David and Lazarus (2022) obtained recently a somewhat similar result in their study of tensile crack growth under the Paris' fatigue law (with a uniform energy release rate being a limiting case). They found, also by numerical observation, that a circular crack solution is sufficient to predict the area of a rupture for any non-circular crack.

3.4.4. *Rupture front $\mathcal{R}(t)$ for the end-member cases*

The asymptotic expressions for the aspect ratio (30) plus Eq. (33), lead to the following closed-form expressions for the evolution of the semi-major $a(t)$ and semi-minor $b(t)$ axes of the rupture front for critically stressed faults ($\lambda \gg 1$):

$$a(t) \sim \sqrt{\frac{2\alpha t}{(1-\nu)T}}, \quad b(t) \sim \sqrt{\frac{(1-\nu)\,2\alpha t}{T}}, \tag{34}$$

and for marginally pressurized faults ($\lambda \ll 1$)

$$a(t) \sim \sqrt{\frac{3-\nu}{3-2\nu}}\sqrt{\alpha t} \cdot e^{(2-\gamma-T)/2}, \quad b(t) \sim \sqrt{\frac{3-2\nu}{3-\nu}}\sqrt{\alpha t} \cdot e^{(2-\gamma-T)/2}. \tag{35}$$

Since the rupture front is quasi-elliptical, Eqs. (34) and (35) fully define the spatiotemporal evolution of the rupture front $\mathcal{R}(t)$ for the end-member cases.

3.4.5. *Non-axisymmetric slip profiles and accumulated fault slip at the injection point*

The non-axisymmetric self-similar slip profiles are unique for a given combination of T and ν. Some typical slip profiles along the x-axis (normalized by $a(t)$) are shown in Fig. 7a–b for different values of the stress-injection parameter T and $\nu = 0.3$. The accumulated fault slip at the injection point $\delta(r = 0, t)$ is plotted in Fig. 7c for all simulations as a function of the stress-injection parameter T and the Poisson's ratio ν. In Fig. 7c, we include the circular rupture case ($\nu = 0$) and $\delta(r = 0, t)$ is further normalized in Fig. 7d by the geometric mean $\sqrt{a(t)b(t)}$ which is Poisson's ratio-independent and in the limit of $\nu \to 0$ corresponds to the rupture radius $R(t)$.

Fig. 7c–d shows that the accumulated fault slip at the injection point decreases for increasing values of the Poisson's ratio. In addition, we recover a similar scaling for $\delta(r = 0, t)$ that in the circular rupture case: $\delta(r = 0, t) \sim f\Delta p_* R(t)/\mu$ in the marginally pressurized limit, with the characteristic rupture scale $R(t)$ taken as $\sqrt{a(t)b(t)}$ in Fig. 7d; and $\delta(r = 0, t) \sim f\Delta p_* L(t)/\mu$ in the critically stressed limit.

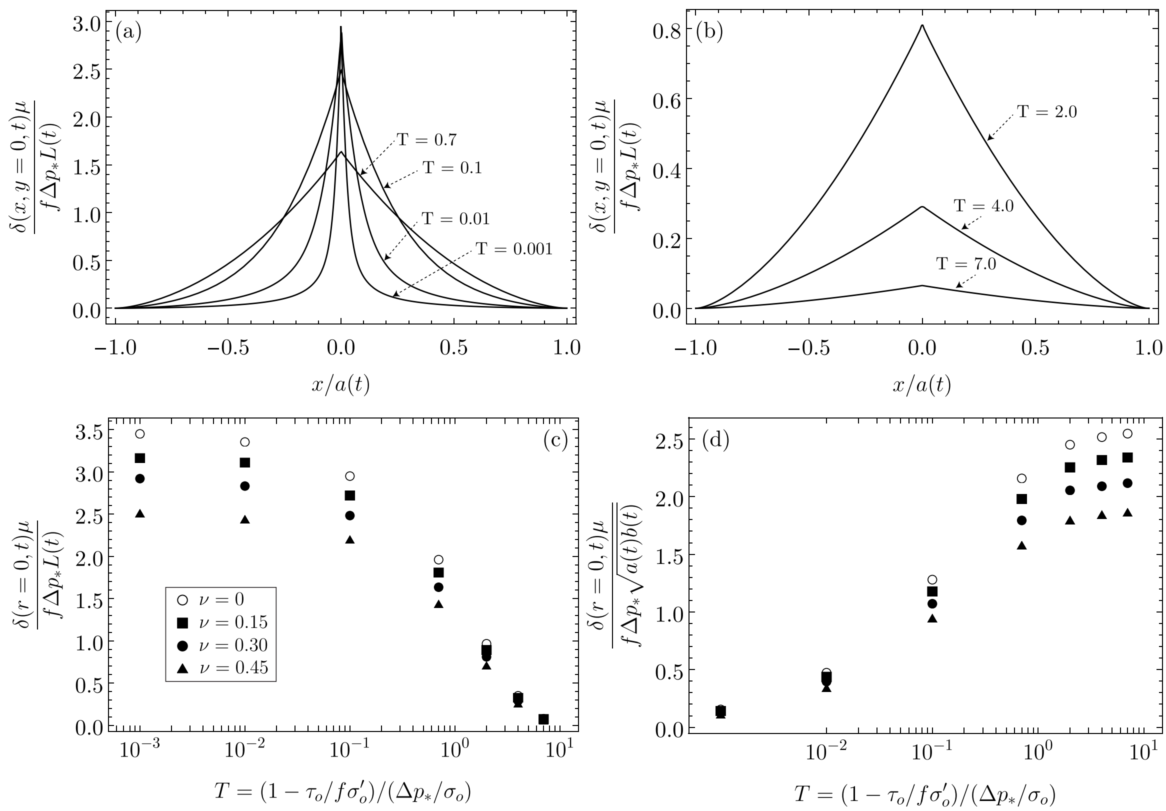

Fig. 7. (a) and (b) Self-similar slip profiles along the x-axis (normalized by $a(t)$) for different values of the stress-injection parameter T and for $\nu = 0.3$. (c) and (d) Normalized accumulated fault slip at the injection point as a function of the stress-injection parameter T for different values of the Poisson's ratio, scaled by $L(t)$ and $R(t) = \sqrt{a(t)b(t)}$, respectively.

3.5. Aseismic moment

The scalar moment release M_0 is a key measurement in seismology to quantify the potency of a rupture (Aki and Richards, 2002). In our planar fault model with a uniform direction of slip δ, the time-dependent aseismic moment (we focus on the case of a circular rupture) is $M_0(t) = 2\pi\mu \int_0^{R(t)} \delta(r, t) r \mathrm{d}r$, where $R(t)$ is the evolving rupture radius. We can thus compute the aseismic moment numerically for all the seven values of T considered. Furthermore, we can use the asymptotic solutions of the slip distribution, Eqs. (25) and (26), to derive closed-form expressions for the limiting behaviors of the aseismic moment. We obtain that

$$M_0(t) \sim \frac{16}{9} f \Delta p_* R^3(t) \tag{36}$$

in the marginally pressurized limit, and

$$M_0(t) \sim \frac{8}{3} f \Delta p_* L^2(t) R(t) \tag{37}$$

in the critically stressed limit.

Both previous equations provide the proper scaling of the aseismic moment. We use these scalings to normalized the numerical results that are presented in Fig. 8 as a function of the stress-injection parameter T. In this figure, we include the corresponding prefactors of Eqs. (36) and (37). Note that the prefactor 8/3 in the critically stressed limit is in good agreement with the numerical solution, despite the slip profile being approximated by the "outer" asymptotic solution of this limit only.

Moreover, Eqs. (36) and (37) allow us to establish the corresponding scaling relation between the moment release M_0 and the injected volume V that has been extensively sought with the purpose of constraining the magnitude of injection-induced earthquakes (McGarr, 2014; van der Elst et al., 2016; Galis et al., 2017; McGarr and Barbour, 2018). Because $R(t) = \lambda L(t)$, $L(t) = \sqrt{4\alpha t}$ and $V(t) = Q_w t$, the aseismic moment M_0 scales to the injected volume V as

$$M_0 \propto V^{3/2}. \tag{38}$$

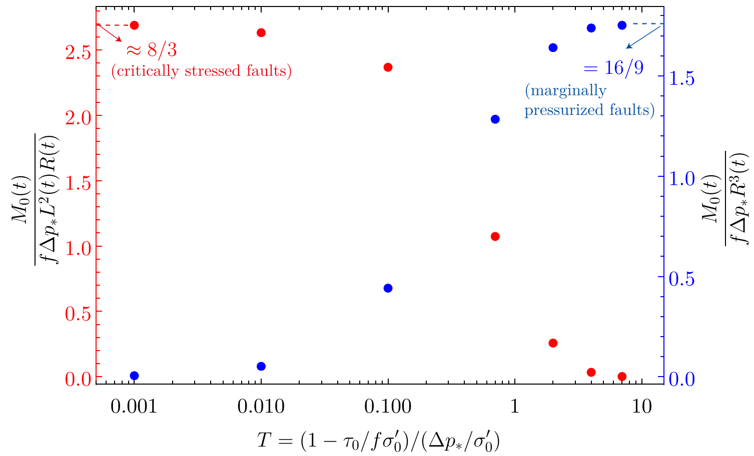

Fig. 8. Normalized aseismic moment for circular ruptures ($\nu = 0$) as a function of the stress-injection parameter T. Numerical results and asymptotic behaviors for critically stressed ($T \ll 1$, $\lambda \gg 1$) and marginally pressurized ($T \gg 1$, $\lambda \ll 1$) faults.

4. Non-self-similar rupture growth due to injection at constant pressure

4.1. Scaling and similarity

Under the scenario of constant pressure injection, the evolution of fluid pressure given by Eq. (6) is no longer self-similar. This is due to the presence of a finite wellbore radius r_w where the pressure is set constant which introduces a new characteristic length in the problem. As a result, the frictional rupture will not evolve self-similarly, like for a constant injection rate. We recall that self-similar solutions always correspond to idealized models in which the dimensional parameters of the independent variables (space and time in our case) are equal to zero or infinity (Barenblatt, 1996). The infinitesimal nature of the constant-volume-rate fluid source of the previous section and its subsequent self-similarity, can be seen in fact as an intermediate-asymptotic behavior of a more realistic physical system in which both the fluid source and the domain are finite. In this view, the solution of Section 3 is valid for times $t \gg r_*^2/\alpha$, where r_* is the characteristic length of the fluid source, and for $t \ll R_*^2/\alpha$, where R_* is the characteristic length of a finite domain. Note that the introduction of, for instance, a frictional lengthscale to the problem of injection at constant volume rate, would also cause the loss of self-similarity in the model.

The scaling thus differs slightly from the scaling of the previous section. The finite wellbore radius r_w introduces a characteristic diffusion timescale $t_c = r_w^2/\alpha$ with α the fault hydraulic diffusivity, such that we obtain:

$$\frac{t}{t_c} \to t, \quad \frac{\vec{x}}{r_w} \to \vec{x}, \quad \frac{\tau - f\sigma_o'}{f\Delta p_w} \to \tau, \quad \frac{\delta}{\delta_c} \to \delta, \quad \frac{p - p_0}{\Delta p_w} \to p, \tag{39}$$

where Δp_w is the constant overpressure imposed at the wellbore, and $\delta_c = f\Delta p_w r_w/\mu$ is the characteristic slip.

As already mentioned, the loss of self-similarity is due to the finite size of the wellbore. In fact, radial flow from an infinitesimal fluid source at constant pressure is not physically possible. Injection of a finite volume from an infinitesimal fluid source in such geometrical conditions always leads to infinite pressure.

The dimensionless solution of the problem depends now on three dimensionless parameters, a slightly different stress-injection parameter T that is a function of the constant wellbore overpressure Δp_w

$$T = \frac{1 - \tau_o/f\sigma_o'}{\Delta p_w/\sigma_o'}, \tag{40}$$

the Poisson's ratio ν, and the dimensionless time $\alpha t/r_w^2$.

The limiting values of T are determined by the condition for fault slip activation, $f\Delta p_w \geq f\sigma_o' - \tau_o$, and the condition for no slip prior to injection, $f\sigma_o' - \tau_o > 0$. Together, these conditions imply that T varies between 0 and 1, so that the stress-injection parameter is now upper bounded, unlike the case of injection at constant volume rate in which T can theoretically go up to $+\infty$.

The limit of $T \to 1$ is characterized by the condition $f\Delta p_w \to f\sigma_o' - \tau_o$. This condition can be interpreted as a scenario in which the pressure at the fluid source, Δp_w, is just enough to activate fault slip. This is the reason why such end-member case has been named in prior studies as *marginally pressurized faults* (Garagash and Germanovich, 2012; Bhattacharya and Viesca, 2019; Viesca, 2021). On the other hand, considering that Δp_w is always positive and finite, the limit of $T \to 0$ is associated with the condition $\tau_0 \to f\sigma_0'$. This condition represents the case of faults that are about to fail before injection, and is thus named as *critically stressed faults*. Unlike the problem of injection at constant volume rate in which the fluid pressure near the injection point is always increasing, here the pressure at the wellbore is fixed and thus the terminology of *critically stressed* and *marginally pressurized* faults is unambiguous. Note that $\sigma_0' > \Delta p_w > 0$, with the upper bound being the transition to fault opening that we do not cross in this study.

4.2. Approximate analytical solution for circular ruptures

The solution of the diffusion equation for injection at constant pressure from a finite source, Eq. (6), does not allow to treat the problem of a circular rupture analytically. Nevertheless, as we are interested in solutions for times that are in general large compared to the characteristic diffusion time, $t_c = r_w^2/\alpha$, we can use the following asymptotic expansion for the instantaneous pressure profile that is valid for $t \gg t_c$ (Jaeger, 1955)

$$\Pi(r,t) \approx 1 - 2\ln(\bar{r})\left\{\frac{1}{\ln(4\bar{t}) - 2\gamma} - \frac{\gamma}{(\ln(4\bar{t}) - 2\gamma)^2}\right\} \tag{41}$$

where $\bar{r} = r/r_w$ and $\bar{t} = \alpha t/r_w^2$ are the dimensionless radial coordinate and the dimensionless time, respectively, and $\gamma = 0.577216...$ is the Euler–Mascheroni's constant.

Fig. 9a shows the comparison between the *exact* numerical solution for the fluid pressure profile, Eq. (6) (solved via numerical inversion of the Laplace transform, Stehfest, 1970) and the asymptotic expansion (41). In Fig. 9a, we also include an asymptotic expansion of $\Pi(r,t)$ with higher order corrective terms that are function of $\bar{r}$ and the successive time derivatives of the terms in curly brackets in (41) (Jaeger, 1955). The higher order terms have cumbersome expressions but are necessary to capture the "near front" behavior of the fluid pressure profile as shown in Fig. 9a. However, for the sake of simplicity, we neglect these corrective terms in the following.

Similarly to the case of injection at constant volume rate, we define the instantaneous rupture radius $R(t)$ and use the condition for quasi-static propagation of a circular crack with zero fracture energy under axisymmetric shear load, Eq. (18), with now $\Delta\tau(r,t) = \tau_o - f\left(\sigma'_o - \Delta p_w \Pi(r,t)\right)$. After some algebraic operations, this propagation condition can be rewritten as

$$\frac{1}{R(t)}\int_0^{R(t)} \frac{\Pi(r,t)}{\sqrt{R(t)^2 - r^2}} r\mathrm{d}r = T \tag{42}$$

where T is the stress-injection parameter defined in Eq. (40) for the constant pressure injection case. We approximate $\Pi(r,t) = \left(p(r,t) - p_0\right)/\Delta p_w$ by the asymptotic expansion (41). Note that in Eq. (41), one could consider to drop the term of $O\left(1/\ln(\bar{t})^2\right)$ and use a first-order approximation for $\Pi(r,t)$ instead; however, we found that better results are systematically obtained by keeping the second order term in any further mathematical operation and performing first-order approximations afterwards.

The integration limits of Eq. (42) have to be considered carefully, since the asymptotic expansion for $\Pi(r,t)$ gives non-physical values that are greater than unity for $r/r_w < 1$ and negative for r/r_w beyond the intersection with the abscissa (see Fig. 9a). In fact, the intersection with the abscissa defines conveniently a nominal position of the fluid pressure front, $\tilde{L}(t)/r_w = \exp(-(1/2)\left(2\gamma - \ln\left(4\bar{t}\right)\right)^2/\left(3\gamma - \ln\left(4\bar{t}\right)\right))$, that is given at the first order by

$$\tilde{L}(t) = \sqrt{c_1 \alpha t} \tag{43}$$

where $c_1 = e^{\ln(4)-\gamma} = 2.245838... \approx 2.25$. The position of the fluid pressure front $\tilde{L}(t)$ given by Eq. (43) is shown in Fig. 9a at different dimensionless times. With a change of variable $s = r/R$ and taking care of the integration limits as discussed before, we can rewrite Eq. (42) in dimensionless form as

$$\int_0^{\beta_0} \frac{1}{\sqrt{1-s^2}} s\mathrm{d}s + \int_{\beta_0}^{\beta} \frac{\Pi(sR,t)}{\sqrt{1-s^2}} s\mathrm{d}s = T \tag{44}$$

where $\beta_0 = r_w/R$, and $\beta = 1$ if $R \le \tilde{L}$, or $\beta = \tilde{L}/R$ otherwise ($R > \tilde{L}$).

Eq. (44) can be solved to obtain the evolution of the normalized rupture radius $R(t)/r_w$ as a function of the dimensionless time $\alpha t/r_w^2$ and the stress-injection parameter T. The solution is piecewise due to the piecewise definition of β that indeed separates the two possible rupture regimes. One regime is characterized by $R(t) < \tilde{L}(t)$ which represents a rupture front that lags the fluid pressure front, whereas the other regime is characterized by $R(t) > \tilde{L}(t)$ in which the rupture front outpaces the fluid pressure front.

In addition, the first integral of the left-hand side of Eq. (44) can be neglected if we assume that the rupture radius $R(t)$ is much bigger than the wellbore radius r_w, so that $\beta_0 = r_w/R \ll 1$. Hereafter, we consider $\beta_0 = 0$. Let us first consider the case in which $R(t) < \tilde{L}(t)$. After integrating Eq. (44) with $\beta = 1$, we obtain at the first order the following explicit expression for the evolution of the normalized rupture radius in the form of a power-law

$$R(t)/r_w = g(T)\left(\frac{\alpha t}{r_w^2}\right)^{(1-T)/2} \tag{45}$$

where $g(T) = c_2 e^{-c_3 T}$, with $c_2 = e^{(2-\gamma)/2} = 2.036825...$ and $c_3 = (\ln(4) - \gamma)/2 = 0.404539....$

Note that the transition between the two rupture regimes happens at a certain time t^* when $R(t^*) = \tilde{L}(t^*)$. Using the first-order Eqs. (43) and (45), we obtain that this transition time is

$$\frac{\alpha t^*}{r_w^2} = \left(\frac{g(T)}{c_1}\right)^{2/T} \tag{46}$$

Finally, the solution for the case $R(t) > \tilde{L}(t)$ is obtained by integrating Eq. (44) with $\beta(t) = \tilde{L}(t)/R(t)$. The solution for the rupture radius is now implicit and it is given by

$$f_1(\beta)\ln\left(R(t)/r_w\right) + f_2(\beta) = \ln\left(\tilde{L}(t)/r_w\right)\left(f_1(\beta) - T\right) \tag{47}$$

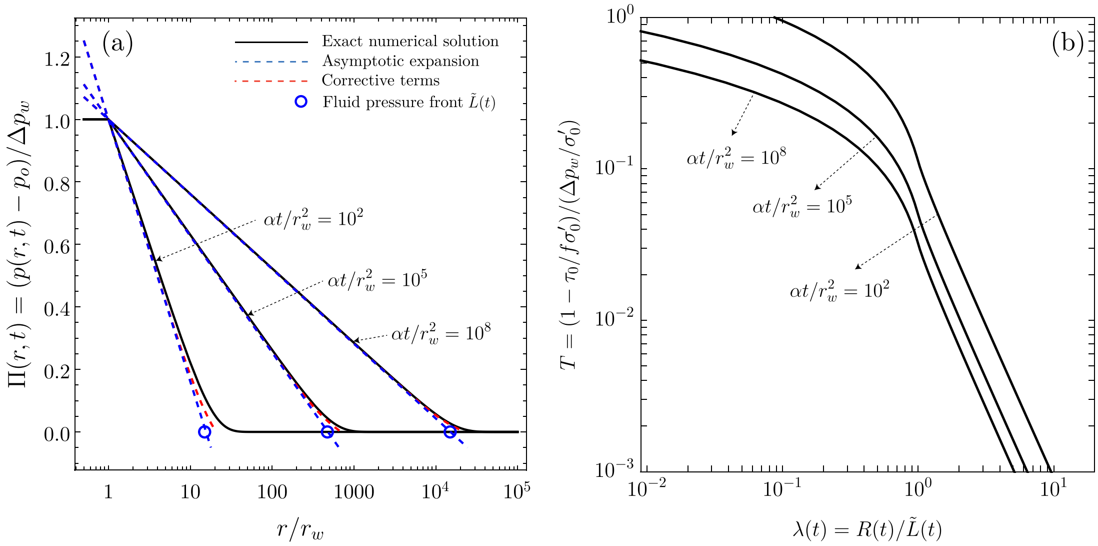

Fig. 9. (a) Instantaneous spatial profile of fluid pressure for injection at constant pressure, $\Pi(r,t)$, as function of the dimensionless radial coordinate r/r_w at different dimensionless times $\alpha t/r_w^2$. Comparison between the exact solution given by Eq. (6), the asymptotic expansion (41) valid for $\alpha t/r_w^2 \gg 1$, and an asymptotic expansion with higher order corrective terms (Jaeger, 1955). (b) Approximate analytical solution for circular ruptures driven by injection at constant pressure, given by the amplification factor $\lambda(t) = R(t)/\tilde{L}(t)$ as a function of the stress-injection parameter T at different dimensionless times $\alpha t/r_w^2$.

where

$$f_1(\beta) = 1 - \sqrt{1-\beta^2}, \text{ and } \quad f_2(\beta) = \ln\left(\frac{2\beta}{1+\sqrt{1-\beta^2}}\right) + \sqrt{1-\beta^2}\,(1 - \ln(\beta)) - 1 \tag{48}$$

Eqs. (45) to (48) can be used to define a time-dependent amplification factor in the form $\lambda(t) = R(t)/\tilde{L}(t)$. Such approximate analytical solution for $\lambda(t)$ is plotted in Fig. 9b at different dimensionless times, as a function of the stress-injection parameter T.

4.3. Numerical solution for circular ruptures

We now solve numerically for the case of circular ruptures to obtain the evolution of the axisymmetric slip profiles $\delta(r,t)$. In addition, the computation of the slip profiles allows us to calculate numerically the rupture radius $R(t)$ and test the accuracy of the approximate analytical solution derived in the previous section. For this purpose, we run six simulations for values of the stress-injection parameter $T = 0.01$, 0.1, 0.3, 0.5, 0.7 and 0.9 and set $\nu = 0$. We perform 9 fully implicit time steps per simulation for values of the dimensionless time logarithmically spaced between 1 to 10^8.

4.3.1. Axisymmetric slip profiles and accumulated fault slip at the rupture center

Fig. 10a, b and c display the non-self-similar slip profiles for different values of the stress-injection parameter T. Since the solution is not self-similar, the dimensionless slip profiles are not unique for a single value of the stress-injection parameter, but rather time-dependent. Note that the slip profiles near the injection point are now smooth due to the finite size of the fluid source. On the other hand, Fig. 10d shows the normalized accumulated fault slip at the center of the rupture $\delta(r=0,t)$ as a function of the dimensionless time $\alpha t/r_w^2$ for different values of the stress-injection parameter T. This figure suggests that at large times $\delta(r=0,t) \sim (f\Delta p_w/\mu)R(t)$, up to a factor 0.1 to 0.2 approximately, for the values of T considered.

4.3.2. Rupture radius and comparison with approximate analytical solution

Based on the numerical solution of the axisymmetric slip profiles $\delta(r,t)$, we compute the instantaneous rupture radius $R(t)$ at every time step for each simulation. We use the same procedure described in Section 3.3 for building the rupture front and computing the rupture radius. The results are plotted in Fig. 11a together with the approximate analytical solution derived in the previous section.

The approximate analytical solution (valid for large times, $\alpha t/r_w^2 \gg 1$) is in good agreement with the numerical results for values of T ranging from 0.1 to 0.7, with an average relative difference of about 5%. Near the limit of a marginally pressurized fault ($T = 0.9$), the analytical solution is less accurate (average relative difference around 20%) due to the fact that the assumption $R(t) \gg r_w$ is not properly satisfied. On the other hand, near the limit of a critically stressed fault ($T = 0.01$), the analytical solution loses accuracy possibly due to the fact that the "near front" behavior of the fluid pressure profile is not well captured by the asymptotic expansion, Eq. (41). The absolute value of the relative difference between the approximate analytical solution and the numerical results is around 30% in average.

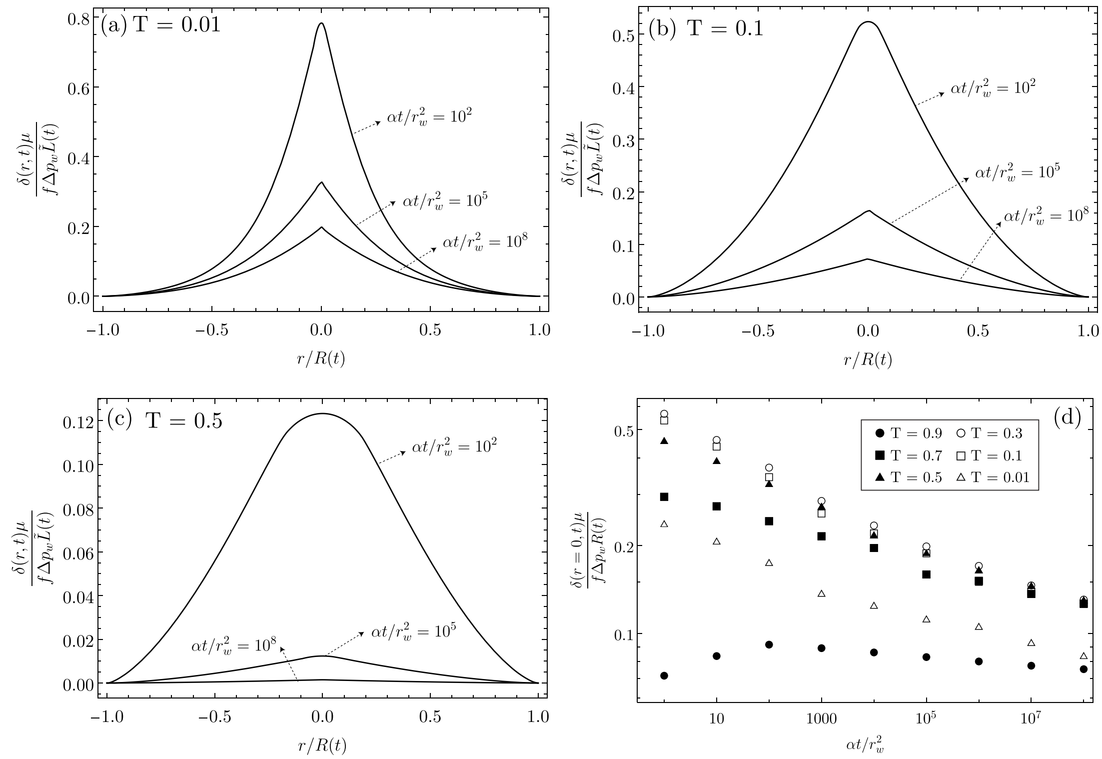

Fig. 10. Non-self-similar normalized slip profiles for circular ruptures driven by injection at constant pressure as a function of the normalized radial coordinate $r/R(t)$ at different dimensionless times $\alpha t/r_w^2$. (a) Stress-injection parameter $T = 0.01$, (b) $T = 0.1$, (c) $T = 0.5$. (d) Normalized accumulated fault slip at the center of the rupture as a function of dimensionless time $\alpha t/r_w^2$ for different values of the stress-injection parameter T.

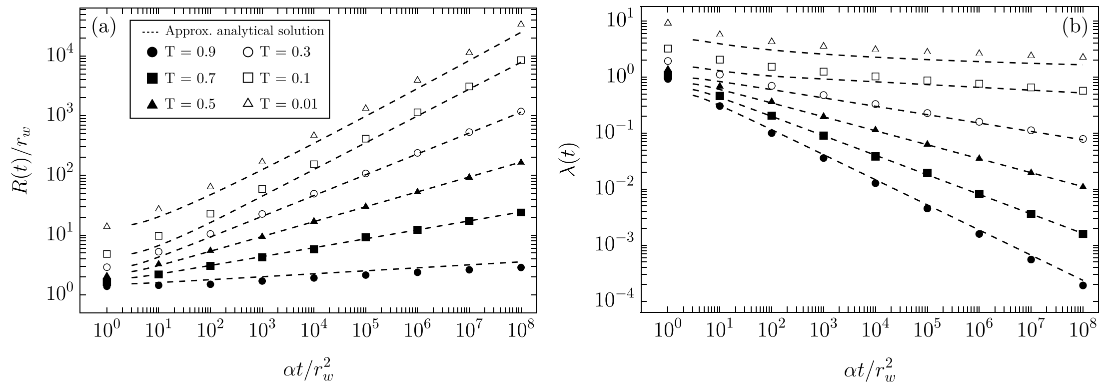

Fig. 11. Comparison between numerical results and approximate analytical solution for circular ruptures driven by injection at constant pressure. (a) Dimensionless rupture radius $R(t)/r_w$ as a function of dimensionless time $\alpha t/r_w^2$ for different values of the stress-injection parameter T. (b) Same as (a) but for the time-dependent amplification factor $\lambda(t) = R(t)/\tilde{L}(t)$.

Finally, Fig. 11b displays the numerical results for the time-dependent amplification factor $\lambda(t) = R(t)/\tilde{L}(t)$ and the corresponding approximate analytical solution for it. Note that for values of $T \gtrsim 0.7$, the rupture lags the fluid pressure front at all times, whereas for $T \lesssim 0.01$ the rupture outpaces the fluid pressure front at all times considered here. The case of intermediate values, $0.5 \lesssim T \lesssim 0.1$, is interesting because a transition of propagation regime occurs at early times.

4.4. Numerical solution for non-circular ruptures

Finally, we solve numerically for the more general case where the Poisson's ratio is different than zero. We run 12 simulations for four values of the stress-injection parameter $T = 0.1$, 0.3, 0.5, and 0.7, plus three values of the Poisson's ratio $\nu = 0.15$, 0.30, and 0.45.

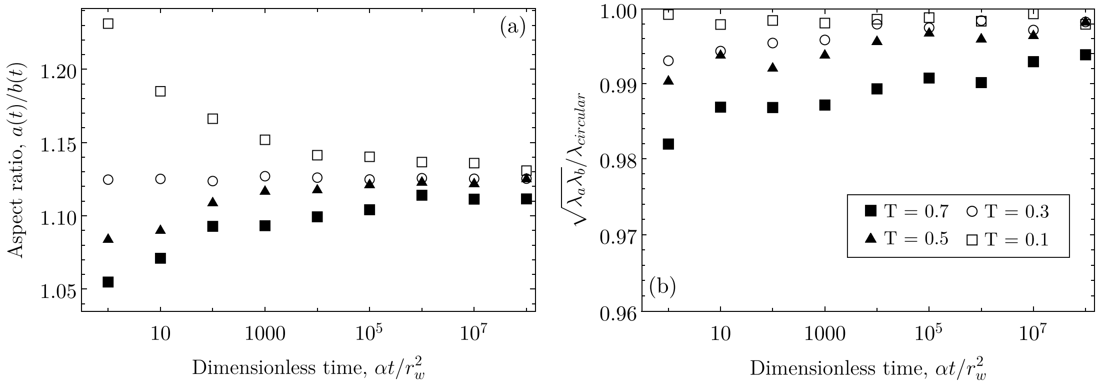

Fig. 12. (a) Aspect ratio a/b as a function of dimensionless time $\alpha t/r_w^2$ for different values of the stress-injection parameter T. (b) Geometric mean $\sqrt{\lambda_a(t)\lambda_b(t)}$ for $\nu = 0.3$ divided by the amplification factor for circular ruptures ($\nu = 0$), $\lambda_{circular}$, as a function of dimensionless time $\alpha t/r_w^2$ for different values of the stress-injection parameter T.

Similarly to the case of injection at constant volume rate, the simulations show that ruptures evolve systematically in a nearly elliptical shape. We thus define the rupture front $\mathcal{R}(t)$ according to the equation of an ellipse (Eq. (29)), and compute the semi-major $a(t)$ and semi-minor $b(t)$ axes of the elliptical front following the same procedure described in Section 3.4. Fig. 12a shows the temporal evolution of the aspect ratio $a(t)/b(t)$ for $\nu = 0.3$ and different values of the stress-injection parameter T. It can be observed that for values of T closer to zero (critically stressed faults), the aspect ratio decreases over time and tends to a constant value at large times, whereas for values of T closer to one (marginally pressurized faults), the aspect ratio increases over time and tends at large times to a constant value as well. Finally, for intermediate values of T, the aspect ratio is nearly constant (see results for $T = 0.3$).

Fig. 12b displays the ratio between the geometric mean $\sqrt{\lambda_a(t)\lambda_b(t)}$ for $\nu = 0.3$, where λ_a and λ_b are defined as $\lambda_a(t) = a(t)/\tilde{L}(t)$ and $\lambda_b(t) = b(t)/\tilde{L}(t)$, respectively, and the numerical values of the amplification factor $\lambda(t)$ for the circular rupture case ($\nu = 0$). We observe that like the case of injection at constant volume rate, the (now time-dependent) geometric mean $\sqrt{\lambda_a\lambda_b}$ is almost equal to the amplification factor $\lambda(t)$ for circular ruptures, meaning that the rupture areas for the values of $\nu = 0$ and $\nu = 0.3$ are approximately the same for the values of T considered here.

5. Discussions

5.1. Comparison between 2-D and 3-D models

We examine here the differences between our 3-D model and its counterpart in 2-D. In the two-dimensional case, the diffusion of fluid pressure along the one-dimensional frictional interface is self-similar under both injection scenarios (constant volume rate and constant pressure) when considering a fluid point source (Carslaw and Jaeger, 1959). Injection-induced fault slip will thus evolve in a self-similar fashion in both cases in the absence of other lengthscales in the model.

The solution in 2-D elasticity for the evolution of the crack length under injection at constant pressure was presented by Bhattacharya and Viesca (2019) and Viesca (2021). They showed that the amplification factor $\lambda = \ell(t)/\ell_d(t)$, where $\ell(t)$ is the position of the crack tip (equal to the half-crack length) and $\ell_d(t)$ is a nominal position of the fluid pressure front, is time-invariant and depends only on the stress-injection parameter T (Eq. (40)). Interestingly, we found qualitatively the same response in our 3-D model but for injection at constant volume rate.

On the other hand, the solution of the 2-D model for injection at constant volume rate has not been presented yet. We derive such solution in Appendix D and found that the amplification factor λ is time-dependent (and hence, not self-similar) and follows

$$\exp\left(-\lambda^2/2\right)\left[\left(1+\lambda^2\right)I_0\left(\lambda^2/2\right)+\lambda^2 I_1\left(\lambda^2/2\right)\right]-2\lambda/\sqrt{\pi}=x_c/\ell_d, \tag{49}$$

where $\ell_d = \sqrt{4\alpha t}$ and $x_c = \sqrt{4\pi}k\left(f\sigma_o' - \tau_o\right)/fq_w\eta$. I_0 and I_1 are the Bessel functions of the first kind of zero and first order, respectively. Eq. (49) represents a unique relation between the amplification factor λ and the ratio between the position of the fluid pressure front ℓ_d and the characteristic length x_c, which is plotted in Fig. 13a together with the corresponding asymptotes for small λ (short-run-out rupture regime) and large λ (long-run-out rupture regime, details in Appendix D).

The characteristic length x_c corresponds to the position of the fluid pressure front at the onset of crack growth (activation of slip or crack nucleation). Upon crack initiation, the rupture lags the fluid pressure front and expands faster than the diffusion of fluid pressure. The crack catches the fluid pressure front ($\lambda = 1$) when the normalized fluid pressure front $\bar{\ell}_d \approx 3.1435$ or, in other words, when the fluid pressure front ℓ_d has grown approximately three times the size x_c necessary for the crack to start growing. After that, the rupture outpaces the fluid pressure front and the crack keeps propagating faster than the diffusion of fluid pressure until it reaches a steady propagation regime that is characterized by a constant rupture speed V_R equal to (see Appendix D)

$$V_R = \frac{f\alpha q_w\eta}{\pi k\left(f\sigma_o' - \tau_o\right)}, \tag{50}$$

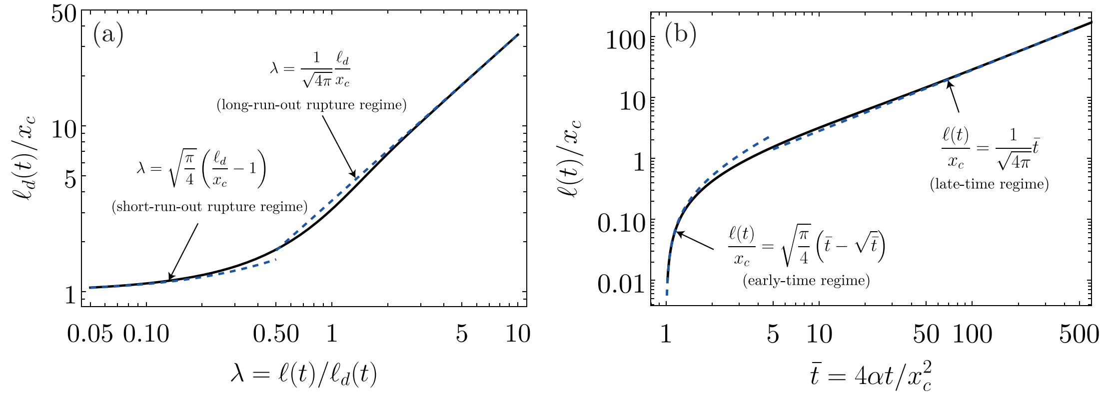

Fig. 13. Analytical solution for a frictional shear crack in 2-D elasticity driven by injection at constant volume rate from a point source. (a) Ratio between the position of the fluid pressure front ℓ_d and the position of the fluid pressure front at the onset of crack growth x_c, with $\ell_d = \sqrt{4\alpha t}$ and $x_c = \sqrt{4\pi}k\left(f\sigma_o' - \tau_o\right)/f q_w \eta$, versus the amplification factor $\lambda = \ell(t)/\ell_d(t)$ (solid black curve), where $\ell(t)$ is the half-crack length. Dashed blue curves correspond to the asymptotes of the short-run-out ($\lambda \ll 1$) and long-run-out ($\lambda \gg 1$) rupture regimes. (b) Dimensionless half-crack length $\ell(t)/x_c$ versus dimensionless time $\bar{t} = \left(\ell_d/x_c\right)^2 = 4\alpha t/x_c^2$ (solid black curve). Dashed blue curves correspond to the same asymptotes of panel (a) but in terms of dimensionless half-crack length and time, which show themselves in this plot as early-time and late-time solutions.

where q_w $\left[L/T\right]$ is the constant injection volume rate per unit fault thickness w_h and unit out-of-the-plane length b, such that $q_w = Q_w/w_h b$ with Q_w the injection volume rate $\left[L^3/T\right]$.

The temporal evolution of the crack half length can seen directly in Fig. 13b, in which the analytical solution is recast in terms of dimensionless half-crack length and dimensionless time. Here, the short-run-out regime translates into an early-time solution that is valid for t near $x_c^2/4\alpha$, and a late-time solution that is approached asymptotically in the limit $t \gg x_c^2/4\alpha$.

This response of the 2-D model under constant rate of injection has no analog in 3-D. Injection at constant volume rate in the 3-D model leads to a rupture speed that decreases with the squared root of time, $V_R = \lambda\sqrt{\alpha/t}$ (Eq. (24)). Moreover, the relative position of the rupture front and the fluid pressure front is time-invariant in 3-D.

Our analysis shows that the response of the 2-D and 3-D models under the same injection scenario are qualitatively different. These differences have to be carefully considered when linking theoretical and numerical predictions to laboratory measurements and field observations in which, generally, 3-D models prevail.

5.2. Assumption of constant friction

In the context of rock friction and earthquake mechanics, laboratory-derived friction laws (Dieterich, 1979; Ruina, 1983; Marone, 1998) have been widely used to describe the entire spectrum of slip rates in natural faults (Scholz, 2019). These empirical friction laws capture the dependence of friction on slip rate and the history of sliding (via a state variable) as observed during velocity-step laboratory experiments on bare rock surfaces and simulated fault gouge (Marone, 1998). It seems then interesting to discuss under what conditions a constant friction coefficient can mimic more complex models of fluid-driven frictional ruptures with rate-and-state friction.

Results in 2-D antiplane elasticity of fluid-driven fault slip propagating on a strengthening (aging) rate-and-state frictional interface have been notably reported by Dublanchet (2019), for the case of injection of fluid at a constant volume rate. Two distinct regimes of crack propagation were observed in Dublanchet's numerical simulations (following a first initial phase of slip rate acceleration): a stable crack growth that tends ultimately to a constant rupture speed, and an unstable crack growth in which the rupture speed blows up in a finite time. He observed that what determines the stable/unstable fault response is the sign of the difference between the residual shear stress left within the crack τ_r and the initial shear stress resolved on the fault plane τ_o. If $\tau_r - \tau_o > 0$ (a condition that is guaranteed in a constant-friction model), crack propagation is always stable, whereas if $\tau_r - \tau_o < 0$, the crack may evolve towards an instability. Such ultimate stability condition can be indeed understood under the classic Griffith energy-balance and the small scale yielding approximation (Rice, 1968), as performed by Garagash and Germanovich (2012) for a fluid-driven slip-weakening frictional shear crack in 2-D.

The stable regime of crack propagation found by Dublanchet (2019) is indeed the most relevant in the context of aseismic ruptures. Furthermore, during such a stable propagation regime, Dublanchet noticed that the crack behaves exactly as if it were governed by a constant friction coefficient within the slipping patch. This is because in that regime, the leading-order terms of the quasi-static elastic equilibrium are the nonlocal stress transfer along the fault and the effect of fluid pressure change on reducing the constant part of the friction coefficient in the rate-and-state friction law. It is not surprising then that our 2-D model of a constant-friction shear crack derived in Appendix D and summarized in Fig. 13, shows qualitatively the same response (under the same injection scenario), notably the ultimate steady crack propagation regime characterized by a constant rupture speed V_R. In our 2-D model, $V_R \propto f\alpha q_w/(f\sigma_o' - \tau_o)$ (see Eq. (50)), which depends on the constant friction coefficient f, hydraulic diffusivity α, injection rate q_w, and residual τ_r and initial τ_o shear stress, in the same form as in the rate-and-state model (Eq. 23 in Dublanchet, 2019), considering that $f\sigma_o'$ is the residual shear strength in the constant-friction model.

A similar result, also in 2-D elasticity, has been recently obtained by Garagash (2021) using a different approach. He developed a Griffith-energy-balance-like equation of motion for the evolution of crack length on rate-and-state faults that he then applied to the study of slip transients due to point-force-like fluid injections. He notably showed that for injection at constant volume rate on neutrally and under-stressed (with regard to the ambient slip rate) strengthening rate-and-state faults (obeying the slip law), the frictional ruptures expand initially within the limits of the pressurized fault patch and move faster than the latter, until they eventually outpace the fluid pressure front and reach also a terminal steady propagation regime characterized by a constant rupture speed. This response is again qualitatively the same of our 2-D model of a constant-friction shear crack, and the same found by Dublanchet (2019) for the stable propagation regime. Moreover, as pointed out by Garagash (2021), the ultimate behavior of the crack under these conditions is due to the diminishing effect of rate-and-state fracture energy in the Griffith energy balance compared to the effect of the fluid injection (in the energy release rate) with increasing rupture size, such that, in the limit of large-run-out rupture, the crack behaves as having zero toughness, which is the case of a friction coefficient that is constant.

Our discussion in 2-D elasticity suggests that the assumption of a constant friction coefficient describes to first order the behavior of rate-and-state friction under conditions that are relevant for the study of fluid-driven aseismic ruptures (rate-strengthening in both aging and slip laws, and approaching the large-run-out rupture regime or late time solution), in which the frictional fracture energy can be neglected. We expect our results in 3-D to provide also first-order descriptions of fluid-driven aseismic ruptures in the context of rate-and-state friction, yet this assumption remains to be confirmed in future studies.

5.3. Implications for injection-induced seismicity

As suggested by a number of experimental and observational studies (Hamilton and Meehan, 1971; Scotti and Cornet, 1994; Bourouis and Bernard, 2007; Guglielmi et al., 2015; Wei et al., 2015; Chen et al., 2017; Duboeuf et al., 2017; Eyre et al., 2019; Cappa et al., 2019), aseismic slip seems to be a frequent result of fluid injections into the subsurface and might play a significant role in injection-induced seismicity related to hydrocarbon and geothermal operations. It is thought that fluid motion drives aseismic slip which in turn transmits solid stresses that trigger part of the observed induced seismicity (Guglielmi et al., 2015; Wei et al., 2015; Duboeuf et al., 2017; Eyre et al., 2019; Bhattacharya and Viesca, 2019). Our results open the possibility of quantifying this triggering mechanism in a three-dimensional scenario that is more realistic than previous two-dimensional models for fluid-driven aseismic fault slip (Eyre et al., 2019; Bhattacharya and Viesca, 2019; Dublanchet, 2019; Garagash, 2021; Viesca, 2021).

First, we note that injection protocols generally consist of a series of injections conducted at a constant volume rate. Results of Section 3 are thus more relevant for geo-energy applications. In particular, we showed that aseismic slip induced by injection at constant volume rate is self-similar in a diffusive manner. As a consequence, the rupture front expands proportionally to the square root of time in the same way as the fluid pressure front does. Induced seismicity that is commonly considered to be driven by the direct effect of fluid pressure increase due to the square-root-of-time feature of seismicity clouds (Shapiro et al., 1997, 2005), might instead be controlled by the stress transfer of a propagating aseismic rupture (Bhattacharya and Viesca, 2019). This would notably be the case of critically stressed fractures/faults in which the rupture front is predicted to be systematically ahead of the fluid pressure front. Our results suggest that assessing whether seismicity is induced by aseismic-slip stress transfer or fluid pressure increase might not be possible from the observation of square-root time dependence of seismicity front alone.

Our model is, of course, idealistic in the sense that it represents a single and isolated fracture/fault in 3-D. Nonetheless, recent two-dimensional simulations of fluid-induced aseismic slip in fractured rock masses have shown that the same patterns predicted by a single fracture in 2-D emerge collectively for a set of fractures (Ciardo and Lecampion, 2021). Notably, a collective aseismic slip front outpaces the migration of fluids when the fracture network is in the critically stressed regime in a global sense (Ciardo and Lecampion, 2021). In addition, field observations indicate critically stressed fractures/faults are likely to be preferred, high-permeability, conduits of fluid flow than the fractures/faults that are not optimally oriented with regard to the stress field (Barton et al., 1995). Together, these observations suggest that seismicity triggered by injection-induced aseismic slip might be indeed a general feature of reservoir rocks in response to fluid injections.

Moreover, if aseismic slip is the dominant mechanism for the triggering of seismicity, current estimates of reservoir hydraulic diffusivity α based on the spatio-temporal seismicity patterns (Shapiro et al., 1997) might be rather related to the quantity $\alpha\lambda^2$ (see Eq. (32)), with λ being an equivalent amplification factor of the fractured rock mass. Such an amplification factor would be intrinsically dependent not only on hydraulic properties of the fracture network, but also on the distribution of fracture orientations with regard to the stress field and the rate of injection. To illustrate this point, let us consider characteristic values for a fracture/fault located at around 3 km depth with $\sigma_0' \sim 50$ [MPa]. Assume the fracture is close to the critically stressed limit, say $1-\tau_0/f\sigma_0' \sim 0.1$, plus an injection rate $Q_w \sim 30$ [l/s] (typical of deep geothermal projects) and fluid dynamic viscosity $\eta \sim 10^{-3}$ [Pa s]. The fracture/fault hydraulic transmissivity kw_h can vary over several orders of magnitude (e.g., Wibberley and Shimamoto, 2003). Consider, for instance, a plausible range $kw_h \sim 10^{-13} - 10^{-15}$ [m^3]. The resulting range for the stress-injection parameter is $T \sim 0.002 - 0.2$, which leads to an amplification factor $\lambda \sim 1.6 - 15.8$. If aseismic slip would be the dominant mechanism in this hypothetical case, estimates of α based on the squared root dependence of a purely pore-pressure-driven triggering mechanism would be off (overpredicted) by a factor $\lambda^2 \sim 2.5 - 250$.

Another finding of our study is related to the scaling relation between the aseismic moment release M_0 and the accumulated injected volume of fluid V. This type of relation has been extensively sought with the purpose of constraining the magnitude of injection-induced earthquakes based on operational parameters (McGarr, 2014; van der Elst et al., 2016; Galis et al., 2017; McGarr and Barbour, 2018). We found that the aseismic moment scales to the injected volume of fluid as $M_0 \propto V^{3/2}$, for injection at constant volume rate. Interestingly, the same power-law scaling has been found for self-arrested injection-induced seismic ruptures based on fully-dynamic rupture simulations and fracture mechanics arguments (Galis et al., 2017). We emphasize that our scaling relation is derived for purely aseismic (quasi-static) ruptures, whereas the relation found by Galis et al. (2017) represents seismic (dynamic) events.

5.4. Implications to seismic swarms and aftershock sequences

Seismic swarms and aftershock sequences are often characterized by diffusive spatiotemporal patterns that are thought to be caused by naturally injected fluids into fault zones (Bosl and Nur, 2002; Miller et al., 2004; Parotidis et al., 2005; Chen et al., 2012; Hainzl et al., 2016; Ross et al., 2017, 2020). Moreover, natural fluid releases are likely represented by the sudden increase of injection rate at the fluid source origin followed by stabilization towards a constant rate. This might be the case of, for instance, breaking an initially sealed and highly-pressurized reservoir. Of course, after a certain period of injection at approximately constant rate, the rate of injection has to decrease until the pressure at the initially highly-pressurized fluid source equilibrates the fluid pressure of the surroundings; we neglect the rupture growth during that stage and also after injection ceases. Our results for sustained injection at constant volume rate can be thus discussed in the context of natural fluid-driven seismicity in seismic swarms episodes and aftershock sequences.

Indeed, the previous discussion on injection-induced aseismic slip in fractured rock masses is easily extendable to fault zones. Notably, seismicity is expected to be now constrained into a relatively well-defined fault plane of thickness that equals the size of the damage zone. Observed seismicity would be the result of instabilities that occur either in the main fault plane or in the fracture network of the damage zone. Similarly to the case of a fractured rock mass, the triggering of seismicity by aseismic-slip stress transfer would depend on how critically stressed the main fault plane or the damage zone fracture network is. The square root time migration of seismicity might be insufficient to discriminate whether aseismic slip or elevated fluid pressure is the direct triggering mechanism. Likewise, estimates of fault hydraulic diffusivity α based on seismicity patterns might rather represent the quantity $\alpha\lambda^2$.

5.5. Permeability variations

Our model assumes that fluid flow occurs within a frictional interface characterized by a constant hydraulic transmissivity. However, permeability changes due to variations of the effective normal stress or, equivalently, the normal interfacial deformation/closure, are well-documented in the fracture/joint rock mechanics literature (e.g., Bandis et al., 1983) and fault mechanics literature as well (e.g., Rice, 1992). In addition, fracture/fault dilatant-behavior can also induce significant permeability variations (e.g., Ciardo and Lecampion, 2019). The effect of such hydro-mechanical couplings on the propagation of aseismic slip remains to be investigated in 3-D and requires the solution of the fully-coupled hydro-mechanical problem as solved, for instance, by Ciardo and Lecampion (2019) in 2-D.

6. Summary and concluding remarks

We have studied the quasi-static propagation of aseismic fault slip driven by fluid pressure diffusion under two different injection scenarios, namely, at constant volume rate and at constant pressure. Our model considers a frictional shear crack that grows in mixed mode (II+III) on a planar fault interface that separates two identical half-spaces of a three-dimensional, isotropic, homogeneous, linear elastic and impermeable solid. The fault interface is characterized by: a shear strength that is equal to the product of a constant friction coefficient and the local effective normal stress, a uniform stress state before injection, and a uniform and constant hydraulic transmissivity. The problem admits analytical treatments for circular ruptures which occur in the limit of a Poisson's ratio $\nu = 0$, and it is solved numerically for the more general case in which the frictionally-constrained crack shape is to be determined as part of the solution ($\nu \neq 0$).

For injection at constant volume rate from a point source, the fault rupture is self-similar. For the limiting case of a circular crack ($\nu = 0$), the rupture radius evolves simply as $R(t) = \lambda L(t)$, where $L(t) = \sqrt{4\alpha t}$ is the nominal position of the fluid pressure front and λ is an amplification factor which is similar to the one presented by Bhattacharya and Viesca (2019) and Viesca (2021) in their 2-D model. We derived an analytical solution for λ as a function of a unique dimensionless parameter T. The stress-injection parameter T varies between 0 and $+\infty$ and contains the information related to the pre-injection fault stress state and the strength of the injection. Whenever $\lambda > 1$, the rupture front outpaces the fluid pressure front. As in previous studies (Garagash and Germanovich, 2012; Bhattacharya and Viesca, 2019), two end-member cases have been identified, namely, critically stressed faults ($T \to 0$) that largely outpace the fluid pressure front ($\lambda \gg 1$), and marginally pressurized faults ($T \to +\infty$) that significantly lags the fluid pressure front ($\lambda \ll 1$). Simple closed-form asymptotic expressions have been derived for λ and also for the axisymmetric slip distribution $\delta(r,t)$, for the two end-member cases. Other results include the rupture speed that decays with the square root of time as $V_r(t) = \lambda\sqrt{\alpha/t}$, and the accumulated fault slip at the injection point which is $\delta(r=0,t) \approx 3.5\left(f\Delta p_*/\mu\right)L(t)$ for critically stressed faults, and $\delta(r=0,t) = (8/\pi)\left(f\Delta p_*/\mu\right)R(t)$ for marginally pressurized faults, where f is the friction coefficient, Δp_* is the characteristic overpressure of the injection, and μ is the shear modulus.

For the more general case in which the Poisson's ratio is different than zero, we solved the problem of determining the equilibrium shape of the frictional shear crack over the entire parametric space. We found that the crack shape is quasi-elliptical and the aspect ratio is upper and lower bounded by $1/(1-\nu)$ and $(3-\nu)/(3-2\nu)$. The two bounds are associated with the limiting cases of critically stressed faults and marginally pressurized faults, respectively. There is thus a strong dependence of the aspect ratio not only on the Poisson's ratio but also on the initial stress state and the driving force itself. Moreover, we found that the rupture area is Poisson's ratio-independent and grows simply as $A_r(t) = 4\pi\alpha\lambda^2 t$. If $\lambda > 1$, the rupture area is greater than the diffusively pressurized fault patch. Interestingly, λ is the same amplification factor that for the circular rupture case, meaning that knowing the solution of the circular shear crack is sufficient to determine the area of any other resulting crack shape for any value of the Poisson's ratio and the same value of T. In addition, simple closed-form asymptotic expressions are provided for the semi-major $a(t)$ and semi-minor $b(t)$ axes of the quasi-elliptical crack that fully define the rupture front for the corresponding end-member cases.

For injection at constant pressure from a finite source of radius r_w, the fault rupture is not self-similar. The rupture radius grows at large times as $R(t) = \lambda(t)\sqrt{c_1 \alpha t}$, where $c_1 \approx 2.25$, $\sqrt{c_1 \alpha t}$ is the nominal position of the fluid pressure front and $\lambda(t)$ is an amplification factor known as function of dimensionless time $\alpha t / r_w^2$ and T. The stress-injection parameter T varies in this case between 0 and 1. $\lambda(t)$ decreases monotonically with time and the rupture radius expands as $R(t) \propto (\alpha t)^{(1-T)/2}$. For critically stressed faults ($T \to 0 \implies (1-T)/2 \to 1/2$), the rupture evolves almost diffusively, whereas for marginally pressurized faults ($T \to 1 \implies (1-T)/2 \to 0$), the rupture grows extremely slow. Generally speaking, the rupture front propagates slower than the diffusive fluid pressure front. Yet in some cases the rupture front outpaces the fluid pressure front, the latter will eventually catch the former if injection is sustained for a sufficient time.

Among the two injection scenarios considered, injection at constant volume rate is the one with broader implications. This is due to injection protocols in the geo-energy industry normally consist of a series of injections at constant volume rate, whereas naturally injected fluids into the Earth's crust are likely represented by the same kind of source. Since aseismic ruptures expand diffusively (proportional to the square root of time) for that type of injection, irrespective of the pre-injection stress state and the parameters of the injection, current interpretations of fluid-driven seismicity might need to be revisited.

Indeed, it is commonly assumed that seismicity clouds are driven by the direct effect of fluid pressure increase whenever seismic events are observed to spread away from the injection zone with square root time dependence (Shapiro et al., 1997; Bosl and Nur, 2002; Parotidis et al., 2005; Chen et al., 2012; Hainzl et al., 2016; Ross et al., 2017, 2020). Our results challenge that interpretation and open the possibility that those episodes might be controlled by the stress transfer of a propagating aseismic rupture instead (Bhattacharya and Viesca, 2019). This would be notably the case of critically stressed fractures/faults in which the rupture front is predicted to be systematically ahead of the fluid pressure front ($\lambda \gg 1$). Furthermore, current estimates of reservoir and fault zone hydraulic diffusivity α based on seismicity patterns (e.g., Shapiro et al., 1997, 2005; Ross et al., 2017) might be rather related to the quantity $\alpha\lambda^2$, with λ being a representative amplification factor of the fractured rock mass or fault zone.

Another important finding is related to the scalar moment M_0 due to purely aseismic (quasi-static) motion. We found that it scales to the injected volume of fluid V as $M_0 \propto V^{3/2}$. Interestingly, this relation is the same as the one found by Galis et al. (2017) for self-arrested injection-induced seismic (dynamic) ruptures.

We expect our analytical and numerical results to provide a conceptual and quantitative framework to understand various applied problems in geomechanics and geophysics associated with aseismic fracture/fault slip induced by fluid motion. Moreover, our analytical results provide a simple mean for verifying and benchmarking 3-D numerical solvers as performed here.

CRediT authorship contribution statement

Alexis Sáez: Conceptualization, Methodology, Software, Validation, Formal analysis, Investigation, Writing – original draft, Visualization, Funding acquisition. **Brice Lecampion:** Conceptualization, Methodology, Formal analysis, Software, Writing – review & editing, Supervision, Funding acquisition. **Pathikrit Bhattacharya:** Conceptualization, Methodology, Formal analysis, Writing – review & editing. **Robert C. Viesca:** Conceptualization, Methodology, Formal analysis, Writing – review & editing.

Declaration of competing interest

The authors declare that they have no known competing financial interests or personal relationships that could have appeared to influence the work reported in this paper.

Funding

The results were obtained within the EMOD project (Engineering model for hydraulic stimulation). The EMOD project benefits from a grant (research contract SI/502081-01) and an exploration subsidy (contract number MF-021-GEO-ERK) of the Swiss federal office of energy for the EGS geothermal project in Haute-Sorne, canton of Jura, which is gratefully acknowledged. A. Sáez was partially funded by the Federal Commission for Scholarships for Foreign Students via the Swiss Government Excellence Scholarship. P. Bhattacharya was supported by a start-up research grant from the National Institute of Science Education and Research, India, Bhubaneswar. R. C. Viesca was supported by NSF, USA award 1653382.

Appendix A. The consistent tangent operator

The Newton–Raphson iterations of the backward Euler time integration scheme require the computation of the corresponding Jacobian matrix $\boldsymbol{J} \in \mathbb{R}^{N\times N}$. By differentiating the residual form of Eq. (9), the Jacobian matrix is simply given by $\boldsymbol{J} = \mathbf{E}_{\mathcal{H}} + \mathbf{C}_{TO}$, where $\mathbf{C}_{TO} = -\partial \Delta \boldsymbol{t}'/\partial \Delta \boldsymbol{d}$ is the so-called consistent tangent operator of elastoplasticity. In order to derive an analytical expression for $\mathbf{C}_{TO}$, we consider the consistency condition $\Delta\gamma\dot{\mathcal{F}} = 0$, which states that when plastic flow occurs (i.e., $\Delta\gamma > 0$), the stress state $\boldsymbol{t}'$ has to remain on the yield function and thus $\dot{\mathcal{F}} = 0$. This additional equation can be read in incremental form as

$$\frac{\partial \mathcal{F}}{\partial \boldsymbol{t}'} \cdot \Delta \boldsymbol{t}' = 0.$$

Note that the consistent tangent operator $\mathbf{C}_{TO}$ is a block diagonal matrix and is composed by blocks that we denote as $\mathbf{C}^m_{TO} \in \mathbb{R}^{3\times 3}$. There is one $\mathbf{C}^m_{TO}$ matrix for every mth collocation point. By combining Eqs. (10) to (13) plus the previous consistency condition, we derive the following expression for $\mathbf{C}^m_{TO}$

$$\mathbf{C}^m_{TO} = \begin{pmatrix} k_1 \sin^2(\theta) & -k_1 \sin(\theta)\cos(\theta) & f k_3 \cos(\theta) \\ -k_2 \sin(\theta)\cos(\theta) & k_2 \cos^2(\theta) & f k_3 \sin(\theta) \\ 0 & 0 & k_3 \end{pmatrix},$$

where $\theta = \arctan\left(t_2/t_1\right)$ with t_1 and t_2 the two local components of the shear traction vector at the mth collocation point (the superscript m is omitted), and k_1, k_2 and k_3 are the corresponding entries of the diagonal elastic stiffness matrix $\boldsymbol{D}$.

Note that $\mathbf{C}^m_{TO}$ is a null matrix if $\Delta\gamma^m = 0$ (i.e., if the collocation point state is elastic or, in other words, no slip has occurred).

Appendix B. Propagation condition for a constant-friction circular shear crack under axisymmetric shear load

The stress intensity factors of a circular crack of radius R under an arbitrary shear traction vector of components σ_{xz} and σ_{yz} (with regard to the reference frame showed in Fig. 1) applied anti-symmetrically on the crack surfaces read as (Fabrikant, 1989; Lai et al., 2002)

$$\begin{aligned} K_{II}(R,\phi) + iK_{III}(R,\phi) = \frac{1}{\pi\sqrt{\pi R}} \int_0^{2\pi}\int_0^R \Bigg[& \frac{\left\{\sigma_{xz}(r,\theta) + i\sigma_{yz}(r,\theta)\right\}\sqrt{R^2-r^2}e^{-i\phi}}{R^2+r^2-2Rr\cos(\phi-\theta)} \\ & + \frac{\nu}{2-\nu}\frac{\left\{\sigma_{xz}(r,\theta) - i\sigma_{yz}(r,\theta)\right\}\sqrt{R^2-r^2}\left\{3R - re^{i(\phi-\theta)}\right\}e^{i\phi}}{R(R-re^{i(\phi-\theta)})^2}\Bigg] r\mathrm{d}r\mathrm{d}\theta, \end{aligned}$$

where ϕ is the polar angular coordinate, such that $\tan(\phi) = x/y$.

Consider a shear load of axisymmetric magnitude $\Delta\tau(r)$ along the x direction, such that $\sigma_{xz}(r,\theta) = \Delta\tau(r)$ and $\sigma_{yz}(r,\theta) = 0$. Evaluating the integral of the right-hand side of the previous equation with regard to θ, we obtain:

$$K_{II}(R,\phi) = \frac{2\cos(\phi)}{\sqrt{\pi R}} \int_0^R \Delta\tau(r)\left[\frac{1}{\sqrt{R^2-r^2}} + \frac{3\nu}{2-\nu}\frac{\sqrt{R^2-r^2}}{R^2}\right] r\mathrm{d}r,$$
$$K_{III}(R,\phi) = \frac{2\sin(\phi)}{\sqrt{\pi R}} \int_0^R \Delta\tau(r)\left[-\frac{1}{\sqrt{R^2-r^2}} + \frac{3\nu}{2-\nu}\frac{\sqrt{R^2-r^2}}{R^2}\right] r\mathrm{d}r.$$

Let us consider the energy release rate of a pure shear crack in 3-D elasticity, $\mathcal{G} = K^2_{II}/E' + K^2_{III}/2\mu$ (Lawn, 1993), where E' is the plane strain modulus. Using the previous equations for the stress intensity factors in the limiting case of a material with Poisson's ratio $\nu = 0$ ($E' = E = 2\mu$), we obtain the following expression for the energy release rate,

$$\mathcal{G} = \frac{2}{\pi\mu R}\left(\int_0^R \frac{\Delta\tau(r)}{\sqrt{R^2-r^2}} r\mathrm{d}r\right)^2.$$

The fracture energy $\mathcal{G}_c$ of a constant-friction shear crack is zero, such that Griffith energy balance $\mathcal{G} = \mathcal{G}_c$ reduces simply to

$$\int_0^R \frac{\Delta\tau(r)}{\sqrt{R^2-r^2}} r\mathrm{d}r = 0,$$

that is the expression used in the main text as the condition for crack propagation.

Appendix C. Asymptotics of fault slip for circular ruptures driven by injection at constant volume rate

The quasi-static elastic equilibrium that relates the fault slip distribution δ to the shear stress drop $\Delta\tau$ within an axisymmetric circular shear crack ($\nu = 0$) of radius $R(t)$ is (Salamon and Dundurs, 1971, 1977; Bhattacharya and Viesca, 2019)

$$\Delta\tau(r,t) = \frac{\mu}{2\pi}\int_0^{R(t)} \frac{\partial\delta(\xi,t)}{\partial\xi}\left(\frac{K\left[k(r/\xi)\right]}{\xi+r} + \frac{E\left[k(r/\xi)\right]}{\xi-r}\right)\mathrm{d}\xi,$$

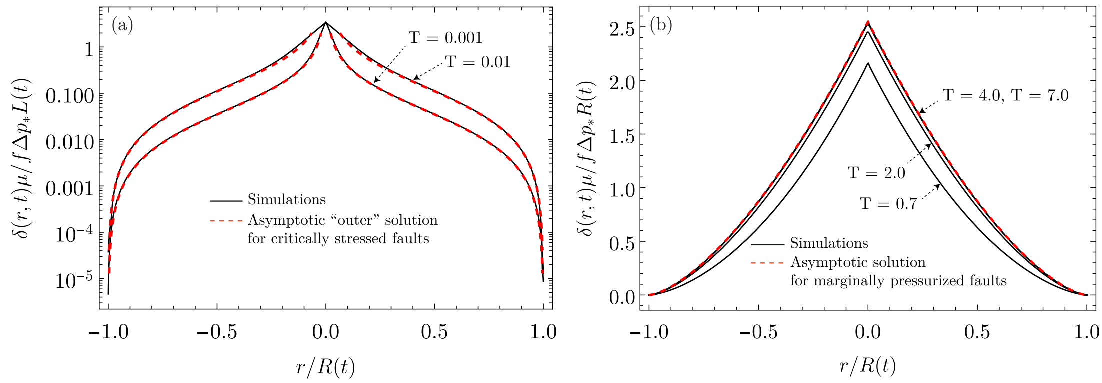

Fig. 14. Comparison between asymptotics of fault slip and results from the simulations for (a) critically stressed faults ($\lambda \gg 1$), and (b) marginally pressurized faults ($\lambda \ll 1$).

where K and E are the complete elliptic integrals of the first and second kind, respectively, and $k(x) = 2\sqrt{x}/(1+x)$.

The inverse relation of the previous equation is given by Sneddon (1951) (Eq. 121, p. 489) as

$$\delta(r,t) = \frac{4R(t)}{\pi\mu}\int_{\bar{r}}^{1}\frac{\xi \mathrm{d}\xi}{\sqrt{\xi^2-\bar{r}^2}}\int_0^1\frac{\Delta\tau(s\xi R(t),t)s\mathrm{d}s}{\sqrt{1-s^2}}, \tag{51}$$

where $\bar{r} = r/R(t)$ is the self-similar radial coordinate.

Considering that the shear stress drop $\Delta\tau(r,t) = \tau_0 - f\left[\sigma_o' - \Delta p_* E_1\left(r^2/4\alpha t\right)\right]$ (Eq. (19)), the stress-injection parameter $T = \left(f\sigma_o' - \tau_o\right)/f\Delta p_*$ (Eq. (17)), and the amplification factor is defined as $\lambda = R(t)/L(t)$ with $L(t) = \sqrt{4\alpha t}$, we can recast the above equation in dimensionless form,

$$\bar{\delta}(\bar{r};T) = \frac{\delta(r,t)\mu}{f\Delta p_* R(t)} = \frac{4}{\pi}\int_{\bar{r}}^{1}\frac{\xi\mathrm{d}\xi}{\sqrt{\xi^2-\bar{r}^2}}\int_0^1\frac{\left(E_1\left(s^2\xi^2\lambda^2\right)-T\right)s\mathrm{d}s}{\sqrt{1-s^2}}, \tag{52}$$

where $\bar{\delta}(\bar{r};T)$ is the normalized self-similar slip distribution that is unique for a given value of T. We recall that the amplification factor λ is known by Eq. (21) as a function of T as well.

Eq. (52) admits analytical integration in the limiting cases of critically stressed ($\lambda \gg 1$) and marginally pressurized ($\lambda \ll 1$) faults. One of the inner integrals, $\int_0^1 E_1\left(s^2\xi^2\lambda^2\right)\mathrm{d}s/\sqrt{1-s^2}$, has indeed the same limiting behaviors than the crack propagation condition, Eq. (20). For large values of λ, such integral is approximated asymptotically as $\sim 1/\left(2\xi^2\lambda^2\right) + O\left(1/\lambda^4\right)$ (see Eq. (22)), whereas for small values of λ is $\sim 2-\gamma-\ln\left(4\xi^2\lambda^2\right)+O\left(\lambda^2\right)$ (see Eq. (23)). Considering the previous asymptotic expressions, Eq. (52) can be evaluated analytically to obtain the following closed-form expressions for the self-similar slip distribution:

$$\frac{\delta(r,t)\mu}{f\Delta p_* R(t)} = \frac{8}{\pi}\left(\sqrt{1-\bar{r}^2} - |\bar{r}|\arccos(|\bar{r}|)\right) \tag{53}$$

in the marginally pressurized limit ($T \gg 1$, $\lambda \ll 1$), and

$$\frac{\delta(r,t)\mu}{f\Delta p_* L(t)} = \frac{2\sqrt{2T}}{\pi}\left(\frac{\arccos(|\bar{r}|)}{|\bar{r}|} - \sqrt{1-\bar{r}^2}\right) \tag{54}$$

in the critically stressed limit ($T \ll 1$, $\lambda \gg 1$).

The latter is indeed valid for $r \gg L(t)$ only. It corresponds to the "outer" solution of the critically stressed limit in which the reduction of frictional strength due to the fluid pressure perturbation can be approximated as a point force. Eqs. (53) and (54) can be equivalently derived by using the asymptotic expressions of the fluid pressure perturbation in the limiting cases (see details on those approximations in Section 3.2). In addition, the condition for having no singularity at the crack tip, $\partial\delta/\partial r = 0$ at $r = R$, is equivalent to the crack propagation condition, Eq. (18), and will lead to same expressions that relates λ and T, Eqs. (22) and (23), in the corresponding end-member cases.

Eqs. (53) and (54) are plotted in Fig. 14 together with the slip profiles obtained from the numerical simulations for values of T that are representative of the limiting cases. We use logarithmic scale in the critically stressed limit in order to facilitate the comparison. Note that the marginally pressurized limit is reached for values of $T \gtrsim 4$ (Fig. 14b). On the other hand, in the critically stressed limit (Fig. 14a), the "outer" solution breaks of course for small r (it diverges at $r = 0$ indeed); an "inner" solution should be derived in order to solve the boundary layer at $r \sim O(L(t))$ as done by Garagash and Germanovich (2012) and Viesca (2021).

Appendix D. Analytical solution in 2-D for a frictional shear crack driven by injection at constant volume rate

Consider the same problem formulated in Section 2.1 but in 2-D elasticity. Fluid is injected via a point source at $x = 0$ into a planar 1-D frictional interface located along the x-axis. Injection is sustained for $t > 0$ at a constant volume rate q_w $\left[L/T\right]$ per unit fault thickness and unit out-of-the-plane length. The quasi-static crack propagation condition for a 1-D straight constant-friction (zero-toughness) symmetric shear crack (either mode II or III) of half-crack length $\ell(t)$ reduces to (Barenblatt, 1962)

$$\int_{-\ell(t)}^{\ell(t)} \frac{\Delta\tau(x,t)}{\sqrt{\ell^2(t)-x^2}}\mathrm{d}x = 0,$$

where $\Delta\tau(x,t)$ is the shear stress drop given by

$$\Delta\tau(x,t) = \tau_0 - f\left(\sigma_o' - \Delta p(t)\Pi(\xi)\right),$$

with $\xi = x/\sqrt{4\alpha t}$ and (section 2.9, eq. 7, Carslaw and Jaeger, 1959)

$$\Delta p(t) = \frac{q_w \eta}{\sqrt{\pi} k}\sqrt{\alpha t}, \quad \Pi(\xi) = \exp\left(-\xi^2\right) - \sqrt{\pi}\,|\xi|\,\mathrm{Erfc}\left(|\xi|\right).$$

As defined in the main text, η is the fluid dynamic viscosity, k is the fault intrinsic permeability, and α is the fault hydraulic diffusivity.

Let us define the nominal position of the fluid pressure front $\ell_d(t) = \sqrt{4\alpha t}$, a time-dependent amplification factor λ in the form $\lambda(t) = \ell(t)/\ell_d(t)$, and the following characteristic length

$$x_c = \sqrt{4\pi}\frac{k\left(f\sigma_o' - \tau_o\right)}{f q_w \eta},$$

The crack propagation condition can be then rewritten in dimensionless form

$$\frac{1}{\pi}\int_{-1}^{1} \frac{\Pi(\lambda s)}{\sqrt{1-s^2}}\mathrm{d}s = \frac{x_c}{\ell_d},$$

that represents a unique relation between the amplification factor λ and the normalized position of the fluid pressure front ℓ_d/x_c.

The left-hand side of the previous integral can be evaluated analytically to obtain the following implicit equation for λ as a function of ℓ_d/x_c,

$$\exp\left(-\lambda^2/2\right)\left[\left(1+\lambda^2\right)I_0\left(\lambda^2/2\right) + \lambda^2 I_1\left(\lambda^2/2\right)\right] - 2\lambda/\sqrt{\pi} = x_c/\ell_d,$$

where I_0 and I_1 are the Bessel functions of the first kind of zero and first order, respectively.

The previous equation is the one reproduced in the main text and it is plotted in Fig. 13a. Asymptotic expansions of the left-hand side of this equation for small and large λ lead to the following closed-form asymptotic solutions for the short-run-out rupture ($\lambda \ll 1$) and long-run-out rupture ($\lambda \gg 1$) regimes:

$$\begin{cases} \lambda = \sqrt{\frac{\pi}{4}}\left(\frac{\ell_d}{x_c} - 1\right) & \text{, for } \lambda \ll 1 \\ \lambda = \frac{1}{\sqrt{4\pi}}\frac{\ell_d}{x_c} & \text{, for } \lambda \gg 1, \end{cases}$$

that are also plotted in Fig. 13a.

From the asymptotic for the short-run-out rupture regime, we note that solutions are defined only for $\ell_d/x_c \geq 1$. The limit of $\ell_d/x_c = 1$ represents the instant in which activation of slip (or crack nucleation) happens and implies that $\ell_d = x_c$ at that moment. From the latter, it becomes clear that the characteristic length x_c is the size of the pressurized patch necessary for the crack to start growing.

On the other hand, the previous asymptotics can be recast in terms of the dimensionless half-crack length $\ell(t)/x_c$ and the dimensionless time $\bar{t} = \left(\ell_d/x_c\right)^2 = 4\alpha t/x_c^2$, to obtain the following expressions:

$$\begin{cases} \frac{\ell(t)}{x_c} = \sqrt{\frac{\pi}{4}}\left(\bar{t} - \sqrt{\bar{t}}\right) & \text{, for } t \text{ near } x_c^2/4\alpha \\ \frac{\ell(t)}{x_c} = \frac{1}{\sqrt{4\pi}}\bar{t} & \text{, for } t \gg x_c^2/4\alpha, \end{cases}$$

which corresponds to early-time and late-time solutions, respectively. From the asymptotic for late times, we can write

$$\ell(t) = \frac{2\alpha}{\sqrt{\pi}x_c}t.$$

Hence, the ultimate behavior of the crack is a steady propagation regime at constant rupture speed V_R equal to

$$V_R = \frac{f\alpha q_w \eta}{\pi k\left(f\sigma_o' - \tau_o\right)},$$

which is the other equation used in the main text.

Table 1
Misfit parameter β of non-linear regression analyzes conducted to compute the rupture radius of circular ruptures ($\nu = 0$) and the semi-major and semi-minor axes of the quasi-elliptical ruptures ($\nu \neq 0$), for the self-similar case of injection at constant volume rate. Values of β are averaged over the 10 time steps for each combination of T and ν.

ν	Stress-injection parameter T						
	0.001	0.01	0.1	0.7	2.0	4.0	7.0
0	0.00574263	0.00608538	0.00571406	0.00689874	0.00732939	0.00664432	0.00668360
0.15	0.00724403	0.00648519	0.00643673	0.00630272	0.00606131	0.00708104	0.00644491
0.30	0.00969618	0.01010820	0.00849989	0.00653986	0.00629030	0.00690700	0.00681493
0.45	0.02028980	0.01888480	0.01005640	0.00754184	0.00639826	0.00671446	0.00691824

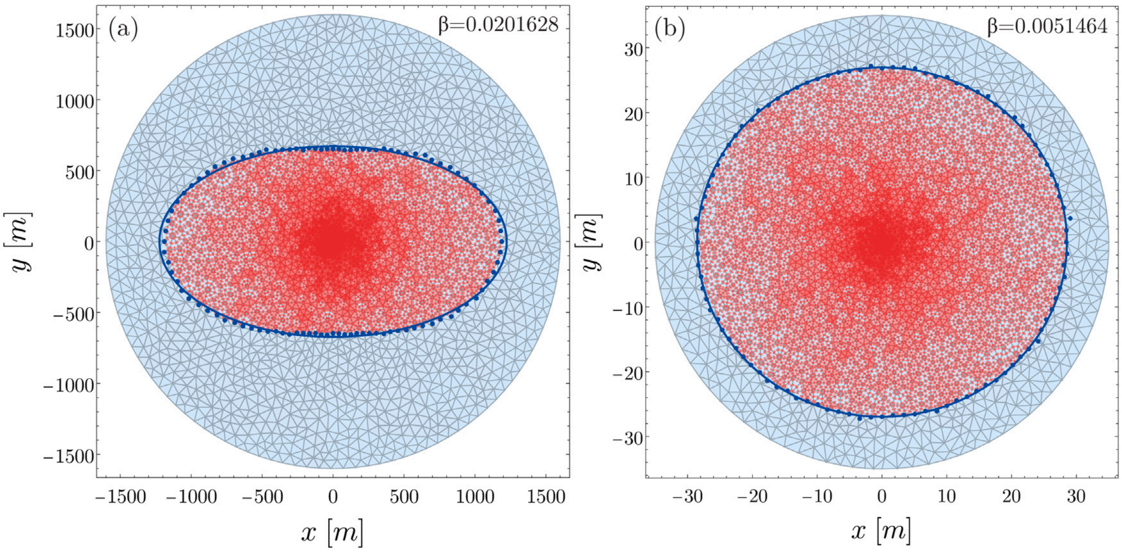

Fig. 15. Two examples of the computation of the elliptical rupture fronts at given snapshots for (a) the most elongated rupture ($T = 0.001$, $\nu = 0.45$) and (b) the least elongated rupture ($T = 7.0$, $\nu = 0.15$). The blue points correspond to the position of the rupture front computed numerically from the solution for fault slip $\delta(x, y, t)$, for each one of the one hundred equally-spaced angular cylindrical directions $\theta_i \in [0, 2\pi)$ considered. The blue solid curves correspond to the ellipsoidal curve fittings to the one hundred coordinate pairs. In the background, the unstructured triangular mesh made on piece-wise quadratic boundary elements used throughout this study.

Appendix E. Numerical computation of rupture fronts

Given the numerical (piece-wise quadratic) solution of fault slip $\delta\left(x, y, t_n\right)$ at a given time step t_n, we take 100 equally-spaced values of the angular cylindrical coordinate $\theta_i \in [0, 2\pi)$ (with $i = 1, \dots, 100$), and compute for each of them, the root of the system of equations $\delta\left(x_i, y_i, t_n\right) = 0$ plus $\tan\left(\theta_i\right) = x_i/y_i$, via a Newton–Raphson procedure. We then use the solution, in the form of a data set of 100 coordinate pairs $\left(x_i, y_i\right)$, to perform nonlinear regression analysis using the routine *NonlinearModelFit* of Wolfram Mathematica. The nonlinear curve fittings are performed considering the equation of a circle for the case $\nu = 0$ (with the rupture radius R^m as the model's parameter) and the equation of an ellipse for the case $\nu \neq 0$ (with the semi-major a^m and semi-minor b^m axes of the ellipse as the model's parameters).

In order to quantify the misfit between the model and the data, we consider the quantity $\beta = \left(1/N_\theta R_*\right) \sum_{i=1}^{N_\theta} \left|r_i^m - r_i^d\right|$, where r_i^m is the radial distance (from the reference system origin to the rupture front) predicted by the model at θ_i, r_i^d is the same quantity but for the data, N_θ is the total number of data points (100), and R_* is used to scale the distances and is taken as R^m for the circular case ($\nu = 0$), and $\sqrt{a^m b^m}$ for the elliptical case ($\nu \neq 0$). Note that $r_i^m = R^m$ for $\nu = 0$, and $r_i^m = a^m b^m / \sqrt{\left(a^m \sin\left(\theta_i\right)\right)^2 + \left(b^m \cos\left(\theta_i\right)\right)^2}$ for $\nu \neq 0$. The values of β averaged over the 10 time steps considered in each simulation are shown in Table 1.

It is worth mentioning that in the case of $\nu = 0$, the exact shape of the rupture front is a circle. Hence, the departure of β from zero corresponds uniquely to numerical errors. The average of β over all values of T in the circular rupture case is 0.00644259. Thus, in the case of non-circular ruptures ($\nu = 0.15$, 0.30 and 0.45), one may consider that values of β that are only larger than the ones for circular ruptures quantify an *actual* departure of the rupture front from an exact ellipse. From Table 1, we observe that such difference increases systematically with increasing values of ν and decreasing values of T, and is at most of 2% in the worst case ($\nu = 0.45$, $T = 0.001$).

Two graphical examples of the computation of the elliptical rupture fronts are displayed in Fig. 15. Fig. 15a corresponds to the case of the most elongated rupture, which is also the case that departs the most from an ellipse. On the other hand, Fig. 15b corresponds to the case of the least elongated rupture, in which the β-value is essentially in the other of numerical errors (circular rupture case).

References

Aki, K., Richards, P., 2002. Quantitative Seismology. University Science Books.
Azad, M., Garagash, D., Satish, M., 2017. Nucleation of dynamic slip on a hydraulically fractured fault. J. Geophys. Res.: Solid Earth 122 (4), 2812–2830.
Bandis, S., Lumsden, A., Barton, N., 1983. Fundamentals of rock joint deformation. Int. J. Rock Mech. Min. Sci. Geomech. Abstr. 20 (6), 249–268.
Bao, X., Eaton, D., 2016. Fault activation by hydraulic fracturing in western Canada. Science 354 (6318), 1406–1409.
Barenblatt, G., 1962. The Mathematical Theory of Equilibrium Cracks in Brittle Fracture. In: Advances in Applied Mechanics, vol. 7, Elsevier, pp. 55–129.
Barenblatt, G., 1996. Scaling, Self-Similarity, and Intermediate Asymptotics. Cambridge University Press.
Barton, C., Zoback, M., Moos, D., 1995. Fluid flow along potentially active faults in crystalline rock. Geology 23 (8), 683–686.
Bear, J., 1972. Dynamics of Fluids in Porous Media. Dover.
Bhattacharya, P., Viesca, R., 2019. Fluid-induced aseismic fault slip outpaces pore-fluid migration. Science 364 (6439), 464–468.
Bosl, W., Nur, A., 2002. Aftershocks and pore fluid diffusion following the 1992 Landers earthquake. J. Geophys. Res.: Solid Earth 107 (B12), ESE 17.
Bourouis, S., Bernard, P., 2007. Evidence for coupled seismic and aseismic fault slip during water injection in the geothermal site of Soultz (France), and implications for seismogenic transients. Geophys. J. Int. 169 (2), 723–732.
Cappa, F., Scuderi, M., Collettini, C., Guglielmi, Y., Avouac, J., 2019. Stabilization of fault slip by fluid injection in the laboratory and in situ. Sci. Adv. 5 (3).
Carslaw, H., Jaeger, J., 1959. Conduction of Heat in Solids. Clarendon Press, Oxford.
Chen, X., Nakata, N., Pennington, C., Haffener, J., Chang, J., He, X., Zhan, Z., Ni, S., Walter, J., 2017. The Pawnee earthquake as a result of the interplay among injection, faults and foreshocks. Sci. Rep. 7 (1), 4945.
Chen, X., Shearer, P., Abercrombie, R., 2012. Spatial migration of earthquakes within seismic clusters in Southern California: Evidence for fluid diffusion. J. Geophys. Res.: Solid Earth 117 (B4).
Ciardo, F., Lecampion, B., 2019. Effect of dilatancy on the transition from aseismic to seismic slip due to fluid injection in a fault. J. Geophys. Res.: Solid Earth 124 (4), 3724–3743.
Ciardo, F., Lecampion, B., 2021. Aseismic slip propagation in fractured rock masses driven by pore-fluid diffusion. In: 55th US Rock Mechanics/Geomechanics Symposium, Houston, Texas, USA.
Ciardo, F., Lecampion, B., Fayard, F., Chaillat, S., 2020. A fast boundary element based solver for localized inelastic deformations. Internat. J. Numer. Methods Engrg. 121, 5696–5718.
Crouch, S., Starfield, A., 1983. Boundary Element Methods in Solid Mechanics. George Allen and Unwin.
David, L., Lazarus, V., 2022. On the key role of crack surface area on the lifetime of arbitrarily shaped flat cracks. Int. J. Fatigue 154, 106512.
de Souza Neto, E., Perić, D., Owen, D., 2008. Computational Methods for Plasticity: Theory and Applications. John Wiley and Sons, Ltd.
Deichmann, N., Giardini, D., 2009. Earthquakes induced by the stimulation of an enhanced geothermal system below Basel (Switzerland). Seismol. Res. Lett. 80 (5), 784–798.
Detournay, E., 2016. Mechanics of hydraulic fractures. Annu. Rev. Fluid Mech. 48 (1), 311–339.
Dieterich, J., 1979. Modeling of rock friction: 1. Experimental results and constitutive equations. J. Geophys. Res.: Solid Earth 84 (B5), 2161–2168.
Dublanchet, P., 2019. Fluid driven shear cracks on a strengthening rate-and-state frictional fault. J. Mech. Phys. Solids 132, 103672.
Duboeuf, L., De Barros, L., Cappa, F., Guglielmi, Y., Deschamps, A., Seguy, S., 2017. Aseismic motions drive a sparse seismicity during fluid injections into a fractured zone in a carbonate reservoir. J. Geophys. Res.: Solid Earth 122 (10), 8285–8304.
Elie, F., Véronique, L., Leblond, J., 2006. Coplanar propagation paths of 3D cracks in infinite bodies loaded in shear. Int. J. Solids Struct. 43 (7), 2091–2109.
Ellsworth, W., Giardini, D., Townend, J., Ge, S., Shimamoto, T., 2019. Triggering of the Pohang, Korea, earthquake (Mw 5.5) by enhanced geothermal system stimulation. Seismol. Res. Lett. 90 (5), 1844–1858.
Eyre, T., Eaton, D., Garagash, D., Zecevic, M., Venieri, M., Weir, R., Lawton, D., 2019. The role of aseismic slip in hydraulic fracturing-induced seismicity. Sci. Adv. 5 (8).
Fabrikant, V., 1989. Applications of Potential Theory in Mechanics. Kluwer Academic Publishers, The Netherlands.
Galis, M., Ampuero, J., Mai, P., Cappa, F., 2017. Induced seismicity provides insight into why earthquake ruptures stop. Sci. Adv. 3 (12).
Gao, H., 1988. Nearly circular shear mode cracks. Int. J. Solids Struct. 24 (2), 177–193.
Garagash, D., 2021. Fracture mechanics of rate-and-state faults and fluid injection induced slip. Phil. Trans. R. Soc. A 379 (2196), 20200129.
Garagash, D., Germanovich, L., 2012. Nucleation and arrest of dynamic slip on a pressurized fault. J. Geophys. Res.: Solid Earth 117 (B10).
Goebel, T., Brodsky, E., 2018. The spatial footprint of injection wells in a global compilation of induced earthquake sequences. Science 361 (6405), 899–904.
Guglielmi, Y., Cappa, F., Avouac, J., Henry, P., Elsworth, D., 2015. Seismicity triggered by fluid injection-induced aseismic slip. Science 348 (6240), 1224–1226.
Hacker, B., Peacock, S., Abers, G., Holloway, S., 2003. Subduction factory 2. Are intermediate-depth earthquakes in subducting slabs linked to metamorphic dehydration reactions? J. Geophys. Res.: Solid Earth 108 (B1).
Hainzl, S., Fischer, T., Čermáková, H., Bachura, M., Vlček, J., 2016. Aftershocks triggered by fluid intrusion: Evidence for the aftershock sequence occurred 2014 in West Bohemia/Vogtland. J. Geophys. Res.: Solid Earth 121 (4), 2575–2590.
Hamilton, D., Meehan, R., 1971. Ground rupture in the Baldwin Hills. Science 172 (3981), 333–344.
Hatch, R., Abercrombie, R., Ruhl, C., Smith, K., 2020. Evidence of aseismic and fluid-driven processes in a small complex seismic swarm near Virginia city, Nevada. Geophys. Res. Lett. 47 (4), e2019GL085477.
Healy, J., Rubey, W., Griggs, D., Raleigh, C., 1968. The Denver earthquakes. Science 161 (3848), 1301–1310.
Hills, D., Kelly, P., Dai, D., Korsunsky, A., 1996. Solution of Crack Problems - the Distributed Dislocation Technique, first ed. In: Solid Mechanics and Its Applications, vol. 44, Springer Netherlands.
Jaeger, J., 1955. Numerical values for the temperature in radial heat flow. J. Math. Phys. 34, 316–321.
Kato, A., Iidaka, T., Ikuta, R., Yoshida, Y., Katsumata, K., Iwasaki, T., Sakai, S., Thurber, C., Tsumura, N., Yamaoka, K., Watanabe, T., Kunitomo, T., Yamazaki, F., Okubo, M., Suzuki, S., Hirata, N., 2010. Variations of fluid pressure within the subducting oceanic crust and slow earthquakes. Geophys. Res. Lett. 37 (14).
Keranen, K., Savage, H., Abers, G., Cochran, E., 2013. Potentially induced earthquakes in Oklahoma, USA: Links between wastewater injection and the 2011 Mw 5.7 earthquake sequence. Geology 41 (6), 699–702.
Keranen, K., Weingarten, M., Abers, G., Bekins, B., Ge, S., 2014. Sharp increase in central Oklahoma seismicity since 2008 induced by massive wastewater injection. Science 345 (6195), 448–451.
Lai, Y., Movchan, A., Rodin, G., 2002. A study of quasi-circular cracks. Int. J. Fract. 113 (1), 1–25.
Lawn, B., 1993. Fracture of Brittle Solids. In: Cambridge Solid State Science Series, Cambridge University Press.
Marone, C., 1998. Laboratory-derived friction laws and their application to seismic faulting. Annu. Rev. Earth Planet. Sci. 26 (1), 643–696.
McGarr, A., 2014. Maximum magnitude earthquakes induced by fluid injection. J. Geophys. Res.: Solid Earth 119 (2), 1008–1019.
McGarr, A., Barbour, A., 2018. Injection-induced moment release can also be aseismic. Geophys. Res. Lett. 45 (11), 5344–5351.
Miller, S., 2020. Aftershocks are fluid-driven and decay rates controlled by permeability dynamics. Nature Commun. 11 (1), 5787.

Miller, S., Collettini, C., Chiaraluce, L., Cocco, M., Barchi, M., Kaus, B., 2004. Aftershocks driven by a high-pressure Co2 source at depth. Nature 427 (6976), 724–727.
Nikolskiy, D., Mogilevskaya, S., Labuz, J., 2013. Complex variables boundary element analysis of three-dimensional crack problems. Eng. Anal. Bound. Elem. 37 (11), 1532–1544.
Parotidis, M., Shapiro, S., Rothert, E., 2005. Evidence for triggering of the Vogtland swarms 2000 by pore pressure diffusion. J. Geophys. Res.: Solid Earth 110 (B5).
Passelègue, F.X., Almakari, M., Dublanchet, P., Barras, F., Fortin, J., Violay, M., 2020. Initial effective stress controls the nature of earthquakes. Nature Commun. 11 (1), 5132.
Rice, J., 1968. Mathematical analysis in the mechanics of fracture. Fract.: Adv. Treatise 2, 191–311.
Rice, J., 1992. Fault stress states, pore pressure distributions, and the weakness of the San Andreas fault. In: Evans, B., Wong, T. Fong (Eds.), Fault Mechanics and Transport Properties of Rocks. In: International Geophysics, vol. 51, Academic Press, pp. 475–503.
Ross, Z., Cochran, E., Trugman, D., Smith, J., 2020. 3D fault architecture controls the dynamism of earthquake swarms. Science 368 (6497), 1357–1361.
Ross, Z., Rollins, C., Cochran, E., Hauksson, E., Avouac, J., Ben-Zion, Y., 2017. Aftershocks driven by afterslip and fluid pressure sweeping through a fault-fracture mesh. Geophys. Res. Lett. 44 (16), 8260–8267.
Ruina, A., 1983. Slip instability and state variable friction laws. J. Geophys. Res: Solid Earth 88 (B12), 10359–10370.
Salamon, N., Dundurs, J., 1971. Elastic fields of a dislocation loop in a two-phase material. J. Elasticity 1 (2), 153–164.
Salamon, N., Dundurs, J., 1977. A circular glide dislocation loop in a two-phase material. J. Phys. C: Solid State Phys. 10 (4), 497–507.
Scholz, C., 2019. The Mechanics of Earthquakes and Faulting. Cambridge University Press.
Scotti, O., Cornet, F., 1994. In situ evidence for fluid-induced aseismic slip events along fault zones. Int. J. Rock Mech. Min. Sci. Geomech. Abstr. 31 (4), 347–358.
Scuderi, M., Collettini, C., 2016. The role of fluid pressure in induced vs. triggered seismicity: insights from rock deformation experiments on carbonates. Sci. Rep. 6 (1), 24852.
Shapiro, S., Huenges, E., Borm, G., 1997. Estimating the crust permeability from fluid-injection-induced seismic emission at the KTB site. Geophys. J. Int. 131 (2), F15–F18.
Shapiro, S., Rentsch, S., Rothert, E., 2005. Characterization of hydraulic properties of rocks using probability of fluid-induced microearthquakes. Geophysics 70 (2), F27–F33.
Sibson, R., 1992. Implications of fault-valve behaviour for rupture nucleation and recurrence. Tectonophysics 211 (1–4), 283–293.
Sneddon, I., 1951. Fourier Transforms. McGraw-Hill, New York.
Stehfest, H., 1970. Numerical inversion of Laplace transforms. Commun. ACM 13 (1), 47–49.
van der Elst, N., Page, M., Weiser, D., Goebel, T., Hosseini, S.M., 2016. Induced earthquake magnitudes are as large as (statistically) expected. J. Geophys. Res.: Solid Earth 121 (6), 4575–4590.
Viesca, R.C., 2021. Self-similar fault slip in response to fluid injection. J. Fluid Mech. 928 (A29).
Wei, S., Avouac, J., Hudnut, K., Donnellan, A., Parker, J., Graves, R., Helmberger, D., Fielding, E., Liu, Z., Cappa, F., Eneva, M., 2015. The 2012 Brawley swarm triggered by injection-induced aseismic slip. Earth Planet. Sci. Lett. 422, 115–125.
Wibberley, C.A.J., Shimamoto, T., 2003. Internal structure and permeability of major strike-slip fault zones: the Median Tectonic Line in Mie prefecture, Southwest Japan. J. Struct. Geol. 25 (1), 59–78.
Wong, T., Ko, S., Olgaard, D., 1997. Generation and maintenance of pore pressure excess in a dehydrating system 2. theoretical analysis. J. Geophys. Res.: Solid Earth 102 (B1), 841–852.
Zhu, W., Allison, K., Dunham, E., Yang, Y., 2020. Fault valving and pore pressure evolution in simulations of earthquake sequences and aseismic slip. Nature Commun. 11 (1), 4833.

PROCEEDINGS A

royalsocietypublishing.org/journal/rspa

Research

Cite this article: Sáez A, Lecampion B. 2023 Post-injection aseismic slip as a mechanism for the delayed triggering of seismicity. *Proc. R. Soc. A* **479**: 20220810.
https://doi.org/10.1098/rspa.2022.0810

Received: 1 December 2022
Accepted: 20 April 2023

Subject Areas:
geophysics, mechanics, civil engineering

Keywords:
injection-induced aseismic slip, post-injection seismicity, shut-in stage, slow slip events

Author for correspondence:
Alexis Sáez
e-mail: alexis.saez@epfl.ch

Electronic supplementary material is available online at https://doi.org/10.6084/m9.figshare.c.6644017.

THE ROYAL SOCIETY PUBLISHING

Post-injection aseismic slip as a mechanism for the delayed triggering of seismicity

Alexis Sáez and Brice Lecampion

Ecole Polytechnique Fédérale de Lausanne, Institute of Civil Engineering, Gaznat Chair on Geo-Energy, Lausanne, Switzerland

AS, 0000-0003-1154-8453

Injection-induced aseismic slip plays an important role in a broad range of human-made and natural systems, from the exploitation of geo-resources to the understanding of earthquakes. Recent studies have shed light on how aseismic slip propagates in response to continuous fluid injections. Yet much less is known about the response of faults after the injection of fluids has stopped. In this work, we investigate via a hydro-mechanical model the propagation and ultimate arrest of aseismic slip during the so-called post-injection stage. We show that after shut-in, fault slip propagates in pulse-like mode. The conditions that control the propagation as a pulse and notably when and where the ruptures arrest are fully established. In particular, critically stressed faults can host rupture pulses that propagate for several orders of magnitude the injection duration and reach up to nearly double the size of the ruptures at the moment of shut-in. We consequently argue that the persistent stressing of increasingly larger rock volumes caused by post-injection aseismic slip is a plausible mechanism for the triggering of post-injection seismicity —a critical issue in the geo-energy industry. Our physical model shows quantitative agreement with field observations of documented cases of post-injection induced seismicity.

1. Introduction

It has been long recognized that subsurface fluid injections can induce fast fault slip [1] that radiates detectable elastodynamic waves, and also slow, sometimes called aseismic slip [2], which is generally more difficult to detect by classical monitoring networks. Evidence for injection-induced aseismic slip dates back to the 1960s, when a slow surface fault rupture was causally linked to fluid injection operations of an oil field in LA, USA [2]. Since then, an increasing number of studies have inferred the occurrence of aseismic slip episodes as a result of anthropogenic subsurface fluid injections [3–6], with recent *in situ* experiments of fluid injection into natural fault systems demonstrating by direct measurements of fault deformation that slow slip was systematically the dominant style of fault motion [7,8].

Injection-induced aseismic slip is thought to play an important role in seismicity induced by industrial fluid injections, a phenomenon that has become critical in ensuring the sustainable development of unconventional hydrocarbon reservoirs [9] and deep geothermal resources [10,11]. It is understood that fluid-driven slow ruptures transmit stresses quasi-statically to unstable fault patches and trigger instabilities at distances that can be far from the region affected by the pressurization of pore-fluid [12,13]. Moreover, a similar mechanism might be also operating behind some natural episodes of seismicity such as seismic swarms and aftershock sequences. In fact, both phenomena are commonly interpreted to be driven by either the diffusion of pore pressure [14,15] or the propagation of aseismic slip [16,17], with recent studies suggesting that both mechanisms might be indeed coupled and responsible for the observed spatio-temporal patterns of seismicity [18–20]. Likewise, tectonic tremors and low-frequency earthquakes are often considered to be driven by slow slip events in subduction zones [21,22], at depths where systematic evidence of over-pressurized fluids is found [22,23]. Metamorphic dehydration reactions [24] and fault-valving behaviour [25] are the two common candidates to explain not only this inferred over-pressurization, but also the very nature of pore pressure and aseismic slip transients in these zones [26].

The seemingly relevant role of fluid-driven aseismic slip in the previous phenomena has motivated the development of physical models that, in recent years, have contributed to a better understanding of the mechanics of this hydro-mechanical problem. Some recent advances include a better notion of how the initial state of stress, the fluid injection parameters, the fault hydraulic properties, and the possible rate-strengthening dependence of rock friction, may affect the dynamics of fluid-driven aseismic slip transients in two- [27–30] and three-dimensional media [31]. The three-dimensional case is the relevant one for field applications and has been shown to be not only quantitatively but also qualitatively very different from two-dimensional configurations [31]. One common aspect of all prior studies is that they focus on fluid sources that are continuous (uninterrupted) in time. Yet much less is known about aseismic ruptures after the injection of fluids has stopped. In particular, the conditions that control the further propagation and ultimate arrest of fluid-driven aseismic slip are fairly unknown, despite a recent investigation for a two-dimensional plane-strain configuration [32]. This is of broad interest since, ultimately, any kind of fluid source and accompanying rupture will have to stop. Understanding the mechanics of post-injection aseismic slip in a realistic three-dimensional scenario is thus of major importance. It corresponds to the first goal of this study.

Our second goal is to understand how and to what extent post-injection aseismic slip can be considered as a possible mechanism for the triggering of seismicity after the end of subsurface fluid injections. It is well known since the Denver earthquakes in the 1960s [1] that upon shutting off the wells, seismicity might continue to occur. Multiple observations suggest that, indeed, it is not rare that the largest events of injection-induced seismic sequences happen during the post-injection stage. Examples of those cases are the 2006 $M_L > 3$ Basel earthquakes in Switzerland, and the 2017 M_w 5.5 Pohang earthquake in South Korea, both causally linked to hydraulic stimulation operations of deep geothermal reservoirs [10,11]. Because the shut-in of the wells does not guarantee the cessation of seismic events, current efforts to manage the seismic risk in the geo-energy industry such as the so-called traffic light systems [33] might be subjected to important limitations in their effectiveness. Understanding the physical mechanisms underpinning post-injection seismicity is thus of paramount importance for the successful development of geo-energy projects. We therefore aim in this study at understanding the combined effect of pore pressure diffusion and solid stress changes due to aseismic slip in the triggering of post-injection seismicity.

2. Governing equations and scaling analysis

(a) Governing equations

We consider a planar fault in an infinite, linearly elastic, isotropic, impermeable and three-dimensional solid, as depicted in figure 1. The initial stress tensor is assumed to be uniform and is characterized by a shear stress τ_0 resolved on the fault plane that acts along the x-direction and a total normal stress σ_0 (acting along the z-direction). We assume a uniform initial pore pressure field of magnitude p_0 that is perturbed by the sudden injection of fluids into a poroelastic fault zone of width w. We model such fluid injection via a line source that is located along the z-axis and crosses the entire fault width. The fault zone permeability k and storage coefficient S are assumed to be uniform and constant. As a result, fluid flow is axisymmetric with regard to the z-axis and occurs only within the fault zone. We further assume that the shear modulus μ and Poisson's ratio ν of the poroelastic fault zone and impermeable elastic host rock are the same. Under such conditions, the displacement field induced by the fluid injection is irrotational and the pore pressure diffusion equation of poroelasticity reduces to its uncoupled version [34], $\partial p/\partial t = \alpha \nabla^2 p$, where $\alpha = k/S\eta$ is the fault hydraulic diffusivity, with η the fluid dynamic viscosity.

By neglecting any poroelastic coupling within the fault zone upon activation of slip, the quasi-static elastic equilibrium that relates fault slip to the shear stress components along the fault can be written as the following boundary integral equations,

$$\tau_i(x,y,t) = \tau_i^0 + \int_\Gamma K_{ij}(x-\xi, y-\zeta; \mu, \nu)\delta_j(\xi,\zeta,t)\,\mathrm{d}\xi\,\mathrm{d}\zeta, \quad \text{with } i,j = x,y, \tag{2.1}$$

where $\tau_i^0 = (\tau_0, 0)^{\mathrm{T}}$ is initial shear traction vector, K_{ij} is the hypersingular (of order $1/r^3$) elastostatic traction kernel (see [35] for example), and $\delta_j = u_j^+ - u_j^-$ is the fault slip vector, with $u_j^\pm$ the displacement vector at the upper (+) and lower (−) faces of the slip surface Γ.

The fault interface is assumed to obey a Mohr–Coulomb shear failure criterion with a constant friction coefficient f and no cohesion expressed as the following local inequality:

$$||\tau_i(x,y,t)|| \le f(\sigma_0' - \Delta p(r,t)), \tag{2.2}$$

where $\sigma_0' = \sigma_0 - p_0$ is the initial effective normal stress, and $\Delta p(r,t) = p(r,t) - p_0$ is the axisymmetric pore pressure perturbation, with r the radial coordinate.

Owing to the unidirectionality of the initial shear traction vector and the axisymmetry property of the equivalent shear load in terms of magnitude, both fault slip and maximum shear stress are characterized by an approximately uniform direction along the x-axis (see the electronic supplementary material). The latter implies that for all practical purposes in this paper, the differences between $||\delta_i||$ and $|\delta_x|$, and $||\tau_i||$ and $|\tau_x|$, are negligible (an approximation that was implicit in [31]). We therefore refer interchangeably hereafter to fault slip as $\delta \equiv \delta_x$ and fault shear stress as $\tau \equiv \tau_x$. Moreover, for the particular case in which $\nu = 0$, $K_{xy} = K_{yx} = 0$ (see, for instance, eqn 7.4 in [35]) and thus the direction of slip (or maximum shear) occurs exactly along the x direction.

The injection of fluid starts at $t = 0$ and consists of two subsequent stages: a continuous injection stage characterized by a constant rate of injection Q, and a post-injection stage in which the injection rate drops instantaneously to zero at $t = t_s$ (figure 1c). Hereafter, we refer to t_s as the shut-in time. The solution of the linear diffusion equation before shut-in (when $0 < t \le t_s$) is known as $\Delta p(r,t) = \Delta p_* E_1(r^2/4\alpha t)$ (section 10.4, eqn 5, [36]), where

$$\Delta p_* = \frac{\Delta p_c}{4\pi} \quad \text{and} \quad \Delta p_c = \frac{Q\eta}{kw}. \tag{2.3}$$

In the previous equations, Δp_* is the intensity of the injection with units of pressure, Δp_c is a characteristic pressure that is of the order of magnitude of the overpressure at the fluid source and $E_1(\cdot)$ is the exponential integral function. The solution after shut-in (when $t > t_s$) is obtained

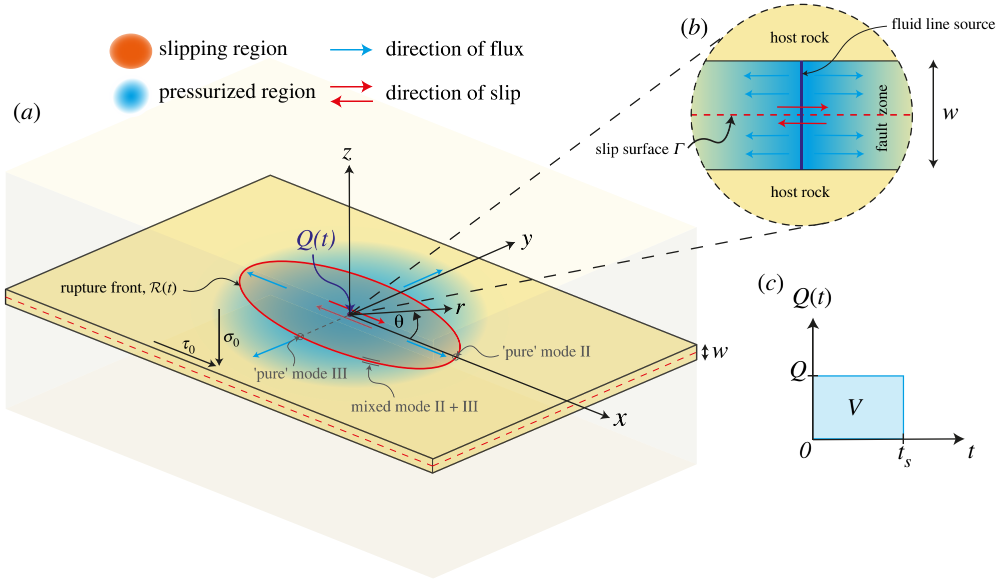

Figure 1. Model schematics. (a, b) Fluid is injected into a permeable fault zone of width w via a line-source that crosses the entire fault zone width. The fault is planar and embedded in an unbounded linearly elastic impermeable host rock. The initial stress tensor is uniform. (c) Fluid is injected at a constant rate Q until $t = t_s$ at which the injection is instantaneously stopped.

simply by superposition as

$$\Delta p(r,t) = \Delta p_* \left\{ E_1\left(\frac{r^2}{4\alpha t}\right) - E_1\left(\frac{r^2}{4\alpha(t-t_s)}\right)\right\}. \tag{2.4}$$

Note that the infinitesimal size of the fluid source in our model provides a proper finite volume of injected fluid $V = Qt_s$, but infinite pressure at the injection point. In this regard, our model must be understood as the late-time asymptotic solution of a more general model where the fluid source possesses a finite characteristic size, say ℓ_*. Our results will be thus applicable when t_s is much larger than the characteristic diffusion time ℓ_*^2/α over the finite source lengthscale. This is indeed the case of most borehole fluid injections, where the borehole radius is $\ell_* \sim 10\,\mathrm{cm}$. By assuming values of hydraulic diffusivity in the range 10^{-4} to $1\ \mathrm{m^2\,s^{-1}}$, the characteristic time ℓ_*^2/α takes values between 100 down to 0.01 s that are much smaller than typical fluid injection duration in geo-energy applications. Moreover, the asymptotic behaviour of the exponential integral function for small values of its argument, $E_1(x) \approx -\gamma - \ln(x)$, where γ is the Euler–Mascheroni's constant, allows us to identify Δp_c as the pressure scale that is of the order of magnitude of the overpressure at $r = \ell_*$ when $t \gg \ell_*^2/\alpha$, as previously stated.

Equations (2.1), (2.2) and (2.4) constitute a complete system of equations to solve for the spatio-temporal evolution of fault slip $\delta(x,y,t)$ and, particularly, the moving boundary representing the slipping region $\mathcal{S}(t)$. The slipping patch $\mathcal{S}(t)$ may be defined mathematically as the region in which the equality of equation (2.2) holds: $\mathcal{S}(t) = \{(x,y) \in \Gamma : |\tau(x,y,t)| = f(\sigma_0' - \Delta p(r,t))\}$. The initial conditions are naturally taken as $\delta(x,y,0) = 0$ and $\dot{\delta}(x,y,0) = 0$ (fault initially at rest and fully locked). The numerical methods used to solve the problem are described in the electronic supplementary material.

(b) Scaling analysis and limiting regimes

The shut-in of the injection provides the natural characteristic time scale of the problem, the shut-in time t_s. This latter introduces, via the solution of the pore-pressure diffusion equation (2.4), a characteristic diffusion lengthscale $\sqrt{4\alpha t_s}$. Alternatively, one may choose (as suggested in [31]) to scale the spatial coordinates by a characteristic rupture lengthscale at the moment of shut-in, say R_s^*. We normalize the pore pressure perturbation $\Delta p(r, t)$, equation (2.4), by the intensity of the injection Δp_*. Introducing the foregoing characteristic scales in the Mohr–Coulomb shear failure criterion, equation (2.2), gives the normalized shear stress, $(\tau - f\sigma_0')/f\Delta p_*$, which in turn is introduced in the balance of momentum, equation (2.1), allowing us to close the scaling of the problem by normalizing the fault slip by $(f\Delta p_*/\mu)\sqrt{4\alpha t_s}$, or alternatively by $(f\Delta p_*/\mu)R_s^*$ if the characteristic rupture lengthscale is chosen for the spatial scale.

It can be shown by using the previous scales (see the electronic supplementary material) that the model depends in addition to dimensionless space and time on one single dimensionless number

$$\mathcal{T} = \frac{f\sigma_0' - \tau_0}{f\Delta p_*}, \tag{2.5}$$

and Poisson's ratio ν.

The so-called stress-injection parameter $\mathcal{T}$ is identical to the one presented recently by Sáez *et al.* [31] for the problem of continuous injection, and similar to the one introduced first by Bhattacharya & Viesca [13] in their two-dimensional plane-strain model. $\mathcal{T}$ is defined as the ratio between the amount of stress necessary to activate fault slip $f\sigma_0' - \tau_0$, and $f\Delta p_*$, which quantifies the effect of the fluid injection on the reduction of fault strength near the injection point. The stress-injection parameter can vary theoretically between 0 and $+\infty$ [31]. However, for practical purposes, we note here that $\mathcal{T}$ is upper bounded. Since $\Delta p_c = 4\pi\Delta p_*$ is of the order of magnitude of the overpressure at the fluid source, the minimum amount of overpressure that one needs to guarantee to activate fault slip under such a line-source approximation is $f\Delta p_c \sim f\sigma_0' - \tau_0$. Substituting the previous relation into (2.5) leads to an order-of-magnitude upper bound $\mathcal{T} \lesssim 10$ (the factor 4π indeed). Note that the introduction of Δp_c and the resulting upper bound for $\mathcal{T}$ in this work put now the results of the continuous-injection problem [31] in a more practical perspective. The limiting values of $\mathcal{T}$ are associated with two end-member scenarios that were first introduced by Garagash & Germanovich [37]. When $\mathcal{T}$ is close to zero, $\tau_0 \to f\sigma_0'$ and thus the fault is critically stressed (about to fail before the injection starts). On the other hand, when $\mathcal{T} \sim 10$, the fault is 'marginally pressurized' as the injection has provided just the minimum amount of overpressure to activate fault slip, $f\Delta p_c \sim f\sigma_0' - \tau_0$. We will make extensive use of the terms critically stressed fault/regime and marginally pressurized fault/regime to refer to these limiting cases throughout this article.

As shown recently by Sáez *et al.* [31], an important aspect of the foregoing two limiting regimes is that they follow different scales during the stage of continuous injection, which is particularly valid in the post-injection problem right at the moment of shut-in t_s. Indeed, the proper slip scale δ_* in the critically stressed limit comes from choosing $\sqrt{4\alpha t_s}$ as the characteristic lengthscale,

$$\delta \sim \delta_* = \frac{f\Delta p_*}{\mu}\sqrt{4\alpha t_s}. \tag{2.6}$$

The proper scale for the slip rate follows from differentiation of the slip scale with respect to time,

$$v \sim v_* = \frac{f\Delta p_*}{\mu}\sqrt{\frac{\alpha}{t_s}}. \tag{2.7}$$

The slip and slip rate scales of the marginally pressurized limit can be obtained likewise by choosing the characteristic rupture scale R_s^* as the spatial lengthscale of the problem, i.e. $\delta \sim (f\Delta p_*/\mu)R_s^*$ and $v \sim (f\Delta p_*/\mu)R_s^*/t_s$. Nonetheless, the latter scales will be seen later to be somewhat irrelevant in the post-injection stage, because marginally pressurized faults will host ruptures that after shut-in arrest almost immediately.

Finally, the second dimensionless parameter of the model, Poisson's ratio ν, is expected to have only an effect on the rupture shape. As shown by Sáez *et al.* [31] for the continuous-injection stage, Poisson's ratio modifies the aspect ratio of the resulting rupture fronts, which become more elongated for increasing values of ν. The position of the elongated rupture fronts is nevertheless determined primarily by the position of circular ruptures, that correspond to a limiting case in which Poisson's ratio of the solid ν is zero. The case of circular ruptures is thus particularly insightful and notably simpler, since in that limit, we can take advantage of the axisymmetry property of the mechanical problem [13,31].

3. Pore-pressure diffusion: the pore-pressure back front

The pore-pressure perturbation $\Delta p(r,t)$ is the only external action driving the rupture after shut-in. It is thus essential to examine in detail its spatio-temporal evolution. Various normalized spatial distributions of pore pressure are plotted in figure 2*a* at different dimensionless times. We first observe that pore pressure decreases quickly after the stop of injection near the fluid source in the sense $r \ll \sqrt{4\alpha(t-t_s)}$, asymptotically as $\Delta p(r,t)/\Delta p_* \approx \ln(\bar{t}/(\bar{t}-1))$ (red dashed curve), with $\bar{t} = t/t_s$ the dimensionless time. Moreover, at large times ($\bar{t} \gg 1$), it decreases simply as $\Delta p(r,t)/\Delta p_* \approx 1/\bar{t}$ (blue dashed curve) for points that are close to the injection now in the sense $r \ll \sqrt{4\alpha t}$. The latter indicates that the region in which the previous asymptotic behaviour is approximately satisfied grows diffusively ($\propto \sqrt{\alpha t}$), and has the shape of a plateau in figure 2*a*.

Moreover, figure 2*a* displays that after shut-in the pore pressure keeps increasing away from the injection line. To better understand such a process, it may be convenient to look at the temporal evolution of pore pressure at fixed normalized positions over the fault plane. Figure 2*b* displays such a plot. Here, we observe that pore pressure remains increasing for some time after injection stops ($\bar{t} > 1$) and eventually reaches a maximum (red circles). After this instant of maximum pressure, the pore pressure decreases following ultimately the same asymptotes of figure 2*a*, meaning that the aforementioned diffusely expanding plateau has reached the corresponding fixed radial positions in figure 2*b*.

The relation between a given position over the fault plane and the time at which the maximum pressure is reached, defines a 'back front' of pore pressure, $\mathcal{P}(t) = \{r(t) \in \Gamma : \partial \Delta p(r,t)/\partial t = 0\}$. Owing to the axisymmetry property of pore pressure diffusion in our model, $\mathcal{P}(t)$ is circular and is thus fully defined by its radius $P(t)$. Differentiating equation (2.4) with respect to time and solving for $\partial \Delta p/\partial t = 0$ leads to the following expression for the normalized radius of the pore-pressure back front,

$$\frac{P(t)}{\sqrt{4\alpha t_s}} = \left[\bar{t}(\bar{t}-1)\ln\left(\frac{\bar{t}}{\bar{t}-1}\right)\right]^{1/2}, \tag{3.1}$$

which further reduces to $P(t)/\sqrt{4\alpha t_s} \approx \sqrt{\bar{t}}$, or simply $P(t) \approx \sqrt{4\alpha t}$, at large times. Note that the large-time asymptote of $P(t)$ is the same expression than that of the radius of the pore-pressure perturbation front $L(t) = \sqrt{4\alpha t}$ for the continuous-injection stage, albeit each expression describes different processes.

On the other hand, the maximum pore pressure increase undergone historically at a given position r, say $\Delta p_m(r)$, is obtained by simply evaluating the pore pressure perturbation $\Delta p(r,t)$ at the time t_m in which the maximum occurs, i.e. $\Delta p(r, t_m(r))$. t_m comes from solving for time in (3.1) with $P(t) = r$. $\Delta p_m(r)$ is displayed in figure 2*a* (grey dashed curve) representing the pore pressure back front $\mathcal{P}(t)$ in this plot, which corresponds to the envelope of all curves (for all times) associated with instantaneous spatial distributions of pore pressure. Note that $\Delta p_m(r)$ cannot be obtained in closed form since equation (3.1) is not invertible for time, nevertheless, in the large-time limit, $t_m(r)/t_s \approx \bar{r}^2$, such that $\Delta p_m(r)/\Delta p_* \approx E_1(1) - E_1(\bar{r}^2/(\bar{r}^2-1))$. The previous asymptotic approximation is also plotted in figure 2*a* (green dashed curve). Similarly, an expression for Δp_m as a function of time t may be derived, which is indeed obtainable in closed form as $\Delta p_m(t) = \Delta p(P(t), t)$ (grey and green dashed curves in figure 2*b*).

4. Pulse-like circular ruptures

Circular ruptures occur in the limit of a Poisson's ratio $\nu = 0$. As discussed in previous sections, a Poisson's ratio different than zero is expected to affect mainly the shape of the resulting ruptures, and less significantly other relevant quantities of the fault response [31]. Circular ruptures are thus a particularly insightful case, in which the axisymmetry property of the mechanical problem

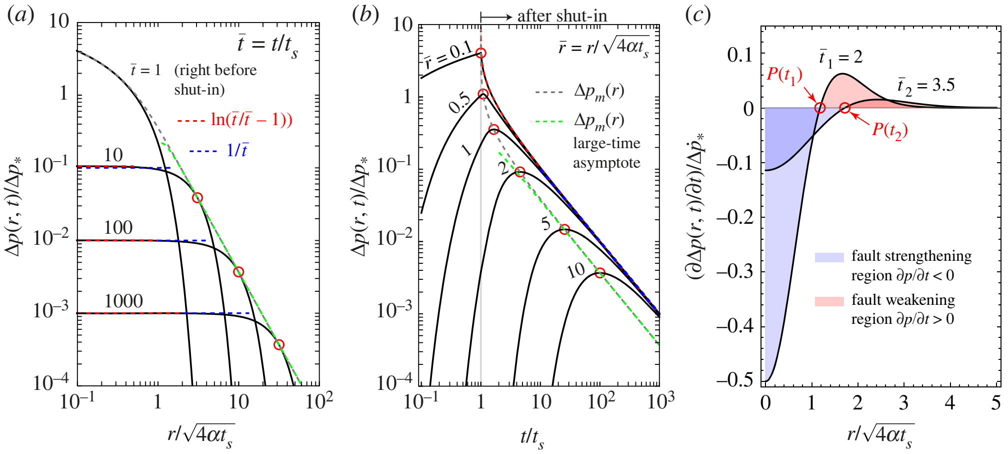

Figure 2. (*a*) Normalized spatial distribution of pore pressure at different dimensionless times. Dashed curves correspond to asymptotic behaviours as explained in the main text. (*b*) Evolution of normalized pore pressure at some fixed dimensionless radial positions. Red circles indicate the instants at which the maximum pressure Δp_m is reached. (*c*) Spatial distribution of pore pressure rate normalized by $\Delta\dot{p}_* = \Delta p_*/t_s$, at two dimensionless times after shut-in. Red circles indicate the position of the pore-pressure back front $P(t)$, equation (3.1).

[13,31] simplifies the analysis of results. The effect of Poisson's ratio on the rupture shape will be quantified in §5.

(a) Recall on the self-similar solution before shut-in

The solution for the continuous-injection stage ($t \le t_s$) of the same problem was presented recently by Sáez *et al.* [31]. We briefly summarize some of their results as they provide the starting point for the understanding of the post-injection phase. Sáez *et al.* showed that fault slip induced by injection at constant volume rate (from an infinitesimal source) is self-similar in a diffusive manner. The rupture radius $R(t)$ evolves simply as $R(t) = \lambda L(t)$, where $L(t) = \sqrt{4\alpha t}$ is the nominal position of the pore-pressure perturbation front, and λ is the so-called amplification factor, for which an analytical solution as function of the stress-injection parameter $\mathcal{T}$ exists (eqn (21) in [31]). The asymptotic behaviour of λ for the limiting values of $\mathcal{T}$ is particularly insightful. For critically stressed faults ($\mathcal{T} \ll 1$), the amplification factor turns out to be large ($\lambda \gg 1$) and thus the rupture front outpaces largely the fluid pressure front ($R(t) \gg L(t)$), with λ obeying the simple asymptotic relation $\lambda \approx 1/\sqrt{2\mathcal{T}}$. On the other hand, for marginally pressurized faults ($\mathcal{T} \sim 10$), the amplification factor is small ($\lambda \ll 1$), such that the rupture front lags significantly the fluid pressure front ($R(t) \ll L(t)$), with $\lambda \approx (1/2)\exp[(2 - \gamma - \mathcal{T})/2]$, where $\gamma = 0.577216\cdots$ is the Euler–Mascheroni's constant. These simple closed-form expressions provide important insights into the response of faults during continuous fluid injections. They allow us to estimate the slip front position in a compact and convenient way that also determines whether aseismic-slip stress transfer ($\lambda > 1$) or pore pressure increase ($\lambda < 1$) is the dominant mechanism in the possible triggering of seismicity associated with coupled fluid flow and fault slip processes.

(b) Transition from crack-like to pulse-like rupture: the locking front

In §3, we showed that the shut-in of the injection is characterized by the emergence of the so-called pore-pressure back front, which corresponds to the instantaneous position at which the pressure has reached its maximum historically. With reference to figure 2*c*, we consequently see that pore pressure is instantaneously increasing at every point on the fault plane located beyond

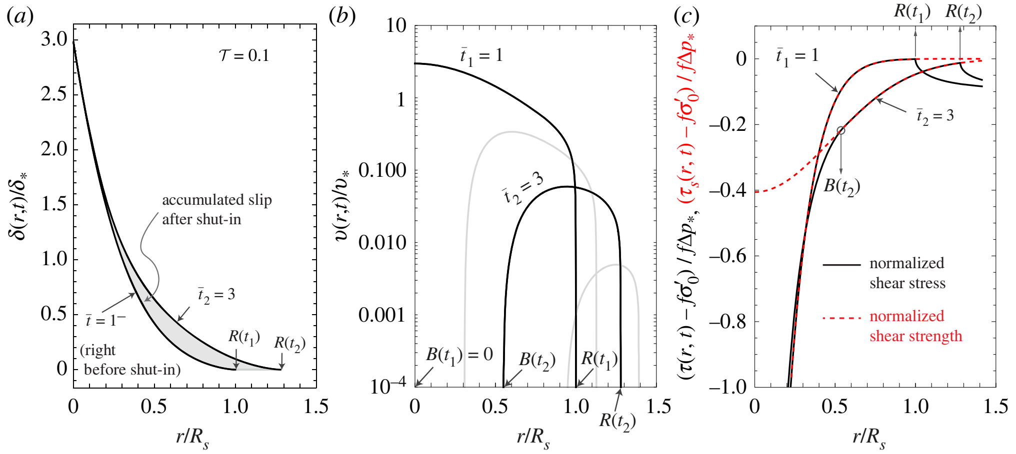

Figure 3. Normalized spatial profiles of (*a*) slip δ, (*b*) slip rate v and (*c*) shear stress τ and shear strength τ_s, for a mildly critically stressed fault with $\mathcal{T} = 0.1$, at two dimensionless times, one right before shut-in ($\bar{t}_1 = 1$) and the other one at some moment after shut-in ($\bar{t}_2 = 3$). The positions of the locking $B(t)$ and rupture $R(t)$ fronts are highlighted throughout (*a–c*). In (*b*), grey curves correspond to aseismic pulses at times $\bar{t} = 1.54$ and 6.25.

the position of this front: $\partial \Delta p(r,t)/\partial t > 0$ for all $r > P(t)$. This results in a moving region where the fault shear strength $\tau_s(r,t) = f(\sigma_0' - \Delta p(r,t))$ is decreasing. Such reduction of fault strength is indeed what uniquely drives the propagation of the rupture after shut-in. On the other hand, in the complementary inner region $r < P(t)$, the opposite holds, and $\partial \Delta p(r,t)/\partial t < 0$ (figure 2*c*). The pore pressure is thus diminishing and the effective normal stress and thus fault shear strength is rising as a result. Furthermore, the enhanced fault shear strength may eventually become locally greater than the resolved shear stress τ, consequently re-locking the slip surface. We observe the development of this re-locking process systematically in all our numerical solutions, starting virtually right after shut-in. Such a re-locking process is characterized by a locking front $\mathcal{B}(t)$ propagating outwardly from the injection location. The emergence of this locking front marks the transition from crack-like (before shut-in) to pulse-like (after shut-in) propagation mode, a prominent feature of post-injection aseismic slip.

Similarly to the rupture front $\mathcal{R}(t)$, the locking front $\mathcal{B}(t)$ must be circular when $\nu = 0$, and is thus fully defined by its radius $B(t)$. Figure 3 shows the transition from crack-like to pulse-like propagation as seen in the normalized slip δ, slip rate v, and shear stress τ and strength τ_s spatial distributions, at times right before shut-in and at some time after shut-in. The aseismic pulses can be seen clearly in figure 3*b* for the slip rate distribution, where the positions of the locking and rupture fronts are highlighted. Note that both the magnitude (peak slip rate) and width of the pulses decrease monotonically with time. On the other hand, the Mohr–Coulomb inequality given by equation (2.2) establishes that, within the slipping patch ($B(t) < r < R(t)$), the shear stress must be equal to the fault shear strength, whereas in the re-locked region ($r < B(t)$), the shear stress must be lower than the fault shear strength. Both cases can be clearly seen in figure 3*c*, where the positions of the rupture and locking fronts are also highlighted. Note that the normalized shear strength in figure 3*c* is equal to $(\tau_s - f\sigma_0')/f\Delta p_* = -\Delta p/\Delta p_*$, which is minus the normalized pore pressure perturbation. In addition, we observe that at some distance away from the locking front and towards the injection point, the shear stress after shut-in is slightly greater than the shear stress right before shut-in. This amplification of fault shear stress after shut-in is due to the amount of slip accumulated through the passage of the slip pulse (shown in figure 3*a*) and the non-local redistribution of stresses associated with it via the quasi-static non-local integral operator of equation (2.1). We further elaborate on the amplification of shear stress behind the locking front when analysing the characteristics of slip rate and shear stress rate along the fault in the electronic supplementary material.

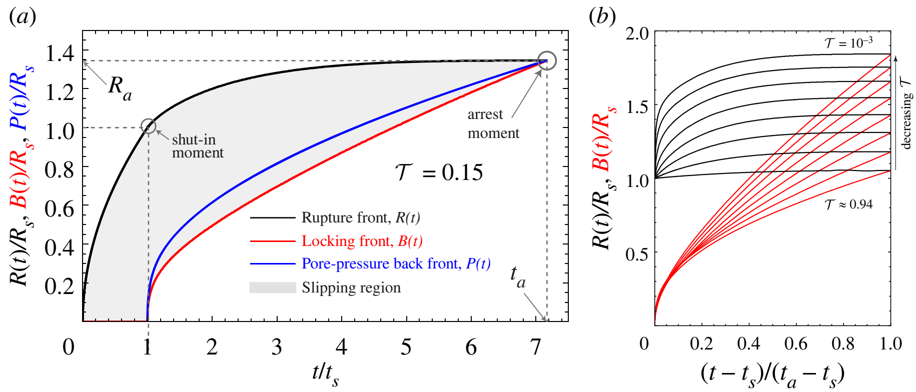

Figure 4. (*a*) Evolution of the rupture front radius, locking front radius and pore-pressure back front radius, for an exemplifying case with $\mathcal{T} = 0.15$. The front radii are normalized by the rupture radius at the moment of shut-in R_s. Instants of shut-in of the injection t_s and arrest of the rupture t_a are highlighted, as well as the maximum run-out distance R_a. (*b*) Evolution of the rupture front radius and locking front radius for many values of $\mathcal{T}$ ranging from $\approx$0.94 to 10^{-3}.

(c) Evolution of the rupture, locking and pore-pressure back fronts: conditions for pulse-like propagation and arrest

We have identified three relevant fronts that propagate simultaneously upon the stop of the injection: the rupture front of radius $R(t)$, the pore-pressure back front of radius $P(t)$ and the locking front of radius $B(t)$. The temporal evolution of these three fronts is shown in figure 4*a* for an exemplifying case with $\mathcal{T} = 0.15$. Since the only external action that drives the rupture pulses is the further increase of pore pressure after shut-in at distances $r > P(t)$, the pore-pressure back front must be located behind the rupture front in order to guarantee the sustained propagation of the rupture: $P(t) < R(t)$. Similarly, the propagation of the locking front is driven by the existence of a region within the pulse where the pore pressure decreases (and thus the shear strength increases to effectively re-lock the fault), such that $P(t) > B(t)$. Hence, the following inequalities must be satisfied during pulse-like propagation in the post-injection stage, $B(t) < P(t) < R(t)$, which are verified in all our numerical solutions, such as the one displayed in figure 4*a*.

On the other hand, since Coulomb's shear strength on the fault plane is always bounded, the shear stress developed at the front of the rupture pulse must be bounded as well, to effectively allow both quantities to be equal. In other words, the slipping patch must propagate with no stress singularity at the 'fracture' front of such a cohesive-like crack [38]. Hence, both stress intensity factors (SIF) in mode II and mode III must be equal to zero at $r = R(t)$. This fracture-mechanics-like propagation condition was derived in appendix A of Sáez *et al.* [31] for any axisymmetric circular shear rupture, and is still valid for pulse-like (annular) ruptures as long as the 'fracture' is understood not as the current slipping patch, but rather as the region that has ever experienced any amount of slip since the start of the injection (i.e. for all $r < R(t)$). The condition reads as [31]

$$\int_0^{R(t)} \frac{\Delta\tau(r,t)}{\sqrt{R(t)^2 - r^2}}\, r\, \mathrm{d}r = 0 \iff \int_0^{B(t)} \frac{\tau_0 - \tau^*(r,t)}{\sqrt{R(t)^2 - r^2}}\, r\, \mathrm{d}r + \int_{B(t)}^{R(t)} \frac{\tau_0 - f(\sigma_0' - \Delta p(r,t))}{\sqrt{R(t)^2 - r^2}}\, r\, \mathrm{d}r = 0. \quad (4.1)$$

Note that $\Delta\tau(r,t) = \tau_0 - \tau(r,t)$, with τ_0 the initial shear stress and $\tau(r,t)$ the instantaneous shear stress distribution. In the right-hand side of equation (4.1), we have split the integral into two parts recognizing that within the slipping patch, the shear stress must be equal to the fault shear strength: $\tau(r,t) = f(\sigma_0' - \Delta p(r,t))$, whereas in the re-locked region, $\tau^*(r,t)$ corresponds to the instantaneous shear stress distribution which depends on the current slip distribution through the quasi-static non-local integral operator of equation (2.1).

The second propagation condition for the post-injection aseismic pulses comes from the analysis of Garagash [39] for seismic and aseismic pulses driven by thermal pressurization. As we discuss in detail in the electronic supplementary material, our aseismic pulses are akin to an annular 'crack' of inner radius $B(t)$ and outer radius $R(t)$, as long as the dislocation density is replaced by the slip rate gradient $\partial v/\partial r$, and the change of shear stress by the shear stress rate $\partial\tau/\partial t$. The near-tip asymptotic behaviour of classical cracks [40] is thus valid but in terms of $\partial\tau/\partial t$ and v. Having this result in mind, we can now invoke Garagash's healing condition [39], which states that the shear stress rate $\partial\tau/\partial t$ must be non-singular at the locking front to effectively allow the fault to re-lock. This is because within the slipping patch and, particularly, at the locking front, the shear stress rate must equal the shear strength rate (the plastic consistency condition, see for example, appendix A in [31]), in our case, $\partial\tau/\partial t = -f\partial\Delta p/\partial t$. Since $\partial\Delta p/\partial t$ is bounded all over the fault plane, it follows that $\partial\tau/\partial t$ cannot be singular at the locking front.

Garagash obtained an integral equation similar to (4.1) based on the non-singularity of shear stress rate at the locking front (eqn (19) in [39]). Such an integral equation is valid under the assumptions of his study in two-dimensional elasticity for a solitary steady pulse travelling in anti-plane (III) or in-plane (II) mode of sliding. Indeed, if our pulse that is non-steady would be solved in two-dimensional elasticity, a similar expression can be derived for the two symmetric pulses (travelling in opposite directions) that would emerge in that case, from known SIF formulae [41]. To the best of our knowledge, the SIF formulae for an annular crack under axisymmetric loading are unknown (numerical procedures have been proposed to calculate them in mode I [42]). Nevertheless, one can still formalize this second propagation condition based on the near-tip asymptotic behaviour of classical cracks as [38,40]

$$K_{\dot\tau} = 0, \quad \text{with } \frac{\partial\tau(r,t)}{\partial t} \simeq \frac{K_{\dot\tau}}{\sqrt{2\pi(B(t)-r)}} \text{ when } r \to B(t)^{-}. \tag{4.2}$$

$K_{\dot\tau}$ is the so-called 'stress-rate intensity factor' [39] with units of (pressure/time) $\times$ length$^{1/2}$. It quantifies the intensity of the leading-order (singular) term of $\partial\tau/\partial t$ near the locking front. Note that $K_{\dot\tau}$ may be also written in terms of the mode II, $K_{2,\dot\tau}$, and mode III, $K_{3,\dot\tau}$, stress-rate intensity factors, as $K_{\dot\tau}^2 = K_{2,\dot\tau}^2 + K_{3,\dot\tau}^2$. Indeed, since the two components of the shear stress rate on the fault plane must be non-singular along the locking front, equation (4.2) can be stated in the stronger form, $K_{2,\dot\tau} = K_{3,\dot\tau} = 0$. Note also that the stress-rate intensity factor is not the same as the SIF rate, at least along the locking front. For the latter, there is no SIF whatsoever, since there is no fracture tip and thus no potential singular term for τ when $r \to B(t)^{-}$. Hence, although it could have been tempting to write the healing condition (4.2) as $\mathrm{d}\mathcal{G}/\mathrm{d}t = 0$, where $\mathcal{G}$ is the energy release rate, such a statement is not true.

Equations (4.1) and (4.2) are, therefore, the necessary conditions for the propagation of post-injection aseismic slip as an annular pulse. Together, these two equations describe the motion of the rupture front $R(t)$ and locking front $B(t)$ that are at quasi-static equilibrium with a given $\Delta\tau(r,t)$. Yet as already mentioned, we cannot solve these two equations without solving the entire moving boundary value problem. However, they provide additional insights into the mechanics of the problem and, as shown in the electronic supplementary material, define important characteristics of the slip rate and shear stress rate distributions along the fault plane.

We now seek for the conditions that characterize the final arrest of the rupture pulses. Figure 4*a* shows that as expected at the moment of arrest, the locking front $B(t)$ catches up the rupture front $R(t)$. Since in that instant the rupture pulse effectively vanishes, equation (4.2) has no relevance. However, the 'fracture' (slipped surface) is still present and, to be at mechanical equilibrium, equation (4.1) must be satisfied. Since the second term of the right-hand side of (4.1) approaches zero at the time of arrest, equation (4.1) takes now the simpler form

$$\int_0^{R_a} \frac{\tau_0 - \tau^*(r,t_a)}{\sqrt{R_a^2 - r^2}} r\,\mathrm{d}r = 0, \tag{4.3}$$

where t_a is the time of arrest and $R_a = R(t_a)$ is the corresponding rupture radius at the arrest time (the maximum run-out distance). In the previous equation, R_a may be equivalently replaced by $B_a = B(t_a)$. Furthermore, since the rupture after shut-in is driven uniquely by the further increase

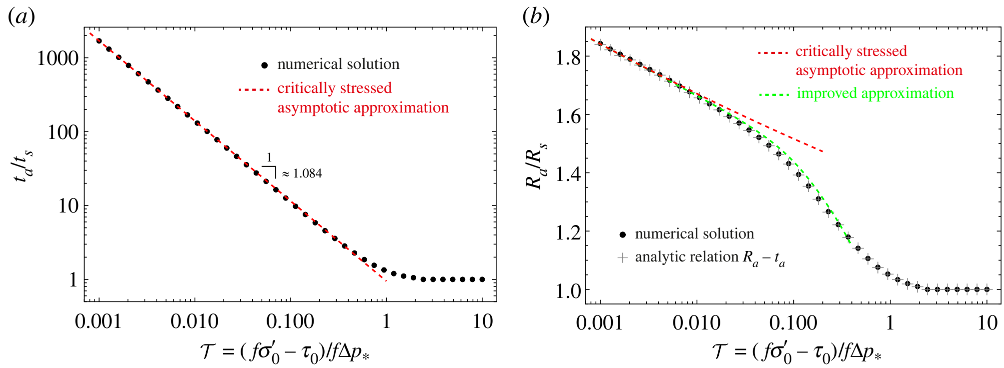

Figure 5. (*a*) Normalized arrest time and (*b*) normalized maximum run-out distance as a function of the stress-injection parameter $\mathcal{T}$. In (*a*, *b*), the red dashed line represents the asymptotic behaviour in the critically stressed regime ($\mathcal{T} \ll 1$), equations (4.6) and (4.7), respectively. In (*b*), the green dashed curve is an improved approximation obtained by substituting equation (4.6) directly into (4.5). The grey crosses correspond to the evaluation of R_a via the analytic relation, equation (4.5), using the numerical solution of t_a.

of pore pressure that occurs in the region $r > P(t)$, the rupture arrest will be also characterized by the moment at which the pore-pressure back front catches up the rupture front (figure 4*a*). Therefore, the following conditions must be also met exactly at the time of arrest,

$$R(t_a) = B(t_a) = P(t_a), \tag{4.4}$$

and more importantly, by combining the previous equation with equation (3.1), we obtain an analytic relation between the radius R_a and time t_a of arrest,

$$R_a = \sqrt{4\alpha t_a}\left((t_a/t_s - 1)\ln\left(\frac{t_a}{t_a - t_s}\right)\right)^{1/2}, \tag{4.5}$$

which in the large-time limit ($t_a \gg t_s$) becomes simply $R_a \approx \sqrt{4\alpha t_a}$. Equations (4.3) and (4.5) provide a complete system of equations to solve for the time at arrest t_a and the maximum run-out distance R_a. However, the shear stress profile left by the arrested rupture $\tau^*(r, t_a)$ in equation (4.3) is unknown analytically. Hence, we must determine at least one of these two quantities numerically.

(d) Arrest time and maximum run-out distance

We now determine numerically the normalized arrest time t_a/t_s and normalized maximum run-out distance R_a/R_s by spanning the relevant parameter space with 40 values of $\mathcal{T}$ ranging from 10^{-3} to 10, equally spaced in logarithmic scale. The results are presented in figure 5. Marginally pressurized faults ($\mathcal{T} \sim 10$) produce slip pulses that arrest almost immediately after the stop of the injection and practically do not grow further than the size of the ruptures at the moment of shut-in (R_s), whereas critically stressed faults ($\mathcal{T} \ll 1$) host events that can last up to $\approx 10^3$ times the injection time t_s and grow approximately up to 1.8 times the rupture radius at the shut-in time (for the smallest value of $\mathcal{T}$ considered). Critically stressed faults are, therefore, the asymptotic regime of more practical interest. We thus focus on determining its behaviour precisely.

For the normalized arrest time, figure 5*a* shows a clear power law between t_a/t_s and $\mathcal{T}$. Using a linear least square regression, we obtain

$$\frac{t_a}{t_s} \approx a\mathcal{T}^{-b}, \tag{4.6}$$

with $a = 0.946876$ and $b = 1.084361$. In solving the least-squares problem, we have considered data points satisfying $\mathcal{T} \lesssim 0.01$ ($\ll 1$) and obtained an R^2 equal to 0.999993.

We can now use the analytic relation between R_a and t_a, equation (4.5), to construct a critically stressed asymptotic approximation for the normalized maximum run-out distance using the power-law relation (4.6). In particular, at large arrest times ($t_a \gg t_s$), (4.5) is approximately equal to $R_a/R_s \approx (1/\lambda)\sqrt{t_a/t_s}$. Substituting $\lambda \approx 1/\sqrt{2\mathcal{T}}$ (see §4a) and (4.6) into the previous expression, leads to the sought critically stressed approximation,

$$\frac{R_a}{R_s} \approx \left(\frac{2a}{\mathcal{T}^{b-1}}\right)^{1/2} \quad \text{or} \quad R_a \approx \left(\frac{4a\alpha t_s}{\mathcal{T}^{b}}\right)^{1/2}. \tag{4.7}$$

In addition, we can substitute equation (4.6) directly into (4.5) to provide an improved asymptotic approximation for the critically stressed regime that is approximately valid over a broader range of values of $\mathcal{T}$ (green curve in figure 5*b*). Note that in figure 5*b*, we have also plotted the values of R_a not from the numerical solution, but rather by evaluating the analytic relation (4.5) (grey crosses) given the numerical solution of t_a. The latter is just to illustrate the exactness of the relation between the radius of arrest and the time of arrest (4.5).

5. Pulse-like non-circular ruptures

In this section, we examine the effect of Poisson's ratio different than zero on the propagation and ultimate arrest of the post-injection aseismic pulses. For this purpose, we consider a fixed value of $\nu = 1/4$ (Poisson's solid).

(a) Recall on the self-similar solution before shut-in

Sáez *et al.* [31] also solved the continuous-injection problem for the case of $\nu \neq 0$. They showed that the rupture front is well-approximated by an elliptical shape that becomes more elongated for increasing values of ν and decreasing values of $\mathcal{T}$: the more critically stressed the fault is, the more elongated the rupture becomes. The aspect ratio of the quasi-elliptical rupture fronts is upper bounded by $1/(1-\nu)$ in the critically stressed limit ($\mathcal{T} \ll 1$), and lower bounded by $(3-\nu)/(3-2\nu)$ in the marginally pressurized limit ($\mathcal{T} \sim 10$). Furthermore, the rupture area $A_r(t)$ evolves simply as $A_r(t) = 4\pi\alpha\lambda^2 t$ (linear with time), and interestingly it does not depend on Poisson's ratio ν (see fig. 6 in [31]). The previous numerical observations led to closed-form approximate expressions for the entire evolution of the quasi-elliptical rupture fronts in the terms of the semi-major $a(t)$ and semi-minor $b(t)$ axes of an ellipse, as $a(t) = R(t)/\sqrt{1-\nu}$ and $b(t) = R(t)\sqrt{1-\nu}$ in the critically stressed regime, and $a(t) = R(t)\sqrt{3-\nu}/\sqrt{3-2\nu}$ and $b(t) = R(t)\sqrt{3-2\nu}/\sqrt{3-\nu}$ in the marginally pressurized regime, with $R(t)$ the rupture radius of a circular rupture for the same value of $\mathcal{T}$, which is known analytically (see §4a).

(b) Effect of ν on the propagation of the aseismic pulses

We summarize the main characteristics of the propagation of pulse-like non-circular ruptures in figure 6. This figure is composed by four snapshots of the normalized slip rate distribution for a mildly critically stressed fault with $\mathcal{T} = 0.1$. Each snapshot represents a remarkably different propagation phase. The first one, figure 6*a*, corresponds to a moment right before stopping the injection, specifically at $\bar{t} = 0.99$, where $\bar{t} = t/t_s$. At this time, the rupture is still propagating in crack-like mode. For this value of $\mathcal{T}$, the quasi-elliptical rupture front outpaces the pore-pressure perturbation front. Note that the spatial coordinates in figure 6 are normalized by the rupture lengthscale $R_s = \lambda\sqrt{4\alpha t_s}$ (radius of a circular rupture with the same value of $\mathcal{T}$, see §4a). The second snapshot, figure 6*b*, displays the rupture after shut-in at approximately 4.75 times the injection duration. In this figure, we can already observe the locking front and thus the propagation of the rupture as an annular pulse. Interestingly, although the rupture front is clearly

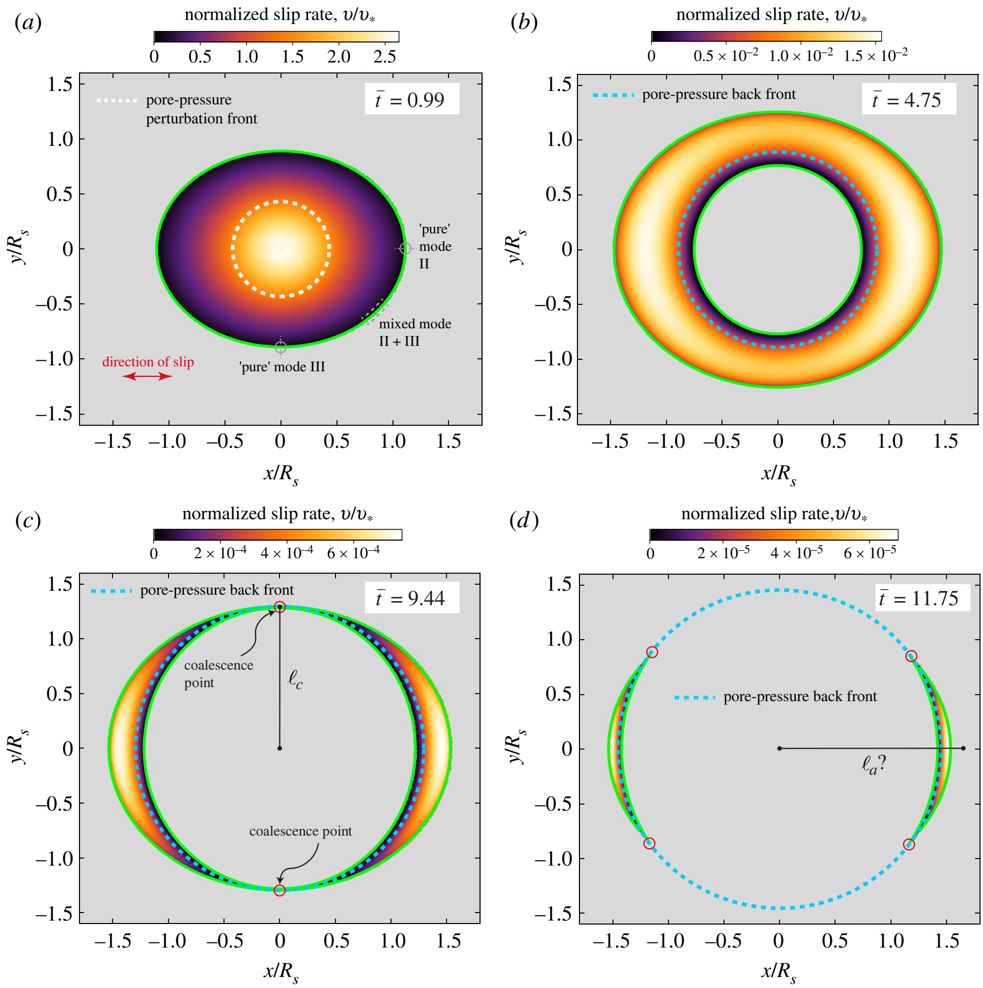

Figure 6. Snapshots of normalized slip rate distribution for a non-circular rupture with $\mathcal{T} = 0.1$ and $\nu = 0.25$. The spatial coordinates x and y are scaled by the rupture radius at the shut-in time R_s for the same $\mathcal{T}$ but $\nu = 0$, whereas dimensionless time $\bar{t} = t/t_s$ as usual. (*a*) Crack-like propagation right before shut-in ($\bar{t} = 0.99$). (*b*) Propagation as an annular pulse after shut-in ($\bar{t} = 4.75$). (*c*) Moment in which the locking and rupture fronts are about to coalesce ($\bar{t} \approx 9.44$). (*d*) Propagation after coalescence of the fronts as two 'moon-shaped' pulses travelling in opposite directions ($\bar{t} = 11.75$). The maximum run-out distance of the rupture ℓ_a that will be eventually reached at some later time is depicted. The positions at which the locking, rupture and pore-pressure back fronts intersect each other are indicated with red circles.

elongated along the mode II direction of sliding (same as it is before shut-in), the locking front seems to be slightly elongated along the mode III direction instead.

Figure 6*c* and 6*d* show the most remarkable effects of considering a Poisson's ratio different than zero. Figure 6*c* corresponds to the instant at which the locking front is about to coalesce with the rupture front along the mode III direction of sliding. Note that at this time of coalescence t_c, approximately equal to 9.44 times the injection duration in this case, the pore-pressure back front is also intersecting both the rupture and locking fronts. Let us denote the maximum run-out distance of the rupture in the mode III direction as ℓ_c (see figure 6*c* for its definition). The previous observation, which was somewhat expected from the analysis of circular ruptures (see equation (4.4)), means that there is a unique relation between ℓ_c and t_c, in the form $\ell_c = P(t_c)$, where $P(t)$ is the instantaneous radius of the pore-pressure back front known analytically from equation (3.1).

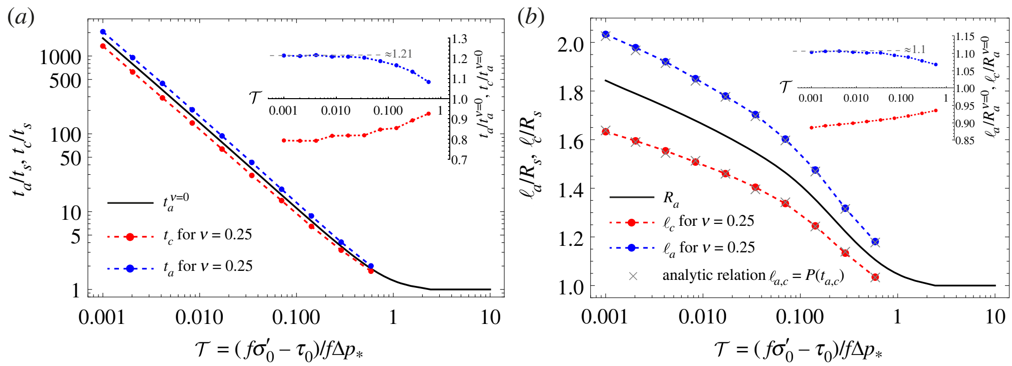

Figure 7. (*a*) Normalized arrest time t_a and coalescence time t_c for $\nu = 0.25$ as a function of the stress-injection parameter $\mathcal{T}$ for values ranging from 10^{-3} to ≈ 0.59. The inset shows the same results but normalized by the arrest time of circular ruptures $t_a^{\nu=0}$. (*b*) Same as (*a*) but for the maximum run-out distance of the rupture in the mode II ℓ_a and mode III ℓ_c directions of sliding. In the inset, same results but normalized by the arrest radius of circular ruptures R_a. Grey crosses in (*b*) come from evaluating t_a and t_c of (*a*) in equation (3.1) for the pore-pressure back front.

Moreover, after the coalescence of the fronts, figure 6*d* displays that the original annular pulse is split into two symmetric 'moon-shaped' pulses that travel in opposite directions. The moving positions at which the locking and rupture fronts are intersecting each other are shown with red circles in figure 6*d*. These positions are again such that the pore-pressure back front is located exactly at the same place. The condition (4.4) for circular ruptures at the time of arrest is thus still valid for non-circular ruptures but now at any time $t_c \le t \le t_a$. Finally, the instantaneous rupture area of each moon-shaped pulse decreases continuously with time and will eventually collapse into a point located along the x-axis at some distance ℓ_a as depicted in figure 6*d*. ℓ_a corresponds to the maximum run-out distance of the entire rupture and, similarly to the case of circular ruptures, equation (4.5) will now take the form $\ell_a = P(t_a)$, where t_a is the time of arrest.

(c) Effect of ν on the arrest time and maximum run-out distance

We calculate the time of arrest t_a and maximum run-out distance of the rupture ℓ_a, as well as the time of coalescence t_c and maximum run-out distance in the mode III direction ℓ_c, for 10 values of the stress-injection parameter $\mathcal{T}$ ranging from 10^{-3} to ≈ 0.59. This range allows us to span the most relevant part of the parameter space associated with critically stressed faults. Figure 7*a* summarizes the results for the normalized arrest time t_a/t_s and normalized time of coalescence t_c/t_s, including the results for the arrest time of circular ruptures $t_a^{\nu=0}$. We observe that the coalescence of the fronts occurs at earlier times than the arrest of circular ruptures. Moreover, Poisson's ratio $\nu \neq 0$ has the clear effect of delaying the arrest of the aseismic pulses with regard to the circular case. To better quantify this delayed arrest, we plot the same results in the inset but normalizing the arrest and coalescence times by the arrest time of circular ruptures. It can be seen that the more critically stressed the fault is, the longer it takes for non-circular ruptures to arrest compared with circular ones. Furthermore, the ratio $t_a/t_a^{\nu=0}$ seems to approach an asymptotic value of ≈ 1.21 in the critically stressed limit (when $\mathcal{T} \to 0$).

Figure 7*b* shows the results for the normalized maximum run-out distance of the rupture ℓ_a/R_s and normalized maximum run-out distance in the mode III direction ℓ_c/R_s. In accordance with the results for t_c and t_a, the distance ℓ_c is lower than the arrest radius of circular ruptures R_a for the same value of $\mathcal{T}$, whereas the maximum run-out distance of non-circular ruptures ℓ_a is greater than the maximum run-out distance of its circular counterpart R_a. In addition, the relations $\ell_c = P(t_c)$ and $\ell_a = P(t_a)$ discussed in the previous section are shown to be in good agreement (grey crosses in figure 7*b*) with the numerical results up to numerical discretization errors. Moreover, the inset shows the run-out distances ℓ_a and ℓ_c but normalized by the arrested radius of circular ruptures R_a. The maximum run-out distance ℓ_a seems to approach an asymptotic value in this case of $\approx 1.1R_a$ in the limit of critically stressed faults.

6. Discussion

(a) Critically stressed regime versus marginally pressurized regime

Figures 5 and 7 summarize one of the most important results of this article. Marginally pressurized faults ($\mathcal{T} \sim 10$) produce aseismic pulses that arrest almost immediately after shut-in, whereas critically stressed faults ($\mathcal{T} \ll 1$) are predicted to host ruptures that propagate for several orders of magnitude the injection duration and grow up to approximately twice the size of the ruptures at the moment of shut-in (for the smallest value of $\mathcal{T}$ considered). Critically stressed faults are therefore the relevant propagation regime that is able to sustain seismicity after shut-in. Under this regime, the long-lived aseismic pulses provide a longer exposure of the surrounding rock mass to continuous stressing due to aseismic slip and, at the same time, their longer run-out distances perturb a larger volume of rock mass up to $\approx 2^3 = 8$ times larger than the volume affected at the moment of shut-in, therefore increasing the likelihood of triggering earthquakes during the post-injection stage compared with the marginally pressurized case.

To illustrate under what conditions these two regimes can occur, let us consider some characteristic values of a fault undergoing fluid injection. Consider that water is injected into a fault zone at a constant volume rate $Q \sim 30\,[\mathrm{l\,s^{-1}}]$, which is typical of hydro-shearing treatments of deep geothermal reservoirs at around 3–4 km depth [11]. Assume also a fluid dynamic viscosity $\eta \sim 10^{-3}\,[\mathrm{Pa\,s}]$. The fault hydraulic transmissivity can vary over several orders of magnitude. Consider, for instance, a plausible value of $kw \sim 10^{-12}\,\mathrm{m^3}$ [43]. This yields a characteristic pressure at the fluid source of $\Delta p_c = 30\,[\mathrm{MPa}]$ and an intensity of the injection $\Delta p_* \approx 2.4\,[\mathrm{MPa}]$ (equation (2.3)). Let us consider for the initial effective normal stress a characteristic value of $\sigma_0' \sim 60\,[\mathrm{MPa}]$, that is somewhat consistent with a depth of 3–4 km under gravitational loading and hydrostatic conditions. Assuming a friction coefficient $f = 0.6$, the initial fault shear strength is $f\sigma_0' = 36\,[\mathrm{MPa}]$, while the intensity of the strength reduction due to fluid injection is $f\Delta p_* \approx 1.4\,[\mathrm{MPa}]$. The amount of initial shear stress τ_0 acting on the fault will finally determine the regime of the fault response in this example. Consider first a fault that is close to failure, say $\tau_0 = 35.9\,[\mathrm{MPa}]$ (0.1 [MPa] to failure). This leads to a small value of the stress-injection parameter $\mathcal{T} \approx 0.07$ (equation (2.5)), and therefore to a fault responding in the so-called critically stressed regime ($\mathcal{T} \ll 1$). Before shut-in, the fluid-induced aseismic slip front in this example is predicted to outpace the pore pressure perturbation front by a constant factor $\lambda \approx 1/\sqrt{2\mathcal{T}} \approx 2.7$ (§4a), for the case of circular ruptures. Consider that the injection was conducted during a period of $t_s = 1$ day. Then, after shut-in, the post-injection aseismic pulse is expected to propagate for $t_a - t_s \approx 16$ days (equation (4.6)) and reach a maximum run-out distance of $\approx$1.54 times the run-out distance at the moment of shut-in (equation (4.7)). To close this dimensional example, let us assume that the fault has a hydraulic diffusivity of, say, $\alpha = 0.01\,\mathrm{m^2\,s^{-1}}$. The radius of the rupture at the moment of shut-in is $R_s = \lambda\sqrt{4\alpha t_s} \approx 159\,\mathrm{m}$ (see again §4a), and the maximum run-out distance of post-injection aseismic slip will be $R_a \approx 1.54 \times 159\,\mathrm{m} \approx 245\,\mathrm{m}$. If the hydraulic diffusivity were 10 times lower, R_s and R_a would decrease by approximately 30%.

Consider the same example of the previous paragraph, but now with a fault that is further away from failure. Assume, for instance, a lower value of the initial shear stress $\tau_0 = 25\,[\mathrm{MPa}]$ (11 [MPa] to failure). The stress-injection parameter for this case becomes $\mathcal{T} \approx 7.9$, well within the marginally pressurized regime ($\mathcal{T} \sim 10$). Prior to shut-in, the slip front is predicted to lag the pore pressure perturbation front by a factor $\lambda \approx (1/2)\exp[(2 - \gamma - \mathcal{T})/2] \approx 0.02$ (§4a). Moreover, upon the stop of the injection, the rupture is expected to arrest almost immediately (figure 5), such that $t_a \approx t_s \approx 1$ [day] and $R_a \approx R_s = \lambda\sqrt{4\alpha t_s} \approx 1.2\,\mathrm{m}$. In the two previous examples, the end-member regimes were achieved by changing only the initial shear stress acting on the fault or, equivalently, the distance to failure. This highlights the importance of the pre-injection stress state in determining the response of the fault. However, there is another relevant quantity that may equally change the fault response regime, namely, the intensity of the injection Δp_*. So far, we have assumed hydraulic parameters resulting in $\Delta p_* \approx 2.4$ [MPa] (and $\Delta p_c = 30$ [MPa]). Imagine now that the fault is still relatively close to failure as in the first example ($\tau_0 = 35.9$ [MPa]) but a much smaller amount of fluid is being injected, say $Q = 1\,[l\,\mathrm{s}^{-1}]$. This is unlikely the case of a hydraulic stimulation but could instead occur in the case of a natural source of fluids occurring at the same depth. The intensity of the injection (equation (2.3)) is now $\Delta p_* \approx 0.08$ [MPa] (with $\Delta p_c = 1$ [MPa]), and the corresponding stress-injection parameter $\mathcal{T} \approx 2.1$. This will lead equivalently to a rupture that lags the fluid pressure front during continuous injection ($\lambda \approx 0.37$) and that arrests almost immediately after shut-in. The latter, despite the fact that the fault was 'just' 0.1 [MPa] away from failure under ambient conditions. On the other hand, a more intense injection than the one with $Q = 30\,[\mathrm{l\,s}^{-1}]$ will act in the direction of moving the fault response towards the critically stressed regime (decreasing values of $\mathcal{T}$). Those injections might however sometimes open the fault (if $\Delta p_c \gtrsim \sigma'_0$), a mechanism that is not accounted for in this work.

(b) Conceptual model of post-injection seismicity

In the next sections, we use our model to investigate to what extent post-injection aseismic slip can be considered as a mechanism for the delayed triggering of seismicity. However, before going into the details of the discussion, it seems convenient to establish first a few general concepts. First, we note that any model that aims at explaining observations of post-injection seismicity must produce spatio-temporal changes of pore pressure or solid stresses after shut-in. Our model produces both of them. In fact, the pore pressure changes alone are essentially equal to the ones already considered by Parotidis *et al.* [44] to explain the so-called back front of seismicity that is sometimes observed after the termination of fluid injections. Note that Parotidis *et al.*'s model assumes the increase of pore pressure as the only triggering mechanism of seismicity. We, instead, elaborate on a mechanism based on the combined effect of transient changes in solid stresses due to aseismic slip and pore pressure after shut-in. For the sake of simplicity, we carry out all discussions in terms of circular ruptures only. Rupture non-circularity does not modify the order of magnitude of the results.

Let us define now conceptually what seismicity means in the context of our model. We consider that a single fault plane undergoes some transient fluid injection that may be approximated as a pulse of injection rate (figure 1*c*). It is assumed that as a result of the injection, the fault slides predominantly aseismically. Seismic events are thought to be triggered on unstable patches of the same fault plane (due to, for instance, heterogeneities in rock frictional properties) or other pre-existing discontinuities in the surroundings of the slowly propagating rupture. The former and latter events are commonly denominated as on-fault and off-fault seismicity, respectively, a terminology that we use later on. Note that an important underlying assumption of this conceptual model is that the unstable patches of the *aseismic* fault do not represent a sufficiently large area to change its predominantly stable mode of sliding to a large dynamic rupture.

We define a Mohr–Coulomb failure function in the form $F(\boldsymbol{x}, t; \boldsymbol{n}) = |\tau(\boldsymbol{x}, t; \boldsymbol{n})| - f(\sigma(\boldsymbol{x}, t; \boldsymbol{n}) - p(\boldsymbol{x}, t))$, where τ and σ are the shear and total normal stresses acting on a certain unstable patch with unit normal vector $\boldsymbol{n}$ at a given position $\boldsymbol{x}$ and time t, p is the pore-fluid pressure and f is a constant (static) friction coefficient. The failure function is such that $F \leq 0$ always. The inequality $F < 0$ holds when no frictional failure occurs, whereas the equality $F = 0$ is valid whenever frictional sliding is activated. The initial stress state is assumed such that $F(\boldsymbol{x}, t < 0; \boldsymbol{n}) < 0$ at all pre-existing discontinuities before injection starts. Once injection begins, the failure function may approach zero by changes in the solid stresses τ and σ and the pore pressure p. Upon failure of a certain patch, slip may evolve seismically only if the friction coefficient is allowed to weaken. The time-dependent nucleation of instabilities and, moreover, the explicit modelling of seismicity, are out of the scope of our study. Instead, we consider a conceptual model in which any positive change of the failure function at a certain position and time may lead to frictional sliding and, subsequently, to the *possibility* of triggering an instability.

We introduce two types of changes of the failure function that will prove to be useful for our analysis. The first one, a static change ΔF between two times, and the second one, an instantaneous change $\dot{F}$. Their mathematical expressions are

$$\Delta F(\boldsymbol{x};\boldsymbol{n}) = \Delta\tau(\boldsymbol{x};\boldsymbol{n}) - f(\Delta\sigma(\boldsymbol{x};\boldsymbol{n}) - \Delta p(\boldsymbol{x})), \tag{6.1}$$

$$\dot{F}(\boldsymbol{x},t;\boldsymbol{n}) = \dot{\tau}(\boldsymbol{x},t;\boldsymbol{n})\mathrm{sgn}(\tau(\boldsymbol{x},t;\boldsymbol{n})) - f(\dot{\sigma}(\boldsymbol{x},t;\boldsymbol{n}) - \dot{p}(\boldsymbol{x},t)). \tag{6.2}$$

ΔF is widely known in seismology as the Coulomb stress change [45], a terminology we adopt hereafter. Note that in equation (6.1), we assume that the change of shear stress $\Delta\tau$ is positive if it occurs in the same direction as the shear stress at the selected initial time. On the other hand, in equation (6.2), sgn(·) is the sign function and the dot over the scalar fields represents a partial derivative in time. $\dot{F}$ is commonly denominated as the Coulomb stressing rate, a quantity that is sometimes correlated to seismicity rates [46]. Finally, we highlight that positive contributions to failure $\Delta F > 0$ ($\dot{F} > 0$) are given by both positive changes of pore pressure $\Delta p > 0$ ($\dot{p} > 0$) and negative changes of total normal stress $\Delta\sigma < 0$ ($\dot{\sigma} < 0$). The effect of the shear stress is however less straightforward and knowledge about the direction of τ and thus about the absolute state of stress is required to evaluate its relative contribution to ΔF ($\dot{F}$).

(c) On-fault seismicity

(i) Theoretical considerations

On fault, both aseismic-slip stress transfer and pore pressure changes are active during the post-injection stage. We use the Coulomb stressing rate $\dot{F}$ as an indicator of the regions where seismicity is expected. Let us first note that due to the planarity of the fault, the total normal stress rate $\dot{\sigma}$ is zero. Hence, the only component of stress rate that is active along the fault plane is the shear one $\dot{\tau}$. Moreover, since the absolute state of stress of the fault is known, we can assume by convention that $\tau > 0$ and consequently that positive rates of shear stress are the ones that contribute to frictional failure. Along the fault plane, equation (6.2) thus further simplifies to

$$\dot{F}(\boldsymbol{x},t) = \dot{\tau}(\boldsymbol{x},t) + f\Delta\dot{p}(\boldsymbol{x},t). \tag{6.3}$$

We first analyse the stress-transfer effect, $\dot{\tau}$ in equation (6.3). With reference to the characteristics of slip rate and shear stress rate that we describe in detail in the electronic supplementary material, it can be readily shown that the shear stress rate acting on possible unstable patches is positive everywhere along the fault plane. For the region outside of the pulse, this can be derived after differentiating equation (2.1) with respect to time and noting that seismicity should be triggered predominantly in the proximity of both the locking and rupture fronts, as a consequence of the amplification of shear stress rate concentrated near the tips of the aseismic pulses (see the electronic supplementary material). Regarding the inside of the pulse, the value of $\dot{\tau}$ in our model, which is simply equal to the fault shear strength rate, is somewhat irrelevant. The actual stress-transfer effect comes rather from considering that unstable patches may be effectively locked and surrounded by aseismic slip. The latter would increasingly load the locked patches in shear until eventually a dynamic event could be triggered.

With regard to the pore-pressure effect, $f\Delta\dot{p}$ in equation (6.3), its contribution to seismicity can be understood readily from the mere definition of the pore-pressure back front. At distances $r > P(t)$, where $P(t)$ is the radius of the front, the pore pressure rate is positive. Therefore, the region ahead of the pore-pressure back front is where fluid-induced instabilities are expected, a result that was already introduced by Parotidis *et al.* [44]. Conversely, at distances $r < P(t)$, the opposite holds $\Delta\dot{p} < 0$, and thus the triggering of instabilities is here inhibited.

We are now ready to superimpose the effects of $\dot{\tau}$ and $f\Delta\dot{p}$ to notably determine the sign of $\dot{F}$. This is schematized in figure 8*a*, where four different regions in which the results of the superposition operate differently, are delineated by the three relevant fronts of the problem, namely, the rupture front $R(t)$, the pore-pressure back front $P(t)$ and the locking front $B(t)$. In region R1 for distances ahead of the pulse $r > R(t)$, the Coulomb stressing rate $\dot{F}$ is always positive.

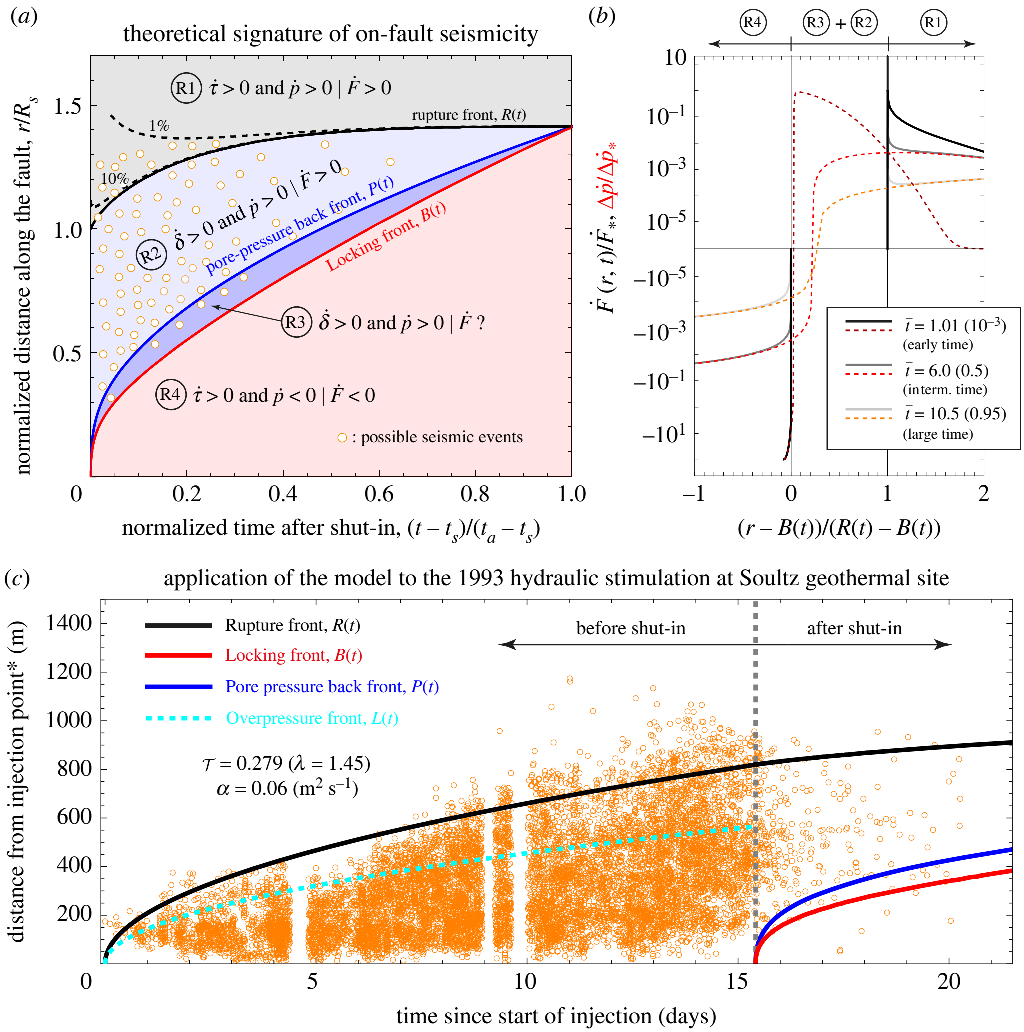

Figure 8. (*a*) Theoretical signature of on-fault seismicity after shut-in. Distance versus time plot showing regions over the fault plane (R1–R4) where the combined effect of aseismic-slip stress transfer ($\dot{\tau}$ or $\dot{\delta}$) and pore pressure changes ($\dot{p}$) operates in different manners. White points represent the location/time of possible seismic events where the Coulomb stressing rate $\dot{F}$ is predicted to be positive. Dashed curves correspond to the position where $\dot{F}$ is 1% and 10% of the characteristic Coulomb stressing rate $\dot{F}_* = f\Delta p_*/t_s$. (*b*) Normalized Coulomb stressing rate $\dot{F}$ (solid lines in grey scale) and pore pressure rate $\Delta\dot{p}$ (dashed lines in red scale) along the fault plane at three dimensionless times for the same rupture than in (*a*), $\mathcal{T} = 0.1$. Dimensionless times in the legend box are in the format $\bar{t} = t/t_s$, $((t - t_s)/(t_a - t_s))$. (*c*) Application of our model to the 1993 hydraulic stimulation of the GPK1 well at the Soultz-sous-Forêts geothermal site in France [47]. The migration of seismicity from the injection point is well represented by our model based on realistic field parameters as described in the main text. *The injection point has been taken at 2925 m depth as in [44].

In this region, seismicity is expected to be triggered by the contribution of both a positive shear stress rate $\dot{\tau} > 0$ and a positive pore pressure rate $\Delta\dot{p} > 0$. Let us further analyse the magnitude and distribution of $\dot{F}$ here. This is shown in figure 8*b*, where the spatial profile of normalized Coulomb stressing rate is plotted at various dimensionless times for an exemplifying case with $\mathcal{T} = 0.1$. The solitary contribution of the pore pressure rate, which is independent of the value of $\mathcal{T}$, is also included in this figure. Note that the scale of the Coulomb stressing rate $\dot{F}_*$ comes from equation (6.3) and is equal to $\dot{F}_* = f\Delta p_*/t_s$. We observe from figure 8*b* that ahead of the rupture pulse and at early times after shut-in, $\dot{F}$ is dominated by the amplification of the shear stress rate ($\dot{\tau} \gg \Delta\dot{p}$), whereas at intermediate times and notably at large times, the pore pressure rate becomes the most dominant quantity ($\Delta\dot{p} \gg \dot{\tau}$) from some distance ahead of the rupture front that gets increasingly closer to the slip front with time. However, at the rupture front itself and very close to it, the shear stress rate will always dominate the magnitude of $\dot{F}$ due to the square-root singularity of $\dot{\tau}$ discussed in the electronic supplementary material.

Let us now consider the regions R2 and R3 that compose the slipping patch. Here, seismic events are promoted by the increase of shear stress $\dot{\tau} > 0$ acting on locked unstable patches that are loaded by surrounding aseismic slip, a mechanism that is denoted by $\dot{\delta} > 0$ in figure 8*a*. Moreover, in region R2 ahead of the pore pressure back front $r > P(t)$, the pore pressure rate is also positive, meaning that the Coulomb stressing rate $\dot{F}$ is strictly positive too. The triggering of instabilities in region R2 is thus expected. Conversely, in the region R3 behind the pore pressure back front $r < P(t)$, the pore pressure rate is negative. As such, its effect counterbalances the positive contribution due to aseismic slip ($\dot{\delta} > 0$). Whether $\dot{F}$ is positive or negative in this region is not possible to know from our calculations, because we do not explicitly model the effect of any potential locked patch on the shear loading. Nevertheless, by assuming that the shear loading $\dot{\tau}$ is some unknown but positive quantity, the solitary effect of the pore pressure changes provides a lower bound for $\dot{F}$ within the slipping patch. Even more, the pore-pressure effect $f\Delta\dot{p}$ is a lower bound of $\dot{F}$ over the entire fault plane since as already discussed, the stress-transfer effect $\dot{\tau}$ is positive everywhere. This can be clearly observed in figure 8*b* when looking at the regions behind (R4) and ahead (R1) of the rupture pulse.

Finally, in the region R4 behind the slip pulse $r < B(t)$, seismicity is promoted by the amplification of the shear stress rate near the locking front (see the electronic supplementary material), albeit such amplification is going to be neutralized to some extent by the negative pore pressure rate operating in this region. In fact, figure 8*b* shows that the negative pore pressure rate appears to completely neutralize the stress rate amplification behind the locking front for the particular case shown in this figure. Furthermore, a general proof of this numerical observation can be developed as follows. First, we recall that $\dot{F} = 0$ within the slipping patch and, particularly, when $r \to B(t)^+$. Note that we have just referred to $\dot{F}$ with the same notation as the Coulomb stressing rate acting on unstable locked patches (equation (6.3)). However, we are rather referring by $\dot{F}$ in this particular case to the rate of the failure function on the portion of the slipping patch that is aseismically sliding. Since $\dot{\tau}$ and $\Delta\dot{p}$ are both continuous at the locking front (the former due to the healing condition discussed in §4c), the previous limit is also valid when approaching $B(t)$ from the outside of the pulse: $\dot{F} = 0$ when $r \to B(t)^-$. Because both $\dot{\tau}$ and $\Delta\dot{p}$ decrease monotonically with increasing distances measured from the locking front and towards the injection point $r = 0$, we conclude that $\dot{F} < 0$ for all points located behind the locking front, $r < B(t)$. We highlight that this statement is valid at any time after shut-in and for any value of $\mathcal{T}$. More importantly, it allows us to establish unequivocally that seismicity is not expected to occur behind the locking front, despite the positive increase of shear stress operating behind the rupture pulse.

The final region along the slip plane where seismicity is theoretically expected after shut-in ($\dot{F} > 0$) is highlighted in figure 8*a* by the white points that represent the location and time of possible seismic events. Note that in this figure, we intentionally draw increasingly less events as time goes by. This is due to the Coulomb stressing rate decreasing by many orders of magnitude at intermediate and large times compared with early times (figure 8*b*) and, as such, the seismicity rate is expected to decrease in a similar manner. Moreover, the lower limit of the seismically active region resembles the back front of seismicity proposed by Parotidis *et al.* [44]. Indeed, Parotidis *et al.*'s back front is equal to the pore-pressure back front $P(t)$ of this work (eqn 5 in [44], equation (3.1) here). Whether some instabilities can be triggered or not in region R3 seems quite irrelevant from an observational point of view, since such small spatial differences between the locking front and the pore pressure back front are very likely indistinguishable in seismic catalogues and, in many cases, possibly even smaller than their location errors. Therefore, the back front of on-fault seismicity of post-injection aseismic slip is for practical purposes equal to the one of Parotidis *et al.* [44].

Finally, unlike the back front of seismicity that corresponds to a sharp front ($\Delta\dot{p} = 0$), the upper limit of the seismically active region or seismicity front is not sharply defined. This is because the Coulomb stressing rate $\dot{F}$ vanishes theoretically only at infinity. The definition of a seismicity front thus requires some degree of arbitrariness likely associated with a chosen threshold to trigger instabilities. In our case, to be somehow consistent with the definition of the back front in terms of rates, one possible choice is to define the front of seismicity as a small percentage of the Coulomb stressing rate undergone in the proximity of the rupture front. Since the scale $\dot{F}_* = f\Delta p_*/t_s$ represents such a quantity at least at early times, we calculate and display curves associated with 1% and 10% of $\dot{F}_*$ in figure 8*a*. We recognize that other choices are possible, notably in terms of Coulomb stress rather than in terms of rates.

(ii) The 1993 hydraulic stimulation at the Soultz geothermal site, France

With the previous theoretical considerations in mind, we aim now at testing our model against field observations of post-injection seismicity. We choose the well-documented case of the 1993 hydraulic stimulation at the Soultz geothermal site in France, where direct evidence of significant aseismic slip induced by the fluid injection exists [48]. Our focus is the first injection test of the GPK1 well, where 25 000 m^3 of water were injected into granite over a period of about 15 days. The injection was conducted with a step incremental flow rate that reached a maximum of 36 $[l\,s^{-1}]$ through a 550 m open-hole section located at depths between 2850 m and 3400 m [48]. Figure 8*c* shows the spatio-temporal evolution of seismicity of the more than 10 000 events recorded during the injection test, before and after shut-in [47].

Previous studies have suggested that this injection test stimulated a network of fractures [49], whereas our model considers the stimulation of only one single planar fault in three dimensions. Nevertheless, recent simulations of injection-induced aseismic slip in a two-dimensional discrete fracture network (DFN) have shown that the same patterns predicted by a single fracture in two dimensions emerge collectively for the DFN [50]. This is notably the case of a set of fractures operating under critically stressed conditions [50]. Since the fractures intersecting the open-hole section of the borehole in this test are known to be critically stressed [51], we make the seemingly reasonable assumption that the response of the fracture network can be approximated by an equivalent single planar fault in three dimensions.

To compute the evolution of the relevant fronts associated with the signature of seismicity predicted by our model, we must estimate two quantities independently: the fault hydraulic diffusivity α and the stress-injection parameter $\mathcal{T}$. Thanks to the estimates of aseismic slip based on borehole-wall deformation by Cornet *et al.* [48], we may estimate the fault hydraulic diffusivity based on the formula of accrued slip at the injection point in the critically stressed regime, $\delta(r = 0, t = t_s) \approx 3.5(f\Delta p_*/\mu)\sqrt{4\alpha t_s}$ (equation (2.6) here, with the pre-factor in equation 28 of [31]), where $t_s = 370$ h is the shut-in time. Considering a shear modulus $\mu = 20$ [GPa] [48] and a constant friction coefficient $f = 0.6$, we just need to estimate Δp_* (equation (2.3)). For the latter, we approximate the injection history as a pulse of injection characterized by the same duration of 370 h and a constant injection rate that equals the actual volume of injected fluid, which yields $Q \approx 19\,[l\,s^{-1}]$. The hydraulic transmissivity kw has been estimated by others at the highest pressures of the test in approximately $1.7 \times 10^{-12}\,[m^3]$ [43]. Assuming a water dynamic viscosity of $\eta = 8.9 \times 10^{-4}$ [Pa s], we can finally calculate the pressure intensity $\Delta p_* \approx 0.8$ [MPa] and the characteristic overpressure at the fluid source $\Delta p_c \approx 10$ [MPa]. The latter is indeed very close to the actual downhole overpressure measured at 2850 m depth, equal to 9.1 [MPa] [48]. Finally, based on the estimates by Cornet *et al.* [48] who reported fracture slip along the open-hole section up to 4.7 cm, we estimate a fault hydraulic diffusivity of $\alpha \approx 0.06\,m^2\,s^{-1}$. This value of α is of the same order of magnitude as the one estimated through a different method by others [44].

With this estimate of diffusivity, we compute the evolution of the pore pressure back front after shut-in (equation (3.1)), and the evolution of the overpressure front $L(t) = \sqrt{4\alpha t}$ before shut-in, both displayed in figure 8*c*. The next step is to compute the evolution of the rupture and locking fronts, for which we must estimate the stress-injection parameter $\mathcal{T}$ (equation (2.5)). From the previous analysis of determining α, we already know that $f\Delta p_* \approx 0.48$ [MPa], so that we just need to estimate the initial distance to failure, $f\sigma_0' - \tau_0$. This is perhaps the most difficult quantity to estimate in our model. Although in this case we do know that the fault is critically stressed [51], the value of $\mathcal{T}$ in the critically stressed regime is very sensitive to changes of the order of tenths or hundredths of one megapascal, which is quite challenging to constrain confidently. It seems then more reasonable to assume *a priori* that the amplification of shear stress near the slip front contributes to some significant extent to drive the seismicity front before shut-in—since the fault is critically stressed and the overpressure front slightly lags the seismicity front—and consequently determine the amplification factor λ that explains well the evolution of seismicity. We find $\lambda = 1.45$ to explain well the data before shut-in (see figure 8*c*). In the previous estimate, we considered the fact that some seismicity is expected to be triggered ahead of the slip front and thus the rupture front must lag the seismicity front to some extent. Finally, this value of λ yields a value of $\mathcal{T} \approx 0.279$ (§4a), which in turn gives a distance to failure of approximately 0.1 [MPa]. The latter is within the range of initial distances to failure of fractures intersecting the open-hole section as estimated by others [51].

The corresponding rupture and locking fronts resulting from $\mathcal{T} \approx 0.279$ are shown in figure 8*c*. We observe that our model seems capable of explaining relatively well the migration of seismicity during this episode of combined fluid flow and aseismic slip, both before and after shut-in. Our hydro-mechanical model enriches previous analyses of the migration of seismicity [44] by considering the previously overlooked effect of stress transfer due to aseismic slip, which was previously suggested to be important in this field case [52] but never tested likely due to the lack of physical models. Notably, the theoretical signature of post-injection seismicity (figure 8*a*) seems to be present in the seismicity cloud. Moreover, the arrest time of the aseismic pulse for this value of $\mathcal{T}$ is predicted as $t_a \approx 3.78 \times t_s \approx 58$ days (equation (4.6)), which is ≈43 days after shut-in. Seismicity was however recorded only within the first 5 days upon the stop of the injection, which is $\bar{t} \approx 0.12$ of normalized time as defined in figure 8*a*. This seems again consistent with our theoretical reasoning that most of the seismicity should be expected at early times after shut-in, when the Coulomb stressing rate is the highest in the post-injection problem (figure 8*b*).

(d) Off-fault seismicity

Seismicity can be triggered not only on unstable patches laying along the *aseismically* sliding fault, but also on unstable patches present in other pre-existing discontinuities nearby the propagating slow rupture. Because fluid flow is assumed to occur only within the permeable fault zone that hosts the reactivated slip plane, off-fault seismicity can be triggered uniquely by the mechanism of stress transfer due to aseismic slip in our model. Equations (6.1) and (6.2) thus take the following forms that exclude the null pore pressure changes, $\Delta F(\boldsymbol{x};\boldsymbol{n}) = \Delta\tau(\boldsymbol{x};\boldsymbol{n}) - f\Delta\sigma(\boldsymbol{x};\boldsymbol{n})$ and $\dot{F}(\boldsymbol{x},t;\boldsymbol{n}) = \dot{\tau}(\boldsymbol{x},t;\boldsymbol{n})\mathrm{sgn}(\tau(\boldsymbol{x},t;\boldsymbol{n})) - f\dot{\sigma}(\boldsymbol{x},t;\boldsymbol{n})$, respectively. Evaluating the previous expressions requires knowledge of the normal vectors $\boldsymbol{n}$ of pre-existing discontinuities and the absolute state of stress, both of which are obviously site-specific and always partially uncertain. Given the site-specific nature of the required information, we address the challenge of exploring the off-fault triggering mechanism by analysing a specific field example. Moreover, in the electronic supplementary material, we discuss some further implications of our model such as the Coulomb stressing rate in the vicinity of the reactivated fault and the off-fault counterpart of the seismicity signature shown in figure 8*a*.

(i) The 2013 hydraulic stimulation at the Rittershoffen geothermal site, France

We focus on the 2013 hydraulic stimulation of the GRT-1 well in the crystalline basement of the Rittershoffen geothermal field in France, at a depth of about 2 km [53,54]. This stimulation lasted for about 1 day and was accompanied by swarm-like seismicity that illuminated a single planar structure that was reactivated in shear due to the fluid injection [53]. Our model of a single planar fault in three dimensions seems therefore a good approximation for this field case. Upon shut-in, seismicity stopped immediately. However, after 4 days in which no seismic activity was detected, a short-lived second swarm began and developed along a nearby sub-parallel structure likely part of an en-echelon fault system [53]. Several hypotheses were discussed by Lengliné *et al.* [53] to explain what possibly led the second fault to failure as well as the 4-days delay of this second swarm. The favoured hypothesis for the failure of the second fault was in fact the stress transfer due to injection-induced aseismic slip associated with the first fault. However, the authors discarded post-injection aseismic slip as a mechanism for explaining the delayed triggering of the second swarm. They argued that slip on the first fault would be difficult to promote after shut-in due to the fault pressure dropping quickly to zero, thus moving the fault interface away from failure [53]. In light of our results, this statement is valid only locally at the injection point, where the fault interface re-locks immediately upon the stop of the injection. However, as we have seen, pore pressure keeps increasing away from the injector after shut-in, which drives the propagation of a pulse-like frictional rupture that further accumulates slip on the fault. Hence, injection-induced aseismic slip can potentially explain as a unique mechanism both the failure of the second fault and the delayed triggering of the swarm of this particular case for which the reactivated fault is indeed thought to be critically stressed [53].

Again, as in the 1993 Soultz case, we want to estimate the fault hydraulic diffusivity α and the stress-injection parameter $\mathcal{T}$. In the absence of reliable estimates of both aseismic slip and hydraulic diffusivity, we assume for the purpose of this illustration a characteristic value of $\alpha = 0.05\,\mathrm{m^2\,s^{-1}}$ for the reactivated fault. This is of the order of magnitude of diffusivities estimated from other fluid injections in nearby reservoirs [44], as well as in this same geothermal field via pressure transient analysis [54]. Yet the latter must be considered with care since the estimates are based on production tests that are strongly influenced by near-well processes [54]. To estimate the stress-injection parameter $\mathcal{T}$, we follow a similar approach to the one used in the previous section for the 1993 Soultz case. We assume the aseismic slip front to play an important role in explaining the migration of seismicity, which consists in this case of more than 1300 events [53]. Considering a rupture radius at the moment of shut-in $R_s = 250\,\mathrm{m}$ (see fig. 9 in [53]), we obtain from $R_s = \lambda\sqrt{4\alpha t_s}$ (§4a) with $t_s = 19\,\mathrm{h}$ in this case, an amplification factor $\lambda \approx 2.14$, which yields a stress-injection parameter $\mathcal{T} \approx 0.117$.

This value of $\mathcal{T}$ gives an arrest time of aseismic slip $t_a \approx 9.70 \times t_s \approx 184\,\mathrm{h}$ (equation (4.6)), which is equivalent to approximately 7 days after the stop of the injection. The latter is indeed longer than the 4-days delay of the second swarm. Yet the relatively short time between the estimated arrest time and the occurrence of the second swarm suggests that most of the post-injection stress transfer from the first to the second fault must have occurred shortly after stopping the injection. To better quantify this, we calculate the Coulomb stress change associated with the reactivation of the main fault in our model. The Coulomb stress calculations are based on the following combination of parameters: $Q = 38\,[\mathrm{l\,s^{-1}}]$, $\eta = 8.9 \times 10^{-4}\,[\mathrm{Pa\,s}]$, $kw = 10^{-11}\,[\mathrm{m^3}]$, $\mu = 20\,[\mathrm{GPa}]$, $f = 0.6$, $\sigma_0' = 10\,[\mathrm{MPa}]$ and $\tau_0 = 5.981\,[\mathrm{MPa}]$. The constant injection rate Q is obtained by equating the injected volume of fluid of the actual injection history considering the same injection duration. The fault hydraulic transmissivity kw is calculated such that the characteristic overpressure at the fluid source Δp_c (equation (2.3)) approximately matches the maximum downhole overpressure measured at a depth of 1920 m during the injection, approximately equal to 3 [MPa] [54]. Finally, the initial stress state (σ_0' and τ_0) is chosen to be consistent with the value of $\mathcal{T}$, the injection intensity Δp_*, and the partially constrained stress state in the zone [53].

Following Lengliné *et al.* [53], we further consider that the fluid injection induced pure left-lateral aseismic slip on a strike-slip fault oriented N25° E and dipping 70° W. As the second swarm occurred over a fault with variable strike, we focus for the purpose of our illustrative example on the northern branch of the second fault only. We thus consider a receiver fault oriented N5° E with the same dip angle as the main fault [53] (figure 9*a*). We calculate the slip distribution over the reactivated fault at three times: right at the moment of shut-in, 1 day after shut-in, and 4 days after shut-in, as displayed in figure 9*b*. In this figure, we can observe that 1 day after stopping the injection most of the post-injection aseismic slip accumulated at the time the second swarm began, has already taken place. The Coulomb stress change associated with the foregoing

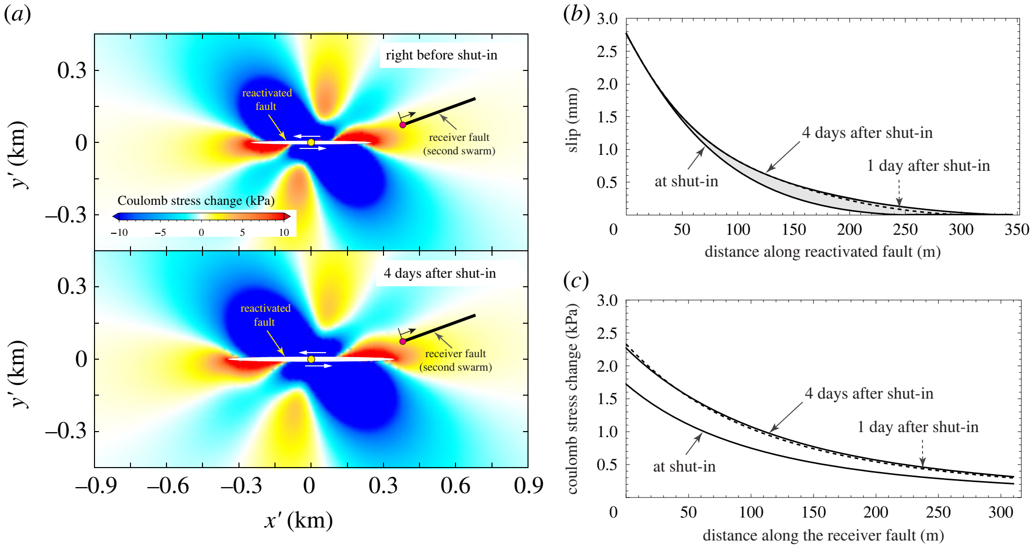

Figure 9. Application example of our model to the 2013 hydraulic stimulation of the GRT-1 well at the Rittershoffen geothermal site in France. (*a*) Coulomb stress change ΔF due to injection-induced aseismic slip on the reactivated fault for discontinuities oriented as the receiver fault. The plane x'–y' is perpendicular to the reactivated fault and crosses at its origin the injection point at a depth of about 2370 m. Yellow and red circles correspond to the injection point and the nearest point of the receiver fault to the injection, respectively. (*b*) Slip distributions over the reactivated fault at different times after shut-in. (*c*) Coulomb stress change along the receiver fault after shut-in. The distance along the receiver fault is measured from the red circle indicated in (*a*) and in the direction of the black arrow.

slip distributions are shown in the top and bottom panels of figure 9*a*, at the shut-in time and 4 days after shut-in (when the second swarm started), respectively. Our Coulomb stress analysis indicates that the location of the second swarm is in a region of positive Coulomb stress change, which is consistent with the calculations in [53]. Note that our distribution of Coulomb stress change is different to the one in [53] since the slip distribution of our model peaked around the injection point and is not uniform.

Finally, figure 9*c* displays the spatio-temporal evolution of the Coulomb stress change along the receiver fault at the same three times as before, with the origin at the red circle indicated in figure 9*a*. Note that the magnitude of the Coulomb stress change is about 2 kPa. This value is quite low and suggests that if aseismic-slip stress transfer is responsible for the delayed triggering of the second swarm, such a fault must be very critically stressed under the assumptions of our example. Given that pore pressure diffusion can sometimes weaken unstable areas even off fault, we can postulate a hydraulic connection between the two faults, possibly created by a wing crack in a step-like en-echelon fault system, and estimate the resulting overpressure 4 days after shut-in. By assuming $\alpha = 0.05\,\mathrm{m^2\,s^{-1}}$ still as a representative value of diffusivity, the overpressure at the nearest point (red circle in figure 9*a*) of the receiver fault with regard to the injection point (yellow circle in figure 9) is approximately 6 kPa (equation (2.4)). The latter is of the same order of magnitude as the Coulomb stress change due to aseismic slip, suggesting that both mechanisms may be equally important in our example. Note that 4 days after the stop of the injection, the increment of Coulomb stress with regard to the moment of shut-in, is just about 0.5 kPa (figure 9*c*). Hence, most of the post-injection increment has already happened within the first day. Although our analysis has oversimplified many aspects of this field case, our physical model seems to have the potential to reproduce field observations of post-injection off-fault seismicity, as illustrated by this application example. However, an in-depth analysis would be needed to fully clarify the role of post-injection aseismic slip in this particular field case.

(e) Possible evidence for post-injection aseismic slip and other relevant field cases

In addition to the foregoing field cases, there are apparently a few other cases of geo-energy projects where observations of seismicity after shut-in suggest the occurrence of post-injection aseismic slip. One of these cases is the 2016 long-lived seismic swarm that persisted for more than 10 months after completion of hydraulic fracturing operations of a hydrocarbon reservoir in western Canada [55]. In this case study, the authors attributed indeed the delayed swarm activity to post-injection aseismic slip. Unlike the off-fault setting of the Rittershoffen case in France, the configuration here is a clear case of on-fault seismicity. Specifically, aseismic slip is thought to be induced by hydraulic fractures that intersect (and pressurize) frictionally stable segments of a nearby fault at the reservoir level (shales), which in turn transmits solid stresses to distal segments of the same fault but in carbonate units that are thought to slide unstably [12]. One key aspect of the proposed conceptual model for post-injection seismicity in this case is the assumption of heterogeneities in fault permeability to explain a remarkable characteristic of the swarm, namely, a nearly constant rate of post-injection seismicity [55]. The proposed model assumes that elevated pore pressure remains trapped within the fault after shut-in at the reservoir level, due to the extremely low permeability of the shale formations. These trapped fluids are therefore thought to be responsible for a nearly steady propagation of aseismic slip that could explain the constant rate of seismicity [55]. Although their proposed model slightly differs from our model (in which the fault permeability is homogeneous), this case study seems to provide relevant evidence for the mechanisms discussed here. Moreover, as suggested by Cornet [52], another case in which aseismic slip might have triggered post-injection seismicity is the Basel earthquakes in 2006 in Switzerland, a hypothesis that has been recently considered in combination with other triggering mechanisms via plane-strain geomechanical modelling [56].

Further and possibly more conclusive evidence for post-injection aseismic slip may come from carefully designed laboratory and/or *in situ* experiments of fluid injection. Laboratory experiments where a finite rupture grows along a pre-existing interface [57–59] are particularly promising to explore the post-injection stage. On the other hand, *in situ* experiments where the fault deformation is monitored simultaneously at the injection point and at another point away from it [60], may also provide the opportunity to investigate this mechanism when combined with hydro-mechanical modelling that includes the depressurization stage [61].

(f) Model limitations: solution as an upper bound

Our model contains the minimal physical ingredients to reproduce post-injection aseismic slip in three-dimensional media. As such, the effects of a number of additional effects remain to be investigated. In particular, we have assumed that fluid flow induces mechanical deformation but not vice versa. It has been however suggested for a long time that variations of effective normal stress may induce permeability changes in fractures [62] and faults [63]. Also, it is known that frictional slip may be accompanied by dilatant (or contracting) fracture/fault-gouge behaviour that would inevitably induce changes in fluid flow and thus in the propagation of fault slip (see [64] for example). Poroelastic effects in the surrounding medium around the fault may be of first order in some cases (see, for instance, [65]). Accounting for a permeable host rock may notably speed up the depressurization of pore-fluid within a fault zone after shut-in due to the leak-off of fluid. Consequently, the arrest time and maximum run-out distance of the rupture pulses would likely decrease. In this regard, our model, in which the leak-off of fluid into the surrounding medium is neglected, would represent an upper bound for the arrest time and maximum run-out distance similarly to the case of the arrest of mode I hydraulic fractures [66].

In relation to friction, we consider the simplest description that allows us to produce unconditionally stable fault slip, namely, a constant friction coefficient. However, laboratory-derived friction laws [67,68] are widely used in the geophysics community to reproduce the entire spectrum of slip velocities of natural earthquakes [69]. Unconditionally stable fault slip may be obtained notably in some regimes of so-called rate-strengthening faults when subjected to continuous fluid sources [27,28]. For the post-injection problem, a more complex constitutive friction law would add a finite amount of fracture energy as well as frictional healing. In this regard, our model represents a situation in which the fracture energy spent during propagation is zero and there is no possibility for the friction coefficient to heal with time. The dissipation of a finite amount of fracture energy at the rupture front would resist propagation of the aseismic pulses. Similarly the healing of the friction coefficient would further contribute to the re-locking process of the fault thus accelerating the propagation of the locking front. Both ingredients are therefore expected to shorten the normalized arrest time and maximum run-out distance of the rupture pulses. Our model thus represents also an upper bound with regard to these two mechanisms.

7. Concluding remarks

We have provided an in-depth investigation of how post-injection aseismic slip propagates and ultimately arrests in three-dimensional media. Our results provide for the first time a conceptual and quantitative framework that may help to understand various observations and applied problems in geomechanics and geophysics associated with slow ruptures driven by the motion of fluids. Among them, a particularly relevant problem for geo-energy applications is the phenomenon of post-injection seismicity. It has been long recognized that aseismic slip may alter the stress state of large rock volumes during borehole fluid injections [3]. Based on our findings, we suggest that aseismic slip may continue stressing even larger and more distant regions after shut-in, during time scales that could span even months for fluid injections of only a few days, if the reactivated discontinuity is critically stressed as quantified by the value of the stress-injection parameter $\mathcal{T}$. Our physical model shows quantitative agreement with field observations of documented cases of post-injection-induced seismicity [48,53], thus providing support for the mechanisms presented here. Further and possibly more conclusive evidence may potentially come from revisiting more case studies via geomechanical modelling, notably from laboratory and/or *in situ* experiments that can either monitor or infer the propagation of slow ruptures.

Current efforts to manage the seismic risk associated with subsurface fluid injections such as the so-called traffic light systems might be subjected to important limitations in their effectiveness in light of our results. Traffic light systems work under the tacit assumption that operational measures will become shortly effective in preventing the occurrence of events of a larger magnitude than some pre-defined threshold [33]. Our results suggest that instead, the stressing of increasingly larger rock volumes perturbed by aseismic slip may be persistent, if the chosen operational measure is shutting in the well. Future works should therefore focus on developing physics-based strategies to mitigate the seismic risk associated with post-injection aseismic slip.

Data accessibility. The data are provided in the electronic supplementary material [70]. The seismic catalogue used in figure 8 is available on the CDGP web services (https://cdgp.u-strasbg.fr/). All raw data of numerical results and computational codes that produce every figure of the paper can be found in https://zenodo.org/record/7859517#.ZEebti8RrFd.

Authors' contributions. A.S.: conceptualization, formal analysis, funding acquisition, investigation, methodology, software, validation, visualization, writing—original draft, writing—review and editing; B.L.: conceptualization, funding acquisition, methodology, software, supervision, writing—review and editing.

Both authors gave final approval for publication and agreed to be held accountable for the work performed therein.

Conflict of interest declaration. We declare we have no competing interests.

Funding. The results were obtained within the EMOD project (Engineering model for hydraulic stimulation). The EMOD project benefits from a grant (research contract no. SI/502081-01) and an exploration subsidy (contract no. MF-021-GEO-ERK) of the Swiss federal office of energy for the EGS geothermal project in Haute-Sorne, canton of Jura, which is gratefully acknowledged. A.S. was partially funded by the Federal Commission for Scholarships for Foreign Students via the Swiss Government Excellence Scholarship.

Acknowledgements. The authors acknowledge discussions with Dmitry Garagash about the tip-asymptotic structure of the slip pulses and the healing condition, as well as with Mathias Lebihain about the rake-angle approximation. The authors also appreciate the helpful comments provided by Pierre Romanet and an anonymous reviewer.

References

1. Healy J, Rubey W, Griggs D, Raleigh C. 1968 The denver earthquakes. *Science* **161**, 1301–1310. (doi:10.1126/science.161.3848.1301)
2. Hamilton D, Meehan R. 1971 Ground rupture in the Baldwin Hills. *Science* **172**, 333–344. (doi:10.1126/science.172.3981.333)
3. Scotti O, Cornet F. 1994 In situ evidence for fluid-induced aseismic slip events along fault zones. *Int. J. Rock Mech. Min. Sci. Geomech. Abstr.* **31**, 347–358. (doi:10.1016/0148-9062(94)90902-4)
4. Bourouis S, Bernard P. 2007 Evidence for coupled seismic and aseismic fault slip during water injection in the geothermal site of Soultz (France), and implications for seismogenic transients. *Geophys. J. Int.* **169**, 723–732. (doi:10.1111/j.1365-246X.2006.03325.x)
5. Wei S*et al.* 2015 The 2012 Brawley swarm triggered by injection-induced aseismic slip. *Earth Planet. Sci. Lett.* **422**, 115–125. (doi:10.1016/j.epsl.2015.03.054)
6. Eyre TS, Samsonov S, Feng W, Kao H, Eaton DW. 2022 InSAR data reveal that the largest hydraulic fracturing-induced earthquake in Canada, to date, is a slow-slip event. *Sci. Rep.* **12**, 2043. (doi:10.1038/s41598-022-06129-3)
7. Guglielmi Y, Cappa F, Avouac J, Henry P, Elsworth D. 2015 Seismicity triggered by fluid injection-induced aseismic slip. *Science* **348**, 1224–1226. (doi:10.1126/science.aab0476)
8. Cappa F, Scuderi M, Collettini C, Guglielmi Y, Avouac J. 2019 Stabilization of fault slip by fluid injection in the laboratory and in situ. *Sci. Adv.* **5**, eaau4065. (doi:10.1126/sciadv.aau406)
9. Bao X, Eaton D. 2016 Fault activation by hydraulic fracturing in western Canada. *Science* **354**, 1406–1409. (doi:10.1126/science.aag258)
10. Deichmann N, Giardini D. 2009 Earthquakes induced by the stimulation of an enhanced geothermal system below Basel (Switzerland). *Seismol. Res. Lett.* **80**, 784–798. (doi:10.1785/gssrl.80.5.784)
11. Ellsworth W, Giardini D, Townend J, Ge S, Shimamoto T. 2019 Triggering of the Pohang, Korea, earthquake (M_w 5.5) by enhanced geothermal system stimulation. *Seismol. Res. Lett.* **90**, 1844–1858. (doi:10.1785/0220190102)
12. Eyre T, Eaton D, Garagash D, Zecevic M, Venieri M, Weir R, Lawton D. 2019 The role of aseismic slip in hydraulic fracturing-induced seismicity. *Sci. Adv.* **5**, eaav7172. (doi:10.1126/sciadv.aav7172)
13. Bhattacharya P, Viesca R. 2019 Fluid-induced aseismic fault slip outpaces pore-fluid migration. *Science* **364**, 464–468. (doi:10.1126/science.aaw7354)
14. Parotidis M, Shapiro S, Rothert E. 2005 Evidence for triggering of the Vogtland swarms 2000 by pore pressure diffusion. *J. Geophys. Res. Solid Earth* **110**, B05S10. (doi:10.1029/2004JB003267)
15. Miller S, Collettini C, Chiaraluce L, Cocco M, Barchi M, Kaus B. 2004 Aftershocks driven by a high-pressure CO_2 source at depth. *Nature* **427**, 724–727. (doi:10.1038/nature02251)
16. Lohman RB, McGuire JJ. 2007 Earthquake swarms driven by aseismic creep in the Salton Trough, California. *J. Geophys. Res. Solid Earth* **112**, B04405. (doi:10.1029/2006JB004596)
17. Perfettini H, Avouac JP. 2007 Modeling afterslip and aftershocks following the 1992 Landers earthquake. *J. Geophys. Res. Solid Earth* **112**, B07409. (doi:10.1029/2006JB004399)
18. Yukutake Y, Yoshida K, Honda R. 2022 Interaction between aseismic slip and fluid invasion in earthquake swarms revealed by dense geodetic and seismic observations. *J. Geophys. Res. Solid Earth* **127**, e2021JB022933. (doi:10.1029/2021JB022933)
19. Sirorattanakul K, Ross ZE, Khoshmanesh M, Cochran ES, Acosta M, Avouac JP. 2022 The 2020 Westmorland, California earthquake swarm as aftershocks of a slow slip event sustained by fluid flow. *J. Geophys. Res. Solid Earth* **127**, e2022JB024693. (doi:10.1029/2022JB024693)
20. Ross Z, Rollins C, Cochran E, Hauksson E, Avouac J, Ben-Zion Y. 2017 Aftershocks driven by afterslip and fluid pressure sweeping through a fault-fracture mesh. *Geophys. Res. Lett.* **44**, 8260–8267. (doi:10.1002/2017GL074634)
21. Rogers G, Dragert H. 2003 Episodic tremor and slip on the Cascadia subduction zone: the Chatter of Silent Slip. *Science* **300**, 1942–1943. (doi:10.1126/science.1084783)

22. Shelly DR, Beroza GC, Ide S, Nakamula S. 2006 Low-frequency earthquakes in Shikoku, Japan, and their relationship to episodic tremor and slip. *Nature* **442**, 188–191. (doi:10.1038/nature04931)
23. Kato A*et al.* 2010 Variations of fluid pressure within the subducting oceanic crust and slow earthquakes. *Geophys. Res. Lett.* **37**, L14310. (doi:10.1029/2010GL043723)
24. Peacock SM. 2009 Thermal and metamorphic environment of subduction zone episodic tremor and slip. *J. Geophys. Res. Solid Earth* **114**, B00A07. (doi:10.1029/2008JB005978)
25. Sibson RH. 2020 Preparation zones for large crustal earthquakes consequent on fault-valve action. *Earth Planets Space* **72**, 31. (doi:10.1186/s40623-020-01153-x)
26. Zhu W, Allison K, Dunham E, Yang Y. 2020 Fault valving and pore pressure evolution in simulations of earthquake sequences and aseismic slip. *Nat. Commun.* **11**, 4833. (doi:10.1038/s41467-020-18598-z)
27. Dublanchet P. 2019 Fluid driven shear cracks on a strengthening rate-and-state frictional fault. *J. Mech. Phys. Solids* **132**, 103672. (doi:10.1016/j.jmps.2019.07.015)
28. Garagash D. 2021 Fracture mechanics of rate-and-state faults and fluid injection induced slip. *Phil. Trans. R. Soc. A* **379**, 20200129. (doi:10.1098/rsta.2020.0129)
29. Viesca RC. 2021 Self-similar fault slip in response to fluid injection. *J. Fluid Mech.* **928**, A29. (doi:10.1017/jfm.2021.825)
30. Yang Y, Dunham EM. 2021 Effect of porosity and permeability evolution on injection-induced aseismic slip. *J. Geophys. Res. Solid Earth* **126**, e2020JB021258. (doi:10.1029/2020JB021258)
31. Sáez A, Lecampion B, Bhattacharya P, Viesca RC. 2022 Three-dimensional fluid-driven stable frictional ruptures. *J. Mech. Phys. Solids* **160**, 104754. (doi:10.1016/j.jmps.2021.104754)
32. Jacquey AB, Viesca RC. 2023 Nucleation and arrest of fluid-induced aseismic slip. *Geophys. Res. Lett.* **50**, e2022GL101228. (doi:10.1029/2022GL101228)
33. Baisch S, Koch C, Muntendam-bos A. 2019 Traffic light systems: to what extent can induced seismicity be controlled? *Seismol. Res. Lett.* **90**, 1145–1154. (doi:10.1785/0220180337)
34. Marck J, Savitski AA, Detournay E. 2015 Line source in a poroelastic layer bounded by an elastic space. *Int. J. Numer. Anal. Methods Geomech.* **39**, 1484–1505. (doi:10.1002/nag.2405)
35. Hills D, Kelly P, Dai D, Korsunsky A. 1996 *Solution of crack problems: the distributed dislocation technique*, vol. **44**, Dordrecht, Netherlands: Kluwer Academic Publishers.
36. Carslaw H, Jaeger J. 1959 *Conduction of heat in solids*, 2nd edn, Oxford, UK: Oxford University Press.
37. Garagash D, Germanovich L. 2012 Nucleation and arrest of dynamic slip on a pressurized fault. *J. Geophys. Res. Solid Earth* **117**, B10310. (doi:10.1029/2012JB009209)
38. Barenblatt G. 1962 The mathematical theory of equilibrium cracks in brittle fracture. *Adv. Appl. Mech.* **7**, 55–129. (doi:10.1016/S0065-2156(08)70121-2)
39. Garagash DI. 2012 Seismic and aseismic slip pulses driven by thermal pressurization of pore fluid. *J. Geophys. Res. Solid Earth* **117**, B04314. (doi:10.1029/2011JB008889)
40. Rice J. 1968 Mathematical analysis in the mechanics of fracture. *Fract.: Adv. Treatise* **2**, 191–311.
41. Tada H, Paris PC, Irwin GR. 2000 *The stress analysis of cracks handbook*, 3rd edn. New York, NY: ASME Press.
42. Clements D, Ang W. 1988 Stress intensity factors for the circular annulus crack. *Int. J. Eng. Sci.* **26**, 325–329. (doi:10.1016/0020-7225(88)90112-7)
43. Evans KF, Genter A, Sausse J. 2005 Permeability creation and damage due to massive fluid injections into granite at 3.5 km at Soultz: 1. Borehole observations. *J. Geophys. Res. Solid Earth* **110**, B04203. (doi:10.1029/2004JB003169)
44. Parotidis M, Shapiro SA, Rothert E. 2004 Back front of seismicity induced after termination of borehole fluid injection. *Geophys. Res. Lett.* **31**, L02612. (doi:10.1029/2003GL018987)
45. King GC, Stein RS, Lin J. 1994 Static stress changes and the triggering of earthquakes. *Bull. Seismol. Soc. Am.* **84**, 935–953. (doi:10.1785/BSSA0840030935)
46. Dieterich J. 1994 A constitutive law for rate of earthquake production and its application to earthquake clustering. *J. Geophys. Res. Solid Earth* **99**, 2601–2618. (doi:10.1029/93JB02581)
47. Baria R, Baumgartner J, Gérard A. 1996 European hot dry rock programme 1992–1995. Extended summary of the final report to EC (DGXII), contract JOU2-CT92-0115.
48. Cornet F, Helm J, Poitrenaud H, Etchecopar A. 1997 Seismic and aseismic slips induced by large-scale fluid injections. *Pure Appl. Geophys.* **150**, 563–583. (doi:10.1007/s000240050093)
49. Evans KF, Moriya H, Niitsuma H, Jones RH, Phillips WS, Genter A, Sausse J, Jung R, Baria R. 2005 Microseismicity and permeability enhancement of hydrogeologic structures during

massive fluid injections into granite at 3 km depth at the Soultz HDR site. *Geophys. J. Int.* **160**, 388–412. (doi:10.1111/j.1365-246X.2004.02474.x)
50. Ciardo F, Lecampion B. 2023 Injection-induced aseismic slip in tight fractured rocks. *Rock Mech. Rock Eng.* (doi:10.1007/s00603-023-03249-8)
51. Evans KF. 2005 Permeability creation and damage due to massive fluid injections into granite at 3.5 km at Soultz: 2. Critical stress and fracture strength. *J. Geophys. Res. Solid Earth* **110**, B04204. (doi:10.1029/2004JB003169)
52. Cornet FH. 2016 Seismic and aseismic motions generated by fluid injections. *Geomech. Energy Environ.* **5**, 42–54. (doi:10.1016/j.gete.2015.12.003)
53. Lengliné O, Boubacar M, Schmittbuhl J. 2017 Seismicity related to the hydraulic stimulation of GRT1, Rittershoffen, France. *Geophys. J. Int.* **208**, 1704–1715. (doi:10.1093/gji/ggw490)
54. Baujard C, Genter A, Dalmais E, Maurer V, Hehn R, Rosillette R, Vidal J, Schmittbuhl J. 2017 Hydrothermal characterization of wells GRT-1 and GRT-2 in Rittershoffen, France: implications on the understanding of natural flow systems in the rhine graben. *Geothermics* **65**, 255–268. (doi:10.1016/j.geothermics.2016.11.001)
55. Eyre TS, Zecevic M, Salvage RO, Eaton DW. 2020 A long-lived swarm of hydraulic fracturing-induced seismicity provides evidence for aseismic slip. *Bull. Seismol. Soc. Am.* **110**, 2205–2215. (doi:10.1785/0120200107)
56. Boyet A, De Simone S, Ge S, Vilarrasa V. 2023 Poroelastic stress relaxation, slip stress transfer and friction weakening controlled post-injection seismicity at the Basel enhanced geothermal system. *Commun. Earth Environ.* **4**, 104. (doi:10.1038/s43247-023-00764-y)
57. Passelègue FX, Almakari M, Dublanchet P, Barras F, Fortin J, Violay M. 2020 Initial effective stress controls the nature of earthquakes. *Nat. Commun.* **11**, 5132. (doi:10.1038/s41467-020-18937-0)
58. Gori M, Rubino V, Rosakis AJ, Lapusta N. 2021 Dynamic rupture initiation and propagation in a fluid-injection laboratory setup with diagnostics across multiple temporal scales. *Proc. Natl Acad. Sci. USA* **118**, e2023433118. (doi:10.1073/pnas.2023433118)
59. Cebry SBL, Ke CY, McLaskey GC. 2022 The role of background stress state in fluid-induced aseismic slip and dynamic rupture on a 3-m laboratory fault. *J. Geophys. Res. Solid Earth* **127**, e2022JB024371. (doi:10.1029/2022JB024371)
60. Cappa F, Guglielmi Y, Nussbaum C, De Barros L, Birkholzer J. 2022 Fluid migration in low-permeability faults driven by decoupling of fault slip and opening. *Nat. Geosci.* **15**, 747–751. (doi:10.1038/s41561-022-00993-4)
61. Larochelle S, Lapusta N, Ampuero JP, Cappa F. 2021 Constraining fault friction and stability with fluid-injection field experiments. *Geophys. Res. Lett.* **48**, e2020GL091188. (doi:10.1029/2020GL091188)
62. Witherspoon P, Wang J, Iwai K, Gale J. 1980 Validity of Cubic Law for fluid flow in a deformable rock fracture. *Water Resour. Res.* **16**, 1016–1024. (doi:10.1029/WR016i006p01016)
63. Rice J. 1992 Fault stress states, pore pressure distributions, and the weakness of the San Andreas fault. *Int. Geophys.* **51**, 475–503. (doi:10.1016/S0074-6142(08)62835-1)
64. Ciardo F, Lecampion B. 2019 Effect of dilatancy on the transition from aseismic to seismic slip due to fluid injection in a fault. *J. Geophys. Res. Solid Earth* **124**, 3724–3743. (doi:10.1029/2018JB016636)
65. Heimisson E, Liu S, Lapusta N, Rudnicki J. 2022 A spectral boundary-integral method for faults and fractures in a poroelastic solid: simulations of a rate-and-state fault with dilatancy, compaction, and fluid injection. *J. Geophys. Res. Solid Earth* **127**, e2022JB024185. (doi:10.1029/2022JB024185)
66. Möri A, Lecampion B. 2021 Arrest of a radial hydraulic fracture upon shut-in of the injection. *Int. J. Solids Struct.* **219**, 151–165. (doi:10.1016/j.ijsolstr.2021.02.022)
67. Dieterich J. 1979 Modeling of rock friction: 1. Experimental results and constitutive equations. *J. Geophys. Res. Solid Earth* **84**, 2161–2168. (doi:10.1029/JB084iB05p02161)
68. Ruina A. 1983 Slip instability and state variable friction laws. *J. Geophys. Res. Solid Earth* **88**, 10 359–10 370. (doi:10.1029/JB088iB12p10359)
69. Scholz C. 2019 *The mechanics of earthquakes and faulting*, 3rd edn. Cambridge, UK: Cambridge University Press.
70. Sáez A, Lecampion B. 2023 Post-injection aseismic slip as a mechanism for the delayed triggering of seismicity. Figshare. (doi:10.6084/m9.figshare.c.6644017)

J. Mech. Phys. Solids 183 (2024) 105506

Contents lists available at ScienceDirect

Journal of the Mechanics and Physics of Solids

journal homepage: www.elsevier.com/locate/jmps

Fluid-driven slow slip and earthquake nucleation on a slip-weakening circular fault

Alexis Sáez *, Brice Lecampion

Ecole Polytechnique Fédérale de Lausanne (EPFL), Institute of Civil Engineering, Gaznat chair on Geo-Energy, CH-1015 Lausanne, Switzerland

ARTICLE INFO

Keywords:
Friction
Fracture
Instability
Geological material
Injection-induced fault slip

ABSTRACT

We investigate the propagation of fluid-driven fault slip on a slip-weakening frictional interface separating two identical half-spaces of a three-dimensional elastic solid. Our focus is on axisymmetric circular shear ruptures as they capture the most essential aspects of the dynamics of unbounded ruptures in three dimensions. In our model, fluid-driven aseismic slip occurs in two modes: as an interfacial rupture that is unconditionally stable, or as the quasi-static nucleation phase of an otherwise dynamic rupture. Unconditionally stable ruptures progress through four stages. Initially, ruptures are diffusively self-similar and the interface behaves as if it were governed by a constant friction coefficient equal to the static friction value. Slip then accelerates due to frictional weakening while the cohesive zone develops. Once the latter gets properly localized, a finite amount of fracture energy emerges along the interface. The rupture dynamics is then governed by an energy balance of the Griffith's type. In this stage, fault slip transitions from a large-toughness to a small-toughness regime due to the diminishing effect of the fracture energy in the near-front energy balance. Ultimately, self-similarity is recovered and the fault behaves again as having a constant friction coefficient, but this time equal to the dynamic friction value. This condition is equivalent to a fault interface operating to leading order with zero fracture energy. When slow slip is the result of a frustrated dynamic instability, slip also initiates self-similarly at a constant peak friction coefficient. The maximum size that aseismic ruptures can reach before becoming unstable can be as small as a critical nucleation radius (shear modulus divided by the slip-weakening rate) and as large as infinity when faults are close to a well-defined limit that separates the two modes of aseismic sliding. In the former case, earthquake nucleation occurs unaffected by the dynamic friction coefficient. In contrast, the latter case exhibits fracture-mechanics behavior, characterized by a finite influx of elastic strain energy being supplied to and dissipated at the rupture front. We provide analytical and numerical solutions for the problem solved over its full dimensionless parameter space, including expressions for relevant length and time scales characterizing the transition between different stages and regimes. Due to its three-dimensional nature, the model enables quantitative comparisons with field observations as well as preliminary engineering design of hydraulic stimulation operations. Existing laboratory and in-situ experiments of fluid injection into simulated and natural faults are briefly discussed in light of our results.

* Corresponding author.
E-mail address: alexis.saez@epfl.ch (A. Sáez).

https://doi.org/10.1016/j.jmps.2023.105506
Received 8 September 2023; Received in revised form 20 November 2023; Accepted 22 November 2023
Available online 28 November 2023

1. Introduction

Sudden pressurization of pore fluids in the Earth's crust has been widely acknowledged as a trigger for inducing slow slip on pre-existing fractures and faults (Hamilton and Meehan, 1971; Scotti and Cornet, 1994; Guglielmi et al., 2015; Wei et al., 2015). Sometimes referred to as injection-induced aseismic slip, this phenomenon is thought to play a significant role in various subsurface engineering technologies and natural earthquake-related phenomena. Notable examples of the natural source include seismic swarms and aftershock sequences, often attributed to be driven by the diffusion of pore pressure (Parotidis et al., 2005; Miller et al., 2004) or the propagation of slow slip (Lohman and McGuire, 2007; Perfettini and Avouac, 2007), with recent studies suggesting that the interplay between both mechanisms may be indeed responsible for the occurrence of some seismic sequences (Ross et al., 2017; Yukutake et al., 2022; Sirorattanakul et al., 2022). Similarly, low-frequency earthquakes and tectonic tremors are commonly considered to be driven by slow slip events occurring downdip the seismogenic zone in subduction zones (Rogers and Dragert, 2003; Shelly et al., 2006), where systematic evidence of overpressurized fluids has been found (Shelly et al., 2006; Kato et al., 2010; Behr and Bürgmann, 2021), with recent works suggesting that the episodicity and some characteristics of slow slip events may be explained by fluid-driven processes (Warren-Smith et al., 2019; Zhu et al., 2020; Perez-Silva et al., 2023).

Anthropogenic fluid injections are, on the other hand, known to induce both seismic and aseismic slip (Scotti and Cornet, 1994; Wei et al., 2015; Guglielmi et al., 2015). For instance, hydraulic stimulation techniques employed to engineer deep geothermal reservoirs aim to reactivate fractures through shear slip, thereby enhancing reservoir permeability by either dilating pre-existing fractures or creating new ones. The occurrence of predominantly aseismic rather than seismic slip, is considered a highly favorable outcome, as earthquakes of relatively large magnitudes can pose a significant risk to the success of these projects (Deichmann and Giardini, 2009; Ellsworth et al., 2019). Injection-induced aseismic slip can, however, play a rather detrimental role in some cases, as slow slip is accompanied by quasi-static changes of stress in the surrounding rock mass which, in turn, may induce failure of unstable fault patches that could sometimes lead to earthquakes of undesirably large magnitude (Eyre et al., 2019). Moreover, since injection-induced aseismic slip may propagate faster than pore pressure diffusion, this mechanism can potentially trigger seismic events in regions that are far from the zone affected by the pressurization of pore fluids (Guglielmi et al., 2015; Bhattacharya and Viesca, 2019; Eyre et al., 2019). Fluid-driven aseismic slip may play a similar role in other subsurface engineering technologies than deep geothermal energy, such as hydraulic fracturing of unconventional oil and gas reservoirs (Eyre et al., 2019), oil wastewater disposal (Chen et al., 2017), and carbon dioxide sequestration (Zoback and Gorelick, 2012).

The apparent relevance of injection-induced aseismic slip in the aforementioned phenomena has motivated the development of physical models that are contributing to a better comprehension of this hydro-mechanical problem. The first rigorous investigations on the mechanics of injection-induced aseismic slip focused, for the sake of simplicity, on idealized two-dimensional configurations. Specifically, on the propagation of fault slip under plane-strain conditions considering either in-plane shear (mode II) or anti-plane shear (mode III) ruptures, with a fluid source of infinite extent along the out-of-the-plane direction. Yet these studies have significantly contributed to establishing a fundamental qualitative understanding of how the initial state of stress, the fluid injection parameters, the fault hydraulic properties, and the fault frictional rheology affect the dynamics of fluid-driven aseismic slip transients (Dublanchet, 2019; Garagash, 2021; Viesca, 2021; Yang and Dunham, 2021), the applicability of such models remains limited as three-dimensional configurations are expected to prevail in nature. Recently, Sáez et al. (2022) examined the propagation of injection-induced aseismic slip under mixed-mode (II+III) conditions, on a fault embedded in a fully three-dimensional domain. An important finding of this study is that for the same type of fluid source (either constant injection rate or constant pressure in Sáez et al. (2022)), the spatiotemporal patterns of fault slip differ even qualitatively between the three-dimensional model and its two-dimensional counterpart, highlighting the importance of resolving more realistic rupture configurations.

In the three-dimensional model of Sáez et al. (2022), the perhaps strongest assumption is the consideration of a constant friction coefficient at the fault interface. This friction model, known as Coulomb's friction, corresponds to the minimal physical ingredient that can produce unconditionally stable shear ruptures. As discussed by Sáez et al. (2022), a model with Coulomb's friction represents a case in which the frictional fracture energy spent during rupture propagation is effectively zero, without the possibility of developing a process zone in the proximities of the rupture front. In this paper, we eliminate this assumption and therefore extend the model of Sáez et al. (2022) to account for a friction coefficient that weakens upon the onset of fault slip. This incorporates into the model the proper growth and localization of a process zone, with the resulting finite amount of fracture energy. We do so by considering the simplest model of friction that can provide the sought physical ingredients, namely, a slip-weakening friction coefficient (Ida, 1972). We consider the two most common types of slip-weakening friction: a linear and an exponential decay of friction with slip, from some peak (static) value towards a constant residual (dynamic) one.

On the other hand, as shown by Sáez et al. (2022) for the Coulomb's friction case, a Poisson's ratio different than zero has mainly an effect on the aspect ratio of the resulting quasi-elliptical ruptures which become more elongated for increasing values of ν. The characteristic size of mixed-mode, quasi-elliptical ruptures is nevertheless determined primarily by the rupture radius of circular ruptures, which occur in the limit of $\nu = 0$ for such an axisymmetric problem. The case of a null Poisson's ratio is therefore particularly insightful and notably simpler since in that limit, we can leverage the axisymmetry property of the problem to compute more efficient numerical solutions (Bhattacharya and Viesca, 2019; Sáez et al., 2022; Sáez and Lecampion, 2023) besides allowing the problem to be tractable analytically to some extent. We therefore focus in this paper on the case of mixed-mode circular ruptures alone. We also note that our model is an extension of the two-dimensional model of Garagash and Germanovich (2012). While Garagash and Germanovich focused their investigation on the problem of nucleation and arrest of dynamic slip, our work here is concerned primarily with a different phenomenon; the propagation of aseismic slip. Nonetheless, since aseismic slip could correspond indeed to the nucleation phase of an ensuing dynamic rupture, we also examine the problem of nucleation of a dynamic instability under mixed-mode conditions. In fact, by pursuing this route, we provide an extension of the nucleation length of Uenishi and Rice (2002) to the three-dimensional, axisymmetric case, for both tensile and shear ruptures. Similarly, we extend some other relevant nucleation lengths identified by Garagash and Germanovich (2012).

We organize this paper as follows. In Section 2, we introduce the mathematical formulation of our physical model. In Section 3, we present two simplified models that will be later shown to be asymptotic and/or approximate solutions of the slip-weakening model under certain regimes. In Section 4, we introduce the scaling of the problem and the map of possible rupture regimes. In Section 5, we examine in detail the case of ruptures that are ultimately stable. In Section 6, we focus on the case in which aseismic slip corresponds to the nucleation phase of an otherwise dynamic rupture. Finally, in Section 7, we provide a brief discussion of recent laboratory and in-situ experiments of fault reactivation by fluid injection in light of our results.

2. Problem formulation

2.1. Governing equations

Fluid is injected into a poroelastic fault zone of width w that is characterized by an intrinsic permeability k and a storage coefficient S, assumed to be constant and uniform (see Fig. 1b). The fault zone is confined within two linearly elastic half-spaces of the same elastic constants, namely, a shear modulus μ and Poisson's ratio ν. The initial stress tensor is assumed to be uniform and is characterized by a resolved shear stress τ_0 and total normal stress σ_0 acting along the x and z directions of the Cartesian reference system of Fig. 1a, respectively. We consider the injection of fluids via a line source that is located along the z axis and crosses the entire fault zone width. Under such conditions, fluid flow is axisymmetric with regard to the z axis and occurs only within the porous fault zone. Moreover, the displacement field induced by the fluid injection is irrotational and the pore pressure diffusion equation of poroelasticity reduces to its uncoupled version (Marck et al., 2015), $\partial p/\partial t = \alpha \nabla^2 p$, where $\alpha = k/S\eta$ is the fault hydraulic diffusivity, with η the fluid dynamic viscosity. Solutions of the previous linear diffusion equation are known extensively for a broad range of boundary and initial conditions (Carslaw and Jaeger, 1959). Here, we focus on the perhaps most practical case in which the fluid injection is conducted at a constant volumetric rate Q. For the following boundary conditions: $2\pi r w (k/\eta)\partial p/\partial r = -Q$ when $r \to 0$ and $p = p_0$ when $r \to \infty$, with p_0 the initial pore pressure field assumed to be uniform, the solution of the diffusion equation in terms of the overpressure $\Delta p(r,t) = p(r,t) - p_0$ reads as (section 10.4, Eq. (5), Carslaw and Jaeger (1959))

$$\Delta p(r,t) = \Delta p_* E_1\left(\frac{r^2}{4\alpha t}\right), \text{ with } \Delta p_* = \frac{Q\eta}{4\pi k w}, \tag{1}$$

where Δp_* is the intensity of the injection with units of pressure, and $E_1(x) = \int_x^\infty \left(e^{-\xi}/\xi\right) \mathrm{d}\xi$ is the exponential integral function.

Let us define the following characteristic overpressure,

$$\Delta p_c = \frac{Q\eta}{kw}, \tag{2}$$

which relates to the injection intensity as $\Delta p_c = 4\pi \Delta p_*$. A close examination of Eq. (1) for the large times in which the line-source approximation is valid, $t \gg r_s^2/\alpha$ with r_s the characteristic size of the actual fluid source, shows that Δp_c is in the order of magnitude of the overpressure at the fluid source. Moreover, as discussed in Appendix C, the fluid-source overpressure, say Δp_w, increases slowly (logarithmically) with time, such that for practical applications, one could think in considering Δp_w to be rather constant and approximately equal to the characteristic overpressure Δp_c. Because of its simplicity, we adopt such approximation $\Delta p_w \approx \Delta p_c$ throughout this work, with the implications further discussed in Appendix C. Having established that, we note that in this work we consider exclusively injection scenarios in which the characteristic fluid-source overpressure satisfies $\Delta p_c \lessapprox \sigma_0'$, where $\sigma_0' = \sigma_0 - p_0$ is the initial effective normal stress. In this way, we make sure that the walls of the fault remain always in contact, thus avoiding hydraulic fracturing. This latter scenario has been notably addressed in the context of slip instabilities by others (Azad et al., 2017).

Suppose now that the fault zone possesses a slip surface located at $z = 0$ where the totality of fault slip is accommodated (see Fig. 1b). The slip surface is assumed to obey a Mohr–Coulomb shear failure criterion without any cohesion such that the maximum shear stress τ and fault strength τ_s satisfy at any position along the slip surface and any time, the following local relation

$$|\tau| \le \tau_s = f \times \left(\sigma_0' - \Delta p\right), \tag{3}$$

where Δp is the overpressure given by Eq. (1) and f is a local friction coefficient that depends on fault slip δ (Ida, 1972). There are two common choices for the slip-weakening friction model, namely, a friction coefficient that decays linearly with slip,

$$f(\delta) = \begin{cases} f_p - \left(f_p - f_r\right)|\delta|/\delta_c & \text{if } |\delta| \le \delta_c \\ f_r & \text{if } |\delta| > \delta_c, \end{cases} \tag{4}$$

and a friction coefficient that decays exponentially with it,

$$f(\delta) = f_r + \left(f_p - f_r\right) e^{-|\delta|/\delta_c}. \tag{5}$$

In the previous equations, f_p is the peak (or static) friction coefficient, f_r is the residual (or kinetic) friction coefficient, and δ_c is the characteristic 'distance' over which the friction coefficient decays from f_p to f_r, as displayed in Fig. 2. Moreover, we assume that the slip surface is fully locked before the injection starts and, as such, the initial shear stress τ_0 must be lower than the in-situ static strength of the fault, $\tau_p^0 = f_p \sigma_0'$.

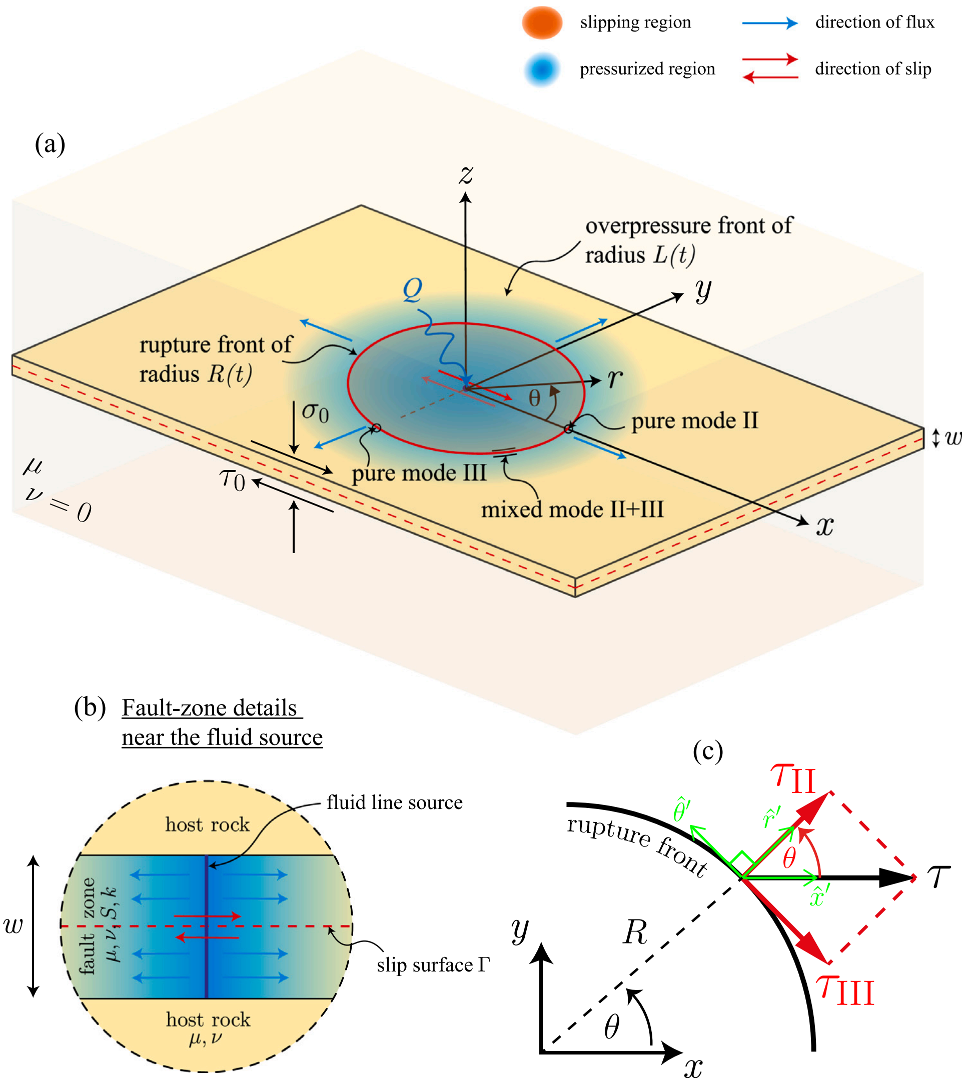

Fig. 1. Model schematics. (a, b) Fluid is injected into a permeable fault zone of width w via a line source that crosses the entire fault zone width. The fault is planar and embedded in an unbounded linearly elastic impermeable host rock of the same elastic constants. The initial stress tensor is uniform. The resulting mixed-mode (II+III) shear rupture is circular when the Poisson's ratio $\nu = 0$. (c) Direction of maximum shear stress τ over the fault and particularly along the rupture front, plus the corresponding mode-II and mode-III components of it, with regard to both the Cartesian and cylindrical coordinate systems. When $\nu = 0$, τ points always along the x axis, the direction of the initial shear stress τ_0.

According to Eq. (3), the injection of fluid has the effect of reducing the fault strength owing to the increase of pore-fluid pressure which decreases the effective normal stress locally. Such pore pressure increase will be eventually sufficient to activate fault slip when the fault strength equates to the pre-injection shear stress τ_0, which marks the onset of an interfacial frictional rupture. Indeed, owing to the line-source approximation of the fluid source, the activation of slip in our model occurs immediately upon the start of the injection as a consequence of the weak logarithmic singularity that the exponential integral function features near the origin (see Appendix C). In the three-dimensional configuration under consideration, the resulting shear rupture will propagate under mixed-mode II+III conditions, where II and III represent the in-plane shear and anti-plane shear deformation modes, respectively. Moreover, as stated in the introduction, we restrict ourselves to the idealized case of a Poisson's ratio $\nu = 0$. Under quasi-static conditions, since the equivalent shear load driving the rupture is axisymmetric in magnitude (the initial shear stress is uniform and the fluid overpressure is axisymmetric), the simplifying assumption that $\nu = 0$ has the following two implications. First, the shape of the rupture is circular if one considers that the energy release rate along the rupture front is uniform for a given crack radius (see appendix B in Sáez et al. (2022)). Second, the direction of the slip rate (and thus of the maximum shear τ) is along the direction of the initial shear traction of magnitude τ_0, which in our model corresponds to the x axis (no rotation of the rake angle, see, for instance, Eq. (7.4) in Hills et al. (1996)). Fig. 1c displays the maximum shear stress τ for such a circular rupture together with the near-front shear stress components associated with the modes II and III of deformation. Note that the only relevant (non-zero)

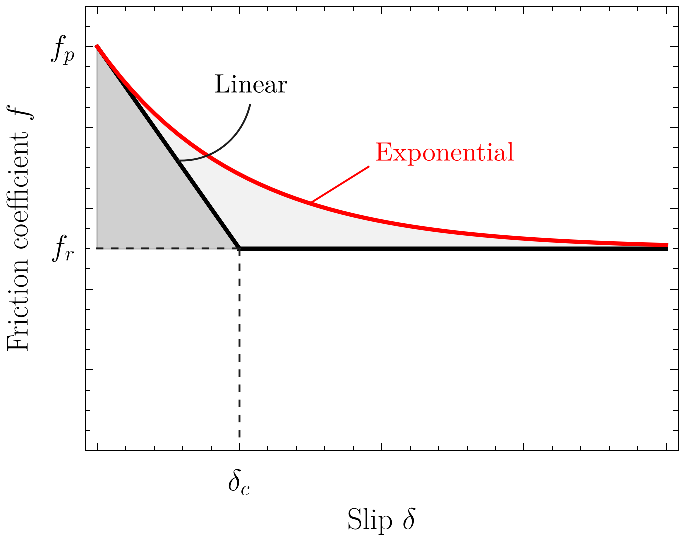

Fig. 2. Slip weakening friction law for (black) linear weakening and (red) exponential decay with slip. If the friction coefficient f is multiplied by some constant effective normal stress that is approximately uniform and representative of the one acting along the process zone, then the gray areas times such effective normal stress represent fracture energy G_c. Note that $G_c^{\text{exp}} = 2 \cdot G_c^{\text{lin}}$ when δ_c is the same in both models.

components of slip and shear stress over the fault plane are the ones along the x axis. Hereafter, we simply denominate them as fault slip δ and shear stress τ.

By neglecting any fault-zone poroelastic coupling upon the onset of the rupture, the quasi-static elastic equilibrium that relates fault slip δ to the shear stress τ can be written as the following boundary integral equation along the x axis (Salamon and Dundurs, 1977; Bhattacharya and Viesca, 2019),

$$\tau(r,t) = \tau_0 - \frac{\mu}{2\pi}\int_0^{R(t)} F(r,\xi)\,\frac{\partial\delta(\xi,t)}{\partial\xi}\mathrm{d}\xi, \tag{6}$$

where the kernel $F(r,\xi)$ is given by

$$F(r,\xi) = \frac{K(k(r/\xi))}{\xi + r} + \frac{E(k(r/\xi))}{\xi - r}, \text{ with } \quad k(x) = \frac{2\sqrt{x}}{1+x}, \tag{7}$$

and $K(\cdot)$ and $E(\cdot)$ are the complete elliptic integrals of the first and second kind, respectively. Note that in Eq. (6), the shear stress τ can be written as a function in space of the radial coordinate only due to the aforementioned axisymmetry property when $\nu = 0$. Eqs. (1), (3), and (6), plus the corresponding constitutive friction law, either (4) or (5), provide a complete system of equations to solve for the spatio-temporal evolution of fault slip $\delta(r,t)$ and the position of the rupture front $R(t)$: our primary unknowns in the problem.

2.2. Front-localized energy balance

Under certain conditions and over a certain spatial range, the previous problem may be formulated equivalently through an energy balance of the Griffith type, that is, as a classical shear crack in the theory of Linear Elastic Fracture Mechanics (LEFM) (Broberg, 1999). The idea that frictional ruptures could be approximated by classical shear cracks is relatively old (Ida, 1972; Palmer and Rice, 1973). Yet it has been just recently validated by modern experiments concerned with the problem of frictional motion on both dry and lubricated interfaces (Svetlizky et al., 2019).

Let us assume that there exists a localization length ℓ_* near the rupture front such that the shear stress evolves from some peak value τ_p at the rupture front $r = R$ to some residual and approximately constant amount τ_r at distances $r < R - \ell_*$. The localization length ℓ_* is sometimes called the process zone size or cohesive zone size for the similarity of the shear rupture problem to the case of tensile fractures (Barenblatt, 1962). Let us further assume that ℓ_* is small in comparison to the rupture radius R. Under such conditions, we can invoke the 'small-scale yielding' approximation of LEFM to shear ruptures (Palmer and Rice, 1973). In particular, during rupture propagation, the influx of elastic energy into the edge region G, also known as energy release rate, must equal the frictional fracture energy G_c. The energy release rate for an axisymmetric, circular shear rupture is (Appendix B of Sáez et al. (2022))

$$G = \frac{2}{\pi\mu R(t)}\left[\int_0^{R(t)} \frac{\tau_0 - \tau_r(r,t)}{\sqrt{R(t)^2 - r^2}} r\mathrm{d}r\right]^2. \tag{8}$$

In the previous equation, it is assumed that the current shear stress acting on the 'crack' faces is the residual strength τ_r. This is consistent with the small-scale yielding approach where the details of the process zone are neglected for the calculation of G (Rice, 1968; Palmer and Rice, 1973). On the other hand, the fracture energy G_c corresponds to the energy dissipated within the process zone per unit area of rupture growth, which in the case of a frictional shear crack is equal to the work done by the fault strength τ_s against its residual part τ_r (Palmer and Rice, 1973),

$$G_c = \int_0^{\delta_*} \left[\tau_s(\delta) - \tau_r(\delta_*)\right] \mathrm{d}\delta, \tag{9}$$

where δ_* is the accrued slip throughout the process zone assuming, again, that there exists a proper localization length ℓ_*.

Let us now recast the Griffith's energy balance, $G = G_c$, in a way that will be more convenient for analytic derivations. For a mixed-mode shear rupture, the energy release rate can be expressed as $G = K_{\mathrm{II}}^2(1-\nu)/2\mu + K_{\mathrm{III}}^2/2\mu$ (Irwin, 1958), where K_{II} and K_{III} are the mode-II and mode-III stress intensity factors. Here, K_{II} and K_{III} are understood as the intensities of the singular fields of LEFM that emerge as intermediate asymptotics at distances $\ell_* \ll r \ll R$. Moreover, since $\nu = 0$, we can conveniently define

$$K^2 = K_{II}^2 + K_{III}^2 = 2\mu G, \quad \text{and} \quad K_c = \sqrt{2\mu G_c}, \tag{10}$$

where K is an 'axisymmetric stress-intensity factor' and K_c an 'axisymmetric fracture toughness'. Note that if one considers the singular terms of the mode-II and mode-III shear stress components acting nearby and ahead of the rupture front, say τ_{II} and τ_{III} respectively (see Fig. 1c), then K represents the intensity of the square-root singularity associated with the absolute (maximum) shear stress τ (acting along the x-direction of our Cartesian reference system) which relates to the in-plane shear and anti-plane shear stress components as $\tau^2 = \tau_{\mathrm{II}}^2 + \tau_{\mathrm{III}}^2$.

By combining Eqs. (8) and (10), we can rewrite the Griffith's energy balance in the sought Irwin's form, $K = K_c$, which yields

$$\frac{2}{\sqrt{\pi R(t)}} \int_0^{R(t)} \frac{\tau_0 - \tau_r(r,t)}{\sqrt{R(t)^2 - r^2}} r\mathrm{d}r = K_c. \tag{11}$$

Let us now consider some details about the calculation of G_c in Eq. (9). Upon the arrival of the rupture front at a certain location over the fault plane, the fault strength τ_s weakens according to Eq. (3) due to both the decrease of the friction coefficient f and the increase of overpressure Δp. However, the near-front processes associated with energy dissipation for rupture growth in Eq. (9) are for the most part related to the frictional process only. This can be readily seen after closely examining Eq. (1) for the spatio-temporal evolution of Δp. Eq. (1) introduces the well-known diffusion length scale $L(t) = \sqrt{4\alpha t}$ in the problem, which is itself a proxy for the radius of the nominal area affected by the pressurization of pore fluid (see Fig. 1a). We note that if the overpressure front L is either in the order of or much greater than the rupture radius R, then Δp varies smoothly over the process zone — whose length ℓ_* is at this point by definition much smaller than R. On the other hand, if L is much smaller than R, then Δp varies abruptly over the slipping region but is highly localized near the rupture center over a small zone that is far away from the process zone, such that the overpressure within the process zone is negligibly small. Hence, the overpressure has the simple role of approximately setting the current amount of effective normal stress within the process zone, which can be reasonably taken as uniform at a given time and evaluated at the rupture front, $\Delta p(R,t)$. The fracture energy G_c can be thus approximated as

$$G_c \approx \left[\sigma_0' - \Delta p(R,t)\right] \int_0^{\delta_*} \left[f(\delta) - f_r\right] \mathrm{d}\delta. \tag{12}$$

Note that in addition to the separation of scales between the diffusion of pore pressure and the frictional weakening process just discussed, the previous equation assumes that the friction coefficient itself must effectively evolve throughout ℓ_* (or equivalently over δ_*) towards an approximately constant residual value $f_r(\delta_*) = f_r$. This latter is guaranteed in the linear-weakening model (4) as $\delta_* = \delta_c$, and it seems a good approximation for the exponential-weakening case (5) at some $\delta_* > \delta_c$. Assuming this latter separation of scales too, the residual strength of the fault can be then written as

$$\tau_r(r,t) = f_r \times \left[\sigma_0' - \Delta p(r,t)\right]. \tag{13}$$

Substituting the previous equation into (11) leads after some manipulations to an energy-based equation for the rupture front $R(t)$,

$$\underbrace{\frac{2}{\sqrt{\pi}} \frac{f_r \Delta p_*}{\sqrt{R}} \int_0^R \frac{E_1\left(r^2/L^2\right)}{\sqrt{R^2 - r^2}} r\mathrm{d}r}_{K_p} + \overbrace{\frac{2}{\sqrt{\pi}} \left[\tau_0 - f_r\sigma_0'\right] \sqrt{R}}^{K_\tau} = K_c(R,t), \tag{14}$$

where the explicit dependence of the rupture front R and overpressure front L on time t has been omitted for simplicity.

Eq. (14) is an insightful form of the near-front energy balance, equivalent to the one obtained by Garagash and Germanovich (2012) in two dimensions. It shows that the instantaneous position of the rupture front is determined by the competition between three distinct 'crack' processes that are active during the propagation of the rupture. The first term on the left-hand side K_p is an axisymmetric stress intensity factor (SIF) associated with the equivalent shear load induced by the fluid injection alone, which continuously unclamps the fault. The second term on the left-hand side K_τ is an axisymmetric SIF due to a uniform shear load that is equal to the difference between the initial shear stress τ_0 and the residual strength of the fault without any overpressure, $f_r\sigma_0'$, commonly known as stress drop. Note that this term may be either positive or negative, whereas the first term is always positive.

Finally, the right-hand side of the near-front energy balance is associated with the fracture energy G_c that is dissipated within the process zone or, in the Irwin's form, the fracture toughness K_c. Note that in our model, the fracture energy may generally depend on the rupture radius R and time t due to variations in overpressure (see Eq. (12)).

3. Two simplified models

3.1. The constant friction model

The constant friction model is the simplest idealization of friction that produces fluid-driven stable frictional ruptures. It has been extensively studied in two-dimensional configurations for different injection scenarios (Viesca, 2021; Sáez et al., 2022) and more recently in the fully three-dimensional case (Sáez et al., 2022). Here, we briefly summarize the main characteristics of the circular rupture model (Sáez et al., 2022), whose results will be later put in a broader perspective in relation to the slip-weakening model.

Sáez et al. (2022) showed that fault slip induced by injection at a constant volumetric rate is self-similar in a diffusive manner. The rupture radius $R(t)$ thus evolves simply as

$$R(t) = \lambda L(t), \tag{15}$$

where $L(t) = \sqrt{4\alpha t}$ is the diffusion length scale and nominal position of the overpressure front, and λ is the so-called amplification factor for which an analytical solution was derived (Sáez et al., 2022) from the condition that the rupture grows with no stress singularity at its front,

$$\int_0^1 \frac{E_1(\lambda\eta)}{\sqrt{1-\eta^2}}\eta \mathrm{d}\eta = \mathcal{T}, \tag{16}$$

which leads after evaluating analytically the corresponding integral to

$$2-\gamma+\frac{2}{3}\lambda^2 {}_2F_2\left[\begin{matrix}1 & 1\\ 2 & 5/2\end{matrix};-\lambda^2\right]-\ln(4\lambda^2) = \mathcal{T}, \tag{17}$$

where $\gamma = 0.577216\ldots$ is the Euler–Mascheroni's constant and ${}_2F_2[\,]$ is the generalized hypergeometric function. Note that λ is a function of a sole dimensionless number, the so-called stress-injection parameter

$$\mathcal{T} = \frac{f_{\mathrm{cons}}\sigma_0' - \tau_0}{f_{\mathrm{cons}}\Delta p_*}, \tag{18}$$

where f_{cons} is the constant friction coefficient.

The parameter $\mathcal{T}$ is defined as the ratio between the amount of shear stress that is necessary to activate fault slip $f_{\mathrm{cons}}\sigma_0'-\tau_0$, and $f_{\mathrm{cons}}\Delta p_*$ which quantifies the intensity of the fluid injection. $\mathcal{T}$ can vary in principle between 0 and $+\infty$ (Sáez et al., 2022). However, for practical purposes $\mathcal{T}$ is upper bounded. Indeed, as described previously, $\Delta p_* = \Delta p_c/4\pi$ with Δp_c taken as approximately equal to the overpressure at the fluid source. Hence, one can estimate the minimum amount of overpressure that is required to activate fault slip as $f_{\mathrm{cons}}\Delta p_c \approx f_{\mathrm{cons}}\sigma_0'-\tau_0$. Substituting the previous relation into Eq. (18) leads to an approximate upper bound for $\mathcal{T} \lessapprox 10$, where we have replaced the factor 4π by 10 to keep the spirit of the order-of-magnitude approximation behind Δp_c when representing the fluid-source overpressure. The lower and upper bounds of $\mathcal{T}$ are associated with two end-member regimes that were first introduced by Garagash and Germanovich (2012). When $\mathcal{T}$ is close to zero, $\tau_0 \to f_{\mathrm{cons}}\sigma_0'$ and thus the fault is critically stressed or about to fail before the injection starts. On the other hand, when $\mathcal{T} \sim 10$, the fault is 'marginally pressurized' as the injection has provided just the minimum amount of overpressure to activate fault slip. The asymptotic behavior of λ for the limiting values of $\mathcal{T}$ is particularly insightful. For critically stressed faults ($\mathcal{T} \ll 1$), the amplification factor turns out to be large ($\lambda \gg 1$) and thus the rupture front outpaces largely the fluid pressure front ($R(t) \gg L(t)$), whereas for marginally pressurized faults ($\mathcal{T} \sim 10$), the amplification factor is small ($\lambda \ll 1$) and thus the rupture front lags significantly the overpressure front ($R(t) \ll L(t)$).

In the critically stressed limit, since $\lambda \gg 1$, the equivalent shear load due to fluid injection can be approximated as a point force,

$$f_{\mathrm{cons}}\Delta p(r,t) \approx f_{\mathrm{cons}}\Delta P(t)\delta^{dirac}(r)/2\pi r, \text{ with } \Delta P(t) = \Delta p_* \int_0^\infty E_1\left(\frac{r^2}{4\alpha t}\right)2\pi r \mathrm{d}r = 4\pi\alpha t\Delta p_*, \tag{19}$$

whereas in the marginally pressurized limit, its asymptotic form comes simply from expanding the exponential integral function for small values of its argument as $\lambda \ll 1$: $f_{\mathrm{cons}}\Delta p(r,t) \approx -f_{\mathrm{cons}}\Delta p_*\left[\ln\left(r^2/4\alpha t\right)+\gamma\right]$. Substituting the previous asymptotic forms for the fluid-injection 'forces' into the rupture propagation condition (16) leads to the following asymptotes for the amplification factor (Sáez et al., 2022):

$$\lambda \approx \begin{cases} 1/\sqrt{2\mathcal{T}} & \text{for critically stressed faults, } \mathcal{T} \ll 1,\\ \frac{1}{2}\exp\left(\left[2-\gamma-\mathcal{T}\right]/2\right) & \text{for marginally pressurized faults, } \mathcal{T} \sim 10. \end{cases} \tag{20}$$

Comparing the previous asymptotes with the exact solution (17) suggests that the asymptotic approximations (20) are accurate up to 5% in the critically stressed and marginally pressurized regimes, for $\mathcal{T} \lessapprox 0.16$ and $\mathcal{T} \gtrapprox 2$, respectively.

3.2. The constant fracture energy model

Consider the simple case in which the fracture energy G_c is constant (and so the fracture toughness K_c). Although this is an idealized scenario, it accounts already for one of the main ingredients of the slip-weakening friction model, that is, a finite fracture energy. At the same time, the constant fracture energy model allows us to examine quickly the different regimes of propagation that emerge from the competition between the three distinct terms that compose the front-localized energy balance (14). Furthermore, a constant fracture energy model will result to be an excellent approximation of some important rupture regimes in the slip-weakening model.

3.2.1. Scaling and structure of the solution

Similarly to the case of Coulomb's friction, let us define an amplification factor in the form

$$\lambda(t) = \frac{R(t)}{L(t)}. \tag{21}$$

Unlike the solution of the previous section that is self-similar, here the introduction of a finite fracture energy breaks the self-similarity of the problem and makes the solution for λ be now time-dependent.

Non-dimensionalization of the front-localized energy balance shows that the solution for the amplification factor λ can be written as

$$\lambda\left(\mathcal{T}_r, \mathcal{K}(t)\right), \tag{22}$$

where $\mathcal{T}_r$ and $\mathcal{K}$ are two dimensionless parameters with the physical meanings that we explain below. Interestingly, the dependence of λ on time is only in the second parameter $\mathcal{K}$.

The first parameter $\mathcal{T}_r$ is a dimensionless number in the form

$$\mathcal{T}_r = \frac{f_r\sigma_0' - \tau_0}{f_r \Delta p_*}, \tag{23}$$

which turns out to be identical to the stress-injection parameter of the constant friction model (Eq. (18)) except that the constant friction coefficient f_{cons} is now the residual friction coefficient f_r. For this reason, we name it as the 'residual' stress-injection parameter.

$\mathcal{T}_r$ quantifies the combined effect of the two equivalent shear loads that drive the propagation of the 'fractured' slipping patch, namely, the uniform stress $f_r\sigma_0' - \tau_0$ and the distributed load associated with fluid injection $f_r\Delta p(r,t)$ whose intensity is $f_r\Delta p_*$. The uniform stress is equal to the difference between the residual fault strength under ambient conditions $f_r\sigma_0'$ and the initial shear stress τ_0. Note that depending on the sign of $f_r\sigma_0' - \tau_0$, $\mathcal{T}_r$ can be either positive or negative. Moreover, as noted first by Garagash and Germanovich (2012) in their two-dimensional model, the sign of $f_r\sigma_0' - \tau_0$ is expected to strongly affect the overall stability of the fault response. According to Garagash and Germanovich, if the condition $f_r\sigma_0' < \tau_0$ is satisfied ($\mathcal{T}_r$ negative), ruptures may ultimately run away dynamically and never stop within the limits of such a homogeneous and infinite fault model. Conversely, when $f_r\sigma_0' > \tau_0$ ($\mathcal{T}_r$ positive), ruptures would propagate ultimately in a quasi-static, stable manner. Assuming for now that the ultimate stability condition of Garagash and Germanovich (2012) holds in the circular rupture configuration, we consider only ultimately quasi-static cases in this section and, therefore, values for $\mathcal{T}_r$ that are strictly positive. We will soon show that this assumption is indeed satisfied.

Let us now find the limiting values of $\mathcal{T}_r$. As lower bound, $\mathcal{T}_r$ can be as small as possible ($\mathcal{T}_r \to 0$) when $f_r\sigma_0' \to \tau_0$. Since in this limit, the fault is approaching the ultimate unstable condition of Garagash and Germanovich (2012), we refer to it as the 'nearly unstable' limit. As an upper bound, similarly to the case of constant friction, the maximum value of $\mathcal{T}_r$ is set by the minimum possible magnitude of Δp_*, which in turn relates to the minimum amount of overpressure that is required to activate fault slip. This is given by the approximate relation $f_p\Delta p_c \approx f_p\sigma_0' - \tau_0$, where f_p is the peak friction coefficient and Δp_c is the characteristic overpressure of the fluid source (Eq. (2)). By substituting this previous relation into (23), we find the sought upper bound to be $\mathcal{T}_r \lessapprox 4\pi(\sigma_0' - \tau_0/f_r)/(\sigma_0' - \tau_0/f_p)$. Since the ratio f_r/f_p is always between 0 and 1 and the maximum value of the upper bound is obtained when $f_r/f_p \to 1$, we obtain such a maximum upper bound as $\mathcal{T}_r \lessapprox 10$ (again, the factor 4π). Given that in this limit the upper bound is still related to the minimum amount of overpressure that is required to activate a frictional rupture, we still denominate it as marginally pressurized limit. Note that the upper bound limit has a quite similar meaning to the one of $\mathcal{T}$ in the constant friction model. Conversely, the lower bound limit of $\mathcal{T}_r$ has no longer the interpretation of a critically stressed fault as for $\mathcal{T}$.

The second parameter of the constant fracture energy model, $\mathcal{K}$, corresponds to a time-dependent dimensionless toughness. It can be either defined using the stress scales of the nearly unstable or marginally pressurized limits depending on the proper regime characterizing the fault response. These two choices are:

$$\mathcal{K}_{nu}(t) = \frac{K_c}{\left(f_r\sigma_0' - \tau_0\right)\sqrt{R(t)}}, \text{ and } \quad \mathcal{K}_{mp}(t) = \frac{K_c}{f_r\Delta p_*\sqrt{R(t)}}, \tag{24}$$

for the nearly unstable ($\mathcal{T}_r \ll 1$) and marginally pressurized ($\mathcal{T}_r \sim 10$) regimes, respectively. Note that in (24), the explicit dependence of R on time has been emphasized as it provides the time dependence of $\mathcal{K}$.

The dimensionless toughness $\mathcal{K}$ quantifies the relevance of the fracture energy in the near-front energy balance at a given time t. Since for any physically admissible solution, the rupture radius must increase monotonically with time, the solution will always evolve from a large-toughness regime ($\mathcal{K} \gg 1$) to a small-toughness regime ($\mathcal{K} \ll 1$). Moreover, the effect of the fracture energy in the energy balance can be ultimately neglected as the dimensionless toughness effectively vanishes ($\mathcal{K} \to 0$) in the limit $R \to \infty$ (or $t \to \infty$). We denominate this ultimate solution as the zero-toughness or zero-fracture-energy solution. Since the effect of the fracture energy becomes irrelevant in this limit, such asymptotic solution is self-similar (λ in (22) becomes time-independent).

Finally, the transition between the large- and small-toughness regimes is characterized by the following rupture length scales (obtained by setting $\mathcal{K}_{nu} = 1$ and $\mathcal{K}_{mp} = 1$, respectively),

$$R^*_{nu} = \left(\frac{K_c}{f_r\sigma'_0 - \tau_0}\right)^2 \quad \text{and} \quad R^*_{mp} = \left(\frac{K_c}{f_r \Delta p_*}\right)^2. \tag{25}$$

Note that the two dimensionless toughnesses in (24) are of course not independent as they are two choices of the same parameter. They are indeed related through the residual stress-injection parameter $\mathcal{T}_r$ as

$$\mathcal{K}_{mp} = \mathcal{T}_r \mathcal{K}_{nu}. \tag{26}$$

3.2.2. General and ultimate zero-fracture-energy solutions

Considering the scaling of the previous section plus the definition of the following non-dimensional integral:

$$\Psi(\lambda) = \int_0^1 \frac{E_1(\lambda\eta)}{\sqrt{1-\eta^2}}\eta \mathrm{d}\eta, \tag{27}$$

the front-localized energy balance (14) can be written in dimensionless form as

$$\frac{\Psi(\lambda)}{\mathcal{T}_r} - 1 = \frac{\sqrt{\pi}}{2}\mathcal{K}_{nu}, \text{ and } \quad \Psi(\lambda) - \mathcal{T}_r = \frac{\sqrt{\pi}}{2}\mathcal{K}_{mp}, \tag{28}$$

in the nearly unstable ($\mathcal{T}_r \ll 1$) and marginally pressurized ($\mathcal{T}_r \sim 10$) regimes, respectively. Note that the non-dimensional integral Ψ is identical to the one in Eq. (16) and can be thus evaluated analytically to obtain the left-hand side of Eq. (17). Moreover, the limiting behaviors of such integral are: $\Psi(\lambda) \approx 1/2\lambda^2 + O(\lambda^{-4})$ when $\lambda \gg 1$, and $\Psi(\lambda) \approx 2 - \gamma - \ln\left(4\lambda^2\right) + O(\lambda^2)$ when $\lambda \ll 1$. Using the previous asymptotic expansions and assuming similarly to the constant friction model that $\lambda \gg 1$ when $\mathcal{T}_r \ll 1$, and $\lambda \ll 1$ when $\mathcal{T}_r \sim 10$, we derive from Eqs. (28), the following closed-form asymptotic expressions for the amplification factor:

$$\lambda \approx \begin{cases} 1/\sqrt{\left(2 + \sqrt{\pi}\mathcal{K}_{nu}\right)\mathcal{T}_r} & \text{for nearly unstable faults, } \mathcal{T}_r \ll 1, \\ \frac{1}{2}\exp\left[\left(2 - \gamma - \mathcal{T}_r - \mathcal{K}_{mp}\sqrt{\pi}/2\right)/2\right] & \text{for marginally pressurized faults, } \mathcal{T}_r \sim 10, \end{cases} \tag{29}$$

where the dependence of both $\mathcal{K}$ and λ on time has been omitted for simplicity.

The full solution of the model given by Eqs. (28) together with the asymptotics (29) are shown in Fig. 3a and b. The direction of time in these plots goes from right to left as the dimensionless toughness $\mathcal{K}(t)$ decreases with time. Moreover, since ultimately ($t \to \infty$, $R \to \infty$) the dimensionless toughness is negligibly small ($\mathcal{K} \to 0$), Eqs. (28)a and (28)b become both identical to the rupture propagation condition of the constant friction model, Eq. (16), as long as the constant friction coefficient f_{cons} is now understood as the residual one f_r. The solution of the constant friction model (17) with $f_{\text{cons}} = f_r$ is also displayed in Fig. 3a and b. It is now clear how the constant fracture energy solution approaches asymptotically the constant residual friction solution as $\mathcal{K} \to 0$. This can be also seen in the asymptotics (29) that become identical to (20) when $\mathcal{K} = 0$.

The previous result has an important implication: the constant friction model analyzed in Sáez et al. (2022) can be now interpreted in two distinct manners: as a scenario in which the friction coefficient does not significantly weaken ($f_{\text{cons}} \approx f_p$), or as the ultimate asymptotic solution of a model with constant fracture energy provided that $f_{\text{cons}} = f_r$. In the former, the fracture energy $G_c = 0$ by definition. In the latter, the effect of the non-zero fracture energy in the rupture-front energy balance is to leading order negligible compared to the other two terms that drive the propagation of the rupture. In addition, because the integral $\Psi(\lambda)$ is strictly positive and in the ultimate asymptotic regime $\mathcal{K} \to 0$, the near-front energy balance (28) admits ultimate quasi-static solutions only if $\mathcal{T}_r > 0$. Negative values of $\mathcal{T}_r$ which are equivalent to the condition $f_r\sigma'_0 < \tau_0$ may be thus related to ultimately unstable solutions, not accounted for the quasi-static energy balance. This result supports our assumption that the ultimate stability condition of Garagash and Germanovich (2012) holds in the circular rupture configuration.

We now recast the solution of the constant fracture energy model in a perhaps more intuitive way, as the evolution of the rupture radius with time:

$$R(t) = \lambda(\mathcal{T}_r, \mathcal{K}(t)) \cdot L(t). \tag{30}$$

Recalling that $L(t) = \sqrt{4\alpha t}$ and noting that

$$\mathcal{K}_{nu} = (R/R^*_{nu})^{-1/2}, \text{ and } \quad \mathcal{K}_{mp} = (R/R^*_{mp})^{-1/2}, \tag{31}$$

we solve Eqs. (28)a and (28)b for R/R^* as a function of the normalized squared root of time $\sqrt{4\alpha t}/R^*$ and $\mathcal{T}_r$, where R^* represents the characteristic rupture length scale of either the nearly unstable or marginally pressurized regime (Eq. (25)).

This version of the solution is displayed in Fig. 3c and d. In these plots, the normalized square root of time can be also interpreted as the normalized position of the overpressure front $L(t)$. Indeed, the thicker dashed line corresponds to the current position of the

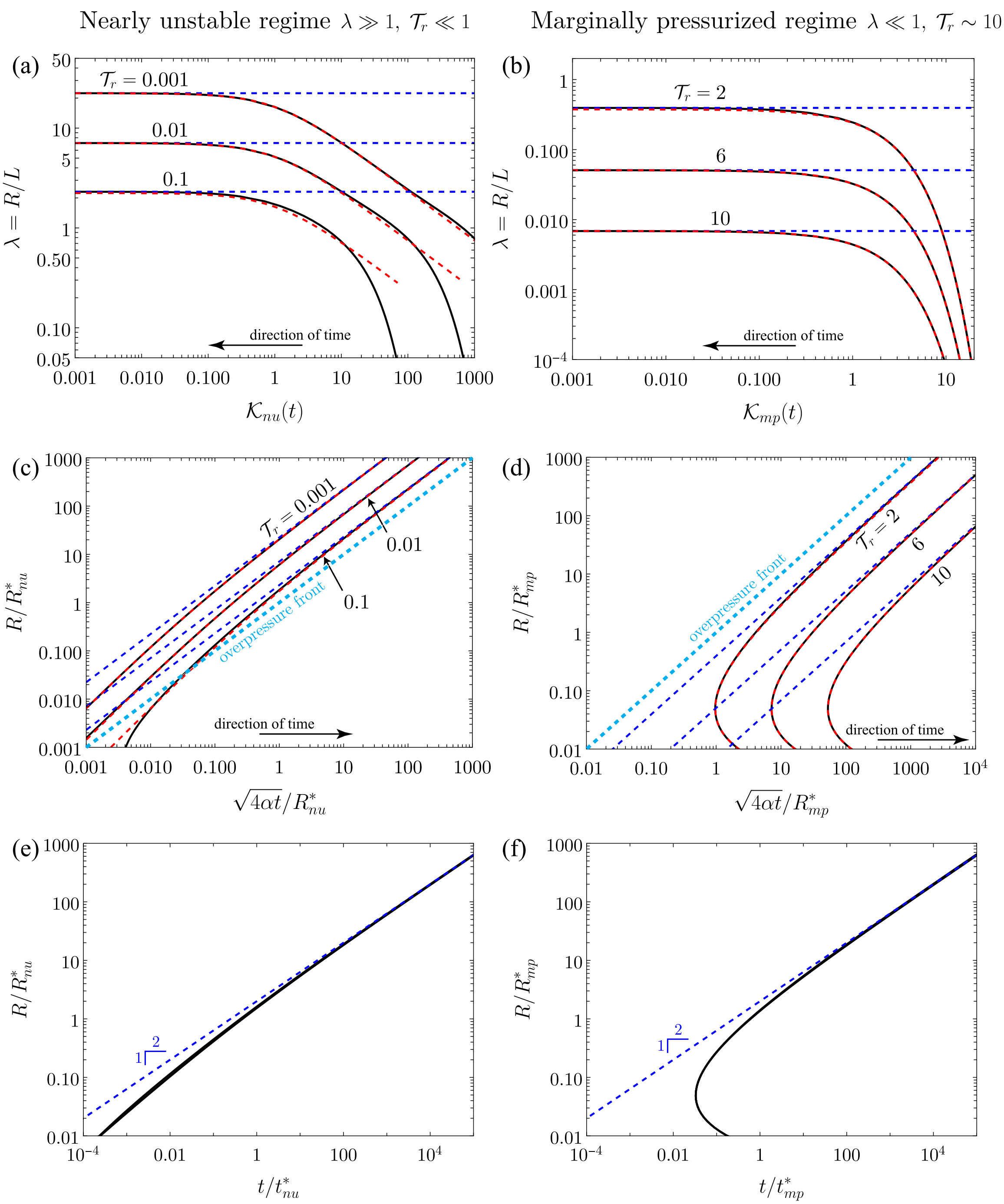

Fig. 3. The constant fracture energy model. (Left) Nearly unstable regime ($\lambda \gg 1$, $\mathcal{T}_r \ll 1$) and (right) marginally pressurized regime ($\lambda \ll 1$, $\mathcal{T}_r \sim 10$). (a, b) Amplification factor λ as a function of dimensionless toughness $\mathcal{K}(t)$ for different values of $\mathcal{T}_r$. (c, d) Normalized rupture radius R as a function of the normalized squared root of time or position of the overpressure front $L(t) = \sqrt{4\alpha t}$. (e, f) Normalized rupture radius R as a function of dimensionless time t. All curves tend to collapse when using the latter scaling. Legends: black solid lines are the general solution of the constant fracture energy model; red dashed lines correspond to the asymptotes for λ (29) in (a, b), and the asymptotes for the normalized rupture radius (32) and (33) in (c) and (d), respectively; blue dashed lines represent the constant residual friction, ultimate zero-fracture-energy solution.

overpressure front. Slip fronts propagating above this line represent cases in which the rupture front outpaces the overpressure front. We observe that such a situation is a common feature of nearly unstable faults ($\mathcal{T}_r \ll 1$), being the analog regime of critically stressed faults in the constant friction model. Moreover, taking into account (30) and (31), the asymptotics (29) can be recast as the following implicit equations for the normalized rupture radius R/R^* as a function of time:

$$\sqrt{4\alpha t}/R^*_{nu} = \frac{R}{R^*_{nu}}\left[\left(2+\frac{\sqrt{\pi}}{\sqrt{R/R^*_{nu}}}\right)\mathcal{T}_r\right]^{1/2} \tag{32}$$

for nearly unstable faults, and

$$\sqrt{4\alpha t}/R^*_{mp} = \frac{2\left(R/R^*_{mp}\right)}{\exp\left[\left(2-\gamma-\mathcal{T}_r-\left(\sqrt{\pi}/2\right)\left(R/R^*_{mp}\right)^{-1/2}\right)/2\right]} \tag{33}$$

for marginally pressurized faults.

Note that the transition from the large-toughness ($\mathcal{K} \gg 1$) to small-toughness ($\mathcal{K} \ll 1$) regime in Fig. 3c and d occurs along the vertical axis when $R/R^*_{nu} \sim 1$ and $R/R^*_{mp} \sim 1$, respectively. The characteristic time at which this transition occurs can be approximated by using the constant residual friction solution or, what is the same, the ultimate zero-fracture-energy solution, $\lambda_r = \lambda\left(\mathcal{T}_r, \mathcal{K}=0\right)$, which yields

$$t^*_{nu} \approx \frac{1}{\alpha\lambda_r^2}\left(\frac{K_c}{f_r\sigma'_0-\tau_0}\right)^4, \text{ and } \quad t^*_{mp} \approx \frac{1}{\alpha\lambda_r^2}\left(\frac{K_c}{f_r\Delta p_*}\right)^4. \tag{34}$$

λ_r can be estimated from the asymptotes presented in Eq. (20) for both nearly unstable ($\mathcal{T}_r \ll 1$) and marginally pressurized ($\mathcal{T}_r \sim 10$) faults, provided that $\mathcal{T}$ is replaced by $\mathcal{T}_r$. Normalizing time by the previous characteristic times naturally tends to collapse all solutions for every value of $\mathcal{T}_r$ as displayed in Fig. 3e and f, where the power law 1/2 reflects the diffusively self-similar property of the ultimate zero-fracture-energy solution.

Finally, it seems worth mentioning that the solution for marginally pressurized faults is nonphysical at times in which the rupture is small, $R/R^*_{mp} \lessapprox 0.05$ (see Fig. 3d and f). This could be related either to the occurrence of a dynamic instability or to a rupture size that is too small compared to realistic process zone sizes. Indeed, the solution constructed here for the case of constant fracture energy has the inherent limitations of LEFM theory. First, it does not account for the initial stage in which the process zone is under development ($R < \ell_*$) and, second, it is an approximate solution that relies on the small-scale yielding assumption ($R \gg \ell_*$). Both limitations are overcome in the next sections by solving numerically the governing equations of the coupled initial boundary value problem for slip-weakening friction.

4. Scaling analysis, map of rupture regimes and ultimate stability condition

4.1. Scaling analysis

The scaling of the slip-weakening problem comes directly from the two-dimensional linear-weakening model of Garagash and Germanovich (2012), which is also valid for the exponential-weakening version of the friction law. We summarize the scaling as follows:

$$\bar{t} = \frac{t}{R_w^2/\alpha}, \quad \bar{r} = \frac{r}{R}, \quad \bar{\tau} = \frac{\tau}{f_p\sigma'_0}, \quad \bar{\delta} = \frac{\delta}{\delta_w}, \quad \Delta\bar{p} = \frac{\Delta p}{\Delta p_*}, \tag{35}$$

where the bar symbol represents dimensionless quantities, δ_w is the slip weakening scale, and R_w is an elasto-frictional rupture length scale, given respectively by (see also Uenishi and Rice (2002))

$$\delta_w = \frac{f_p}{f_p-f_r}\delta_c, \text{ and } \quad R_w = \frac{\mu}{\left(f_p-f_r\right)\sigma'_0}\delta_c. \tag{36}$$

In the previous equation, $(f_p - f_r)\sigma'_0/\delta_c$ is the so-called slip-weakening rate (Uenishi and Rice, 2002).

Nondimensionalization of the governing equations of the model using the previous scaling shows that the normalized fault slip $\bar{\delta}$ depends in addition to dimensionless space $\bar{r}$ and time $\bar{t}$, on the following three dimensionless parameters:

$$\mathcal{S} = \frac{\tau_0}{f_p\sigma'_0}, \quad \mathcal{P} = \frac{\Delta p_*}{\sigma'_0}, \quad \mathcal{F} = \frac{f_r}{f_p}. \tag{37}$$

The first parameter $\mathcal{S}$ is the pre-stress ratio or sometimes called, stress criticality. It is the quotient between the initial shear stress τ_0 and the initial static fault strength $f_p\sigma'_0$. The pre-stress ratio $\mathcal{S}$ quantifies how close to frictional failure the fault is under ambient (pre-injection) conditions. The range of values for $\mathcal{S}$ is naturally

$$0 \le \mathcal{S} < 1, \tag{38}$$

being zero when the fault has no initial shear stress whatsoever, and close to one when the fault is critically stressed or about to fail under ambient conditions, $\tau_0 \to f_p\sigma'_0$.

The second parameter $\mathcal{P}$ is the overpressure ratio, which quantifies the intensity of the injection Δp_* with regard to the initial effective normal stress σ'_0. The range of possible values for $\mathcal{P}$ is determined as follows. Its upper bound comes from the maximum possible amount of overpressure that in our model corresponds to a scenario in which the fault interface is about to open: $\Delta p_c \approx \sigma'_0$, where $\Delta p_c = 4\pi \Delta p_*$ (Eq. (2)). On the other hand, the lower bound of $\mathcal{P}$ comes from the minimum amount of overpressure that is required to activate fault slip: $f_p \Delta p_c \approx f_p \sigma_0' - \tau_0$. By replacing the previous approximate relations into $\mathcal{P} = \Delta p_*/\sigma_0'$, we obtain the sought range of values for $\mathcal{P}$ in an approximate sense as

$$10^{-1}(1-\mathcal{S}) \lessapprox \mathcal{P} \lessapprox 10^{-1}, \tag{39}$$

where $\approx 10^{-1}$ comes from the factor $1/4\pi$. Finally, the third parameter, the residual-to-peak friction ratio $\mathcal{F}$ is such that

$$0 \le \mathcal{F} \le 1. \tag{40}$$

$\mathcal{F}$ is zero when there is a total loss of frictional resistance upon the passage of the rupture front, a situation that is unlikely to occur for stable, slow slip, as opposed to fast slip in which thermally-activated dynamic weakening mechanisms could make the fault reach quite low values for $\mathcal{F}$ (Rice, 2006). On the other hand, $\mathcal{F}$ is equal to one when the friction coefficient does not weaken at all, which corresponds indeed to the particular case of Coulomb's friction $f_{\text{cons}} = f_p$.

Finally, it will result useful to define the residual stress-injection parameter $\mathcal{T}_r$ of the constant fracture energy model, Eq. (23), as a combination of the three dimensionless parameters of the slip-weakening model,

$$\mathcal{T}_r = \frac{1-\mathcal{S}/\mathcal{F}}{\mathcal{P}}. \tag{41}$$

In addition, one can also define a stress-injection parameter based on the peak value of friction f_p instead of the residual one. Such a parameter reads as

$$\mathcal{T}_p = \frac{f_p \sigma_0' - \tau_0}{f_p \Delta p_*} = \frac{1-\mathcal{S}}{\mathcal{P}}. \tag{42}$$

We denominate $\mathcal{T}_p$ as the 'peak' stress-injection parameter. The latter is indeed the maximum possible value of the residual stress-injection parameter $\mathcal{T}_r$ (when $\mathcal{F} = 1$), so that

$$\mathcal{T}_r \le \mathcal{T}_p. \tag{43}$$

As a final comment on the scaling, when comparing the fault response for each version of the friction law, the results that we present in the next sections are particularly valid under the assumption that both friction laws are characterized by the same slip-weakening scale δ_c (see Fig. 2). Alternatively, one could compare the effect of both friction laws under a different condition such as, for instance, an equal fracture energy G_c, or any other criterion. In the case of equal G_c, the characteristic slip weakening scales would be related as $\delta_{c,\text{lin}} = 2\delta_{c,\text{exp}}$. Our results can be then easily re-scaled using the previous relation as the dimensionless solution remains unchanged, and the same could be done with any other criterion.

4.2. Map of rupture regimes and ultimate stability condition

Given the similarity of the scaling between our three-dimensional axisymmetric rupture model and the two-dimensional plane-strain model of Garagash and Germanovich (2012), we find, not surprisingly, that the map of regimes of fault behavior in our model is essentially the same as in the two-dimensional problem (Garagash and Germanovich, 2012). Fig. 4 summarizes the map of regimes in the parameter space composed by $\mathcal{S}$, $\mathcal{P}$ and $\mathcal{F}$. Moreover, as anticipated when examining the constant fracture energy model, the ultimate stability condition of Garagash and Germanovich (2012) holds in the circular rupture case. Therefore, mixed-mode circular ruptures will propagate ultimately ($t \to \infty$, $R \to \infty$) in a quasi-static, stable manner, if any of the following three equivalent conditions is satisfied:

$$f_r \sigma_0' > \tau_0 \iff \mathcal{S} < \mathcal{F} \iff \mathcal{T}_r > 0. \tag{44}$$

Notably, the residual stress-injection parameter $\mathcal{T}_r$ must be strictly positive. Otherwise, ruptures will propagate ultimately in an unstable, dynamic manner. In the latter case, dynamic ruptures will run away and never stop within the limits of such a homogeneous and infinite fault model. Since in this work, we are mainly interested in the propagation of quasi-static slip, the regimes of major interest are the ones corresponding to ultimately stable ruptures and the quasi-static nucleation phase preceding dynamic ruptures. We examine both scenarios in what follows.

5. Ultimately stable ruptures

Fig. 5 displays the propagation of the slip front in the case of ultimately stable ruptures: $f_r \sigma_0' > \tau_0$. Without loss of generality, we fix the residual-to-peak friction ratio $\mathcal{F} = 0.7$ and examine for both the linear- and exponential-weakening friction laws the parameter space for $\mathcal{P}$ and $\mathcal{S} < 0.7$. The case of an overpressure ratio $\mathcal{P} = 0.05$ is shown in Fig. 5a. For all values of $\mathcal{S}$ in this figure, we obtain ruptures that propagate in a purely quasi-static manner without any dynamic excursion, that is, the regime R1 in Fig. 4. Fig. 5b shows, on the other hand, the case of a lower overpressure ratio $\mathcal{P} = 0.035$. For this value of $\mathcal{P}$, we observe the occurrence of the regime R2 for the linear-weakening case and both regimes R1 and R2 for the exponential-weakening case. The regime R2 corresponds to a situation in which a dynamic rupture nucleates, arrests, and is then followed by a purely quasi-static slip.

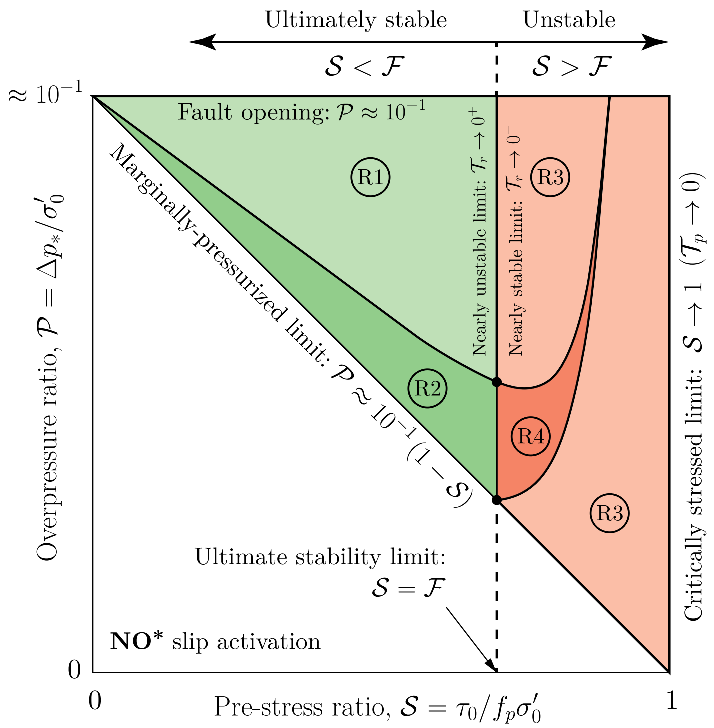

Fig. 4. Map of rupture regimes for linear slip-weakening model (adapted from figure 11 in Garagash and Germanovich (2012)). (R1) Unconditionally stable fault slip. (R2) Quasi-static slip up to the nucleation of a dynamic rupture, followed by arrest and then purely quasi-static slip. (R3) Quasi-static slip until the nucleation of a run-away dynamic rupture. (R4) Quasi-static slip up to the nucleation of a dynamic rupture, followed by arrest and then re-nucleation of a run-away dynamic rupture. *The condition of no slip is established in the approximate sense discussed in Appendix C.

5.1. Early-time Coulomb's friction stage and localization of the process zone

It is clear from Fig. 5 that at early times and for both regimes (R1 and R2), the propagation of the slip front is well approximated by the Coulomb's friction model, $f_{\text{cons}} = f_p$. The rupture radius thus evolves in this stage as

$$R(t) \approx \lambda_p L(t), \tag{45}$$

where λ_p is the amplification factor given by Eq. (17) considering the peak stress-injection parameter $\mathcal{T}_p$, and $L(t) = \sqrt{4\alpha t}$ is the position of the overpressure front as usual. This early-time Coulomb's friction similarity solution is meant to be valid while the friction coefficient does not decrease significantly throughout the slipping region, as shown for a few cases in the examples of Fig. 8d and e, when looking at the spatial distribution of the friction coefficient for the earliest times (t_1 and t_2). Note that in Fig. 5, we also include the evolution of the overpressure front with time (light blue dashed line). In the spatial range covered by this figure, the slip front of ultimately stable ruptures always lags the overpressure front ($R(t) \ll L(t)$) as the corresponding values of $\mathcal{T}_p$ are well into the marginally pressurized regime ($\mathcal{T}_p \sim 10$).

Now, beyond this early stage, the propagation of the slip front starts departing from the Coulomb's friction similarity solution while the slipping region experiences further weakening of friction. At this point, a dynamic instability could nucleate, arrest, and be followed by aseismic slip (examples in Fig. 5b), within a relatively narrow region of the parameter space (R2 in Fig. 4). More generally, ruptures will propagate in a purely quasi-static manner (examples in Fig. 5a, regime R1 in Fig. 4). Either way, when this transition happens, the rupture radius becomes greater than the rupture length scale R_w, which is around the same order as the process zone size ℓ_* for the linear weakening law (see, for an example, Fig. 8f). In the case of the exponential weakening law, Fig. 5 shows that the transition is smoother and occurs later than for the linear weakening case, whereas the localization of the process zone occurs also at a later time and for rupture lengths that seem to be many times or even an order of magnitude greater than the elasto-frictional length scale R_w (see, also, an example in Fig. 8f). Furthermore, starting from this point, the process zone has fully developed and thus a proper fracture energy G_c can be calculated. In this way, we can now examine the evolution of the rupture front through the near-front energy balance (14), to an accuracy set by the small-scale yielding approximation.

5.2. Front-localized energy balance, large- and small-toughness regimes

Using Eq. (12) in combination with (1), (4) and (5), we obtain an expression for the fracture energy of the slip-weakening model as

$$G_c \approx \kappa \left(f_p - f_r\right) \delta_c \left[\sigma_0' - \Delta p_* E_1\left(\lambda^2\right)\right] \tag{46}$$

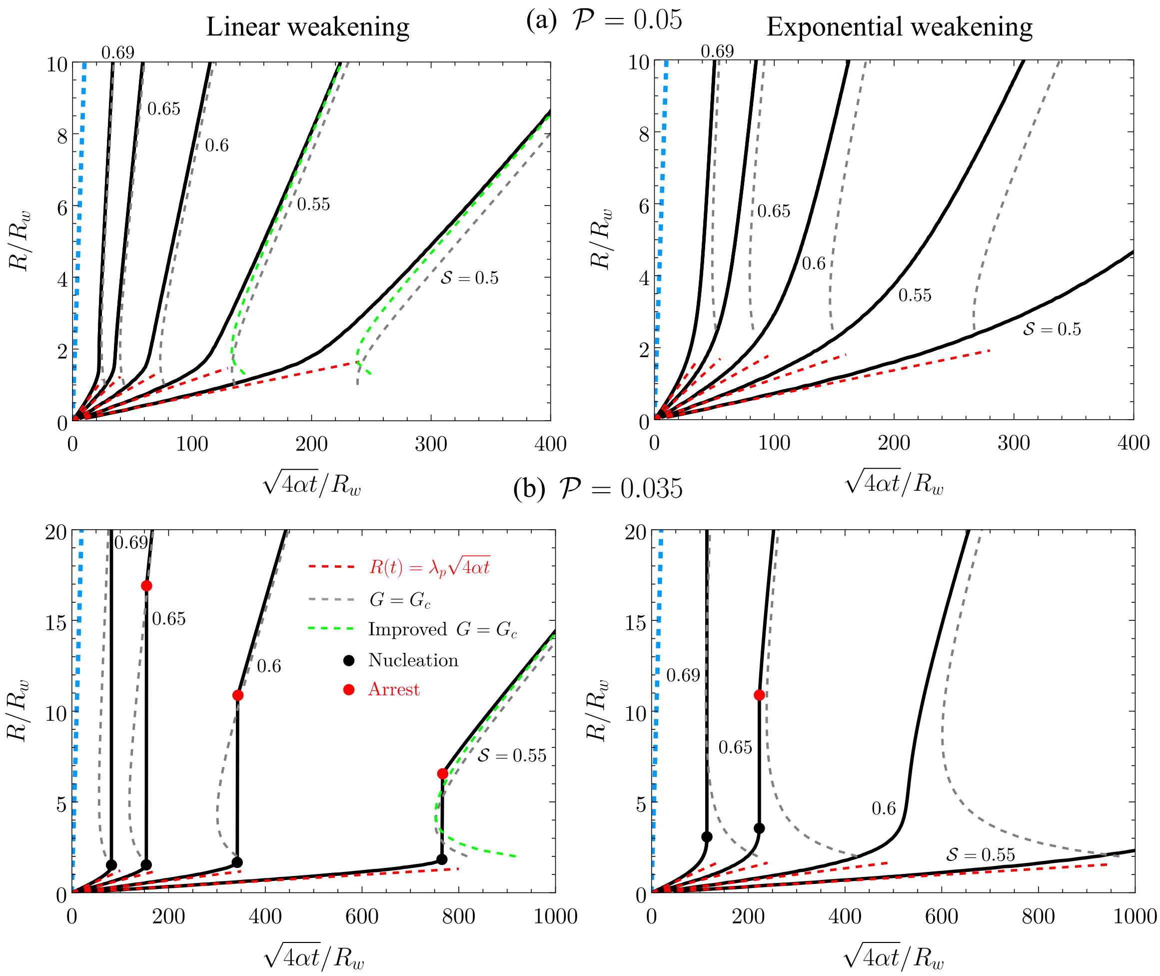

Fig. 5. Ultimately stable faults, $\mathcal{S} < \mathcal{F} = 0.7$, at distances $R/R_w < 20$. Normalized rupture radius versus square root of dimensionless time for (left) linear and (right) exponential weakening versions of the friction law. (a) $\mathcal{P} = 0.05$ and (b) $\mathcal{P} = 0.035$. Red dashed lines correspond to the analytical constant friction solution considering the peak friction coefficient. Gray dashed lines correspond to the solution of the front-localized energy balance, $G = G_c$. Green dashed lines correspond to an improved version of the front-localized energy balance as explained in the main text, shown here for only a few cases. Light blue dashed lines represent the position of the overpressure front $L(t) = \sqrt{4\alpha t}$. Note that for all cases, $R(t) \ll L(t)$.

with $\lambda(t) = R(t)/L(t)$ as usual, and κ is a coefficient equal to $1/2$ for the linear weakening case, and 1 for the exponential law, reflecting that the fracture energy of the latter is twice the fracture energy of the former at equal δ_c.

Introducing the scaling of the slip weakening model (35) into Eq. (14), one can nondimensionalize the front-localized energy balance in the following form,

$$\mathcal{F}\mathcal{P}\Psi(\lambda) + (\mathcal{S} - \mathcal{F}) = \frac{\sqrt{\pi}}{2}\sqrt{2\kappa}(1 - \mathcal{F})\frac{\sqrt{1 - \mathcal{P}E_1(\lambda^2)}}{\sqrt{R/R_w}}, \tag{47}$$

where $\Psi(\lambda)$ is the non-dimensional integral (27) whose evaluation is know analytically in (17). As expected from the scaling of the problem, Eq. (47) shows that the normalized rupture radius R/R_w depends in addition to dimensionless time $L(t)/R_w$ (which is implicit in λ) on the three dimensionless parameters of the model: $\mathcal{S}$, $\mathcal{P}$ and $\mathcal{F}$.

Considering that for any physically admissible quasi-static solution, the rupture radius must increase monotonically with time, we solve Eq. (47) by imposing R/R_w and then calculating $L(t)/R_w$ for a given combination of dimensionless parameters. The solution of the front-localized energy balance (47) is shown in Fig. 5 together with the full numerical solutions. We observe that in the linear weakening case, the near-front energy balance yields a good approximation of the full numerical solution already for $R \gtrapprox 2R_w$. On the other hand, in the exponential decay case, a good approximation is reached only after $R \gtrapprox 10R_w$. The difference is due to the fact that the localization of the process zone is less sharp and takes longer for the exponential decay in comparison to the linear weakening case, as exemplified in Fig. 8f. Moreover, the approximate nature of the energy-balance solution is of course due to the finite size of the process zone as opposed to the infinitesimal size required by LEFM. Indeed, in the two-dimensional problem, a

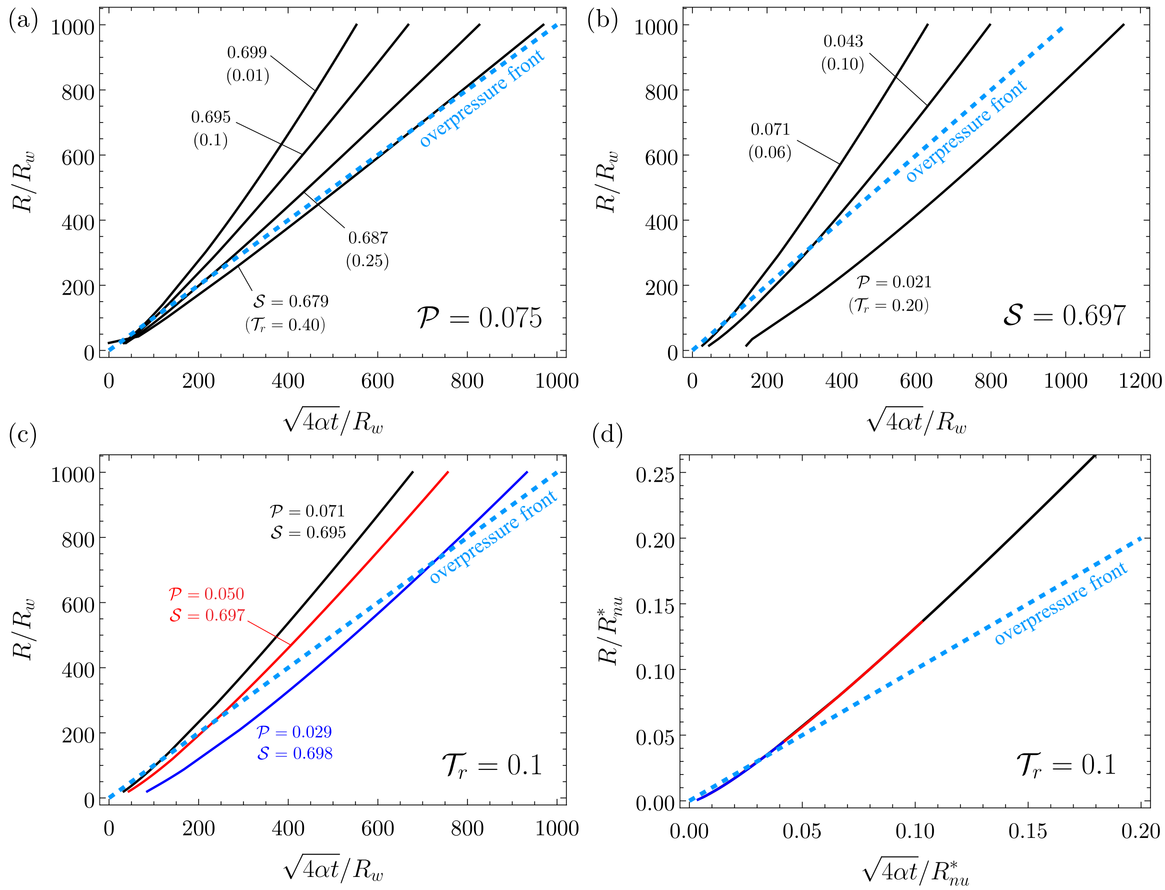

Fig. 6. Ultimately stable ruptures, $\mathcal{S} < \mathcal{F} = 0.7$, at distances $10 \leq R/R_w \leq 10^3$ for the linear-weakening friction law. Normalized rupture radius R/R_w versus square root of dimensionless time $\sqrt{4\alpha t}/R_w$ for: (a) $\mathcal{P} = 0.075$ and different values of $\mathcal{S}$ (values of $\mathcal{T}_r$ indicated between brackets); (b) $\mathcal{S} = 0.697$ and different values of $\mathcal{P}$; (c) different combinations of $\mathcal{P}$ and $\mathcal{S}$ for the same $\mathcal{T}_r = 0.1$; and (d) same as (c) but re-scaling both axes using R^*_{nu}. Note that all curves collapse under the new scaling in the latter plot.

correction due to the finiteness of the process zone for the linear weakening case was considered by Garagash and Germanovich (2012) based on the work on cohesive tensile crack propagation due to uniform far-field load by Dempsey et al. (2010), providing a solution with improved accuracy. Fig. 5 shows the results of this correction for a few cases in our model. The solution gets slightly better despite our frictional shear crack is circular and as such, the pre-factors in the scaling relations of the two-dimensional problem should differ from ours.

The front-localized energy balance allows us notably to examine the evolution of the rupture radius beyond the spatial range covered by Fig. 5, without the need to calculate the full numerical solutions. Note that the energy-balance solution is not only a good approximation over this spatial range but will also become an exact asymptotic solution in the LEFM limit $\ell_*/R \to 0$. Solutions for $10 \leq R/R_w \leq 10^3$ are displayed in Fig. 6. In particular, Fig. 6a shows that the higher the pre-stress ratio is, the faster the rupture propagates. Similarly, Fig. 6b displays that the more intense the injection is (higher overpressure ratio), the faster the rupture propagates too. Both effects are intuitively expected and consistent with the definition and effect of the stress-injection parameter in the constant friction model (Section 3.1). Moreover, initially ($R/R_w \leq 10$), we observe in Fig. 5 that the rupture front lags the overpressure front ($\lambda < 1$) as faults are governed at early times by Coulomb's friction with a peak stress-injection parameter $\mathcal{T}_p$ well into the marginally pressurized regime ($\mathcal{T}_p \sim 10$). Nonetheless, as the rupture accelerates due to the further weakening of friction, Fig. 6 shows that at later times, the slip front may end up outpacing the overpressure front ($\lambda > 1$). We examine the conditions leading to such behavior in what follows.

5.2.1. *Nearly unstable faults,* $\lambda(t) \gg 1$

When $\lambda(t) \gg 1$, the term $\Delta p_* E_1\left(\lambda^2\right)$ in (46) can be neglected as the overpressure within the process zone is vanishingly small. Hence, the fracture energy G_c becomes approximately constant and simply equal to

$$G_c \approx \kappa\left(f_p - f_r\right)\delta_c\sigma'_0. \tag{48}$$

At these length scales and in this regime, the problem becomes now identical to the constant fracture energy model that we extensively analyzed in Section 3.2. All the results and insights obtained for nearly unstable faults in that model are therefore inherited here. In fact, the rupture front will always outpace the overpressure front provided that the fault responds in the nearly unstable regime as quantified by the residual stress-injection parameter $\mathcal{T}_r \ll 1$, which is indeed intentionally the case of all the examples shown in Fig. 6.

Introducing (48) into (24)a via (10), and then (24)a into (28)a, leads to the dimensionless form of the front-localized energy balance in the nearly unstable regime,

$$\frac{1}{\mathcal{T}_r}\Psi(\lambda) - 1 = \frac{\sqrt{\pi}}{2}\sqrt{2\kappa}\frac{1}{\sqrt{R/R^*_{nu}}}, \tag{49}$$

with

$$\frac{R^*_{nu}}{R_w} = \left(\frac{f_p\sigma'_0 - f_r\sigma'_0}{f_r\sigma'_0 - \tau_0}\right)^2 = \left(\frac{1-\mathcal{F}}{\mathcal{F}-\mathcal{S}}\right)^2. \tag{50}$$

Eqs. (49) and (50) can be also obtained by neglecting the term $\mathcal{P}E_1\left(\lambda^2\right)$ in (47) and then dividing the latter by $\mathcal{F}-\mathcal{S}$. What is interesting to highlight, is that when the overpressure across the process zone becomes approximately constant or zero in this case (and so the fracture energy G_c is constant), the mathematical structure of the solution for the rupture front in the slip weakening model changes and it is no longer dependent on three but only one single dimensionless number, the residual stress-injection parameter $\mathcal{T}_r$.

The new scaling is exemplified in Fig. 6c and d. The former figure shows the evolution of the rupture front as given by Eq. (47) for different combinations of $\mathcal{S}$ and $\mathcal{P}$ that are all characterized by the same value of the residual stress-injection parameter, $\mathcal{T}_r = 0.1$. After re-scaling the solution using the characteristic rupture length scale R^*_{nu} (50), Fig. 6d displays how all curves in Fig. 6c collapse under the new, constant-fracture-energy scaling. Moreover, by using the asymptotic behavior of $\Psi(\lambda)$ for large λ, Eq. (32) provides an implicit equation for the normalized rupture radius R/R^*_{nu} as a function of the normalized square root of time $\sqrt{4\alpha t}/R^*_{nu}$ and the residual stress-injection parameter $\mathcal{T}_r$, provided that R^*_{nu} is replaced by (50).

5.2.2. Marginally pressurized faults, $\lambda(t) \ll 1$

A similar reasoning can be considered now for the case in which $\lambda(t) \ll 1$. Here, the overpressure within the process zone can be taken as approximately equal to the overpressure at the fluid source, Δp_w, as the rupture radius is much smaller than the pressurized zone, $R(t) \ll L(t)$. Note that the line-source approximation implies that $\Delta p_w \approx -\Delta p_c\left[\gamma + \ln(r_s^2/4\alpha t)\right]/4\pi$ at the relevant times $t \gg r_s^2/\alpha$ of the model, with r_s the fluid source radius. As discussed in Appendix C, the previous expression shows that the fluid-source overpressure increases slowly (logarithmically) with time, such that Δp_w can be taken as approximately constant and equal to Δp_c (Eq. (2)). Therefore, we can approximate the fracture energy (46) as

$$G_c \approx \kappa\left(f_p - f_r\right)\delta_c\left(\sigma'_0 - \Delta p_c\right), \tag{51}$$

which is constant as well. Again, all the results and insights from the constant fracture energy model are inherited now in this regime. Particularly, the so-called marginally pressurized regime as quantified by the residual stress-injection parameter ($\mathcal{T}_r \sim 10$) is the one related to $\lambda(t) \ll 1$. We recall that this marginally pressurized regime is not defined exactly as the one emerging during the early-time Coulomb's friction stage. The latter is defined by the condition $f_p\Delta p_c \approx f_p\sigma'_0 - \tau_0$, whereas the former relates to the residual friction coefficient instead, $f_r\Delta p_c \approx f_r\sigma'_0 - \tau_0$. We use the same name for these two regimes, yet there is this subtle difference between them.

By introducing (51) into (24)b via (11), and then (24)b into (28)b, we obtain the dimensionless form of the front-localized energy balance in the marginally-pressurized regime,

$$\Psi(\lambda) - \mathcal{T}_r = \frac{\sqrt{\pi}}{2}\sqrt{2\kappa}\frac{1}{\sqrt{R/R^*_{mp}}}, \tag{52}$$

with

$$\frac{R^*_{mp}}{R_w} = \frac{\left(f_p - f_r\right)^2\sigma'_0\left(\sigma'_0 - \Delta p_c\right)}{\left(f_r\Delta p_*\right)^2} \approx \left(\frac{1-\mathcal{F}}{\mathcal{F}\mathcal{P}}\right)^2(1 - 10\mathcal{P}). \tag{53}$$

In the latter equation, we have replaced the factor 4π by 10 as usual in the marginally pressurized limit to keep the spirit of the order-of-magnitude approximation behind Δp_c when representing the fluid-source overpressure. Alternatively, Eqs. (52) and (53) can be derived by approximating the term $\mathcal{P}E_1\left(\lambda^2\right) \approx 10\mathcal{P}$ in (47) and then dividing the latter by $\mathcal{F}\mathcal{P}$. Moreover, by using the asymptotic behavior of $\Psi(\lambda)$ for small λ, Eq. (33) provides an implicit equation for the normalized rupture radius R/R^*_{mp} as a function of the normalized square root of time $\sqrt{4\alpha t}/R^*_{mp}$ and the residual stress-injection parameter $\mathcal{T}_r$, provided that R^*_{mp} is replaced by (53).

The meaning of the rupture length scales R^*_{nu} and R^*_{mp} are the same as in the constant fracture energy model. Essentially, when $R \ll R^*$, the fracture energy plays a dominant role in the near-front energy balance. This is the large-toughness regime. On the other hand, when $R \gg R^*$, the fracture energy becomes increasingly less relevant in the rupture-front energy budget, corresponding to the small-toughness regime. Hence, likewise in the constant fracture energy model, unconditionally stable ruptures in the slip-weakening model will always transition from a large-toughness to a small-toughness regime. This transition is shown in Fig. 3c and d for both nearly unstable and marginally pressurized faults, respectively, with R^*_{nu} and R^*_{mp} as in Eqs. (50) and (53).

5.3. Ultimate zero-fracture-energy similarity solution

By taking the ultimate limit $R/R^* \to \infty$ in Eqs. (49) and (52), it is evident that the fracture-energy term in the energy balance (the right-hand side) vanishes for both the nearly unstable ($\mathcal{T}_r \ll 1$) and marginally pressurized regimes ($\mathcal{T}_r \sim 10$). Hence, in this limit, Eqs. (49) and (52) become simply

$$\Psi(\lambda) = \mathcal{T}_r, \tag{54}$$

which is exactly the rupture propagation condition of the constant friction model (Eq. (16)) but with a constant friction coefficient f_{cons} equal to the residual one f_r. The self-similar constant friction model is therefore the ultimate asymptotic solution of the slip-weakening model, provided that $f_{\text{cons}} = f_r$. The transition from the small-toughness regime to the constant residual friction solution, also denominated as ultimate zero-fracture-energy solution, is shown in Fig. 3c and d for both nearly unstable and marginally pressurized faults, respectively. Note that one could alternatively define a dimensionless toughness $\mathcal{K}$ for both regimes ($\lambda(t) \gg 1$ and $\lambda(t) \ll 1$) as in Section 3.2 (Eq. (24)) to show the same type of transition than in Fig. 3a–b, since the solution for the amplification factor can be written as $\lambda\left(\mathcal{T}_r, \mathcal{K}(t)\right)$. Such a dimensionless toughness will always decrease with time and ultimately tend to zero, $\mathcal{K} \to 0$.

Finally, using the constant residual friction solution λ_r, one can estimate as done in Section 3.2 (Eq. (34)) the transition timescales between the large-toughness and small-toughness regimes, which results in

$$t^*_{nu} \approx \frac{\left(R^*_{nu}\right)^2}{\alpha \lambda_r^2}, \text{ and } \quad t^*_{mp} \approx \frac{\left(R^*_{mp}\right)^2}{\alpha \lambda_r^2}. \tag{55}$$

6. The nucleation phase preceding a dynamic rupture

Fig. 7 displays the case of ultimately unstable ruptures: $f_r \sigma'_0 < \tau_0$. Again, without loss of generality, we fix the residual-to-peak friction ratio as $\mathcal{F} = 0.7$, and examine the parameter space for $\mathcal{P}$ and now $\mathcal{S} > 0.7$, for both versions of the slip-weakening friction law. The case of an overpressure ratio $\mathcal{P} = 0.1$ which corresponds to an injection that is about to open the fault, is shown in Fig. 7a and b. For all values of $\mathcal{S}$ in these figures, we observe the nucleation of a dynamic rupture that runs away and never stops within the limits of our model, this is, the regime R3 in Fig. 4. On the other hand, the case of a lower overpressure ratio $\mathcal{P} = 0.05$ is shown in Fig. 7c and d. For the linear weakening model, we observe the occurrence of both regimes R3 and R4 of Fig. 4. The latter corresponds to cases in which a dynamic rupture nucleates, propagates, and arrests, with a new rupture instability nucleating afterward on the same fault, which is ultimately unstable (run-away). Moreover, in Fig. 7d for the exponential weakening version of the friction law, we do not observe the regime R4, at least for the numerical solutions we include in this figure.

6.1. Early-time Coulomb's friction stage and acceleration towards rupture instability

Similarly to the case of ultimately stable ruptures, here, unstable ruptures are also well-described by the Coulomb's friction model at early times (see Fig. 7). Therefore, the rupture radius evolves approximately as Eq. (45), with λ_p given by Eq. (17) considering the peak stress-injection parameter $\mathcal{T}_p$. Moreover, Fig. 7 also shows that during the nucleation phase, the slip front may largely outpace the overpressure front ($\lambda_p \gg 1$) when faults are critically stressed as quantified by the peak stress-injection parameter ($\mathcal{T}_p \ll 1$), or significantly lag the overpressure front ($\lambda_p \ll 1$) when faults are marginally pressurized ($\mathcal{T}_p \sim 10$). Fig. 8d and e display, on the other hand, the spatial distribution of the friction coefficient for critically stressed and marginally pressurized cases, respectively. We can clearly observe that at the Coulomb's friction stage, $f/f_p \approx 1$ throughout most of the slipping region. Note that in this stage, we could also approximate the spatio-temporal evolution of fault slip in the critically stressed and marginally pressurized regimes, using the analytical asymptotic expressions derived by Sáez et al. (2022) (equations (25) and (26) in Sáez et al. (2022)), provided that $f_{\text{cons}} = f_p$. The same can be done for the ultimate zero-fracture-energy solution of ultimately stable ruptures, with $f_{\text{cons}} = f_r$.

Now, beyond this early-time stage, the propagation of the slip front starts departing from the Coulomb's friction similarity solution due to the further weakening of friction. The latter can be seen in Fig. 8d and e for intermediate times (t_2) and times close to nucleation (t_c). The slip front accelerates indeed towards the nucleation of a dynamic rupture. Fig. 7 shows that the rupture radius at the instability time increases with decreasing pre-stress ratio $\mathcal{S}$ and increasing overpressure ratio $\mathcal{P}$, for both versions of the friction law. This is consistent with the extensive analysis of earthquake nucleation provided by Garagash and Germanovich (2012) for the two-dimensional, linear weakening model. Moreover, Fig. 7 also displays that one of the main effects of the exponential weakening version of the friction law is to smooth the transition of the rupture towards the dynamic instability with regard to the linear law. Furthermore, the exponential law retards the instability time and generally increases the critical radius for the rupture to become unstable. Such effect of the exponential law becomes stronger when the pre-stress ratio $\mathcal{S}$ decreases towards its minimum value in the ultimately unstable case, this is, the ultimate stability limit $\mathcal{S} = \mathcal{F}$.

Given the importance of the nucleation radius to characterize the maximum size that quasi-static ruptures can afford in the ultimately unstable case, we calculate in the next sections theoretical bounds for it, following the procedure of Uenishi and Rice (2002) and Garagash and Germanovich (2012). This corresponds to an extension of their results from the two-dimensional (mode II or III) fault model to the three-dimensional circular (modes II+III) configuration.

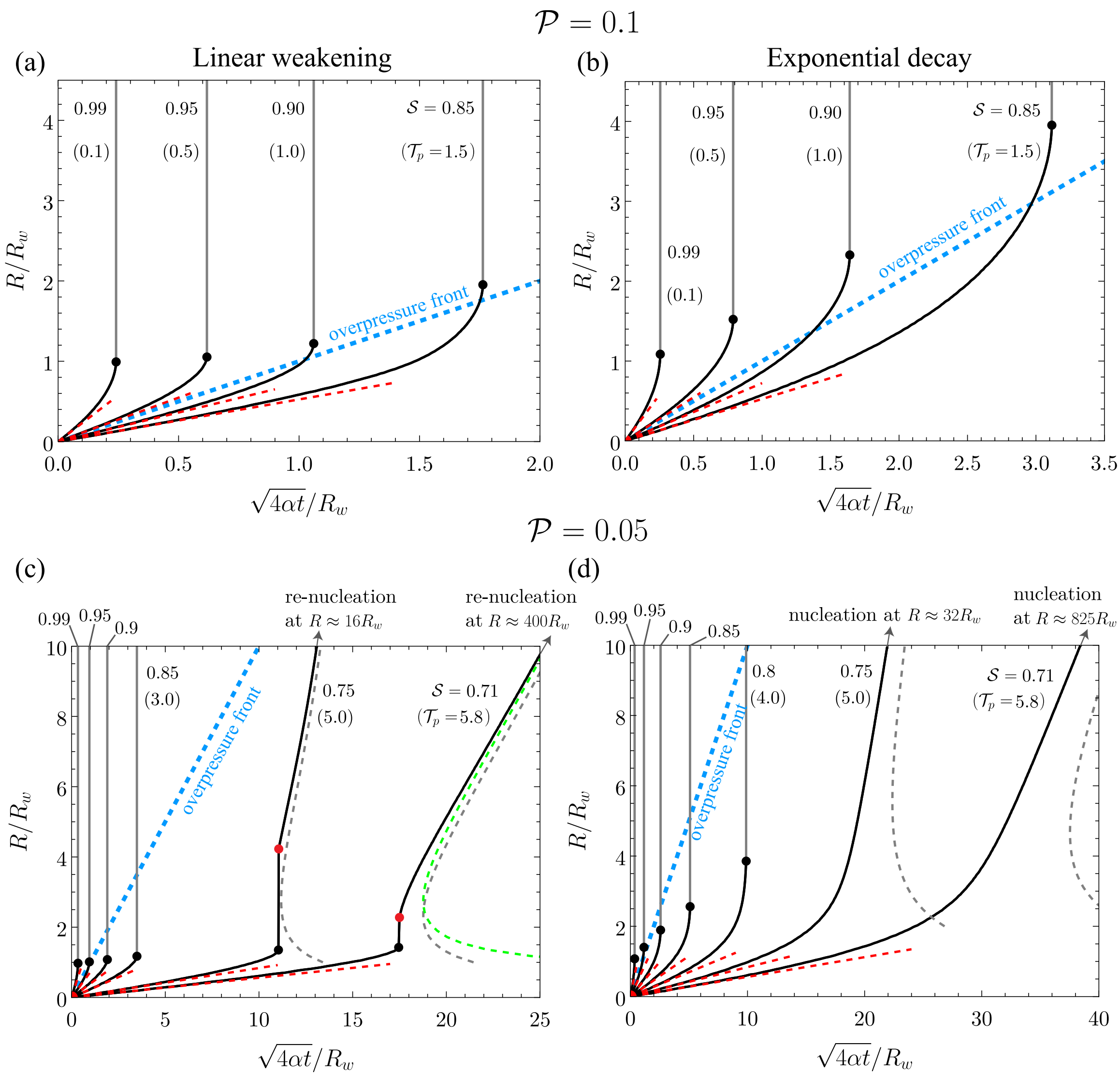

Fig. 7. Ultimately unstable faults, $\mathcal{S} > \mathcal{F} = 0.7$. Normalized rupture radius versus square root of dimensionless time for (left) linear weakening and (right) exponential decay versions of the slip weakening friction law. (a, b) $\mathcal{P} = 0.1$ and (c, d) $\mathcal{P} = 0.05$. Black and red circles indicate the nucleation and arrest of a dynamic rupture, respectively. Red dashed lines correspond to the analytical Coulomb's friction model considering the peak friction coefficient. In (c) and (d), gray dashed lines represent the near-front energy balance solution. In (c), the green dashed line corresponds to an improved energy-balance solution as explained in the main text.

6.2. Theoretical bounds for the nucleation radius

6.2.1. Critically stressed and marginally pressurized limits

Equilibrium dictates that within the slipping region $r \leq R(t)$, the fault strength τ_s (3) must be locally equal to the fault shear stress τ (6). Equating the two previous equations and then differentiating with respect to time, leads to (see Appendix A for further details)

$$v\,(r,t)\,\frac{\mathrm{d}f}{\mathrm{d}\delta}\left[\sigma_0' - \Delta p(r,t)\right] - f(\delta)\frac{\partial \Delta p(r,t)}{\partial t} = -\frac{\mu}{2\pi}\int_0^{R(t)} F\,(r,\xi)\,\frac{\partial v(\xi,t)}{\partial \xi}\mathrm{d}\xi, \tag{56}$$

where $v = \partial\delta/\partial t$ is the fault slip rate. When differentiating the integral term previously, we have considered Leibniz's integral rule and applied the condition of having non-singular shear stresses along the rupture front.

We focus now on the critically stressed ($\mathcal{T}_p \ll 1$) and marginally pressurized ($\mathcal{T}_p \sim 10$) limits. Here, both limiting cases are characterized by small slip at the nucleation time t_c, $\delta(r = 0, t_c) \ll \delta_c$ (see, for example, Fig. 8). This latter was also found by Garagash and Germanovich (2012) in their two-dimensional model. Moreover, it takes just a simple Taylor expansion to show that in this

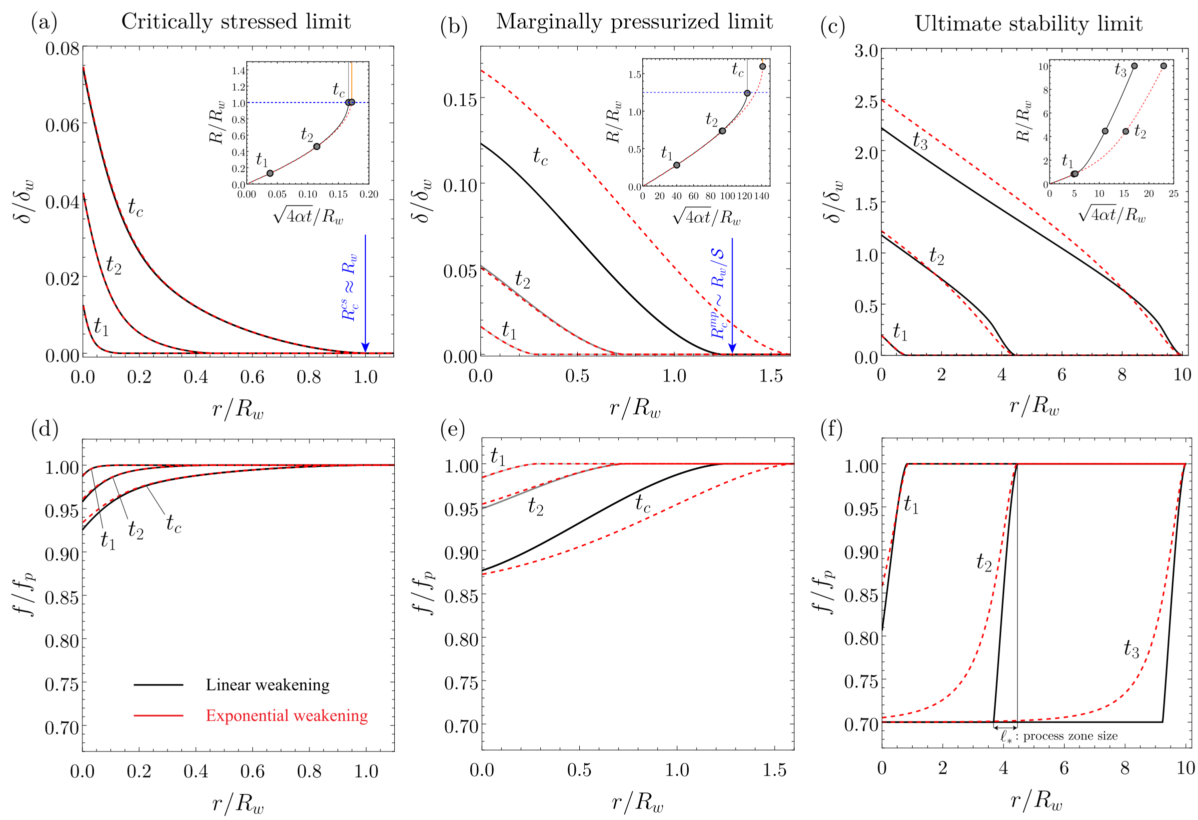

Fig. 8. (a, b, c) Normalized spatial distribution of slip at the times indicated in the insets and commented in the main text. Insets: normalized rupture radius as a function of the normalized squared root of time. Blue arrows in (a) and (b) represent the theoretical prediction for the nucleation radius in the critically stressed and marginally pressurized limits. (d, e, f) Spatial profile of the normalized friction coefficient at the same times indicated previously. (Left) Critically stressed limit, $\mathcal{S} = 0.995$, $\mathcal{P} = 0.1$, $\mathcal{F} = 0.7$, and associated $\mathcal{T}_p = 0.05$. (Center) Marginally pressurized limit, $\mathcal{S} = 0.8$, $\mathcal{P} = 0.02$, $\mathcal{F} = 0.7$, and associated $\mathcal{T}_p = 10$. (Right) Ultimate stability or nearly stable limit, $\mathcal{S} = 0.71$, $\mathcal{P} = 0.075$, and $\mathcal{F} = 0.7$.

range of slip, the exponential weakening version of the friction law is, to first order in δ/δ_c, asymptotically equal to the linear weakening case. Hence, the term $\mathrm{d}f/\mathrm{d}\delta$ can be simply approximated as $-(f_p - f_r)/\delta_c$ for both friction laws.

Following Uenishi and Rice (2002), at the instability time t_c, the slip rate diverges all over the fault plane, such that the only non-vanishing terms in Eq. (56) are the first term on the left-hand side and the integral term on the right-hand side. Considering the previous linear approximation for $\mathrm{d}f/\mathrm{d}\delta$, the relation (36) $\mu\delta_c = (f_p - f_r)\sigma_0' R_w$, and the following non-dimensional quantities: $\bar{r} = r/R$, $\bar{\xi} = \xi/R$, and $\bar{v} = v/v_{\mathrm{rms}}$, with v_{rms} the root mean square of the slip rate distribution given by Eq. (69), one can show (details in Appendix A.1) that the time derivative of the balance of momentum (56) can be written as the following generalized eigenvalue problem:

$$\frac{R}{R_w}\bar{v}(\bar{r})\frac{\sigma'(\bar{r}R)}{\sigma_0'} = \frac{1}{2\pi}\int_0^1 F\left(\bar{r},\bar{\xi}\right)\frac{\partial \bar{v}(\bar{\xi})}{\partial \bar{\xi}}\mathrm{d}\bar{\xi}, \tag{57}$$

which corresponds to the mixed-mode, circular rupture version of equation (14) in Garagash and Germanovich (2012). Note that in Appendix A.1, we derive Eq. (57) under more general statements. Moreover, it is shown in Appendix A.2 that in the critically stressed and marginally pressurized regimes, the generalized eigenvalue problem (57) can be approximated by the following regular eigenvalue problem:

$$\frac{1}{2\pi}\int_0^1 F\left(\bar{r},\bar{\xi}\right)\frac{\partial \bar{v}(\bar{\xi})}{\partial \bar{\xi}}\mathrm{d}\bar{\xi} = \beta\bar{v}(\bar{r}), \tag{58}$$

where the eigenvalue

$$\beta = \frac{R}{R_w}\cdot\begin{cases} 1 & \text{for critically stressed faults } \mathcal{T}_p \ll 1 \\ \tau_0/f_p\sigma_0' & \text{for marginally pressurized faults } \mathcal{T}_p \sim 10. \end{cases} \tag{59}$$

Note that in Eqs. (57)–(59), the dependence of $\bar{v}$ and R on the instability time t_c has been omitted for simplicity.

The solution of (58) for the eigenvalues and eigenfunctions is calculated in Appendix A.3. This is done by discretizing the linear integral operator on the left-hand side of (58) via a collocation boundary element method using piece-wise ring 'dislocations' of constant slip rate. The most important result is the smallest eigenvalue β_1, which was shown by Uenishi and Rice (2002) for the two-dimensional problem to give the critical nucleation radius. We find (see Table 1)

$$\beta_1 \approx 1.003, \tag{60}$$

which is interestingly, for all practical purposes, approximately equal to one. Taking hereafter $\beta_1 \approx 1$, the nucleation radius is recovered from Eq. (59) as

$$R_c^{cs} \approx R_w \tag{61}$$

for critically stressed faults ($\mathcal{T}_p \ll 1$, vertical line $\mathcal{S} = 1$ on the right side of Fig. 4), and

$$R_c^{mp} \approx \frac{f_p \sigma_0'}{\tau_0} R_w = \frac{R_w}{\mathcal{S}}, \tag{62}$$

for marginally pressurized faults ($\mathcal{T}_p \sim 10$, inclined line $\mathcal{P} \approx 10^{-1}(1 - \mathcal{S})$ in Fig. 4).

The theoretical estimates (61) and (62) are compared to numerical solutions that are representative of each limiting regime in Fig. 8a and b, respectively. In these figures, the blue arrows indicate the theoretical radii at the instability time t_c. We highlight that the critically stressed nucleation radius (61) is a proper asymptote that is always reached in the limit $\tau_0 \to f_p\sigma_0'$, up to the numerical approximation made for the eigenvalue (60). On the other hand, the marginally pressurized nucleation radius (62) can be defined only in an approximate sense due to the reasons explained in Appendix C. Although this approximation seems to be quite accurate for the linear weakening law (see Fig. 8b), the exponential decay version does not seem to follow this trend. This is likely due to the additional assumption of small slip that the exponential weakening law requires in order to be well approximated by a linear relation. In the example of Fig. 8b, slip does not seem to be small enough. Because of the approximate nature of the marginally pressurized limit, it is challenging to find the model parameters that will result in sufficiently small slip at the nucleation time for the linear approximation of the exponential weakening law to be valid. Furthermore, Eqs. (61) and (62) suggest that the minimum possible nucleation radius is the one associated with critically stressed faults (61), whereas the greatest possible nucleation radius can be as large as infinity for marginally pressurized faults (62), in the limit of zero pre-stress $\tau_0 \to 0$. Yet such a limit corresponds indeed to an ultimately stable rupture, specifically, a case in which the fault is about to open (top left corner of Fig. 4) so that the dynamic rupture will eventually arrest and then propagate ultimately in a quasi-static manner. Moreover, as shown in Appendix A, the nucleation radius in the critically stressed limit (61) is independent of the specific form of the spatio-temporal evolution of pore pressure, that is, Eq. (61) is also valid for other types of fluid injections than the constant volumetric rate considered here. On the other hand, the nucleation radius in the marginally pressurized limit (62) is, under certain conditions (details in Appendix A.2), also independent of the injection scenario.

Finally, it is also shown in Appendix A that the critically stressed nucleation radius (61) is itself an extension of the nucleation length of Uenishi and Rice (2002) (found also previously by Campillo and Ionescu (1997) under different assumptions) from their two-dimensional fault model to the three-dimensional axisymmetric configuration. Since for the shear mixed-mode (II+III) rupture, the circular front shape is strictly valid only when $\nu = 0$, our results could be used in combination with perturbation techniques such as the work of Gao (1988) to characterize the corresponding non-circular slipping region at the nucleation time of a shear rupture for $\nu \neq 0$. Indeed, since the work of Gao (1988) is based on linear elastic fracture mechanics (valid in the small-scale yielding limit) and the nucleation radius (61) (and (62)) is smaller than the process zone size, one should rather consider a variational approach as the one proposed recently by Lebihain et al. (2022) for cohesive cracks based on the perturbation of crack face weight functions. The approach of Gao (1988) would still be useful to characterize non-circularity in the nearly stable limit of the next section. This would provide an alternative to the work of Uenishi (2018) who considered a simplified energy approach based on a Rayleigh–Ritz approximation while fixing the rupture shape to an ellipse. An elliptical rupture shape may be a very good approximation for a shear rupture (Sáez et al., 2022), yet not necessarily the actual equilibrium shape. In the circular limit ($\nu = 0$), the approximate results of Uenishi (2018) can be compared to our solution, which is exact up to the numerical approximation for the smallest eigenvalue $\beta_1 \approx 1.003$. In our notation, Uenishi's results give $R_c^{cs} \approx 0.980 R_w$ (Eq. (16) or Eq. (20) with $\nu = 0$ in Uenishi (2018)). This means a difference of about 2.3% with regard to our exact solution, which is in the same order as the difference between the exact solution in the two-dimensional problem (Uenishi and Rice, 2002) and the same type of energy-based approximation in 2D (Rice and Uenishi, 2010). It is also informative to compare our results with the numerical work on three-dimensional shear rupture instability by Favreau et al. (2002). In this study, they considered a linear slip-weakening fault of *a priori* fixed size (and shape). Considering again the case $\nu = 0$ and switching to our notation, their results give after some manipulations, $R_c^{cs} \approx ((1.2 \pm 0.05)\pi/4) R_w$. The sign $\pm$ comes from the numerical precision associated with their finite difference scheme. The previous expression results in a range of values for $R_c^{cs}/R_w \approx 0.903 - 0.982$. The upper bound of this range is close to the estimate of Uenishi (2018), which is closer to our exact solution.

We would like to finally mention that the nucleation radius (61) is also valid for a tensile (mode I) rupture. In this case, it is indeed valid for any value of ν, as long as the shear modulus μ is replaced by the quantity $\mu/(1-\nu)$ and the load driving the rupture growth is peaked around the crack center and axisymmetric in magnitude. Further details about this generalization of our results can be found in Appendix A.

6.2.2. Nearly stable limit

Fig. 7c and d show that the nucleation radius of ultimately unstable ruptures becomes very large, $R(t_c) \gg R_w$, when approaching the ultimate stability condition $f_r\sigma_0' \to \tau_0$ (vertical line $\mathcal{S} = \mathcal{F}$ in Fig. 4). Specifically, Fig. 7c displays a case of large re-nucleation radius (regime R4) in the linear weakening model for $\mathcal{S} = 0.71$ ($\mathcal{F} = 0.7$), whereas Fig. 7d shows an example of large nucleation radius for the exponential weakening model and the same parameters than before. In the two-dimensional model, Garagash and Germanovich (2012) not only found this same behavior but provided also an asymptote for the nucleation length in this limit, that we also derive here for the circular rupture model.

First, let us note that the condition $R(t_c) \gg R_w$ implies also that $R(t_c) \gg \ell_*$, since the process zone size ℓ_* for the linear weakening model is roughly around the same order than the elasto-frictional lengthscale R_w, and about an order of magnitude larger in the case of the exponential weakening law. Hence, we can invoke the front-localized energy balance, Eq. (14). Indeed, Fig. 7c and d display such energy-balance solution for some ruptures that are on their way to becoming unstable. On the other hand, near the ultimate stability limit, $R(t_c)$ is also much bigger than the radius of the overpressure front $L(t_c)$, such that $\lambda(t_c) \gg 1$. Therefore, we can approximate the equivalent shear load associated with the fluid source as a point force via Eq. (19). The corresponding axisymmetric stress intensity factor for such a point force comes from resolving the integral of the left-hand side of Eq. (14) considering (19) and $f_{\text{cons}} = f_r$, which gives

$$K_p = \frac{f_r \Delta P(t)}{(\pi R)^{3/2}} \tag{63}$$

with $\Delta P(t) = 4\pi\alpha t \Delta p_*$. Substituting the previous equation into (14) leads to the following form of the front-localized energy balance,

$$\underbrace{\frac{f_r \Delta P(t)}{(\pi R)^{3/2}}}_{K_p} + \underbrace{\frac{2}{\sqrt{\pi}}\left[\tau_0 - f_r\sigma_0'\right]\sqrt{R}}_{K_\tau} = K_c, \tag{64}$$

where the fracture toughness $K_c = \sqrt{2\mu G_c}$ is, after combining Eqs. (36) and (48), equal to

$$K_c = (f_p - f_r)\sigma_0'\sqrt{2\kappa R_w}. \tag{65}$$

We recall that the coefficient κ is equal to $1/2$ for the linear weakening friction law and 1 for the exponential weakening case. Moreover, the fracture toughness K_c is constant due to the negligible overpressure within the process zone when $\lambda \gg 1$.

By differentiating Eq. (64) with respect to time and then dividing by the rupture speed $\dot{R}$ on both sides, one can show upon taking the limit at the nucleation time: $R \to R_c$ and $\dot{R} \to \infty$, that $K_p = K_\tau/3$. Substituting this previous relation into (64) allows us to eliminate $\Delta P(t_c)$ and so the instability time t_c in the equation, leading to the sought critical nucleation radius:

$$\frac{R_c^\infty}{R_w} \simeq \frac{9\pi\kappa}{32}\left(\frac{f_p\sigma_0' - f_r\sigma_0'}{\tau_0 - f_r\sigma_0'}\right)^2 = \frac{9\pi\kappa}{32}\left(\frac{1-\mathcal{F}}{\mathcal{S}-\mathcal{F}}\right)^2, \text{ when } f_r\sigma_0' \to \tau_0. \tag{66}$$

Note that the previous equation is a proper asymptote due to the small-scale yielding approximation. In addition, the relation $K_p = K_\tau/3$ plus the previous expression for R_c^∞ can provide together an expression for the nucleation time t_c. Indeed, expressions for the instability time t_c in the critically stressed and marginally pressurized limits might be also obtainable analytically (see, for instance, the asymptotic analysis conducted by Garagash and Germanovich (2012)), yet we do not attempt to pursue this route in this paper. We also note that except by a pre-factor of order unity, the nucleation length (66) is equal to the fracture-mechanics-based nucleation length obtained by Andrews (1976) in its two-dimensional analysis and by Day (1982) after in a three-dimensional work. The difference in the pre-factor is of course due to the different load driving the rupture at the instability time.

7. Discussion

7.1. Frustrated dynamic ruptures and unconditionally stable slip: the two propagation modes of injection-induced aseismic slip

In our model, injection-induced aseismic slip can be the result of either a frustrated dynamic rupture that did not reach the required size to become unstable, or the propagation of slip that is unconditionally stable. Whether injection-induced aseismic ruptures occur in one regime or the other, depends primarily on the ultimate stability condition of Garagash and Germanovich (2012), which we demonstrated here to be applicable to the circular rupture configuration as well (Eq. (44)).

7.1.1. Unconditionally stable ruptures

When the initial shear stress τ_0 is lower than the in-situ residual fault strength, $\tau_0 < f_r\sigma_0'$, faults tend to produce mostly unconditionally stable ruptures (regime R1 in Fig. 4), except for a relatively narrow range of parameters where the nucleation of a dynamic rupture occurs, followed by arrest and purely quasi-static slip (regime R2 in Fig. 4). We found that unconditionally stable ruptures evolve always between two similarity solutions (see Fig. 9). At early times (stage I), they behave as being governed by Coulomb's friction, that is, a constant friction coefficient equal to the peak value f_p. During this initial stage, fault slip is self-similar in a diffusive manner and is governed by one single dimensionless number: the peak stress-injection parameter $\mathcal{T}_p$. After, the response of the fault gets more complex in stages II and III yet ultimately, slip recovers the same type of similarity at very large times (stage

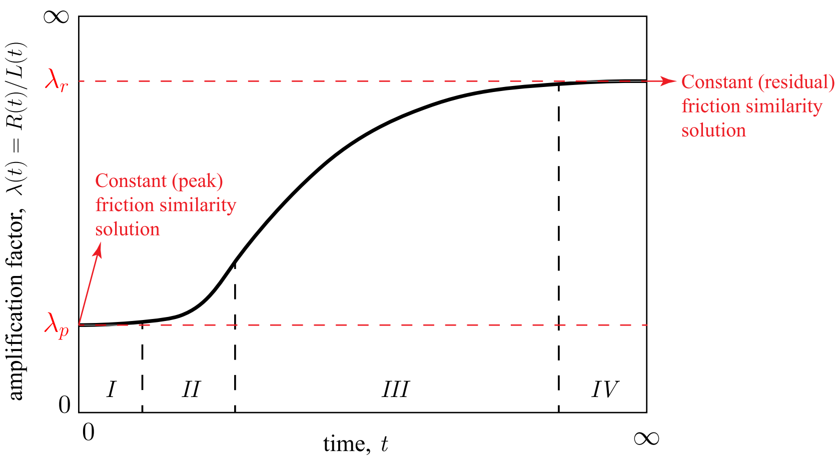

Fig. 9. Schematic solution for unconditionally stable ruptures undergoing four distinct stages in time. Stage (I), Coulomb's friction similarity solution, $f_{\text{cons}} = f_p$. Stage (II), acceleration due to frictional weakening and localization of the process zone. Stage (III), rupture is governed by an energy balance of the Griffith's type, $G = G_c$, transitioning from a large-toughness to a small-toughness regime. Stage (IV), ultimate constant residual friction similarity solution, $f_{\text{cons}} = f_r$, also denominated ultimate zero-fracture-energy solution. Note that in the case of aseismic slip as a frustrated dynamic instability, stage I is always present, while stages II and III might be experienced to different extents depending on how large the nucleation radius is compared to the process zone size.

IV). In this ultimate regime, the rupture behaves as if it were governed by a constant friction coefficient equal to the residual one f_r, and depends also on one single dimensionless number: the residual stress-injection parameter $\mathcal{T}_r$. An interesting characteristic in both limiting regimes is that the rupture propagates as having zero fracture energy G_c. While at early times $G_c = 0$ in an absolute sense as the process zone has not developed yet, at large times the contribution of the finite fracture energy to the rupture-front energy balance is to leading order negligible compared to the other terms that drive the propagation of the rupture. Furthermore, the two similarity solutions are equivalent to the analytical solution for a constant friction coefficient derived in Sáez et al. (2022), as long as the so-called stress-injection parameter $\mathcal{T}$ in Sáez et al. (2022) is replaced by $\mathcal{T}_p$ at early times and $\mathcal{T}_r$ at large times, which are then associated with constant amplification factors λ_p and λ_r, respectively, as shown in Fig. 9. This is a key finding of our work as it puts the results of the former constant-friction model of Sáez et al. (2022) in a more complete picture of the problem of injection-induced aseismic slip.

In between the two similarity solutions, fault slip undergoes two subsequent stages. First, after departing from the Coulomb's friction solution, the rupture accelerates due to frictional weakening (stage II). The details of the friction law matter here as the rupture radius is of the same order as the process zone size. The exponential weakening law tends to slow down the propagation of slip and smooth the acceleration phase with regard to the linear weakening case when considering the same δ_c in both laws. Fault slip depends in addition to dimensionless space and time, on three non-dimensional parameters: the pre-stress ratio $\mathcal{S}$, the overpressure ratio $\mathcal{P}$, and the residual-to-peak friction ratio $\mathcal{F}$. The higher the initial shear stress on the fault is (higher $\mathcal{S}$) or the more intense the injection is (higher $\mathcal{P}$), the faster the rupture propagates. Note that this dependence of the rupture speed on $\mathcal{S}$ and $\mathcal{P}$ is embedded in both the peak stress-injection parameter $\mathcal{T}_p$ and residual stress-injection parameter $\mathcal{T}_r$. Therefore, it is a general feature present in all stages of injection-induced aseismic slip.

In a subsequent stage, once the process zone has adequately localized, the evolution of the slip front is well approximated by the rupture-front energy balance (stage III). The details of how the friction coefficient weakens from its peak value towards its residual value no longer matter in relation to the position of the slip front or the rupture speed. The only two important quantities here associated with the friction law are: the amount of fracture energy that is dissipated near the rupture front, and the residual friction coefficient f_r. Moreover, the fracture energy is approximately constant (albeit of different magnitude) in the two end-member cases of nearly unstable ($\lambda(t) \gg 1$) and marginally pressurized faults ($\lambda(t) \ll 1$), with the amplification factor λ depending on only two dimensionless numbers: a time-dependent dimensionless toughness $\mathcal{K}(t)$ and the residual stress-injection parameter $\mathcal{T}_r$. A constant fracture energy model as the one introduced in Section 3.2 is thus sufficient to capture the dynamics of the slip front for the two end members. The dimensionless toughness $\mathcal{K}(t)$ quantifies the relevance of the dissipation of fracture energy in the rupture-front energy balance, which decreases monotonically with time. The rupture speed thus increases with time as the diminishing effect of the fracture energy offers less 'opposition' for the rupture to advance. Eventually, $\mathcal{K}(t) \to 0$ when $t \to \infty$ and the rupture reaches asymptotically the large-time similarity solution (stage IV), where the only information about the friction law that matters is f_r.

On the other hand, the residual stress-injection parameter $\mathcal{T}_r$ plays a crucial role in stages III and IV. When faults are near the ultimate stability limit ($\mathcal{T}_r \to 0$) thus responding in the so-called nearly unstable regime ($\mathcal{T}_r \ll 1$), the slip front always outpaces the overpressure front $\lambda(t) \gg 1$, even though at early times (stage I) the rupture front would likely lag the overpressure front $\lambda(t) \ll 1$. Conversely, when faults operate in the so-called marginally pressurized regime ($\mathcal{T}_r \sim 10$), the slip front will always move much slower than the overpressure front, $\lambda(t) \ll 1$, over the entire lifetime of the rupture: the slip front will never outpace the overpressure front.

Finally, it is worth mentioning that in our fault model, the in-situ fracture energy $G_c^0 = \kappa(f_p - f_r)\sigma_0'\delta_c$ is constant. In fracture experiments, the fracture energy is however known to increase with crack size, with micro-cracking and plastic deformations among the mechanisms thought to explain such a scale dependence (e.g., Lawn, 1993). Similarly in earthquakes, seismological observations suggest that the fracture energy increases with slip or fault size (Abercrombie and Rice, 2005; Viesca and Garagash, 2015; Gabriel et al., 2023). To the best of our knowledge, there are no experimental or observational works supporting a similar behavior for slow frictional ruptures. Nevertheless, one may expect this behavior to be also present in aseismic slip. This could potentially change the propagation regimes and stages that we have identified for unconditionally stable ruptures. A similar effect has been quantified, for instance, for fluid-driven opening fractures (Liu et al., 2019). To gain some insights into this potential effect in our model, let us consider a power-law relation in the form $G_c^0 \propto R^m$, and thus a fracture toughness $K_c \propto R^{m/2}$, where R is the rupture radius. Considering that the dimensionless toughness $\mathcal{K}(t)$ decreases with the square root of the rupture radius (Eq. (24)), one would expect that for $0 \leq m < 1$, the general picture of the stages summarized in Fig. 9 would remain the same. Perhaps, the only difference would be that the transition from the large-toughness to the small-toughness regime, and then to the ultimate zero-fracture-energy solution, would occur later. The limiting case of $m = 1$ seems interesting. Here, according to (24), the dimensionless toughness $\mathcal{K}(t)$ would be rather constant, implying that no ultimate zero-fracture-energy solution could be attained. Finally, in cases where $m > 1$, the dimensionless toughness may rather increase with time. As a consequence, the four-stage picture of Fig. 9 may significantly change and, perhaps, even a transition towards a regime in which the fracture energy becomes increasingly more relevant in the rupture-front energy balance with time may emerge. Note that this simplified analysis is somewhat tentative at this point, yet it already highlights the possible implications of considering a model with scale-dependent fracture energy. However, we should also keep in mind that quantitative observations at different scales are currently lacking on this matter.

7.1.2. Aseismic slip as a frustrated dynamic instability

When the initial shear stress τ_0 is greater than the in-situ residual fault strength, $\tau_0 > f_r \sigma_0'$, faults will always host a dynamic event, sometimes even more than one (regime R4 in Fig. 4) if the injection is sustained for sufficient time. The maximum size that aseismic ruptures can reach before becoming unstable is as small as the elasto-frictional length scale R_w for faults that are critically stressed, and as large as infinity for faults that are either marginally pressurized and about to open, or near the ultimate stability limit (so-called nearly stable faults). The spatial range for a fault to exhibit aseismic slip as a frustrated dynamic instability is therefore extremely broad. Moreover, similarly to the case of unconditionally stable ruptures, the quasi-static nucleation phase is governed at early times by the Coulomb's friction similarity solution with $f_{\text{cons}} = f_p$ (stage I in Fig. 9). Aseismic ruptures can therefore move much faster than the diffusion of pore pressure right after the start of fluid injection when faults are critically stressed according to the peak stress-injection parameter ($\mathcal{T}_p \ll 1$, $\lambda_p \gg 1$), or propagate much slower than that when faults operate in the so-called marginally pressurized regime ($\mathcal{T}_p \sim 10$, $\lambda_p \ll 1$). After, depending on how large the nucleation radius is with regard to the process zone size, aseismic ruptures may be able to either partially or fully explore stages II and III on their way to reach their critical unstable size. In stage II, the rupture behavior is the same as described in the previous section for unconditionally stable ruptures. Moreover, if the critical nucleation radius is sufficiently large compared to the process zone size, the rupture could transit stage III where the propagation of the slip front is well approximated by an energy balance of the Griffith's type, similarly to stage III of unconditionally stable ruptures.

Finally, it is worth noting that critically stressed faults ($\mathcal{T}_p \ll 1$) and marginally pressurized faults ($\mathcal{T}_p \sim 10$) nucleate dynamic ruptures with very little decrease in the friction coefficient, far from reaching the residual friction value over the entire slipping region at the instability time. Conversely, nearly stable ruptures ($\mathcal{T}_r \ll 1$) undergo dynamic nucleation in a 'crack-like' manner, that is, with a small process zone where the fracture energy is dissipated and the remaining much larger part of the 'fracture' (slipping area) is at the residual friction level. In between these two limiting behaviors of dynamic rupture nucleation, a continuum of instabilities are spanned in our model; a result already found by Garagash and Germanovich (2012) and also present in heterogeneous, mechanically-loaded slip-weakening frictional interfaces (Castellano et al., 2023). With regard to the friction law, the exponential weakening case tends to produce larger nucleation radii. When nucleation occurs unaffected by the residual friction coefficient, this effect is likely due to the decreasing weakening rate with slip of the exponential weakening law that tends to increase the critical nucleation radius compared to the constant (and always greater) weakening rate of the linear weakening case (see Fig. 2). When nucleation occurs in a crack-like manner, this is essentially due to the larger fracture energy ($G_c^{\text{exp}} = 2G_c^{\text{lin}}$) required to be dissipated at the instability time.

7.2. Laboratory experiments

Laboratory experiments of injection-induced fault slip on rock samples where a finite rupture grows along a pre-existing interface (Passelègue et al., 2020; Cebry et al., 2022) have recently confirmed some insights predicted by theory. For instance, the meter-scale experiments of Cebry et al. (2022) showed that the closer to frictional failure the fault is before the injection starts, the faster aseismic slip propagates. A somewhat similar observation was made previously by Passelègue et al. (2020) through a set of centimeter-scale experiments and using a rupture-tip energy balance argument. This general feature of injection-induced aseismic slip can be particularly seen in the closed-form expression for the rupture speed of critically stressed faults responding in the early-time Coulomb's friction stage: $V_r = \left[\left(f_p \Delta p_* / \left(f_p \sigma_0' - \tau_0\right)\right)(\alpha/2t)\right]^{1/2}$ (Sáez et al., 2022). This formula displays, in addition to the previous stress state dependence, some other general and quite intuitive features of injection-induced aseismic slip: the more intense the injection is, or the higher the fault hydraulic diffusivity is; the faster the rupture propagates. The latter dependencies remain to be seen in the laboratory, as well as many other aspects of injection-induced fault slip. We discuss a few of them in the context of published experiments in what follows. Notably, our results provide a means for characterizing the conditions under which distinct regimes and stages of injection-induced aseismic slip are expected to emerge under well-controlled conditions in the laboratory, where the validation of the relevant physics incorporated in our model can be potentially realized.

For example, the type of experiments conducted by Passelègue et al. (2020) could provide important insights into the aseismic slip phase preceding dynamic ruptures. Indeed, the nucleation radius of critically stressed faults, Eq. (61), which is itself the circular analog of Uenishi and Rice's nucleation length, has been estimated under somewhat similar laboratory conditions (confining pressures ~ 100 MPa) in $R_c^{cs} \sim 1$ m (Uenishi and Rice, 2002). Variations of this nucleation radius in one order of magnitude could be reasonably expected due to uncertainties mostly in the critical slip-weakening scale δ_c. Moreover, a nucleation length of about 1 m has been recently measured by Cebry et al. (2022) during meter-scale experiments of fluid injection with fault normal stresses of about 4 MPa. Since the experiments of Passelègue et al. (2020) were carried out in a similar rock, if ones corrects the nucleation length of Cebry et al. (2022) by the effective normal stresses that are representative of Passelègue et al.'s experiments, we obtain roughly $R_c^{cs} \sim 10$ cm. Since the critically stressed nucleation radius (61) is the minimum possible nucleation size of injection-induced dynamic ruptures in our model, and given that Passelègue et al.'s cylindrical rock samples have a diameter of 4 cm, we expect that their aseismic ruptures might have likely been operating in the Coulomb's friction phase (stage I) and perhaps some excursion in the acceleration phase towards a dynamic instability (stage II), yet never reached the onset of a macroscopic dynamic rupture in the sample. Moreover, as the initial shear stress was set to be 90 percent of the 'in-situ' static fault strength, it is likely that the initial shear stress was greater than the residual strength of the fault thus further supporting the ultimately unstable condition assumed for these experiments.

Another interesting set of fluid injection experiments are the ones reported by Cebry et al. (2022). Their 3-meters long, quasi-one-dimensional fault, allowed them to observe not only the nucleation of injection-induced dynamic ruptures but also some details of the quasi-static phase preceding such instabilities . Due to the elasticity and fluid flow boundary conditions in their experimental setup, it is not possible to make direct quantitative comparisons with our three-dimensional model, nor with two-dimensional plane-strain models (Garagash and Germanovich, 2012) . An unbounded rupture may have certainly propagated before the fault slip reached the shortest side of the sample, yet most of the measurements were conducted starting from this moment. In spite of these differences, it is interesting to note at least two experimental observations that are qualitatively consistent with our model: i) the aseismic slip front continuously decelerates during fluid injection except for the moment right before instabilities occur, and (ii) the transition from self-arrested to run-away dynamic ruptures seems to have occurred in relation to the ultimate stability condition (44). This type of experiment is well suited to be analyzed via dynamic numerical modeling to provide the possibility for direct quantitative comparisons.

Finally, using rock analog materials with reduced shear modulus such as PMMA (Cebry and McLaskey, 2021; Gori et al., 2021) could provide important insights into injection-induced aseismic slip by reducing the elasto-frictional length scale R_w in approximately one order of magnitude. This "widens" the observable spatial range of the problem thus providing the chance to explore larger-scale processes and regimes that would be otherwise difficult to observe in the laboratory using rock samples. For instance, stage III, where injection-induced aseismic slip is governed by an energy balance of the Griffith's type, or perhaps even stage IV, where ultimately stable ruptures behave as having nearly zero fracture energy, could be potentially investigated in this type of experimental setting. The front-localized energy balance of dynamic ruptures has been extensively studied on both dry (Svetlizky and Fineberg, 2014; Paglialunga et al., 2022) and fluid-lubricated frictional interfaces (Bayart et al., 2016; Paglialunga et al., 2023). Yet the same kind of energy balance for injection-induced slow slip, which is determined by the competition of three distinct factors (Eq. (14)), remains to be investigated experimentally. Indeed, stages III and IV might be the relevant regimes for subsurface processes such as the reactivation in shear of fractures by fluid injection for geo-energy applications, and natural earthquake-related phenomena where coupled fluid flow and aseismic slip processes are thought to play an important role (e.g., seismic swarms, aftershock sequences, and slow earthquakes).

7.3. In-situ experiments

Fluid injection experiments in shallow natural faults have recently provided important insights into the mechanics of injection-induced fault slip (Guglielmi et al., 2015; Cappa et al., 2022). Yet laboratory experiments under well-controlled conditions are likely better positioned than in-situ experiments to validate the physics of injection-induced fault slip due to the further uncertainties naturally present in the field (e.g., heterogeneities of stress, strength, fracture/fault geometrical complexities, among others), in-situ experiments do have various benefits such as, for instance, covering a larger decameter scale and providing more realistic field conditions, particularly those ones allowing the growth of fully three-dimensional unbounded ruptures initiated from a localized fluid source, as the one considered in this study. Our results thus provide the opportunity to make quantitative comparisons in these cases.

Among them, the experiments of Guglielmi et al. (2015) have been particularly impactful as they were able to measure for the first time not only micro-seismicity and injection-well fluid pressure and volume rate history (as done previously in large-scale field experiments Scotti and Cornet (1994), Cornet et al. (1997)), but also the history of induced fracture slip and opening at the injection point/interval. This unique dataset has been analyzed via dynamic numerical modeling by various researchers (Guglielmi et al., 2015; Bhattacharya and Viesca, 2019; Cappa et al., 2019; Larochelle et al., 2021). The multiplicity of proposed models that have fitted the data suggests indeed that more spatially distributed measurements, as done more recently (Cappa et al., 2022), could further help to constrain the underlying physical processes operating behind these experiments. For the purpose of illustrating the application of our model, hereafter we focus on the modeling work of Bhattacharya and Viesca (2019) for the unique reason that they assumed a slip-weakening fault model which makes the application of our results more straightforward.

Let us first estimate the three dimensionless parameters of our model: $\mathcal{S}$, $\mathcal{P}$, and $\mathcal{F}$ (37). Considering the best-fit model parameters of Bhattacharya and Viesca (2019): $\mu = 11.84$ GPa, $\delta_c = 0.37$ mm, $f_p = 0.6$, $f_r = 0.42$, $\sigma_0' = 5.08$ MPa, and $\tau_0 = 2.41$ MPa; we can directly compute $\mathcal{S} \approx 0.79$ and $\mathcal{F} = 0.7$. Note that the estimated initial shear stress of 2.41 MPa is greater than the in-situ residual fault strength $f_r \sigma_0' \approx 2.1$ MPa (or alternatively $\mathcal{S} > \mathcal{F}$ (44)), so that the injection-induced rupture is inferred to be ultimately unstable. Because no macroscopic dynamic rupture occurred during the experiment, the propagation mode of aseismic slip must be the one of a frustrated dynamic instability. Let us now estimate the remaining dimensionless parameter $\mathcal{P}$. To do so, we need to estimate first the injection intensity Δp_*, Eq. (1). We approximate the injection history via a constant-volume-rate injection characterized by the same total volume of fluid injected during the experiment. This gives roughly $Q \sim 40$ l/min. The fault intrinsic permeability k is widely recognized to have increased during this test (Guglielmi et al., 2015; Cappa et al., 2019; Bhattacharya and Viesca, 2019). It was estimated by Bhattacharya and Viesca (2019) between $k_{\min} = 0.8 \times 10^{-12}$ m^2 and $k_{\max} = 1.3 \times 10^{-12}$ m^2. Consider, for instance, the average $\bar{k} = 1.05 \times 10^{-12}$ m^2. By assuming a fluid dynamic viscosity of $\eta \sim 10^{-3}$ Pa s and fault-zone width $w = 0.2$ m (Bhattacharya and Viesca, 2019), the characteristic wellbore overpressure, Eq. (2), is $\Delta p_c \approx 3.17$ MPa, which is very close to the actual, nearly constant wellbore overpressure measured at the latest part of the injection, ~ 3 MPa (see figure 2a in Bhattacharya and Viesca (2019)). Following this approximation for the fluid injection, we obtain an injection intensity $\Delta p_* \approx 0.25$ MPa, which in turn yields $\mathcal{P} \approx 0.05$. By considering either the minimum or maximum fault permeability, we would obtain $\mathcal{P} \approx 0.065$ and $\mathcal{P} \approx 0.04$, respectively; the higher the permeability, the lower the injection intensity.

To understand under what regime aseismic slip may have developed during the initial Coulomb's friction stage (either critically stressed or marginally pressurized regime), let us calculate the peak stress-injection parameter $\mathcal{T}_p$. Given the known values for $\mathcal{S}$ and $\mathcal{P}$, we obtain via (42) $\mathcal{T}_p \approx 4.22$, which is well into the marginally pressurized regime, with an associated amplification factor $\lambda_p \approx 0.12$ (Eq. (20)). By considering $k_{\min}$ and $k_{\max}$ instead, we would obtain just a modest change in $\mathcal{T}_p$ approximately equal to 3.20 and 5.22, respectively. Furthermore, we can estimate the critical nucleation radius in the marginally pressurized regime via Eq. (62). For that, we must calculate first the elasto-frictional lengthscale R_w, Eq. (36). Given the best-fit model parameters, $R_w \approx 4.79$ m, and the nucleation radius is then $R_c^{mp} \approx 6.06$ m. Considering the size of the aseismic rupture estimated by Bhattacharya and Viesca (2019) at the final time analyzed in their work, $t_f = 1378$ s (see inset of figure 3a in Bhattacharya and Viesca (2019)), one could expect that the aseismic rupture was quite close to become unstable. Note that in Bhattacharya and Viesca (2019), their original circular rupture solutions were modified to appear elliptical considering the perturbative approach for circular shear cracks of Gao (1988), which gives an aspect ratio $a/b = 1/(1-\nu)$ (to first order in ν), where a and b are the semi-major and semi-minor axes of the elliptical rupture front. The calculations of Gao (1988) involve a planar circular crack whose shape is perturbed under uniform shear load and constant energy release rate along the front. Perhaps, a better correction could be done by considering the asymptotic behavior in the marginally pressurized regime obtained in Sáez et al. (2022), $a/b = (3-\nu)/(3-2\nu)$, at least in the Coulomb's friction stage where the previous equation is valid. This would lead to ruptures that are less elongated than the ones considered by Bhattacharya and Viesca (2019). For example, considering a Poisson's ratio $\nu = 0.25$, the marginally-pressurized aspect ratio is $a/b = 1.1$, whereas Gao's aspect ratio is $a/b \approx 1.33$. The latter was indeed found to be the asymptotic behavior in the critically stressed regime ($\mathcal{T}_p \ll 1$) of the Coulomb's friction stage (Sáez et al., 2022).

Let us assume as a first estimate, that the rupture propagates with Coulomb's friction until the final time $t_f = 1378$ s. In this scenario, the rupture radius would be at this time simply $R_f = \lambda_p \sqrt{4\alpha t_f}$, and the corresponding accumulated slip at the injection point, $\delta_f = (8/\pi)(f_p \Delta p_* / \mu) R_f$ (eq. (27) in Sáez et al. (2022)). To perform the previous calculations, we need to estimate the fault hydraulic diffusivity $\alpha = k/\eta S$. Considering the storage coefficient S estimated in 2.2×10^{-8} Pa^{-1} (Bhattacharya and Viesca, 2019), we obtain a hydraulic diffusivity $\alpha \approx 0.048$ m^2/s. The final rupture radius and accrued slip are then $R_f \approx 2.01$ m and $\delta_f \approx 0.07$ mm, respectively. Variations in fault permeability considering $k_{\min}$ and $k_{\max}$ would result in $R_f \approx 2.91$ m and 1.35 m, and $\delta_f \approx 0.12$ mm and 0.04 mm, respectively. In any case, the previous quantities do not account for the total slip measured at the injection point which is an order of magnitude higher (~ 1 mm) and estimated rupture radius ~ 5 m. Moreover, there is a clear acceleration of slip in the final part of the injection (see figure 3a in Bhattacharya and Viesca (2019)) which in our model could only come from frictional weakening (stage II). We therefore calculate the evolution of the rupture front and slip at the injection point numerically.

Our numerical solution shows that the nucleation of a dynamic rupture occurs at $R_c \approx 6.08$ m, which is in excellent agreement with the theoretical nucleation radius for marginally pressurized faults calculated previously. The calculated accrued slip at the center of the rupture at the instability time is 0.35 mm, which is about a third part of the actual measurement. On the other hand, the nucleation time is $t_c = 5885$ s, which is several times longer than t_f. Indeed, at the time t_f the rupture radius is just 2.17 m in our numerical solution, not much larger than the Coulomb's friction approximation (2.01 m). The latter indicates that our model is indeed operating in stage I at t_f. The differences between our calculations and the ones of Bhattacharya and Viesca (2019) are due to time-history variations in permeability not accounted in our model, and the approximation of the fluid injection via an equivalent constant volume rate. Nevertheless, the theoretical nucleation radius is expected to hold as this quantity is relatively independent of the injection scenario. Finally, we note that a rupture propagating in the marginally pressurized regime is expected to be confined within the pressurized area even at the instability time. In this regard, the main difference with Bhattacharya and Viesca (2019) who suggested that the slip front outpaced the migration of fluids is merely a matter of definitions. In our case, the overpressure front $L(t) = \sqrt{4\alpha t}$ represents the radial distance from the injection point at which the overpressure is approximately 2 percent of the fluid-source overpressure, the latter being approximately 3 MPa at the final time. In Bhattacharya and Viesca (2019), various overpressure isobars are drawn. The one with lowest overpressure is at 0.5 MPa, which is around 17 percent of the fluid-source overpressure.

7.4. A note on rate-and-state fault models: similarities and differences

Laboratory-derived friction laws (Dieterich, 1979; Ruina, 1983) are widely used in the earthquake modeling community to reproduce the entire spectrum of slip velocities on natural faults (Scholz, 2019). These empirical friction laws capture the dependence of friction on slip rate and the history of sliding (via a state variable) as observed during velocity-step laboratory experiments on bare rock surfaces and simulated fault gouge (Marone, 1998). In its simplest form, the rate-and-state friction coefficient is expressed as

$$f(v,\theta) = f_0 + a\ln\left(\frac{v}{v_0}\right) + b\ln\left(\frac{v_0\theta}{d_c}\right), \tag{67}$$

where f_0 is the friction coefficient at a reference slip rate v_0 and state variable $\theta_0 = d_c/v_0$ with units of time, d_c is a characteristic slip 'distance' for the evolution of θ, which is usually thought to be an order of magnitude smaller than δ_c of the slip weakening model (Cocco and Bizzarri, 2002; Uenishi and Rice, 2002), and a and b are the rate-and-state friction parameters, both positive and of order 10^{-2}. An additional dynamical equation describing the evolution of the state variable θ is required. The two most widely-used state-evolution equations are the so-called aging law, $\dot{\theta} = 1 - v\theta/d_c$, and the slip law, $\dot{\theta} = -(v\theta/d_c)\ln(v\theta/d_c)$.

The similarities between frictional ruptures obeying slip-weakening and rate-and-state friction have been long recognized (see, for example, Cocco and Bizzarri, 2002; Uenishi and Rice, 2002; Ampuero and Rubin, 2008; Garagash and Germanovich, 2012). Furthermore, in the context of injection-induced fault slip, some similarities were already recognized by Garagash and Germanovich (2012), particularly in relation to the nucleation of dynamic slip. Specifically, for the aging law, they noted that the nucleation length of critically stressed faults for linear slip-weakening friction or, what is the same, the one of Uenishi and Rice (2002), is identical to the nucleation length of rate-and-state faults for $a/b \ll 1$ (Rubin and Ampuero, 2005). On the other hand, the large nucleation length near the ultimate stability limit which is equal (except by a pre-factor of order one) to the one of Andrews (1976), is identical to the nucleation length of rate-and-state faults when approaching the velocity-neutral limit $a/b \to 1$ (Rubin and Ampuero, 2005). The equivalence between the previous nucleation lengths is obtained by recasting the slip-weakening friction law in terms of the rate-and-state parameters, this is, replacing the peak to residual strength drop $(f_p - f_r)\sigma_0'$ by $b\sigma_0'$, and the stress drop $\tau_0 - f_r\sigma_0'$ by $(b-a)\sigma_0'$ (Rubin and Ampuero, 2005; Ampuero and Rubin, 2008). We highlight that the nucleation of dynamic ruptures under the slip law can lead to quite different limiting behaviors compared to the aging law (Ampuero and Rubin, 2008), including a vanishingly small nucleation length (Viesca, 2023).

In addition to the previous similarities, we discuss some additional ones now. For instance, the ultimate stability condition (44) has been observed to determine in rate-and-state models under the aging law, whether velocity-weakening faults ($a/b < 1$) produce either self-arrested or run-away ruptures (Norbeck and Horne, 2018), and whether velocity-strengthening faults ($a/b > 1$) host either purely quasi-static slip or a dynamic instability (Dublanchet, 2019). Both results are essentially the same as predicted by slip-weakening fault models. Indeed, under crack-like propagation, the ultimate stability condition is somehow expected to occur in rate-and-state models (both velocity weakening and velocity strengthening) in the vicinity of the velocity-neutral limit ($a/b \to 1$), as the condition (44) that the residual fault strength drops at nearly the same level of the shear stress present further ahead of the rupture is reminiscent of the case $a \approx b$ when analyzing the steady-state ($\dot{\theta} = 0$) response of Eq. (67) to an incremental velocity step approximating crudely the passage of a rupture front.

Another similarity between slip-weakening and rate-and-state fault models relates to our constant-residual-friction similarity solution, or ultimate zero-fracture-energy regime. As already noted by Sáez et al. (2022) for the particular case of injection at constant volumetric rate in a one-dimensional fault (see section 5.2 in Sáez et al. (2022)), the ultimate regime of rate-and-state faults with aging law (Dublanchet, 2019) coincides with the solution for a constant friction coefficient (Sáez et al., 2022). It is clear now albeit in a three-dimensional configuration, that this friction coefficient corresponds to the residual value in a slip-weakening model and that this regime is characterized by negligible fracture energy. The latter is additionally consistent with the work of Garagash (2021) who found that slip transients driven by a point-force-like injection approach a zero-toughness condition as an ultimate regime in a one-dimensional fault under either the aging or slip laws. Note that the limit of a point-force-like injection is reached in our three-dimensional model in the nearly unstable limit, but not in the marginally pressurized one. Moreover, the features that give rise to this ultimate asymptotic behavior seem rather general and we think are likely expected to hold under other types of fluid injection. As already shown in Sáez et al. (2022) (Section 5.1), the spatio-temporal patterns of injection-induced aseismic slip are strongly influenced by the boundary condition associated with the fluid injection, that is, the injection rate or pore pressure history at the fluid source. Quantifying this effect is important and we will address it soon in a future study.

In addition to the similarities we have just discussed, we would also like to highlight some differences between slip-weakening and rate-and-state fault models. Indeed, one of the main physical ingredients that rate-and-state friction would incorporate in our model is frictional healing. The recovery of the friction coefficient with the logarithm of time is a well-established phenomenon (Dieterich, 1979; Ruina, 1983; Marone, 1998) that is essential in physics-based models that attempt to reproduce earthquake cycles (Tse and Rice, 1986; Lapusta et al., 2000). Frictional healing would provide, for instance, the possibility of nucleating multiple dynamic events on the same fault segment. Yet we highlight that this is not a unique characteristic of rate-and-state friction in the sense that two events can also nucleate on the same slip-weakening fault segment (regime R4 in Fig. 4). Another case in which the rate-and-state framework could be particularly useful is to model the reactivation of faults that are thought to be steadily creeping. This would make aseismic slip transients differ significantly at early times when comparing slip-weakening and rate-and-state models (Garagash and Germanovich, 2012; Dublanchet, 2019). In fact, from a Coulomb's friction perspective, rate-and-state faults are always at failure: the shear stress is at any time and over the entire fault extent equal to the fault strength. The initial stress state is a result of the history of sliding. At an initial time $t = 0$, it will be defined by the initial distribution of slip rate v_i and initial state variable θ_i.

To illustrate this latter point and get some further insights into a rate-and-state fault model, consider our same hydro-mechanical model but with a rate-and-state friction coefficient. Due to the 'always-failing' condition, $R(t) \rightarrow \infty$ in Eq. (6) and the inequality (3) becomes an equality. One possible way of considering the initial stress state is to assume that the initial slip velocity v_i is uniform and it operates at the creep rate that one could further consider as the reference slip rate v_0. The initial stress state is then encapsulated in the initial state variable θ_i. Assuming the latter as uniform as well, one can readily show by dimensional analysis that under both aging and slip laws, the slip rate (the primary unknown in this model together with the state variable) depends in addition to dimensionless space $rb\sigma_0'/d_c\mu$ and time tv_0/d_c, on the following five non-dimensional parameters: a/b, $\Delta p_*/\sigma_0'$, α/α_c, f_0/b and θ_i/θ_0, where $\alpha_c = \mu^2 d_c v_0/b^2\sigma_0'^2$ is a characteristic diffusivity. We note that this rate-and-state version of our model has an increased complexity with two more dimensionless parameters than the slip-weakening model. $\Delta p_*/\sigma_0'$ is indeed our same overpressure ratio $\mathcal{P}$. a/b quantifies the degree of weakening ($a/b < 1$) or strengthening ($a/b > 1$) and, as discussed previously, it would relate to the ultimate stability behavior of the fault. f_0/b quantifies the constant part of the friction coefficient with regard to b which in turn relates to the strength drop (i.e., the decay from the peak to the residual friction). Finally, θ_i/θ_0 is where the initial shear stress or pre-stress ratio $\mathcal{S}$ of the slip-weakening model would equivalently emerge. In fact, by multiplying Eq. (67) by σ_0' and then expressing it at the initial conditions v_i and θ_i, the resulting dimensionless form of such equation reads as $\ln\left(\theta_i/\theta_0\right) = \left(f_0/b\right)\left(\tau_0/f_0\sigma_0' - 1\right)$. The dimensionless parameter θ_i/θ_0 can be then alternatively chosen as $\tau_0/f_0\sigma_0'$, which is similar to the pre-stress ratio of the slip-weakening model.

8. Concluding remarks

We have investigated the propagation of fluid-driven slow slip and earthquake nucleation on a slip-weakening circular fault subjected to fluid injection at a constant volume rate. Despite some simplifying assumptions in our model, our investigation has revealed a very broad range of aseismic slip behaviors, from frustrated dynamic instabilities to unconditionally stable slip, from ruptures that move much faster than the diffusion of pore pressure to ruptures that move much slower than that. The circular fault geometry is likely the simplest one enabling quantitative comparisons with field observations thanks to its three-dimensional nature. It is thus also useful for preliminary engineering design of hydraulic stimulations in geo-energy applications. In addition to the effect of a non-zero Poisson's ratio that will elongate the shape of the rupture along the direction of principal shear, changes in lithologies as commonly encountered in the upper Earth's crust will alter the dynamics of an otherwise unbounded rupture as the one we have examined here. In particular, the effect of layering might promote containment of the reactivated fault surface within certain lithologies, similar to what is observed for hydraulic fractures (Bunger and Lecampion, 2017). This effect may be important in some cases and would require further quantification.

Funding

The results were obtained within the EMOD project (Engineering model for hydraulic stimulation). The EMOD project benefits from a grant (research contract no. SI/502081-01) and an exploration subsidy (contract no. MF-021-GEO-ERK) of the Swiss federal office of energy for the EGS geothermal project in Haute-Sorne, canton of Jura, which is gratefully acknowledged. Alexis Sáez was partially funded by the Federal Commission for Scholarships for Foreign Students via the Swiss Government Excellence Scholarship.

CRediT authorship contribution statement

Alexis Sáez: Conceptualization, Formal analysis, Funding acquisition, Investigation, Methodology, Software, Validation, Visualization, Writing – original draft, Writing – review & editing. **Brice Lecampion:** Conceptualization, Funding acquisition, Methodology, Software, Writing – review & editing.

Declaration of competing interest

The authors declare that they have no known competing financial interests or personal relationships that could have appeared to influence the work reported in this paper.

Data availability

No data was used for the research described in the article.

Acknowledgments

Alexis Sáez would like to thank François Passelègue for discussions about his own experiments. The authors also would like to thank Eric Dunham for helpful comments that allowed us to improve the manuscript during the review process.

Appendix A. Eigenvalue problem at the instability time for unlimited linear weakening of friction

A.1. Generalized eigenvalue problem

Following Uenishi and Rice (2002) and Garagash and Germanovich (2012), we extend their eigenvalue-based stability analysis, valid for unlimited linear weakening of friction under either in-plane shear (II) or anti-plane shear (III) mode of sliding, to the case of a circular rupture propagating under mixed-mode (II+III) conditions.

Equilibrium dictates that within the slipping region $r \leq R(t)$, the fault strength τ_s (3) must be locally equal to the fault shear stress τ (6). Equating the two previous equations and then differentiating with respect to time, leads to

$$v(r,t)\,\frac{\mathrm{d}f}{\mathrm{d}\delta}\sigma'(r,t) + f(\delta)\frac{\partial\sigma'(r,t)}{\partial t} = \frac{\partial\tau_0(r,t)}{\partial t} - \frac{\mu}{2\pi}\int_0^{R(t)} F(r,\xi)\,\frac{\partial v(\xi,t)}{\partial\xi}\mathrm{d}\xi, \tag{68}$$

where $v = \partial\delta/\partial t$ is the fault slip rate. When differentiating the integral term previously, we have considered Leibniz's integral rule and applied the condition of non-singular shear stresses along the rupture front.

In our problem, the effective normal stress $\sigma'(r,t) = \sigma_0' - \Delta p(r,t)$ decreases from the initial uniform value σ_0' due to the overpressure $\Delta p(r,t)$ associated with the fluid injection, whereas the shear stress that would be present on the fault if no slip occurs is a uniform and constant value τ_0. Nevertheless, for the sake of generality, we keep utilizing the generic terms $\sigma'(r,t)$ and $\tau_0(r,t)$. Indeed, $\sigma'(r,t)$ generally contains not only the initial effective normal stress and changes in pore pressure, but also possible changes in total normal stress from the far field, as $\sigma' = \sigma - p$. Similarly, $\tau_0(r,t)$ could be a summation of both the initial shear stress and far-field shear loading. Far-field loads may be due to, for instance, tectonic forces and seasonal variations of stress, among many others. Note that $\sigma'(r,t)$ and $\tau_0(r,t)$ are both axisymmetric in magnitude and at least one of them must be locally peaked around the origin in order to initiate slip at $r = 0$ at a certain time $t = t_0$. Eq. (68) is then valid at any time $t > t_0$ and, as mentioned in the main text, it assumes a Poisson's ratio $\nu = 0$.

Let us scale Eq. (68) by introducing the following non-dimensional quantities: $\bar{r} = r/R$, $\bar{\xi} = \xi/R$, and $\bar{v} = v/v_{\mathrm{rms}}$, where

$$v_{\mathrm{rms}}(t) = \sqrt{\frac{1}{R(t)}\int_0^{R(t)} v^2(r,t)\mathrm{d}r} \tag{69}$$

is the root mean square of the slip rate distribution, such that $\int_0^1 \bar{v}^2(\bar{r})\mathrm{d}\bar{r} = 1$. Note that for the linear-weakening friction law (4), $\mathrm{d}f/\mathrm{d}\delta = -(f_p - f_r)/\delta_c$. The latter has the strong assumption that the residual friction coefficient f_r has not been reached yet at any point within the rupture. Otherwise, wherever $f = f_r$, $\mathrm{d}f/\mathrm{d}\delta = 0$. Moreover, for the exponential-weakening friction law (5), the same expression for $\mathrm{d}f/\mathrm{d}\delta$ is approximately valid in the range of small slip $\delta \ll \delta_c$, to first order in δ/δ_c.

Considering the previous quantities plus the relation (36) $\mu\delta_c = (f_p - f_r)\sigma_0' R_w$, we nondimensionalize Eq. (68) to obtain

$$-\frac{R}{R_w}\bar{v}(\bar{r})\frac{\sigma'(\bar{r}R)}{\sigma_0'} + \frac{R}{\mu v_{\mathrm{rms}}}f(\delta)\frac{\partial\sigma'(\bar{r}R)}{\partial t} = \frac{R}{\mu v_{\mathrm{rms}}}\frac{\partial\tau_0(\bar{r}R)}{\partial t} - \frac{1}{2\pi}\int_0^1 F\left(\bar{r},\bar{\xi}\right)\frac{\partial\bar{v}(\bar{\xi})}{\partial\bar{\xi}}\mathrm{d}\bar{\xi}. \tag{70}$$

In the previous equation, we dropped the explicit dependence on time t of the various variables for simplicity in the notation.

Following Uenishi and Rice (2002), at the instability time t_c, the slip rate diverges all over the fault plane, such that the root mean square of the slip rate distribution $v_{\mathrm{rms}}(t_c) \to \infty$. The only non-vanishing terms of (70) lead to the following generalized eigenvalue problem:

$$\frac{R}{R_w}\bar{v}(\bar{r})\frac{\sigma'(\bar{r}R)}{\sigma_0'} = \frac{1}{2\pi}\int_0^1 F\left(\bar{r},\bar{\xi}\right)\frac{\partial\bar{v}(\bar{\xi})}{\partial\bar{\xi}}\mathrm{d}\bar{\xi}, \tag{71}$$

which corresponds to the mixed-mode, circular rupture version of equation (14) in Garagash and Germanovich (2012).

Given a normalized distribution of effective normal stress at the instability time, $\sigma'(r,t_c)/\sigma_0'$, Eq. (71) can be solved to obtain the corresponding generalized eigenvalues and eigenfunctions. Moreover, what is more important is to calculate the smallest eigenvalue that would be related to the instabilities we observe in the full numerical solutions. In our problem, $\sigma'(r,t_c)$ is set by the distribution of overpressure at the time of instability, which does not allow us to obtain a purely analytical insight as the instability time is generally unknown and, more importantly, information about one of the problem parameters, the pre-stress ratio $\mathcal{S}$, is lost when deriving the eigenproblem (71). The only scenario in which Eq. (71) is independent of t_c is when $\sigma'(r,t_c)$ is uniform, which in turn leads to a regular eigenvalue problem. Furthermore, in the particular case of $\sigma'(r,t) = \sigma_0'$, we obtain the circular rupture version of the eigenvalue problem of Uenishi and Rice (2002) (eq. (12) in their work), which will give the corresponding universal nucleation radius of their problem.

A.2. Eigenvalue problem in the critically stressed and marginally pressurized limits

Let us come back to our particular problem where $\sigma'(r,t) = \sigma_0' - \Delta p(r,t)$ and assume a rather general but self-similar injection scenario such that the overpressure can be written in the similarity form: $\Delta p(r,t) = \Delta p_w(t)\Pi(\xi)$, where $\Delta p_w(t)$ is the overpressure at the fluid source, and $\Pi(\xi)$ is the spatial distribution of overpressure with the properties: $\Pi(0) = 1$ and $\Pi(\infty) \to 0$. Note that such a self-similar injection scenario is possible only if one assumes a line source of fluids such that no length scale associated with the fluid source is introduced into the problem. For a discussion about the line-source approximation, see Appendix C. Introducing the previous relations for the effective normal stress into (71), the generalized eigenvalue problem becomes

$$\frac{R}{R_w}\bar{v}(\bar{r})\left(1-\frac{\Delta p_w}{\sigma_0'}\Pi(\lambda\bar{r})\right)=\frac{1}{2\pi}\int_0^1 F\left(\bar{r},\bar{\xi}\right)\frac{\partial\bar{v}(\bar{\xi})}{\partial\bar{\xi}}\mathrm{d}\bar{\xi}, \tag{72}$$

where $\lambda(t_c)=R(t_c)/\sqrt{4\alpha t_c}$ is the so-called amplification factor at the instability time. We recall that the dependence of the various variables in the previous equation on t_c is omitted for simplicity.

Consider now the critically stressed limit: $\tau_0 \to f_p\sigma_0'$, where the rupture front largely outpaces the overpressure front at the time of instability, such that $\lambda(t_c) \gg 1$. In view of the properties of $\Pi(\xi)$, the term $(\Delta p_w/\sigma_0')\Pi(\lambda\bar{r}) \ll 1$ so that, if neglected, Eq. (72) further simplifies to

$$\frac{R}{R_w}\bar{v}(\bar{r})=\frac{1}{2\pi}\int_0^1 F\left(\bar{r},\bar{\xi}\right)\frac{\partial\bar{v}(\bar{\xi})}{\partial\bar{\xi}}\mathrm{d}\bar{\xi}. \tag{73}$$

The previous equation is a regular eigenvalue problem. It corresponds indeed to the circular rupture version of the eigenvalue problem of Uenishi and Rice (2002). Derivation of Eq. (73) can be alternatively done by following the reasoning of Garagash and Germanovich (2012) that in the critically stressed limit, the effective normal stress over the slipping region is largely unchanged so that $\sigma'(r,t_c)\approx\sigma_0'$, except for a very small region of approximate size $\sqrt{4\alpha t_c}$ near the rupture center that at spatial scales in the order of the rupture size can be neglected. Replacing $\sigma'(r,t_c)\approx\sigma_0'$ into (71) leads equivalently to (73).

Let us now examine the marginally pressurized limit: $f_p\Delta p_w \approx f_p\sigma_0'-\tau_0$, where the rupture front significantly lags the overpressure front at the instability time, so that $\lambda(t_c)\ll 1$. We refer to Appendix C for a discussion about the marginally pressurized limit and its relation to the line-source approximation. Particularly, we note that the property $\Pi(0)=1$ cannot be rigorously defined but, still, it can be established in an order-of-magnitude sense. Furthermore, for injection at a constant volumetric rate, the prefactor is quite close to one for all practical purposes (see Fig. 11b). It is therefore convenient for practical applications to define the marginally pressurized limit in an approximate sense. Hence, we approximate the fluid overpressure within the rupture as $\Delta p_w\Pi(\lambda\bar{r})\approx\sigma_0'-\tau_0/f_p$. After substituting the previous relation into (72), we obtain the following regular eigenvalue problem for marginally pressurized cases,

$$\frac{R}{R_w}\frac{\tau_0}{f_p\sigma_0'}\bar{v}(\bar{r})=\frac{1}{2\pi}\int_0^1 F\left(\bar{r},\bar{\xi}\right)\frac{\partial\bar{v}(\bar{\xi})}{\partial\bar{\xi}}\mathrm{d}\bar{\xi}. \tag{74}$$

It is important to mention that the critically stressed and marginally pressurized limits are both characterized by small slip at the instability time: $\delta(r=0,t_c)\ll\delta_c$. This is observed in our numerical solutions and was also established by Garagash and Germanovich (2012) in the two-dimensional problem. The latter is very important since it implies that the approximation of the exponential-weakening friction law by a linear relation is valid, as well as the assumption of unlimited linear-weakening of friction (never reaching the residual strength of the fault). Finally, as a last comment, we have established the eigenvalue problems in both limits for a general (self-similar) injection scenario, not restricted to the constant-volumetric rate case that we solve in the main text. However, in the marginally pressurized limit, we have implicitly assumed that the overpressure at the fluid source at the instability time is approximately equal to the overpressure at the time of activation of slip. Such approximation is reasonable in the case of constant-volumetric rate as the increase of overpressure at the fluid source is slowly logarithmic (see Fig. 11b) and assumed to be approximately constant, equal to Δp_c, for practical applications. This approximation has to be carefully considered when dealing with other injection scenarios (see, for instance, Garagash and Germanovich, 2012; Ciardo and Lecampion, 2019; Ciardo and Rinaldi, 2021).

A.3. Numerical solution of the regular eigenvalue problem

In the critically stressed and marginally pressurized limits, the eigenproblems (73) and (74) can be recast as:

$$\frac{1}{2\pi}\int_0^1 F\left(\bar{r},\bar{\xi}\right)\frac{\partial\bar{v}(\bar{\xi})}{\partial\bar{\xi}}\mathrm{d}\bar{\xi}=\beta\bar{v}(\bar{r}), \tag{75}$$

with the eigenvalue

$$\beta=\frac{R}{R_w}\cdot\begin{cases}1 & \text{for critically stressed faults } \mathcal{T}_p\ll 1\\ \tau_0/f_p\sigma_0' & \text{for marginally pressurized faults } \mathcal{T}_p\sim 10.\end{cases} \tag{76}$$

We calculate the eigenvalues β_k and eigenfunctions $\bar{v}_k$ of (75), with $k=1,2,\dots,\infty$, by discretizing the linear integral operator on the left-hand side via a collocation boundary element method employing ring 'dislocations' with piece-wise constant slip rate. The details of such implementation can be found in the supplementary material of Sáez and Lecampion (2023). For the numerical calculations, it is convenient to express the discretized form of the eigenproblem (75) in matrix–vector form as

$$\mathbf{E}\bar{\boldsymbol{v}}_k=\beta_k\bar{\boldsymbol{v}}_k, \tag{77}$$

where $\bar{\boldsymbol{v}}_k\in\mathbb{R}^N$ are the discretized eigenfunctions with $k=1,2,\dots,N$, where N is the number of ring-dislocation elements, and $\mathbf{E}\in\mathbb{R}^{N\times N}$ is a non-dimensional matrix that is equivalent to the collocation boundary element matrix of a circular shear crack of unit radius and unit shear modulus (see Sáez and Lecampion, 2023). By collocation boundary element matrix, we mean that the product

Table 1
Eigenvalues β_k as a function of the number of boundary elements N.

k	Number of boundary elements N		
	100	1000	10 000
1	0.998912	1.002648	1.003018
2	2.551356	2.561554	2.562539
3	4.111055	4.128215	4.129803
4	5.671338	5.696629	5.698843
5	7.230949	7.265725	7.268573

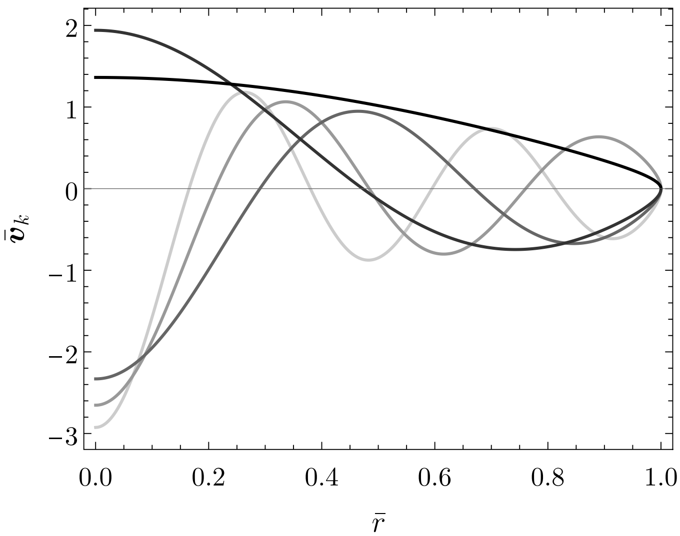

Fig. 10. Normalized eigenfunctions $\bar{v}_k$ for $N = 10000$. Curves in gray scale, from darker to lighter for increasing k.

between $\mathbf{E}$ and a given vector representing a discretized slip distribution $\boldsymbol{\delta}$, would give as a result the corresponding discretized shear stress distribution $\boldsymbol{\tau}$ that is in quasi-static equilibrium with $\boldsymbol{\delta}$, in an infinite and otherwise unstressed solid.

We solve the discretized eigenproblem (77) with the standard Wolfram Mathematica functions *Eigenvalues* and *Eigenvectors* which can be instructed to search only for the smallest eigenvalues and their corresponding eigenvectors. We do not intend here to conduct an extensive analysis of the eigenvalues and eigenfunctions as our unique goal in this work is to determine the smallest eigenvalue that we expect to give the nucleation radii for the critically stressed and marginally pressurized regimes. Nevertheless, we do report the first five (smaller) eigenvalues and their eigenvectors in Table 1 and Fig. 10, respectively. The eigenfunctions are normalized such that $\int_0^1 \bar{\boldsymbol{v}}_k^2(\bar{r})\mathrm{d}\bar{r} = 1$, meaning that the normalized eigenvectors from (77) must be divided by $\sqrt{1/N}$. It is interesting to note that the smallest eigenvalue β_1 is for all practical purposes equal to 1. Also, we note that the eigenfunctions are not orthogonal as the matrix $\mathbf{E}$ is non-symmetric.

A.4. Universal nucleation radius of Uenishi and Rice for tensile and shear circular rupture instabilities

The eigenproblem (73) for the critically stressed limit corresponds to the penny-shaped version of the eigenproblem of Uenishi and Rice (2002). The nucleation radius (61) in the main text is, therefore, the nucleation radius of dynamic instability under conditions similar to the ones analyzed by Uenishi and Rice (2002). Specifically, in our circular configuration, the tectonic shear loading that drives the quasi-static phase of the rupture must be considered to be unidirectional, locally peaked around $r = 0$, and axisymmetric in magnitude. Moreover, this result is not only valid for a mixed-mode (II+III) shear rupture (with $\nu = 0$) but also for a cohesive tensile (mode I) crack. In this latter case, the nucleation radius is valid for any value of ν as long as the shear modulus μ is replaced by the quantity $\mu/(1-\nu)$ or, equivalently, by $E'/2$ with $E' = E/(1-\nu^2)$ the plane-strain Young's modulus. Note that similarly to the shear rupture case, here the far-field tensile load driving the quasi-static growth of the mode-I rupture must be also locally peaked at $r = 0$ (in order to initiate fracture yielding at the origin) and axisymmetric in magnitude.

Appendix B. Numerical solver for slip-dependent friction

We calculate the numerical solutions of the slip-weakening model via a fully implicit boundary-element-based solver with an elasto-plastic-like interfacial constitutive law (Sáez et al., 2022; Sáez and Lecampion, 2023). The details of the three-dimensional version of the solver were presented by Sáez et al. (2022) for the particular case of Coulomb's friction, whereas the necessary modifications to solve in a more efficient manner for the special case of axisymmetric, circular shear ruptures were presented more recently by Sáez and Lecampion (2023). Here, we extend our axisymmetric solver to a case in which the friction coefficient is an arbitrary function of slip. Such extension is indeed relatively straightforward and requires just changes in the integration of the constitutive interfacial law at the collocation point level, plus deriving the proper consistent tangent operator. We present these two changes in Appendices B.1 and B.2 respectively, plus some calculation and implementation details in Appendix B.3.

B.1. Integration of the constitutive interfacial law

The integration of the constitutive interfacial law in three dimensions was described in section 2.2.3 of Sáez et al. (2022) for the case of Coulomb's friction. With reference to this latter section and following the notation in Sáez et al. (2022), the extension to slip-dependent friction requires no further modification than just expressing the former constant friction coefficient f as a function of the magnitude of the shear vector of plastic displacement discontinuity at each collocation point, $f(\|\boldsymbol{d}_s^p\|)$, with $\boldsymbol{d}_s^p = (d_1^p, d_2^p)^\top$, and d_1^p and d_2^p the two shear components of plastic displacement discontinuity at a certain collocation point. The latter is expressed in the local reference system of the triangular boundary elements. Furthermore, in the axisymmetric configuration of interest in this work, the extension is even simpler since the shear part of the displacement discontinuity vector is a scalar (the direction of slip is fixed and known). Hence, the friction coefficient is simply expressed as $f(d_s^p)$, where the subscript 's' denotes the shear component and 'p' is the plastic part of the displacement discontinuity.

With the previous considerations in mind, one can show that when frictional sliding occurs ($\Delta\gamma > 0$), the system of equations (10)-(14) of Sáez et al. (2022) leads to the following implicit equation for the plastic multiplier $\Delta\gamma$,

$$\Delta\gamma = \frac{|t_s^{\text{trial}}| - f\left(d_s^{p,n} - \Delta\gamma \cdot \operatorname{sgn}\left(t_s^{\text{trial}}\right)\right) t_n^{\text{trial}}}{k_s}, \tag{78}$$

where $d_s^{p,n}$ is the 'plastic' (frictional) slip at the previous time step n, t_s^{trial} and t_n^{trial} are the shear and normal components of the elastic-trial traction vector $\boldsymbol{t}^{\text{trial}} = -\mathbf{D}\cdot\boldsymbol{d}^{n+1}$ of the elastic predictor-plastic corrector algorithm adopted in Sáez et al. (2022), with $\boldsymbol{d}^{n+1}$ the total (elastic + plastic) displacement discontinuity vector at the current time step $n+1$ (coming from the global Newton–Raphson scheme that solves the quasi-static elastic equilibrium), and k_s the shear component of the diagonal elastic stiffness matrix $\mathbf{D}$. We recall our adopted geomechanics convention of positive stresses in compression. At a given iteration of the global Newton–Raphson scheme, Eq. (78) is solved at every collocation point via a Newton–Raphson procedure, using as initial guess $\Delta\gamma = 0$.

B.2. The consistent tangent operator

The global Newton–Raphson iterations of the fully implicit time integration scheme (Sáez et al., 2022; Sáez and Lecampion, 2023) require the calculation of the so-called consistent tangent operator $\mathbf{C}_{TO}$, which depends on the specific constitutive interfacial law under consideration. For the case of Coulomb's friction, the consistent tangent operator has been derived analytically for both fully 3D (see Appendix A in Sáez et al. (2022)) and axisymmetric (see Supplemental Material 2 in Sáez and Lecampion (2023)) cases. Here, we derive the proper axisymmetric operator for the case in which the friction coefficient is an arbitrary function of slip.

Using again the same notation than in Sáez et al. (2022), we define the tangent operator as $\mathbf{C}_{TO} = -\partial\Delta\boldsymbol{t}'/\partial\Delta\boldsymbol{d}$, where $\Delta\boldsymbol{t}'$ is the increment of the effective traction vector and $\Delta\boldsymbol{d}$ is the increment of the displacement discontinuity vector. Note that the consistent tangent operator $\mathbf{C}_{TO}$ is a block diagonal matrix of size $2N \times 2N$, where N is the number of collocation points, and is composed by squared blocks $\mathbf{C}_{TO}^i$ of size 2×2, where $i = 1, \ldots, N$ is the collocation point index. Combining equations (10), (11), and (13) from Sáez et al. (2022), one can obtain $\Delta\boldsymbol{t}'$ as a function of $\Delta\boldsymbol{d}$:

$$\Delta\boldsymbol{t}' = -\mathbf{D}\cdot\left[\Delta\boldsymbol{d} + \Delta\gamma\left(\Delta\boldsymbol{d}\right)\left\{\operatorname{sgn}\left(t_s^{\text{trial}}\right), 0\right\}^\top\right]. \tag{79}$$

Differentiation of the latter expression with respect to $\Delta\boldsymbol{d}$ leads to the following expression for the squared blocks that composed the tangent operator:

$$\mathbf{C}_{TO}^i = \mathbf{D} - \mathbf{C}_{TO}^p\,, \text{ with } \quad \mathbf{C}_{TO}^p = -\begin{pmatrix} k_s \operatorname{sgn}\left(t_s^{\text{trial}}\right) \\ 0 \end{pmatrix} \otimes \begin{pmatrix} \partial\Delta\gamma/\partial\Delta d_s \\ \partial\Delta\gamma/\partial\Delta d_n \end{pmatrix}, \tag{80}$$

where $\mathbf{C}_{TO}^p$ is the plastic part of the tangent operator and $\otimes$ is the tensor product. Note that if $\Delta\gamma = 0$, that is, if the collocation point state is elastic or, in other words, no frictional slip occurs, then $\mathbf{C}_{TO}^p$ is a null matrix, and $\mathbf{C}_{TO}^i = \mathbf{D}$.

At this point, we just need the partial derivatives of the plastic multiplier $\Delta\gamma$ with respect to $\Delta\boldsymbol{d}$ to obtain the consistent tangent operator. To do so, we consider the incremental form of the consistency condition (see Appendix A in Sáez et al. (2022)), which in the case of slip-dependent friction $f(d_s^p)$ reads

$$\frac{\partial\mathcal{F}}{\partial\boldsymbol{t}'}\cdot\Delta\boldsymbol{t}' + \frac{\partial\mathcal{F}}{\partial d_s^p}\cdot\Delta d_s^p = 0. \tag{81}$$

Using the previous equation in combination with equations (10), (11) and (13) in Sáez et al. (2022), one obtains $\Delta\gamma$ as a function of $\Delta\boldsymbol{d}$, to finally calculate the sought partial derivatives

$$\frac{\partial\Delta\gamma}{\partial\Delta d_s} = \frac{k_s \operatorname{sgn}\left(t_s^{\text{trial}}\right)}{A}, \text{ and } \quad \frac{\partial\Delta\gamma}{\partial\Delta d_n} = -\frac{f\left(d_s^p\right)k_n}{A}, \tag{82}$$

where $A = f'\left(d_s^p\right) t_n^{\text{trial}} \operatorname{sgn}\left(t_s^{\text{trial}}\right) - k_s$, with f' the first derivative of the arbitrary function describing the dependence of friction on slip. Note that if the friction coefficient f is constant, we effectively recover the axisymmetric consistent tangent operator for Coulomb's friction presented in Supplemental Material 2 of Sáez and Lecampion (2023).

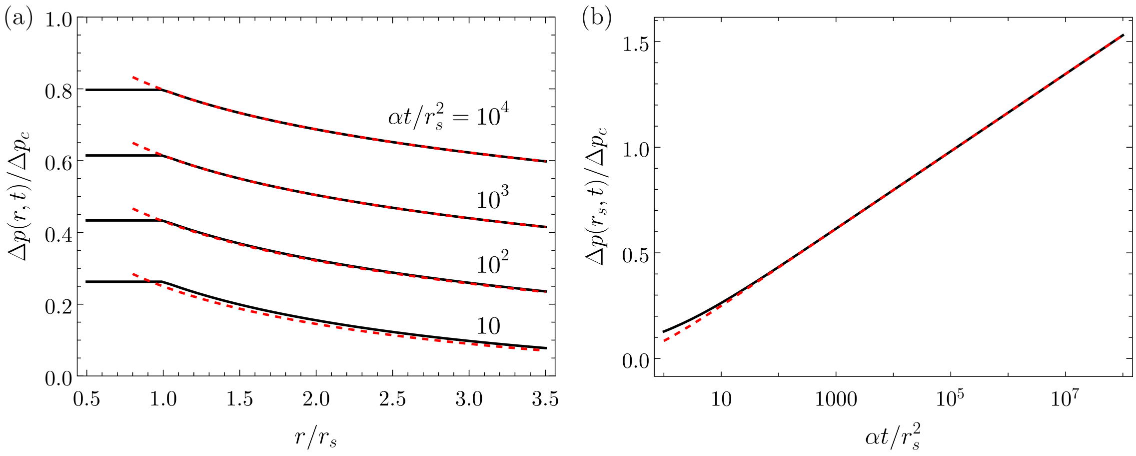

Fig. 11. Finite source (solid black) versus line-source approximation (dashed red). (a) Spatial profile of normalized overpressure. (b) Normalized temporal evolution of the overpressure at the fluid source.

B.3. Some calculation and implementation details

We use the adaptive time-stepping scheme based on the rupture speed described in Supplemental Material 2 of Sáez and Lecampion (2023). The parameter β that controls the number of elements that the front advances during one time step is fixed for most simulations as 2.5, which results in a front advancement of 2 to 3 elements per time step. To resolve properly the cohesive zone, we consider no less than 100 elements covering the elasto-frictional length scale R_w. Verification tests for the numerical solver in the case of a constant friction coefficient were performed in Sáez and Lecampion (2023). Here, the solver is further verified for the slip-dependent friction case through the systematic match between the numerical solutions and the analytical asymptotic and approximate solutions derived in the main text for the different stages and regimes of the problem. With regard to numerical convergence, we consider that our Newton–Raphson scheme employed to solve every backward Euler time step converges when the relative increment of the L^2 norm of the displacement discontinuity vector (our primary unknown) between two consecutive iterations falls below 10^{-4}. On the other hand, the tangent mechanical system at each Newton–Raphson iteration is solved using a biconjugate gradient stabilized iterative solver (BiCGSTAB) with a tolerance set to 10^{-4}.

Appendix C. A note on the line-source approximation of the fluid injection and the marginally pressurized limit

In our model, we idealize the fluid injection as a line source. Such approximation is of course valid for times $t \gg r_s^2/\alpha$, where r_s is the characteristic size of the actual fluid source. This is graphically shown in Fig. 11a, where the line-source approximation is compared to the solution for a finite circular source of radius r_s. The latter is calculated from the known solution in the Laplace domain (section 13.5, Eq. (16), Carslaw and Jaeger (1959)) that we then invert numerically using the Stehfest's method (Stehfest, 1970). Fig. 11a shows clearly how at large times the line-source and finite-source solutions become asymptotically equal at distances $r \geq r_s$. In particular, the overpressure at the fluid source can be approximated at large times by simply evaluating $\Delta p(r,t)$ (Eq. (1)) at $r = r_s$. By doing so, the argument of the exponential integral function is very small, $r_s^2/4\alpha t \ll 1$, and the overpressure at the fluid source can be asymptotically approximated as

$$\Delta p(r = r_s, t) \approx \frac{\Delta p_c}{4\pi}\left(-\gamma - \ln\left(\frac{r_s^2}{4\alpha t}\right)\right), \tag{83}$$

where $\gamma = 0.577216...$ is the Euler–Mascheroni's constant.

Eq. (83) indicates that the overpressure at the fluid source increases logarithmically with time. This is further displayed in Fig. 11b, where the temporal evolution of $\Delta p(r_s,t)$ is plotted for both the line-source and finite-source solutions. From this figure, we observe that the line-source approximation is already quite accurate for times $\alpha t/r_s^2 \gtrapprox 10$. Furthermore, Fig. 11b shows that the characteristic overpressure Δp_c (Eq. (2)) is in the order of magnitude of the overpressure at the fluid source for a wide range of practically relevant times. Consider, for instance, the case of geo-energy applications where fluid injections are conducted through a wellbore of radius $r_s \sim 10$ cm. By assuming plausible values of hydraulic diffusivity in the range 10^{-5} to $1\ m^2/s$, the characteristic time r_s^2/α takes values between 1000 down to 0.01 s which are much smaller than typical fluid injection duration in geo-energy applications. The large time limit is therefore commonly satisfied.

Note that we had already introduced Δp_c in a previous work (Sáez and Lecampion, 2023) with the purpose of defining the marginally pressurized limit in a form that is more convenient for practical applications than in Sáez et al. (2022). We recall that the marginally pressurized limit is defined by the condition that the overpressure at the fluid source Δp_w is just sufficient to activate fault slip, $f_p \Delta p_w \approx f_p \sigma_0' - \tau_0$. As we have seen, we can approximate Δp_w quite well through a line source, yet its magnitude is not constant but rather increases with time. This increase is nevertheless logarithmically slow, so one could think in approximating Δp_w as constant and equal to the characteristic overpressure Δp_c. Indeed, the pre-factor in the order-of-magnitude relation $\Delta p_w \sim \Delta p_c$ is quite close to unity over a wide range of times (see Fig. 11b). We, therefore, enforce $\Delta p_w \approx \Delta p_c$ with the aim of defining the marginally pressurized limit in the more practically convenient way: $f_p \Delta p_c \approx f_p \sigma_0' - \tau_0$. In this way, we essentially avoid introducing the length scale of the fluid source r_s into the problem that, we think, would unnecessarily complexify the model and its practical applications. This subtle 'assumption' is all over the main text. Moreover, because the so-called intensity of the injection is $\Delta p_* = \Delta p_c / 4\pi$, the factor 4π is usually replaced by 10 to keep the spirit of the order-of-magnitude approximation behind Δp_c when representing the fluid-source overpressure.

References

Abercrombie, R.E., Rice, J.R., 2005. Can observations of earthquake scaling constrain slip weakening? Geophys. J. Int. 162 (2), 406–424.
Ampuero, J.-P., Rubin, A.M., 2008. Earthquake nucleation on rate and state faults – aging and slip laws. J. Geophys. Res.: Solid Earth 113 (B1).
Andrews, D.J., 1976. Rupture propagation with finite stress in antiplane strain. J. Geophys. Res. (1896-1977) 81 (20), 3575–3582.
Azad, M., Garagash, D., Satish, M., 2017. Nucleation of dynamic slip on a hydraulically fractured fault. J. Geophys. Res.: Solid Earth 122 (4), 2812–2830.
Barenblatt, G., 1962. The mathematical theory of equilibrium cracks in brittle fracture. Adv. Appl. Mech. 7, 55–129.
Bayart, E., Svetlizky, I., Fineberg, J., 2016. Slippery but tough: The rapid fracture of lubricated frictional interfaces. Phys. Rev. Lett. 116, 194301.
Behr, W.M., Bürgmann, R., 2021. What's down there? The structures, materials and environment of deep-seated slow slip and tremor. Phil. Trans. R. Soc. A 379 (2193), 20200218.
Bhattacharya, P., Viesca, R., 2019. Fluid-induced aseismic fault slip outpaces pore-fluid migration. Science 364 (6439), 464–468.
Broberg, K.B., 1999. Cracks and Fracture. Academic Press, San Diego.
Bunger, A.P., Lecampion, B., 2017. Four critical issues for successful hydraulic fracturing applications. In: Feng, X.-T. (Ed.), Rock Mechanics and Engineering. In: Surface and Underground Projects, vol. 5, CRC Press/Balkema.
Campillo, M., Ionescu, I.R., 1997. Initiation of antiplane shear instability under slip dependent friction. J. Geophys. Res.: Solid Earth 102 (B9), 20363–20371.
Cappa, F., Guglielmi, Y., Nussbaum, C., De Barros, L., Birkholzer, J., 2022. Fluid migration in low-permeability faults driven by decoupling of fault slip and opening. Nat. Geosci. 15 (9), 747–751.
Cappa, F., Scuderi, M., Collettini, C., Guglielmi, Y., Avouac, J., 2019. Stabilization of fault slip by fluid injection in the laboratory and in situ. Sci. Adv. 5 (3).
Carslaw, H., Jaeger, J., 1959. Conduction of Heat in Solids, second edition. Oxford University Press, Oxford, UK.
Castellano, M., Lorez, F., Kammer, D.S., 2023. Nucleation of frictional slip: A yielding or a fracture process? J. Mech. Phys. Solids 173, 105193.
Cebry, S.B.L., Ke, C.-Y., McLaskey, G.C., 2022. The role of background stress state in fluid-induced aseismic slip and dynamic rupture on a 3-m laboratory fault. J. Geophys. Res.: Solid Earth 127 (8), e2022JB024371.
Cebry, S.B.L., McLaskey, G.C., 2021. Seismic swarms produced by rapid fluid injection into a low permeability laboratory fault. Earth Planet. Sci. Lett. 557, 116726.
Chen, X., Nakata, N., Pennington, C., Haffener, J., Chang, J., He, X., Zhan, Z., Ni, S., Walter, J., 2017. The Pawnee earthquake as a result of the interplay among injection, faults and foreshocks. Sci. Rep. 7 (1), 4945.
Ciardo, F., Lecampion, B., 2019. Effect of dilatancy on the transition from aseismic to seismic slip due to fluid injection in a fault. J. Geophys. Res.: Solid Earth 124 (4), 3724–3743.
Ciardo, F., Rinaldi, A.P., 2021. Impact of injection rate ramp-up on nucleation and arrest of dynamic fault slip. Geomech. Geophys. Geo-Energy Geo-Resour. 8 (1), 28.
Cocco, M., Bizzarri, A., 2002. On the slip-weakening behavior of rate- and state dependent constitutive laws. Geophys. Res. Lett. 29 (11).
Cornet, F., Helm, J., Poitrenaud, H., Etchecopar, A., 1997. Seismic and aseismic slips induced by large-scale fluid injections. Pure Appl. Geophys. 150, 563–583.
Day, S.M., 1982. Three-dimensional simulation of spontaneous rupture: The effect of nonuniform prestress. Bull. Seismol. Soc. Am. 72 (6A), 1881–1902.
Deichmann, N., Giardini, D., 2009. Earthquakes induced by the stimulation of an enhanced geothermal system below Basel (Switzerland). Seismol. Res. Lett. 80 (5), 784–798.
Dempsey, J.P., Tan, L., Wang, S., 2010. An isolated cohesive crack in tension. Contin. Mech. Thermodyn. 22 (6), 617–634.
Dieterich, J., 1979. Modeling of rock friction: 1. Experimental results and constitutive equations. J. Geophys. Res.: Solid Earth 84 (B5), 2161–2168.
Dublanchet, P., 2019. Fluid driven shear cracks on a strengthening rate-and-state frictional fault. J. Mech. Phys. Solids 132, 103672.
Ellsworth, W., Giardini, D., Townend, J., Ge, S., Shimamoto, T., 2019. Triggering of the Pohang, Korea, earthquake (Mw 5.5) by enhanced geothermal system stimulation. Seismol. Res. Lett. 90 (5), 1844–1858.
Eyre, T., Eaton, D., Garagash, D., Zecevic, M., Venieri, M., Weir, R., Lawton, D., 2019. The role of aseismic slip in hydraulic fracturing-induced seismicity. Sci. Adv. 5 (8).
Favreau, P., Campillo, M., Ionescu, I.R., 2002. Initiation of shear instability in three-dimensional elastodynamics. J. Geophys. Res.: Solid Earth 107 (B7).
Gabriel, A.-A., Garagash, D.I., Palgunadi, K.H., Mai, P.M., 2023. Fault-size dependent fracture energy explains multi-scale seismicity and cascading earthquakes. arXiv:2307.15201.
Gao, H., 1988. Nearly circular shear mode cracks. Int. J. Solids Struct. 24 (2), 177–193.
Garagash, D., 2021. Fracture mechanics of rate-and-state faults and fluid injection induced slip. Phil. Trans. R. Soc. A 379 (2196), 20200129.
Garagash, D., Germanovich, L., 2012. Nucleation and arrest of dynamic slip on a pressurized fault. J. Geophys. Res.: Solid Earth 117 (B10).
Gori, M., Rubino, V., Rosakis, A.J., Lapusta, N., 2021. Dynamic rupture initiation and propagation in a fluid-injection laboratory setup with diagnostics across multiple temporal scales. Proc. Natl. Acad. Sci. 118 (51).
Guglielmi, Y., Cappa, F., Avouac, J., Henry, P., Elsworth, D., 2015. Seismicity triggered by fluid injection-induced aseismic slip. Science 348 (6240), 1224–1226.
Hamilton, D., Meehan, R., 1971. Ground rupture in the Baldwin Hills. Science 172 (3981), 333–344.
Hills, D., Kelly, P., Dai, D., Korsunsky, A., 1996. Solution of Crack Problems: The Distributed Dislocation Technique, Vol. 44. Kluwer Academic Publishers, Dordrecht, Netherlands.
Ida, Y., 1972. Cohesive force across the tip of a longitudinal-shear crack and Griffith's specific surface energy. J. Geophys. Res. 77 (20), 3796–3805.
Irwin, G.R., 1958. Fracture. Elast. Plast. 551–590.
Kato, A., Iidaka, T., Ikuta, R., Yoshida, Y., Katsumata, K., Iwasaki, T., Sakai, S., Thurber, C., Tsumura, N., Yamaoka, K., Watanabe, T., Kunitomo, T., Yamazaki, F., Okubo, M., Suzuki, S., Hirata, N., 2010. Variations of fluid pressure within the subducting oceanic crust and slow earthquakes. Geophys. Res. Lett. 37 (14).
Lapusta, N., Rice, J.R., Ben-Zion, Y., Zheng, G., 2000. Elastodynamic analysis for slow tectonic loading with spontaneous rupture episodes on faults with rate- and state-dependent friction. J. Geophys. Res.: Solid Earth 105 (B10), 23765–23789.
Larochelle, S., Lapusta, N., Ampuero, J.-P., Cappa, F., 2021. Constraining fault friction and stability with fluid-injection field experiments. Geophys. Res. Lett. 48 (10), e2020GL091188.

Lawn, B., 1993. Fracture of Brittle Solids, second edition. In: Cambridge Solid State Science Series, Cambridge University Press.
Lebihain, M., Roch, T., Molinari, J.-F., 2022. Quasi-static crack front deformations in cohesive materials. J. Mech. Phys. Solids 168, 105025.
Liu, D., Lecampion, B., Garagash, D.I., 2019. Propagation of a fluid-driven fracture with fracture length dependent apparent toughness. Eng. Fract. Mech. 220, 106616.
Lohman, R.B., McGuire, J.J., 2007. Earthquake swarms driven by aseismic creep in the Salton Trough, California. J. Geophys. Res.: Solid Earth 112 (B4).
Marck, J., Savitski, A.A., Detournay, E., 2015. Line source in a poroelastic layer bounded by an elastic space. Int. J. Numer. Anal. Methods Geomech. 39 (14), 1484–1505.
Marone, C., 1998. Laboratory-derived friction laws and their application to seismic faulting. Annu. Rev. Earth Planet. Sci. 26 (1), 643–696.
Miller, S., Collettini, C., Chiaraluce, L., Cocco, M., Barchi, M., Kaus, B., 2004. Aftershocks driven by a high-pressure CO2 source at depth. Nature 427 (6976), 724–727.
Norbeck, J., Horne, R., 2018. Maximum magnitude of injection-induced earthquakes: A criterion to assess the influence of pressure migration along faults. Tectonophysics 733, 108–118.
Paglialunga, F., Passelègue, F.X., Brantut, N., Barras, F., Lebihain, M., Violay, M., 2022. On the scale dependence in the dynamics of frictional rupture: Constant fracture energy versus size-dependent breakdown work. Earth Planet. Sci. Lett. 584, 117442.
Paglialunga, F., Passelègue, F., Latour, S., Gounon, A., Violay, M., 2023. Influence of viscous lubricant on nucleation and propagation of frictional ruptures. J. Geophys. Res.: Solid Earth 128 (4), e2022JB026090.
Palmer, A., Rice, J., 1973. The growth of slip surfaces in the progressive failure of over-consolidated clay. Proc. R. Soc. Lond. Ser. A Math. Phys. Eng. Sci. 332 (1591), 527–548.
Parotidis, M., Shapiro, S., Rothert, E., 2005. Evidence for triggering of the Vogtland swarms 2000 by pore pressure diffusion. J. Geophys. Res.: Solid Earth 110 (B5).
Passelègue, F.X., Almakari, M., Dublanchet, P., Barras, F., Fortin, J., Violay, M., 2020. Initial effective stress controls the nature of earthquakes. Nature Commun. 11 (1), 5132.
Perez-Silva, A., Kaneko, Y., Savage, M., Wallace, L., Warren-Smith, E., 2023. Characteristics of slow slip events explained by rate-strengthening faults subject to periodic pore fluid pressure changes. J. Geophys. Res.: Solid Earth 128 (6), e2022JB026332.
Perfettini, H., Avouac, J.-P., 2007. Modeling afterslip and aftershocks following the 1992 Landers earthquake. J. Geophys. Res.: Solid Earth 112 (B7).
Rice, J., 1968. Mathematical analysis in the mechanics of fracture. Fracture: Adv. Treatise 2, 191–311.
Rice, J., 2006. Heating and weakening of faults during earthquake slip. J. Geophys. Res.: Solid Earth 111 (B5).
Rice, J.R., Uenishi, K., 2010. Rupture nucleation on an interface with a power-law relation between stress and displacement discontinuity. Int. J. Fract. 163 (1), 1–13.
Rogers, G., Dragert, H., 2003. Episodic tremor and slip on the cascadia subduction zone: The chatter of silent slip. Science 300 (5627), 1942–1943.
Ross, Z., Rollins, C., Cochran, E., Hauksson, E., Avouac, J., Ben-Zion, Y., 2017. Aftershocks driven by afterslip and fluid pressure sweeping through a fault-fracture mesh. Geophys. Res. Lett. 44 (16), 8260–8267.
Rubin, A.M., Ampuero, J.-P., 2005. Earthquake nucleation on (aging) rate and state faults. J. Geophys. Res.: Solid Earth 110 (B11).
Ruina, A., 1983. Slip instability and state variable friction laws. J. Geophys. Res.: Solid Earth 88 (B12), 10359–10370.
Sáez, A., Lecampion, B., 2023. Post-injection aseismic slip as a mechanism for the delayed triggering of seismicity. Proc. R. Soc. A: Math., Phys. Eng. Sci. 479 (2273), 20220810.
Sáez, A., Lecampion, B., Bhattacharya, P., Viesca, R.C., 2022. Three-dimensional fluid-driven stable frictional ruptures. J. Mech. Phys. Solids 160, 104754.
Salamon, N., Dundurs, J., 1977. A circular glide dislocation loop in a two-phase material. J. Phys. C: Solid State Phys. 10 (4), 497–507.
Scholz, C., 2019. The Mechanics of Earthquakes and Faulting, third edition. Cambridge University Press, Cambridge, UK.
Scotti, O., Cornet, F., 1994. In situ evidence for fluid-induced aseismic slip events along fault zones. Int. J. Rock Mech. Min. Sci. Geomech. Abstr. 31 (4), 347–358.
Shelly, D.R., Beroza, G.C., Ide, S., Nakamula, S., 2006. Low-frequency earthquakes in Shikoku, Japan, and their relationship to episodic tremor and slip. Nature 442 (7099), 188–191.
Sirorattanakul, K., Ross, Z.E., Khoshmanesh, M., Cochran, E.S., Acosta, M., Avouac, J.-P., 2022. The 2020 Westmorland, California earthquake swarm as aftershocks of a slow slip event sustained by fluid flow. J. Geophys. Res.: Solid Earth 127 (11), e2022JB024693.
Stehfest, H., 1970. Numerical inversion of Laplace transforms. Commun. ACM 13 (1), 47–49.
Svetlizky, I., Bayart, E., Fineberg, J., 2019. Brittle fracture theory describes the onset of frictional motion. Annu. Rev. Condens. Matter Phys. 10 (1), 253–273.
Svetlizky, I., Fineberg, J., 2014. Classical shear cracks drive the onset of dry frictional motion. Nature 509 (7499), 205–208.
Tse, S.T., Rice, J.R., 1986. Crustal earthquake instability in relation to the depth variation of frictional slip properties. J. Geophys. Res.: Solid Earth 91 (B9), 9452–9472.
Uenishi, K., 2018. Three-dimensional fracture instability of a displacement-weakening planar interface under locally peaked nonuniform loading. J. Mech. Phys. Solids 115, 195–207.
Uenishi, K., Rice, J., 2002. Universal nucleation length for slip-weakening rupture instability under non-uniform fault loading. J. Geophys. Res. 108.
Viesca, R.C., 2021. Self-similar fault slip in response to fluid injection. J. Fluid Mech. 928, A29.
Viesca, R.C., 2023. Frictional state evolution laws and the non-linear nucleation of dynamic shear rupture. J. Mech. Phys. Solids 173, 105221.
Viesca, R.C., Garagash, D.I., 2015. Ubiquitous weakening of faults due to thermal pressurization. Nat. Geosci. 8 (11), 875–879.
Warren-Smith, E., Fry, B., Wallace, L., Chon, E., Henrys, S., Sheehan, A., Mochizuki, K., Schwartz, S., Webb, S., Lebedev, S., 2019. Episodic stress and fluid pressure cycling in subducting oceanic crust during slow slip. Nat. Geosci. 12 (6), 475–481.
Wei, S., Avouac, J., Hudnut, K., Donnellan, A., Parker, J., Graves, R., Helmberger, D., Fielding, E., Liu, Z., Cappa, F., Eneva, M., 2015. The 2012 Brawley swarm triggered by injection-induced aseismic slip. Earth Planet. Sci. Lett. 422, 115–125.
Yang, Y., Dunham, E.M., 2021. Effect of porosity and permeability evolution on injection-induced aseismic slip. J. Geophys. Res.: Solid Earth 126 (7), e2020JB021258.
Yukutake, Y., Yoshida, K., Honda, R., 2022. Interaction between aseismic slip and fluid invasion in earthquake swarms revealed by dense geodetic and seismic observations. J. Geophys. Res.: Solid Earth e2021JB022933.
Zhu, W., Allison, K., Dunham, E., Yang, Y., 2020. Fault valving and pore pressure evolution in simulations of earthquake sequences and aseismic slip. Nature Commun. 11 (1), 4833.
Zoback, M., Gorelick, S., 2012. Earthquake triggering and large-scale geologic storage of carbon dioxide. Proc. Natl. Acad. Sci. 109 (26), 10164–10168.

Rock Mechanics and Rock Engineering
https://doi.org/10.1007/s00603-023-03249-8

ORIGINAL PAPER

Injection-Induced Aseismic Slip in Tight Fractured Rocks

Federico Ciardo[1] · **Brice Lecampion**[2]

Received: 8 August 2022 / Accepted: 24 January 2023

Abstract

We investigate the problem of fluid injection at constant pressure in a 2D Discrete Fracture Network (DFN) with randomly oriented and uniformly distributed frictionally-stable fractures. We show that this problem shares similarities with the simpler scenario of injection in a single planar shear fracture, investigated by Bhattacharya and Viesca (2019); Viesca (2021) and whose results are here extended to include closed form solutions for aseismic moment as function of injected volume V_{inj}. Notably, we demonstrate that the hydro-mechanical response of the fractured rock mass is at first order governed by a single dimensionless parameter $\mathcal{T}$ associated with favourably oriented fractures: low values of $\mathcal{T}$ (critically stressed conditions) lead to fast migration of aseismic slip from injection point due to elastic stress transfer on critically stressed fractures. In this case, therefore, there is no effect of the DFN percolation number on the spatio-temporal evolution of aseismic slip. On the other hand, in marginally pressurized conditions ($\mathcal{T} \gtrsim 1$), the slipping patch lags behind the pressurized region and hence the percolation number affects to a first order the response of the medium. Furthermore, we show that the aseismic moment scales $\propto V_{\text{inj}}^2$ in both limiting conditions, similarly to the case of a single planar fracture subjected to the same injection condition. The factor of proportionality, however, depends on the DFN characteristics in marginally pressurized conditions, while it appears to be only mildly dependent on the DFN properties in critically stressed conditions.

Highlights

- The problem of injection at constant pressure in a two-dimensional Discrete Fracture Network shares similarities with the simpler case of injection in a planar shear fracture.
- Injection-induced aseismic slip propagation is at first order governed by a single dimensionless parameter associated with favorably oriented fractures.
- In critically stressed conditions, the aseismic slipping patch migration from injection point is driven by elastic stress transfer and outpaces pore-fluid diffusion.
- In marginally pressurized conditions, the aseismic slipping patch lags the pressurization region, and the percolation number affects the response of the medium.
- The aseismic moment scales quadratically to the injected fluid volume, both in critically stressed and marginally pressurized conditions.

Keywords Aseismic slip · Discrete fracture network · Fluid injection · Fluid-driven ruptures

✉ Federico Ciardo
federico.ciardo@sed.ethz.ch

Brice Lecampion
brice.lecampion@epfl.ch

1 Swiss Seismological Service (SED), ETH Zürich, Sonneggstrasse 5, Zürich 8092, Switzerland

2 Geo-energy Laboratory-Gaznat Chair on Geo-energy, EPFL, Rte Cantonale, Lausanne 1015, Switzerland

1 Introduction

Field observations reveal that human activities associated with injection of fluids in the sub-surface can re-activate pre-existing fractures/faults and trigger micro-seismicity (Healy et al. 1968; Hamilton and Meehan 1971; Zoback and Harjes 1997; Ellsworth 2013; Keranen and Weingarten 2018). Although with different purposes and different techniques, current industry practices, such as the ones operating in the

Published online: 09 February 2023

field of deep geothermal energy or hydrocarbon extraction, utilize micro-seismic events to determine the extent of the stimulated rock volume and often correlate its propagation with a pore fluid diffusion process. As demonstrated by many observations, indeed, the migration of these "wet" events is bounded by a power-law which grows proportional to the square-root of pressurization time (Shapiro et al. 1997, 2002; Parotidis et al. 2003; Hainzl et al. 2012). Although a possible explanation could be attributed to the presence of highly hydraulically conductive fractures at large scale, an increasing number of evidences show that seismic slip is not the only possible result of fluid injection [e.g. see Cornet (2016) and references therein], and "dry" micro-seismicity may be triggered and driven by elastic stress transfers to unstable patches caused by aseismic slip migrating away from injection point (Eyre et al. 2019).

As demonstrated by in-situ large-scale injection campaigns (Scotti and Cornet 1994; Cornet et al. 1997; Bourouis and Bernard 2007) and recent field and laboratory experiments (Guglielmini et al. 2015; Scuderi and Collettini 2016; Cappa et al. 2019), aseismic slip is primarily induced by fluid injection and micro-earthquakes are only indirect effects associated with a stable aseismic rupture propagation. Actually, the deformation that led to ground ruptures in the Baldwin Hills associated with injection waterflooding was shown to have a large aseismic component as early as 1971 (Hamilton and Meehan 1971). The interest in the spatio-temporal evolution of fluid-driven slip on predominantly frictionally stable pre-existing discontinuities has prompted recent theoretical investigations. Bhattacharya and Viesca (2019) showed that fluid-induced aseismic slip on a critically stressed two-dimensional fault can outpace pore fluid diffusion if the ratio between the initial distance to failure of the fault over the injection strength is small. Similar results for a planar three-dimensional fault have been recently obtained by Sáez et al. (2022). In that "critically stressed" limit, the fast migration of aseismic slip compared to the pore-pressure diffusion front may be the primary cause of observed (micro-)seismicity during in-situ injection experiments [e.g. (Duboeuf et al. 2017)]. In these studies, micro-seismicity is conceptually understood as the result of instabilities triggered by quasi-static stress perturbations on unstable patches around or on the main slipping fault plane of different sizes. Although this can clearly occur if a single main fault plane accommodate most of the slip, an injection in a deep fracture/fault zone most likely re-activates several pre-existing structural discontinuities present at various length scales, from meters to kilometres (Wibberley et al. 2008; Faulkner et al. 2010). Such heterogeneous discontinuities would plausibly serve as main fluid conduits for pore-pressure diffusion (Witherspoon and Gale 1977) and may host aseismic slip that would cause elastic stress re-distribution in the fractured rock mass, leading potentially to a more complex spatio-temporal evolution of micro-seismicity. Additionally, at a decameter scale, how does a highly fractured rock mass respond to fluid injection at pressures lower than the minimum stress (thus not promoting hydraulic fracturing) but sufficient to induce shear ruptures is an important topic in rock mechanics at large—from grouting to geothermal energy (Cornet 2021).

In this context, we study how fluid-driven stable frictional ruptures propagate when a fluid is injected at constant pressure in a fractured rock mass. Notably, we model the fractured rock mass discretely accounting for fractures at multiple scales using a Discrete Fracture Network approach. We focus on the case of randomly oriented and uniformly distributed pre-existing fractures. The rock matrix is assumed to be impermeable at the time scale of injection and hence fluid can flow only along the hydraulically connected pre-existing fractures.

This paper is organized as follows: In Sect. 2, we present the mathematical formulation of the problem as well as a quick description of the methods used for its numerical resolution. As a limiting scenario of fluid injection into a fracture/fault that is not hydraulically connected to others, we revisit in Sect. 3 the problem of fluid injection at constant pressure and aseismic slip propagation on a 2-dimensional planar shear fracture. The numerical results are thoroughly benchmarked against the analytical asymptotic solutions of Bhattacharya and Viesca (2019) and Viesca (2021). In Sect. 4, we extend the results of Sect. 3 and investigate the problem of injection at constant pressure in a 2D Discrete Fracture Network, with randomly oriented and uniformly distributed fractures. Scaling considerations allow to identify the important governing parameters and drive the numerical experiments. Finally, in Sect. 5 we discuss the implications of our results to injection-induced micro-seismicity, as well as the limits of our modelling assumptions.

2 Problem Formulation and Methods

We consider a homogeneous, isotropic and linear elastic infinite medium that hosts a set of inter-connected planar fractures, forming a so called Discrete Fracture Network (DFN). Under the assumption of plane strain conditions, these two-dimensional discontinuities reduce to one-dimensional entities in the $\mathbb{R}^2$ Euclidean space with a canonical global basis $\mathbf{e_x} = (1, 0)$, $\mathbf{e_y} = (0, 1)$. The fractured medium is subjected to a uniform far-field stress state[1] which, resolved on each fracture ^{k}, leads to a uniform shear stress $t^k_{s,o}$ and effective normal stress $t'^{,k}_{n,o} = t^k_n - p_o$, with p_o the in-situ uniform pore

[1] With principal stress components denoted by $\sigma_{xx,o}$ and $\sigma_{yy,o}$, aligned along the principal $x-$ and $y-$axis, respectively. The subscript $_o$ refers to initial conditions.

pressure field. We assume that frictional resistance of each pre-existing fracture is governed by Coulomb's friction with a constant friction coefficient f. Initially, we assume that the frictional resistance of all fractures is sufficient to prevent any slip. Such an equilibrium is perturbed by internal pore-fluid pressurization due to fluid injection into one fracture. Since we assume that the host medium is impermeable at the time scale of injection (i.e. tight rock such as granite), the induced pressure gradient generates fluid flow that propagates inside the hydraulically connected permeable fractures, all characterized by a constant and uniform hydraulic aperture $w_h[L]$ and longitudinal permeability $k_f\left[L^2\right]$. The local reduction of effective normal stresses due to internal pore fluid pressurization may cause the shear resistance to drop below the applied stresses (in absolute terms). This activates slip, manifested with a local shear stress drop, that forces the applied stress to be equal (or lower) to the available frictional resistance, here assumed to obey the Mohr–Coulomb yielding criterion without cohesion. In other words, for all fractures, at any time

$$|t_s^k| \leq f\left(t_{n,o}^{\prime,k} - \bar{p}(\mathbf{x}, t)\right), \tag{1}$$

where $\bar{p}(\mathbf{x}, t) = p(\mathbf{x}, t) - p_o$ is the internal pore fluid over-pressure. Upon frictional yielding (when $|t_s^k| = f\left(t_{n,o}^{\prime,k} - \bar{p}(\mathbf{x}, t)\right)$), the fracture(s) can slip following a non-associated plastic flow rule (Ciardo et al. 2020). We assume here that slip occurs at critical state (without any volumetric change), such that the slip component δ of the displacement discontinuity is the only unknown, while its opening part w always remain zero.

The conservation of momentum under quasi-static approximation leads to a linear relationship between tractions and slip on the pre-existing fracture network. This relation is represented mathematically by the following boundary integral equations (Mogilevskaya 2014):

$$t_i^k(\mathbf{x}, t) = t_{i,o}^k(\mathbf{x}) + \int_\Gamma K_{is}\left(\mathbf{x} - \boldsymbol{\xi}, E', \nu\right)\delta(\boldsymbol{\xi}, t)\,\mathrm{d}\xi, \quad \mathbf{x} \in \Gamma, \quad i,j = s,n \tag{2}$$

where Γ denotes the boundary region in the medium traced by the DFN and locus of slip δ, t_i^k is the current total traction vector on the generic fracture ^{k} and $t_{i,o}^k$ its initial value under the in-situ stress state. Finally, K_{is} is the singular elastostatic traction kernel function of both plane-strain elastic modulus E' and Poisson's ratio ν. Its mathematical expression is known in closed form for an infinite 2-dimensional medium [see e.g. (Gebbia 1891; Hill et al. 1996)]. The assumption of zero dilatancy as the frictional slip develops entails that on all fracture the opening displacement discontinuity w remains zero. The non-local elastic kernel K_{is}, therefore, maps the effects of slip distribution on the normal and shear component of the traction vector along Γ.

Isothermal single-phase fluid flow inside the permeable fracture network is governed by the width-averaged fluid mass conservation equation over the fractures hydraulic thickness, whose expression in terms of the pore fluid over-pressure reads

$$w_h\beta\frac{\partial\bar{p}}{\partial t} + \nabla_{||}q_{||} = 0, \tag{3}$$

where $\beta\left[M^{-1}T^2L\right]$ is a coefficient sums of the fluid and pore compressibility, and $q_{||}$ is the longitudinal fluid flux inside the fracture(s) Γ given by Darcy's law

$$q_{||} = -\frac{w_k k_f}{\mu}\nabla_{||}\bar{p}, \tag{4}$$

with $\mu\left[ML^{-1}T^{-1}\right]$ is the fluid dynamic viscosity. In this contribution, we investigate sustained fluid injection into a single fracture at the centre of the DFN and we denote this fracture as ^{k_*}. Notably, we assume that the injection is performed at constant over-pressure:

$$\bar{p}\left(x_{\text{inj}}^{k_*}, y_{\text{inj}}^{k_*}, t\right) = \Delta P, \quad \forall t \tag{5}$$

where the injection over-pressure ΔP remains always below the minimum principal effective stress in order to avoid the creation of an hydraulic fracture.

As previously stated, shear-induced dilatancy is neglected and all the fractures have a uniform and constant hydraulic transmissivity $k_f w_h$. The hydro-mechanical problem, therefore, uncouples such that the flow Equations (3) and (4) reduce to a simple diffusion equation

$$\frac{\partial\bar{p}}{\partial t} - \alpha\nabla_{||}^2\bar{p} = 0, \tag{6}$$

where $\alpha = \dfrac{k_f}{\mu \cdot \beta}$ is the constant hydraulic diffusivity $\left[L^2T^{-1}\right]$.

In the following sub-section, we discuss the numerical methods used to solve numerically the system of equations (1–5) in terms of spatial-temporal distribution of shear displacement discontinuities δ and pore fluid over-pressure $\bar{p}$.

2.1 Numerical Methods

The hydro-mechanical problem described in the previous section uncouples thanks to the assumption of constant fracture(s) permeability and negligible dilatancy. The fluid flow problem can thus be solved separately first, and the resulting pressure input into the mechanical problem (i.e. quasi-static elastic equilibrium and Mohr's Coulomb criterion).

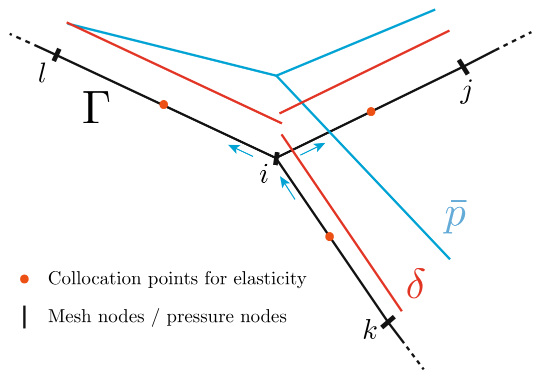

Fig. 1 Sketch of spatial discretization of displacement discontinuities (slip—red) and pore fluid over-pressure (blue) field along three mesh elements converging in one generic node i. The former is based on a piece-wise constant variation between different segments, with one collocation point per element for the evaluation of elasticity equations (2) (orange dots). The latter, instead, varies linearly and continuously between adjacent elements

We use a continuous Galerkin Finite Element method for the spatial discretization of the fluid flow problem and solve for the unknown pore fluid over-pressure field $\bar{p}(\mathbf{x}, t)$ at nodes. The set of fractures Γ is discretized into a number of finite 1D linear iso-parametric elements. The nodal (pressure) values coincide with mesh nodes as depicted in Fig. 1, and thus continuity between elements and fractures intersection are automatically handled. Using a backward Euler time integration scheme, Equations (3-5) upon discretization reduces to a linear system of equations

$$\mathbf{A}\bar{\mathbf{p}}^{n+1} = \mathbf{b}, \tag{7}$$

where $\mathbf{A}$ is a sparse matrix (combining the storativity and conductivity matrices) and $\mathbf{b}$ is the right hand side that contains the injection condition (5). The sparse system of equations (7) is solved numerically using a Lower-Upper decomposition method (Quarteroni et al. 2000) for the over-pressure distribution at time t^{n+1}. The latter is then entered as change of effective normal tractions to a boundary-element-based solver with an elasto-plastic like constitutive interfacial law for the simultaneous resolution of the quasi-static elastic equilibrium and elasto-plastic non-associated Mohr–Coulomb interface law. Such a solver is similar to the one reported in Sáez et al. (2022) (albeit its usage was only showed for 3D problems) where additional details can be found. The only difference compared to that contribution is the problem dimension, the type of boundary elements adopted and their interpolation order for displacement discontinuity field. Notably, we employ piece-wise constant boundary elements (straight segments) with only one collocation point located at their middle point (see Fig. 1). This results in having one degree of freedom (slip) for each boundary element in the computational mesh.

Note also that we adopt an automatic adaptive time-stepping scheme (Söderlind and Wang 2003) based on an estimate of the local truncation error obtained via an explicit predictor implicit corrector.

3 Injection in a Planar Shear Fracture

Before investigating the problem of injection into a discrete fracture network, we present the case of an injection in an isolated planar fracture. This represents the limiting case where a pre-existing fracture network is loose, poorly connected and fluid is injected into a fracture/fault which is not hydraulically connected to others. The large inter-distances between pre-existing fractures further avoid elastic stress interactions, owing to the spatial decay of the elastic kernel K_{is}, which in 2-dimension scales as $\sim 1/r^2$ (with r being the Euclidean distance). Since we assume the fracture plane to be planar, the elastic equation uncouple ($K_{ns} = 0$ in Equation (2)) such that slip does not induce any variation of normal traction along the planar fracture. Fluid flow is confined inside the conductive fracture characterised by constant and uniform hydraulic transmissivity $k_f w_h$. Equation (3), or equivalently Equation (6), together with injection condition (5) and the following boundary and initial conditions

$$\bar{p}(x, 0) = 0, \quad \bar{p}(\pm\infty, t) = 0, \tag{8}$$

can be solved analytically for the spatial and temporal evolution of pore-fluid over-pressure (Carslaw and Jaeger 1959)

$$\bar{p}(x, t) = \Delta P \cdot \mathrm{Erfc}\left(\frac{|x|}{\ell_d(t)}\right), \tag{9}$$

where x is the fracture longitudinal coordinate, Erfc is the complementary error function and $\ell_d(t) = \sqrt{4\alpha t}$ is the fluid diffusion length-scale (function of pressurization time t). Plastic flow, manifested as a symmetric shear crack propagating away from injection point, occurs when

$$\Delta P > t'_{n,o} - t_{s,o}/f \tag{10}$$

Note that the superscript ^{k} has been dropped for clarity for this single fracture case.

This single planar fracture problem has been solved by Bhattacharya and Viesca (2019) and Viesca (2021) in details. In the next sub-sections, we recall their main findings that—on one hand—will provide benchmark solutions for our numerical solver, and—on the other hand—will pave the way for later investigations.

3.1 Self-Similar Shear Crack Propagation

Under the specific conditions previously defined, fluid injection activates a shear crack that propagates symmetrically from injection point paced by pore fluid diffusion (and we denote its half-length as $a(t)$). Its propagation, however, is always stable (aseismic) due to the assumption of a constant frictional coefficient. No dynamic instabilities can occur. Bhattacharya and Viesca (2019) and Viesca (2021) showed that, in this particular case, the one-way coupled hydro-mechanical problem is self-similar: the shear crack front propagates strictly proportional to the pore-pressure diffusion front

$$\frac{a(t)}{\ell_d(t)} = \lambda, \tag{11}$$

where λ is simply the ratio between the shear crack length and the pore-pressure diffusion front. Values of λ lower or greater than 1 means that the crack lags or outpaces the diffusion of pore-pressure, respectively. Using scaling analysis, they also showed that the solution of the problem is governed by a single dimensionless parameter

$$\mathcal{T} = \left(\frac{ft'_{n,o} - t_{s,o}}{f\Delta P}\right), \tag{12}$$

which can be obtained by scaling shear tractions, spatial variables and slip in the shear elasticity equation (2), respectively, with ambient fracture shear strength $ft'_{n,o}$, fracture half-length L and $l_* = \dfrac{f\Delta P}{E'}L$ (the latter being a length-scale that results from the normalization of elasticity equation and yielding criterion (1)).

It is interesting to note that the $\mathcal{T}$ parameter includes i) the distance to failure $ft'_{n,o} - t_{s,o}$ that quantifies how far the fracture/fault stress state is from failure prior fluid injection and ii) the destabilizing effect due to pressurization $f\Delta P$. For this reason we call this parameter as *fracture-stress-injection* parameter.

Following the nomenclature of Garagash and Germanovich (2012), we define the condition when the crack lags well behind the fluid front ($\lambda \ll 1$) as *marginally pressurized* condition. Indeed, this occurs when injection over-pressure is just enough to activate slip, i.e. when $f\Delta P \simeq ft'_{n,o} - t_{s,o}$ and hence when $\mathcal{T} \to 1$. On the other hand, in the limit when $\mathcal{T} \to 0$, the crack rapidly outpaces the fluid front upon fluid injection ($\lambda \gg 1$). Whilst such a condition can be attained for increasing values of normalized injection over-pressure, the ratio $\Delta P/t'_{n,o}$ must be below 1 in order to avoid tensile opening. This implies that the limit $\mathcal{T} \to 0$ can be achieved only when the fault is critically stressed prior fluid injection, i.e. when $t_{s,o} \simeq ft'_{n,o}$. For this reason, we define this limit as *critically stressed* limit.

By considering these two limiting behaviors, Bhattacharya and Viesca (2019) derived two corresponding asymptotic solutions that link the $\mathcal{T}$ parameter with the self-similarity factor λas follows:

$$\begin{aligned} &\mathcal{T} = 1 - \lambda\frac{4}{\pi^{3/2}} \qquad \text{(Marginally Pressurized)} \\ &\mathcal{T} = \frac{2}{\pi^{3/2}\lambda} \qquad \text{(Critically Stressed)} \end{aligned} \tag{13}$$

For a given value of $\mathcal{T}$, Equation (13) can be easily inverted to estimate the λ parameter, which can then be used to evaluate the corresponding slip distribution obtained in (Viesca 2021). Notably, the analytical solutions of the slip distributions follow

$$\delta(\bar{x}) \simeq \frac{\lambda^2\ell_d(t)f\Delta P}{E'/4}\frac{2}{\pi^{3/2}}\left(\sqrt{1-\bar{x}^2} - \bar{x}^2\text{Atanh}\sqrt{1-\bar{x}^2}\right) \tag{14}$$

in the marginally pressurized limit, and

$$\begin{aligned} &\delta(\bar{x}) \simeq \frac{\ell_d(t)f\Delta P}{E'/4}\frac{2}{\pi^{3/2}}\left(\text{Atanh}\sqrt{1-\bar{x}^2} - \sqrt{1-\bar{x}^2}\right) \\ &\text{(Outer solution)} \\ &\delta(x/\ell_d(t)) \simeq \delta(0) - \frac{\ell_d(t)f\Delta P}{\mu}\int_0^{x/\ell_d(t)}\left[\frac{1}{\pi}\int_{-\infty}^{\infty}\frac{\text{erfc}(\hat{s})}{\hat{x}-\hat{s}}\text{d}\hat{s}\right]\text{d}\hat{x} \\ &\text{(Inner solution)} \end{aligned} \tag{15}$$

in the critically stressed limit[2]. Note that the slip distribution in the critically stressed limit is decomposed into an outer asymptotic solution that is valid on distances comparable to the rupture distance $a(t)$ (i.e. when $|\bar{x}| = |x/a(t)| \sim 1$), and an inner asymptotic solution valid on distances comparable to the diffusion length scale $\ell_d(t)$ [see (Viesca 2021) for the complete details of the solution].

From Equations (11) and (15), we observe that rupture velocity is $\lambda\sqrt{\alpha}/\sqrt{t}$ and the slip rate scales as $\sqrt{\alpha}f\Delta P/\left(E'\sqrt{t}\right)$. Taking realistic values $f = 0.6$, $E' = 50$ GPa, ΔP =10 MPa and $\alpha = 10^{-3}\text{m}^2/s$, after few seconds, we obtain micro meters per second for the slip rate and, assuming $\lambda \sim 100$ (critically stressed condition), a rupture speed of 1 m/s (clearly below the Rayleigh wave speed). This kind of rupture is, therefore, clearly aseismic.

3.2 Aseismic Moment

Using the asymptotic slip solutions previously reported, we can take a further step and derive

[2] The slip at the centre is obtained by matching the inner with the outer solution at intermediate distances and is given by $\delta(0) \simeq \frac{\ell_d(t)f\Delta P}{\mu}\frac{2}{\pi^{3/2}}(\ln(2\lambda) + \gamma/2)$, where γ is the Euler-Maraschoni constant (Viesca 2021).

closed-form expressions of the scalar aseismic moment $M_o(t) = E/(2(1+\nu)) \int_{-a(t)}^{a(t)} \delta(x)\mathrm{d}x$ (Aki 1966) for the two limiting regimes. In the marginally pressurized limit, we integrate the analytical solution (14) and obtain

$$M_o(t) \simeq \frac{4}{3\sqrt{\pi}} \cdot \left(\frac{a(t)^3 f \Delta P (1-\nu)}{\ell_d(t)} \right) \tag{16}$$

In the critically stressed limit, the pressurization region is always very confined near injection point ($\ell_d \gtrsim 0$), while the slipping patch continuously accelerates and outpaces pore-fluid front ($a(t) \gg \ell_d(t)$). The pressure distribution can be effectively replaced by an equivalent "point-force" distribution and the second term of the inner asymptotic solution (15)b can be neglected. The main contribution to the spatial slip accumulation is thus given by the outer asymptotic solution and, for this reason, we use its analytical expression (15)a to obtain the expression of the scalar aseismic moment in the critically stressed limit as follows:

$$M_o(t) \simeq \frac{2}{\sqrt{\pi}} \cdot \left(a(t) f \Delta P (1-\nu) \ell_d(t) \right) \tag{17}$$

Interestingly, we find that the aseismic moment scales linearly to pressurization time t in both limits (since $a(t) = \lambda \ell_d(t)$ and $\ell_d(t) = \sqrt{4\alpha t}$). If we define the injected volume as $V_{\mathrm{inj}} = Q_{\mathrm{inj}} \cdot t$, with $Q_{\mathrm{inj}} = -\frac{w_h k_f}{\mu} \frac{\partial \bar{p}}{\partial x}|_{x=0^\pm}$ being the fluid flux entering into the fault at injection point $x = 0$, using Equation (9) we can obtain its analytical expression

$$V_{\mathrm{inj}}(t) = \frac{2 k_f w_h \Delta P \sqrt{t}}{\sqrt{\pi} \mu \sqrt{\alpha}}, \tag{18}$$

and thus come to the observation that the aseismic moment, in both marginally pressurized and critically stressed limit, scales *quadratically* to the injected volume.

Indeed, by replacing time t in Equations (16) and (17) with the corresponding expression obtained from Equation (18), after few manipulations we find that the aseismic moment can be expressed as

$$M_o(t) \simeq \frac{4}{3}\sqrt{\pi} \left(\frac{\lambda^3 f (1-\nu)}{\beta^2 w_h^2 \Delta P} \right) V_{\mathrm{inj}}^2 \tag{19}$$

in the marginally pressurized limit, and as

$$M_o(t) \simeq 2\sqrt{\pi} \left(\frac{\lambda f (1-\nu)}{\beta^2 w_h^2 \Delta P} \right) V_{\mathrm{inj}}^2 \tag{20}$$

in the critically stressed limit. If we introduce the following characteristic scales for the aseismic moment and the injected volume

$$\frac{V_{\mathrm{inj}}(t)}{w_h \beta \Delta P L} \to \mathcal{V}_{\mathrm{inj}} \qquad \frac{M_o(t)}{f \Delta P L^2 (1-\nu)/2} \to \mathcal{M}_o, \tag{21}$$

we can express these two scalar quantities in function of only the dimensionless fracture-stress-injection parameter:

$$\begin{aligned} \mathcal{M}_o &\simeq \frac{1}{24}\pi^5 (1-\mathcal{T})^3 \cdot \mathcal{V}_{\mathrm{inj}}^2 \qquad \text{(Marginally Pressurized)} \\ \mathcal{M}_o &\simeq \frac{8}{\pi \mathcal{T}} \cdot \mathcal{V}_{\mathrm{inj}}^2 \qquad \text{(Critically Stressed)} \end{aligned} \tag{22}$$

Not surprisingly, the aseismic moment, in the marginally pressurized limit, decreases non-linearly with increasing values of $\mathcal{T}$ parameter and vanishes when $\mathcal{T} \to 1$. Conversely, in the critically stressed limit, the aseismic moment is unbounded with respect to the parameter $\mathcal{T}$ and a singularity appears when $\mathcal{T} \to 0$, which corresponds for example to the case where prior to injection the system is on the verge of failure.

3.3 Verification

The theoretical considerations previously recalled provide important solutions against which we verify our numerical solver. We consider a 1-dimensional planar fracture and discretize its total length $2L$ with 2000 straight finite elements. We fix the injection over-pressure ΔP as well as the friction coefficient f, and vary the initial effective stress state on the fracture plane, in order to obtain different values of $\mathcal{T}$ parameter to simulate the marginally pressurized and critically stressed limit. Figure 2a displays the temporal evolution of crack half-length $a(t)/L$ for different values of fracture-stress-injection parameter. We can note that the slipping patch grows in time always quasi-statically for each value of $\mathcal{T}$ parameter considered, with its tips located inside or ahead of the pressurized region. These different scenarios do depend on the value of $\mathcal{T}$ and it can be easily grasped by comparing the numerical results with the blue dashed line that represents the case in which the fluid front coincides with crack tips ($\lambda = 1$). In the marginally pressurized limit (large values of $\mathcal{T}$), the slipping patch lags well behind the pressurized region, while the opposite occurs for low values of $\mathcal{T}$ at all times. It is worth mentioning that the coefficient of proportionality λ obtained with different values of $\mathcal{T}$ parameter in the two limiting conditions, i.e. $\mathcal{T}$=0.9, 0.8 and $\mathcal{T}$=0.1, 0.15, matches perfectly with the analytical expressions (13) (see Fig. 2c). Furthermore, panels (b) and (d) in Fig. 2 show that the relative error in terms of temporal evolution of crack half-length is always below 2%, under both marginally pressurized and critically stressed conditions.

A very good agreement with the analytical solutions (14) and (15) is also obtained in terms of slip distributions. As demonstrated in Fig. 3a, c, the numerical results in the

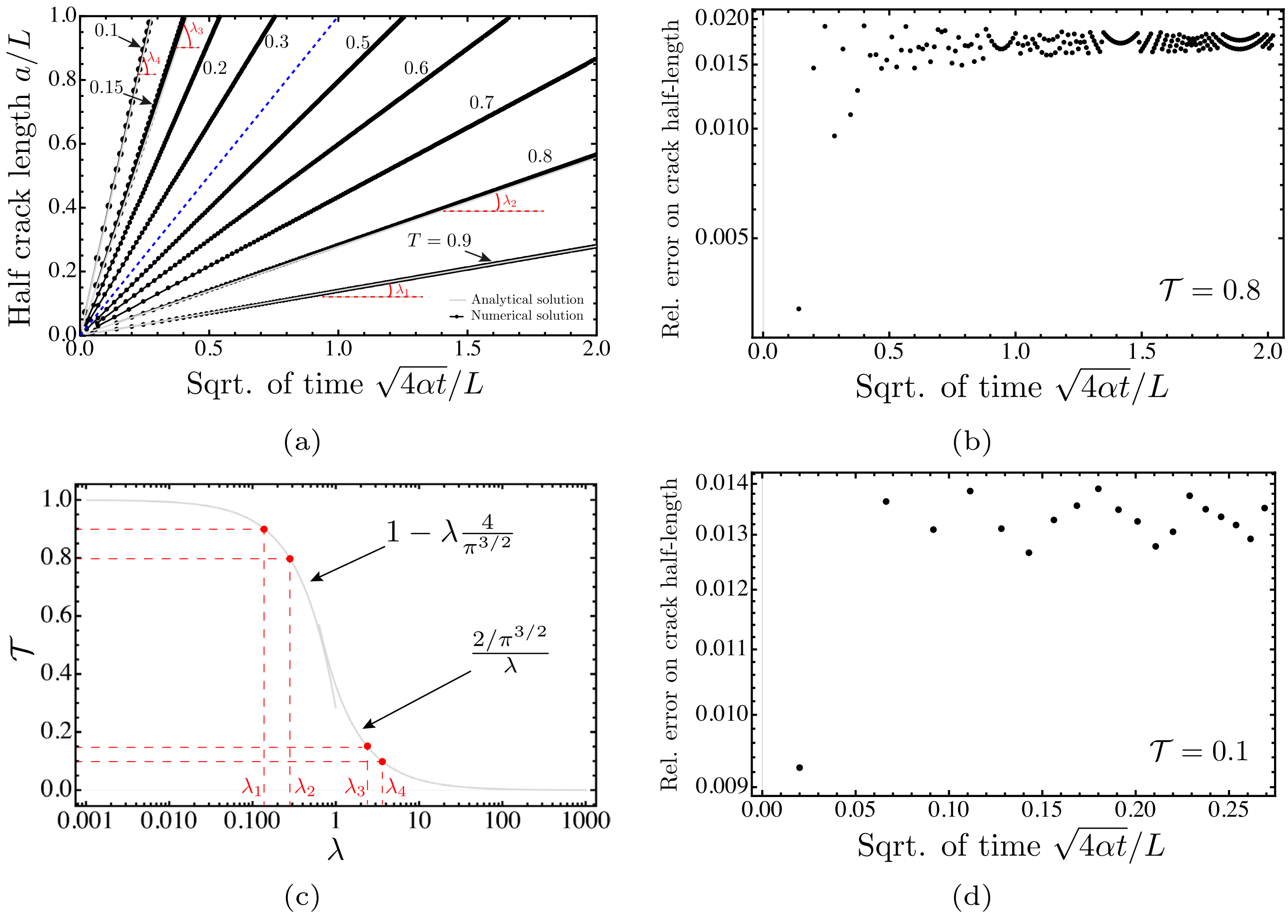

Fig. 2 **a** Evolution of normalized crack half-length $a(t)/L$ (where L is half-length of the fault) with normalized time $\sqrt{4\alpha t}/L$, for different values of $\mathcal{T}$ parameter. The blue dashed line represents the scenario in which fluid front and shear crack tips coincide (i.e. $\lambda = 1$). The obtained self-similarity parameter λ for two numerical simulations corresponding to marginally pressurized ($\mathcal{T} = 0.9, 0.8$) and critically stressed ($\mathcal{T} = 0.1, 0.15$) limiting conditions matches the one retrieved from the asymptotic analytical solutions (13) [see **c**]. **b**, **d** Relative error in terms of time evolution of crack half-length for one marginally pressurized (**b**) and critically stressed (**d**) scenario

marginally pressurized limit collapse in one curve due to the scaling adopted and match perfectly with the asymptotic solution (14). The absolute error as well as the relative error are very small everywhere within the crack, with the latter that increases near fracture tips (due to the fact that slip goes to zero such that the absolute error provides a true comparison near the tip). Similar results are obtained in the critically stressed limit: the numerical result matches very well with the outer asymptotic solution for $|x/a(t)| \lesssim 1$, as well as with the inner asymptotic solution near injection point $|x/a(t)| \sim 0$, i.e. within the pressurization region (see Fig. 3b). The relative error in panel (d) is everywhere below 1% in the centre region around the injection point, and the absolute error drops to very small values near fracture tips.

Finally, Fig. 4 shows the aseismic moment evolution as function of normalized time (a) and normalized injected volume (b), in both marginally pressurized (gray) and critically stressed (orange) limit. On the left panel, we can observe that our numerical results (empty circles) are in very good agreement with the analytical expressions (16) and (17) under both limit conditions. Note, however, that the lower the $\mathcal{T}$ parameter, the closer the numerical aseismic moment to the analytical expression (17) (due to the lower spatial effect of pore-fluid pressurization). Similarly, the log–log plot on the right panel shows a good match between our numerical results and the analytical expressions (22) (denoted by dashed lines). The quadratic scaling between normalized injected volume and aseismic moment can be grasped by comparing the slopes of all the analytical and numerical curves with the one of the hypothenuse of the small black triangle (which is equal to 2).

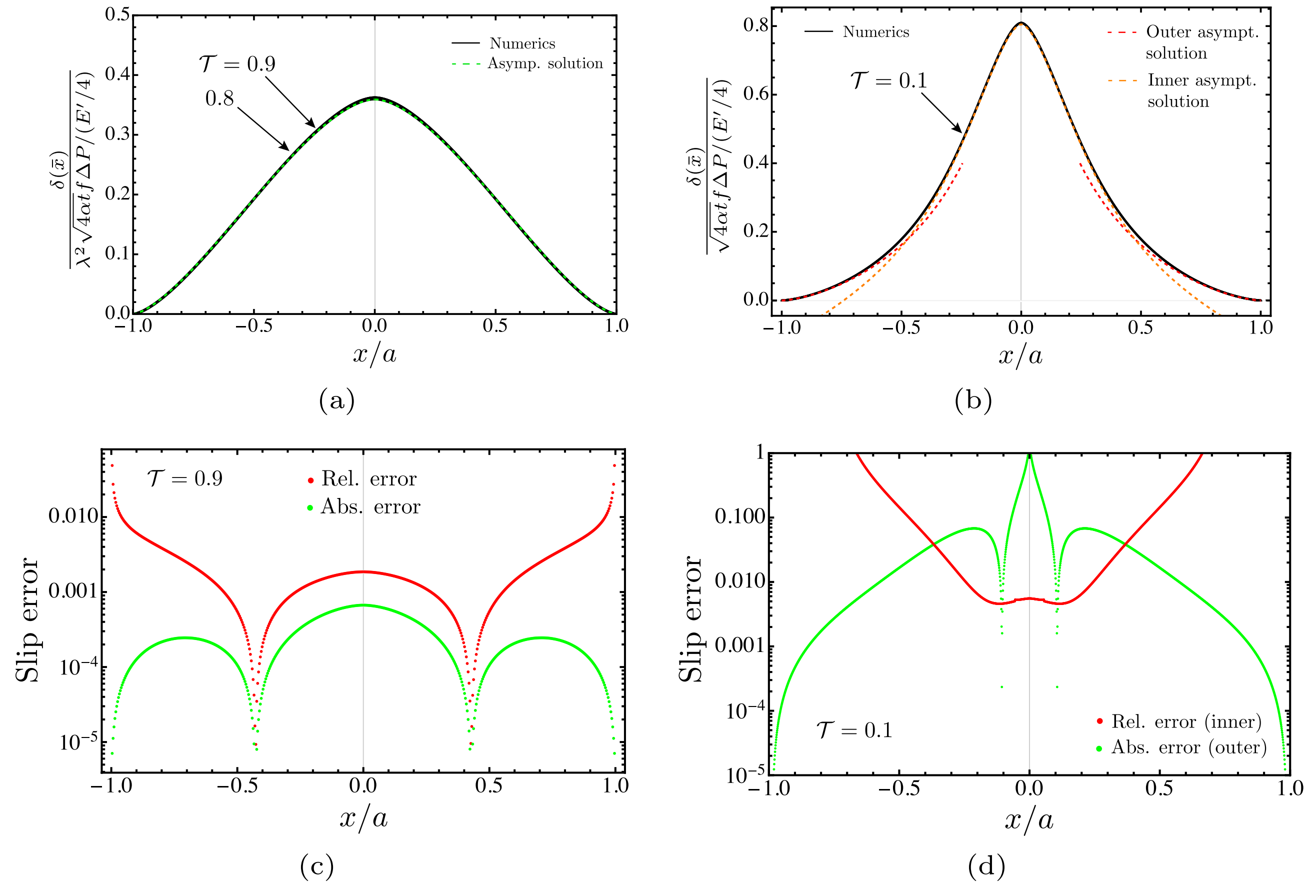

Fig. 3 **a**, **c** Comparison between normalized slip profiles for marginally pressurized conditions (which collapse into one black curve due to scaling adopted) and asymptotic solution (14), together with the corresponding relative and absolute errors. **b** Comparison between normalized slip profile for $\mathcal{T}=0.1$ (critically stressed condition) and asymptotic inner and outer solutions (15). The corresponding relative and absolute errors are displayed in **d**, with the former calculated with respect to the inner solution (15b) and the latter with respect to the outer solution (15a)

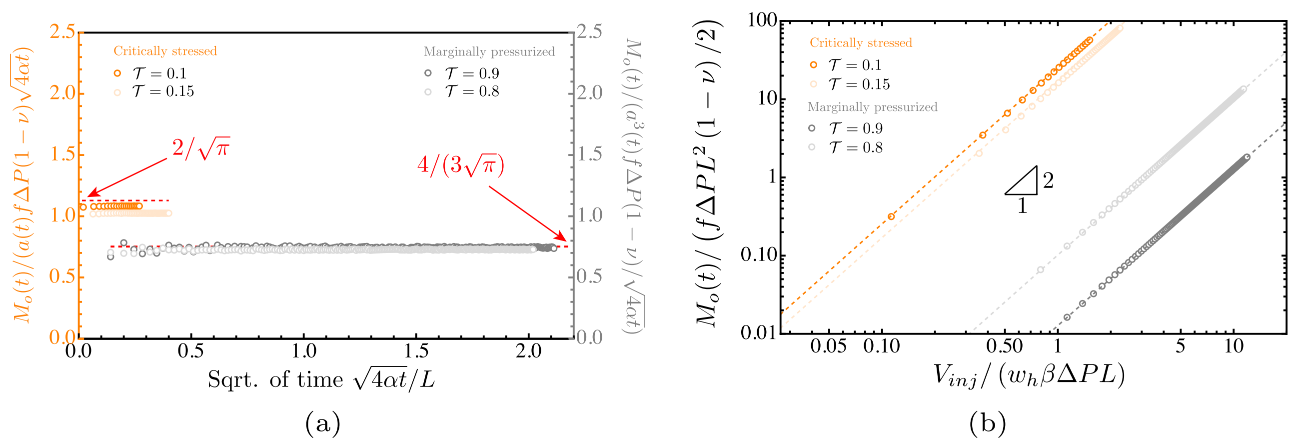

Fig. 4 **a** Time evolution of normalized aseismic moment in both critically stressed conditions (orange) and marginally pressurized conditions (gray). The scaling adopted for the two limits is directly obtained from analytical expressions (16) and (17). **b** Evolution of normalized aseismic moment with normalized injected volume in a log–log plot, for different values of fracture-stress-injection parameters $\mathcal{T}$. Dashed lines refer to the corresponding analytical solutions (22)

4 Injection in a Discrete Fracture Network

Now, we extend the previous findings to the case in which fluid is injected in one fracture that is hydraulically connected to a large number of pre-existing fractures, forming a Discrete Fracture Network. In the next sub-sections, we first describe the DFN model adopted in this contribution and then present the key dimensionless parameters that will guide our numerical investigations.

4.1 DFN Model

Formally, a DFN model provides the number of fractures in any given volume, with given lengths and orientations (Davy et al. 2006). Several fracture distributions models have been introduced in literature, such as lognormal distribution, gamma law, exponential law among others (see Bonnet et al. (2001); Lei et al. (2017) for reviews). Each distribution model, however, must contain a scaling law that assembles scattered real data at different scales into an unified scaling model.

In this contribution, we adopt a distribution model that contains two scaling laws: a fractal density (given by the fractal dimension D_{2d}) and a power-law distribution for fracture length generation (characterised by an exponent b) with cut-off for minimum and maximum fracture lengths (denoted by $l_{\min}$ and $l_{\max}$, respectively). This choice has been used in numerous studies at different scales and in different tectonic settings (Hatton et al. 1994; Sornette et al. 1993; Anders and Wiltschko 1994; Kranz 1983; Walmann et al. 1996). Assuming fracture lengths, positions (or density) and orientations independent entities, we can write the DFN model as

$$N_{2d}(L,l,\theta,\psi) = \rho(\theta,\psi)L^{D_{2d}}l^{-b}, \quad \text{for} \quad l \in \left[l_{\min}, l_{\max}\right] \tag{23}$$

where $\rho(\theta,\psi)$ is the fracture density term, which depends on orientations θ and positions ψ. Note that the only intrinsic characteristic length scales in this model are the smallest $l_{\min}$ and the largest $l_{\max}$ fracture lengths. The exponents D_{2d} and b quantify the scaling aspects of the DFN model (Lei and Wang 2016; Lei and Gao 2018): the former governs the fracture density, whereas the latter governs the lengths distribution. According to extensive outcrop data, D_{2d} typically varies between 1.5 and 2.0, whereas b ranges between 1.2 and 3.5 (Bonnet et al. 2001). In this investigation, we assume that fractures are uniformly distributed within the region of interest $L \times L$, with random locations and orientations (albeit this may not reflect most of the real cases, in which discrete sets of joints with given orientations are observed). This assumption implies that the fractal dimension D_{2d} equals the Euclidean dimension and hence $D_{2d} = 2$ (homogeneous and isotropic case).

In order to build a DFN model representative of systems of various sizes, we normalize (23) with $L^{D_{2d}}$ and $\dfrac{(l_{\max}l_{\min})^{-b}(l_{\max}^{b}l_{\min} - l_{\max}l_{\min}^{b}) \cdot \rho(\theta,\psi)}{-1+b}$, the latter being the number of fractures with length greater than $l_{\min}$ but lower than $l_{\max}$. We obtain

$$n_{2d}(l) = \frac{(-1+b)(l_{\max}l_{\min})^{b}}{l_{\max}^{b}l_{\min} - l_{\max}l_{\min}^{b}} \cdot l^{-b}, \quad \text{for} \quad l \in \left[l_{\min}, l_{\max}\right] \tag{24}$$

which represents the scaling law for fracture lengths for a given DFN. Typically, this law must span at least two orders of magnitude. It is worth mentioning that the choice of a given scaling law strongly impacts fluid flow organization, especially if flow is confined only inside the DFN. A parameter that assesses the geometrical connectivity of a DFN is the *percolation* parameter, which is commonly denoted in literature as p. For non-fractal discrete fracture networks (like the ones used in this contribution), such a dimensionless parameter is defined as (Bour and Davy 1997)

$$p(l) = \int_{l_{\min}}^{l_{\max}} \frac{n_{2d}(l)l^2}{L^2} \mathrm{d}l. \tag{25}$$

The larger is the percolation parameter, the more connected is the system and thus the more homogeneous is the fluid diffusion inside the DFN. Typically, a DFN is *statistically connected* if p is greater than a percolation threshold p_c, with $p_c \sim 5.6$ for 2D networks (Bour and Davy 1997).

4.2 Governing Dimensionless Parameters

The scaling analysis of the governing equations (elasticity equations (2), yielding criterion (1) and fluid mass conservation equation (3)) is similar to the one proposed by Bhattacharya and Viesca (2019) for the case of injection in a planar shear fracture (and discussed in Sect. 3.1). However, for a Discrete Fracture Network, fluid flow is not known analytically, but is part of the numerical solution of the coupled hydro-mechanical problem. Without loss of generality, we can express the pore fluid over-pressure field as

$$\bar{p}(\mathbf{x},t) = \Delta P \times \mathcal{H}\left(\theta^k, \alpha, r, p, t\right), \tag{26}$$

where $\mathcal{H}$ is a dimensionless function that depends on local fracture orientation θ of fracture ^{k}, pressurization time t, constant hydraulic diffusivity α, percolation parameter p, and distance to injection point r. Following the same scaling procedure qualitatively described in Sect. 3.1, but now considering the generic over-pressure field (26), it is straightforward to show that the hydro-mechanical problem in the case of injection in a DFN is governed by a family of dimensionless parameters, namely one for each pre-existing fracture

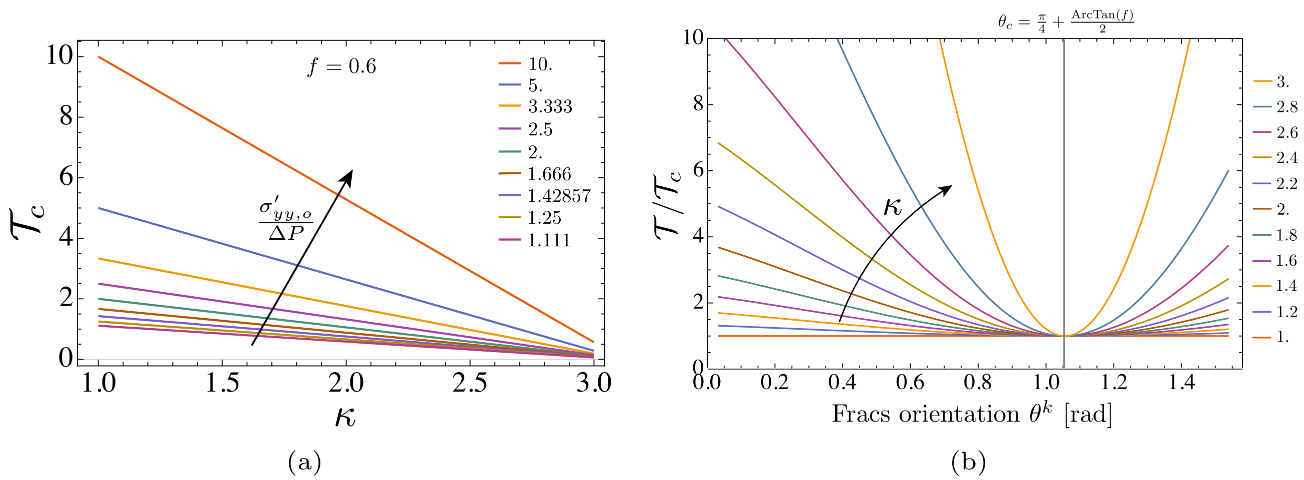

Fig. 5 **a** Variation of the critical $\mathcal{T}$ parameter in function of effective stress anisotropy ratio κ and increasing values of the inverse of normalized injection over-pressure $\frac{\sigma'_{yy,o}}{\Delta P}$, for a fixed value of friction coefficient $f = 0.6$. **b** Variation of $\mathcal{T}/\mathcal{T}_c$ in function of local fracture orientation θ^k and increasing values of effective stress anisotropy ratio κ, for a fixed value of friction coefficient $f = 0.6$. The grey vertical line corresponds to the critical fracture orientation $\theta_c = \pi/4 + \frac{\text{ArcTan}(f)}{2} \simeq 1.056$ radians

$$\mathcal{T} = \frac{f t'^{,k}_{n,o}\left(\theta^k, \sigma'_{xx,o}, \sigma'_{yy,o}\right) - t^k_{s,o}\left(\theta^k, \sigma'_{xx,o}, \sigma'_{yy,o}\right)}{f \Delta P}, \tag{27}$$

on top of the percolation parameter p (25) that characterizes the geometrical connectivity of the DFN.

The initial effective tractions on each fracture can be obtained by projecting the principal effective stress tensor $\Sigma = \begin{pmatrix} \sigma'_{xx,o} & 0 \\ 0 & \sigma'_{yy,o} \end{pmatrix}$ onto each fracture plane. Assuming θ the angle between the trace of fracture ^{k} and the direction of the minimum far-field principal effective stress $\sigma'_{yy,o}$ (in absolute terms), we get

$$\begin{aligned} t'^{,k}_{n,o} &= \sigma'_{xx,o} \cos(\theta^k)^2 + \sigma'_{yy,o} \sin(\theta^k)^2 \\ t^k_{s,o} &= \sigma'_{xx,o} \cos(\theta^k)\sin(\theta^k) - \sigma'_{yy,o} \sin(\theta^k)\cos(\theta^k) \end{aligned} \tag{28}$$

For a given pressurization scenario, large values of $\mathcal{T}$ parameter suggest that the fractures are not favourably oriented with respect to the in-situ stress field. On the contrary, low values of $\mathcal{T}$ suggest that the fractures are critically stressed at ambient conditions and thus prompt to fail upon stress perturbation. Given an initial effective stress state, the critical orientation at which the $\mathcal{T}$ parameter reaches a minimum value or, equivalently, at which the distance to failure is minimum, can be obtained knowing the in-situ friction coefficient and reads

$$\theta_c = \pm\left(\frac{\pi}{4} + \frac{\text{ArcTan}(f)}{2}\right) \tag{29}$$

The expression of $\mathcal{T}$ parameter at critical angle θ_c, therefore, can be retrieved by replacing (29) into (27-28) and reads[3]

$$\mathcal{T}_c = \frac{\sigma'_{yy,o}}{2f\Delta P}\left(f(\kappa+1) - \sqrt{f^2+1}(\kappa - 1)\right) \tag{30}$$

where $\kappa = \frac{\sigma'_{xx,o}}{\sigma'_{yy,o}} \geq 1$ is the in-situ effective stress anisotropy ratio. It is interesting to note that $\mathcal{T}_c$ is given by a product of two functions: one strictly related to in-situ conditions (namely friction coefficient and far-field stress state), while the other is related to the pressurization scenario. This is an unique parameter that characterizes each DFN and is the complete analogy of the $\mathcal{T}$ parameter introduced by Bhattacharya and Viesca (2019) for the case of injection in a single shear fracture (see Sect. 3).

As displayed in Fig. 5a, for a given pressurization scenario $\Delta P/\sigma'_{yy,o}$ (or its inverse), large values of κ lead to low values of $\mathcal{T}_c$ (with the maximum value of κ achieved in the limit when $\mathcal{T}_c \to 0$). This means that the fractures oriented at θ_c are critically stressed and thus prone to fail upon fluid injection. Vice-versa, lower values of κ lead to increasing values of $\mathcal{T}_c$. Hence, even if the fractures are oriented at the critical angle θ_c, the far-field effective stress state induces tractions that well satisfy the activation criterion (1). The maximum value of $\mathcal{T}_c$ is reached in the limit when $\kappa \to 1$, for which $\mathcal{T}_c = \frac{\sigma'_{yy,o}}{\Delta P}$ (always greater than one). Finally, it is worth mentioning that large values of normalized injection

[3] Here we consider only the positive angle.

over-pressure lead to relatively low values of $\mathcal{T}_c$ for any in-situ effective stress states, similarly to the case of injection in a single fracture.

By taking the ratio between the generic $\mathcal{T}$ parameter (27-28) and its value at critical angle $\mathcal{T}_c$ (30), we can uncouple the effect of in-situ conditions and pressurization scenario. Indeed, after few manipulations we obtain

$$\frac{\mathcal{T}}{\mathcal{T}_c} = \frac{2\sqrt{f^2+1}\left(f\kappa\cos^2(\theta^k) - (\kappa-1)\sin(\theta^k)\cos(\theta^k) + f\sin^2(\theta^k)\right)}{1-\kappa+f\left(\sqrt{f^2+1}(\kappa+1)+f(1-\kappa)\right)} \tag{31}$$

Figure 5b displays the variation of $\mathcal{T}/\mathcal{T}_c$ as function of fracture orientation θ^k (expressed in radians) and increasing effective stress anisotropy ratios κ (denoted by the arrow), for a given value of friction coefficient f. Specifically, we consider a friction coefficient of $f = 0.6$ that is a typical value for granitic rocks under confinements between 10 to 80 MPa (Byerlee 1978), with this range being plausible at few kilometer depths. We can readily observe that the orientation at which the $\mathcal{T}$ parameter is minimum always correspond to the critical value θ_c (see grey vertical line), regardless of the value of stress anisotropy ratio κ. Furthermore, for increasing values of κ, only the fractures with orientations similar to θ_c are critically stressed and thus characterized by a ratio of $\mathcal{T}/\mathcal{T}_c$ that tends to one, with $\mathcal{T}_c$ being very close to zero (see panel a). The remaining fractures are instead characterized by initial stress states that are far from failure prior fluid injection (large values of $\mathcal{T}/\mathcal{T}_c$). We refer to this specific condition as critically stressed condition due to the presence of some highly critically stressed fractures in the DFN.

On the other hand, the lower the value of κ, the more uniform the distribution of $\mathcal{T}/\mathcal{T}_c$ over all the fracture angles, implying that more and more fractures are far from being critically stressed. In the limit case of $\kappa = 1$, all the fractures of the DFN are characterized by $\mathcal{T}/\mathcal{T}_c = 1$, with $\mathcal{T}_c$ that has achieved its maximum value equal to $\frac{\sigma'_{yy,o}}{\Delta P}$ (see left panel). Therefore, we define this condition as marginally pressurized condition, in complete analogy with what presented in Sect. 3.

These considerations suggest that a critically stressed DFN (low value of $\mathcal{T}_c$) subjected to fluid injection exhibits fast aseismic slip regardless of the percolation value that characterises its fluid inter-connectivity as well as the value of injection over-pressure (as long as it is sufficient to activate slip). This is because the main driving force for the slipping patch propagation is the stress-interactions between the pre-existing critically stressed fractures. On the other hand, the scenario may change for marginally pressurized or slightly critically stressed DFN characterized by a large/moderate $\mathcal{T}_c$. The aseismic slip propagation in this case is directly affected by pore pressure diffusion inside the DFN and as a result the corresponding percolation parameter plays an important role. Low percolation values may lead to fluid localization and possibly contained ruptures.

In order to verify these fore-thoughts, we present several numerical investigations using a number of DFN realizations with different degrees of fluid percolation (see Appendix 1). Each DFN realization includes 1000 fractures whose lengths are sampled from a power law distribution (24), using different power law coefficients b and maximum fracture length $l_{\max}$ (see Appendix 1 for more details). For a given value of friction coefficient $f = 0.6$ and a given value of normalized injection over-pressure $\frac{\Delta P}{\sigma'_{yy,o}} = 1.0$, we vary the effective stress anisotropy ratio κ in order to reproduce critically stressed and marginally pressurized conditions.

4.3 Marginally Pressurized Conditions

We fixed the effective stress anisotropy ratio at a relative low value $\kappa = 2$, obtaining a moderate value of $\mathcal{T}_c$ (specifically $\mathcal{T}_c \simeq 0.528$) representative of marginally pressurized conditions (for which $\lambda = a(t)/\sqrt{4\alpha t} \ll 1$ for the single fracture case). In each DFN realization considered (see Fig. 14), all the pre-existing fractures within the region of interest $L \times L$ are characterized by a relatively low stress criticality $(f t'^{,k}_{n,o})/t^k_{s,o}$ or a relative large $\mathcal{T}$ parameter. Fluid is injected approximately around the centre of the domain area, i.e. $\sim (L/2, L/2)$, in a point crossed by a pre-existing fracture that is hydraulically connected to at least another one and with an orientation θ different than $\pi/2$ (in order to avoid tensile opening due to the injection condition $\frac{\Delta P}{\sigma'_{yy,o}} = 1.0$). All the simulations are stopped when the normalized over-pressure $\bar{p}/\Delta P$ reached the boundaries of the simulation box.

For sake of space, we do not report all the numerical results in terms of spatial and temporal evolution of pore fluid over-pressure and aseismic rupture extent. As a representative example, we display only those associated with the DFN with percolation parameter $p = 12.21$ (see Fig. 14).

Figure 6 displays the spatial variation of the $\mathcal{T}$ parameter (27) on each pre-existing fracture as a result of the applied far-field effective stress state (see panel b for its representation in the Mohr–Coulomb plot). As one can observe, the effective stress state, which is represented by a circle whose diameter is equal to the difference between the two principal effective stress at ambient conditions (i.e. $\sigma'_{xx,o}$ and $\sigma'_{yy,o}$), is relatively far from the yielding failure line (1) (denoted by red lines). All the pre-existing fractures that are randomly oriented and uniformly distributed within the region $L \times L$ are thus characterised by a $\mathcal{T}$ parameter not lower than its critical value $\mathcal{T}_c \simeq 0.528$ (see panel a).

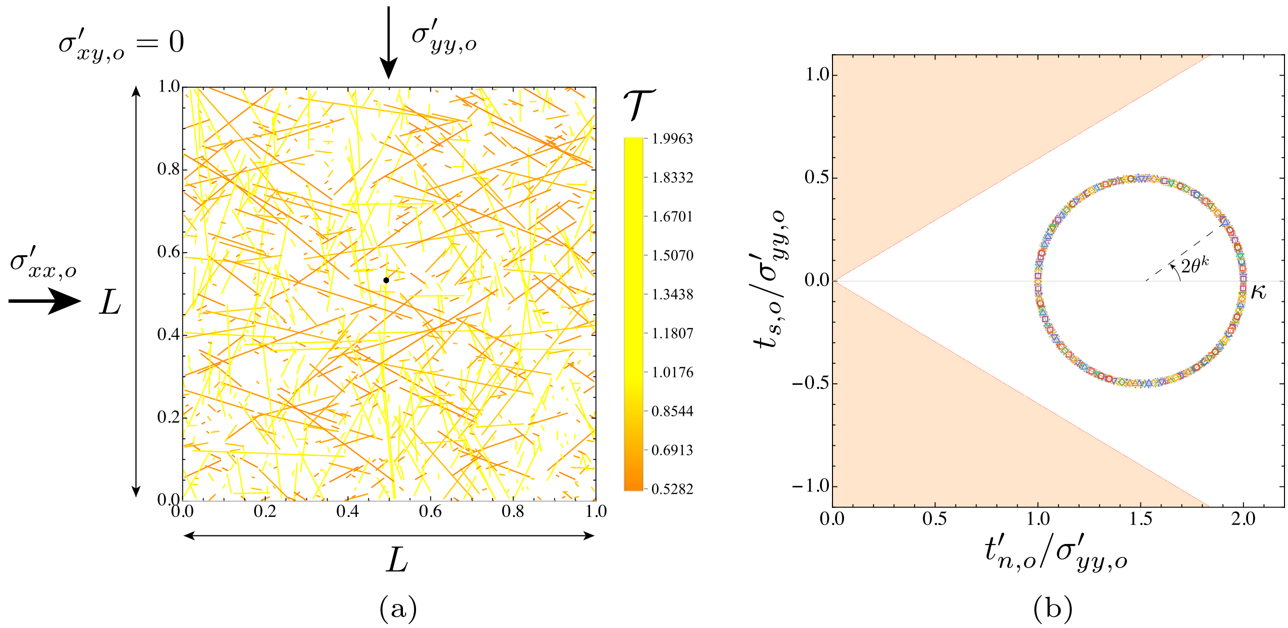

Fig. 6 **a** Marginally pressurized discrete fracture network with percolation parameter $p = 12.21$, subjected to an in-situ principal effective stress state. The color of each fracture denotes the corresponding magnitude of the fracture-stress-injection parameter $\mathcal{T}$ prior fluid injection. The black dot, instead, denotes the location of injection point. **b** Initial effective stress state in the Mohr–Coulomb plane. Note that the effective tractions are normalized with the minimum far-field principal effective stress $\sigma'_{yy,o}$. Along the Mohr–Coulomb circle, whose diameter equals the value of stress anisotropy ratio considered (i.e. $\kappa = 2$), all the uniform stress states of each pre-existing fracture are reported. Since all the pre-existing fractures are randomly oriented within the region $L \times L$, the whole circle is uniformly "covered" by the fractures' initial stress states

We discretized the DFN with 11690 finite straight segments (mean mesh size $0.005L$) and used the numerical methods described in Sect. 2.1 to solve the coupled hydro-mechanical problem. We used a hierarchical approximation of the fully populated elasticity matrix for computational efficiency that resulted in a memory compression ratio of $c_r = 0.114$ with a relative accuracy of 10^{-4} for the approximated far-field contributions [see (Ciardo et al. 2020) and references therein for more details]. This was sufficient to be able to run the simulation with a 2.8 GHz Quad-Core Intel Core i7 processor with 16 GB of memory.

Upon fluid injection in a point located at $\sim (0.493, 0.533)$ (see black dot in Fig. 6a), the slipping patch starts to expand paced by pore fluid diffusion. Because of the in-situ marginally pressurized conditions, the aseismic slipping patch always lags the pressurized region, even at large pressurization times. This can be clearly grasped from Fig. 7 in which the over-pressurized region (left column) is compared to the shear rupture extent (right column), at different normalized time snapshots. At $\sqrt{4\alpha t}/L \simeq 1.045$, the normalised fluid over-pressure $\bar{p}/\Delta P$ has nearly reached the external boundaries of the region $L \times L$, while the slipping patch is confined near the injection point (where the over-pressure is maximum and equal to $\bar{p}/\Delta P = 1.0$). Not surprisingly, such limited extent of aseismic rupture occurs in all the different DFNs considered.

Figure 8, indeed, shows the time evolution of the total rupture length $L_{\text{rupt}}(t)/L$, defined as the total sum of yielded elements during pressurization, for each DFN realization. We can observe that throughout pressurization the total rupture length is always limited for every value of percolation parameter p. Interestingly, at large pressurization time, the rupture length is larger for lower values of DFN percolation. This is because low percolation values promote zones of flow localization where pore fluid over-pressure can increase during sustained injection. On the contrary, a high percolation degree facilitates the dissipation of pore fluid over-pressure via a rather homogeneous radial diffusion from injection point. The rupture lengths evolution reported in Fig. 8 actually confirm these considerations: for $p = 26.75$, the rupture extent is really localized near injection point (i.e. $\max\left(L_{\text{rupt}}(t)/L\right) \simeq 0.004$) throughout the whole pressurization history, whereas for $p = 4.62$ the rupture extent increases in time with the local over-pressure accumulation.

Obviously, these results depend on the level of effective stress anisotropy adopted and the resulting value of $\mathcal{T}_c$. Lower values of κ would lead to larger values of $\mathcal{T}_c$ and thus to even more confined aseismic ruptures or—ultimately—to

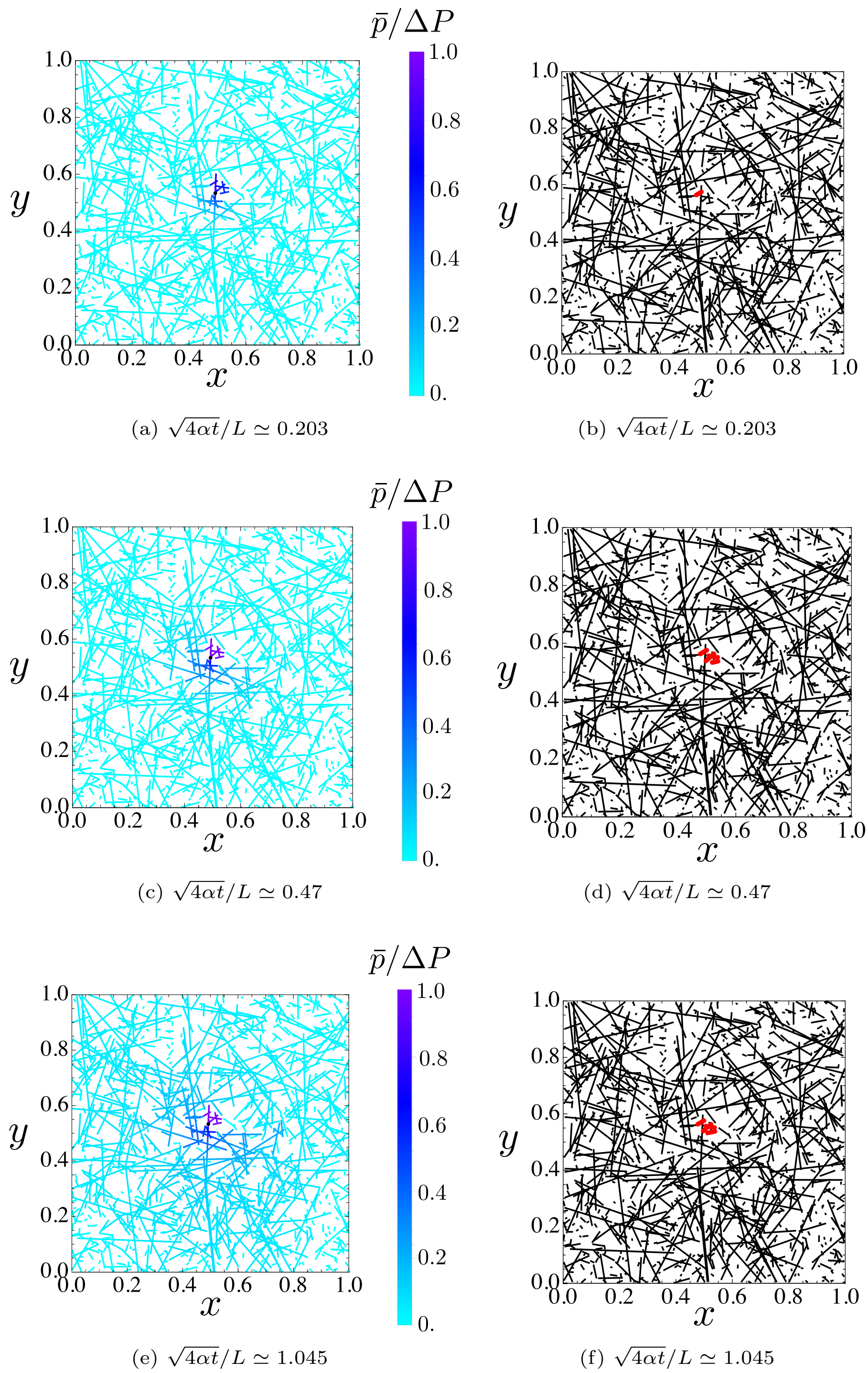

Fig. 7 Evolution of normalized over-pressure $\bar{p}/\Delta P$ (**a**, **c**, **e**) and aseismic rupture extent (denoted by red color—(**b**, **d**, **f**)) along the marginally pressurized DFN with $p = 12.21$, at different normalized time snapshots $\sqrt{4\alpha t}/L$. Fluid is injected at ~ (0.493, 0.533), in one fracture that is hydraulically connected to many others

(a) $\sqrt{4\alpha t}/L \simeq 0.203$ (b) $\sqrt{4\alpha t}/L \simeq 0.203$

(c) $\sqrt{4\alpha t}/L \simeq 0.47$ (d) $\sqrt{4\alpha t}/L \simeq 0.47$

(e) $\sqrt{4\alpha t}/L \simeq 1.045$ (f) $\sqrt{4\alpha t}/L \simeq 1.045$

the absence of any ruptures (i.e. when the injection over-pressure is not enough to activate slip). Finally, it is worth mentioning that the only scenario in which the rupture extent might be similar to the extent of the over-pressurization region is when the percolation parameter of the DFN is very very low. In such a case, in fact, fluid flow is most likely confined in a sub-region of the DFN where, upon over-pressure accumulation, it may lead to its complete rupture (if the stress state is critical enough).

4.4 Critically Stressed Conditions

We ran the same numerical experiments (i.e. same DNF realizations, same injection conditions and same locations of injection point), but now with an effective stress anisotropy

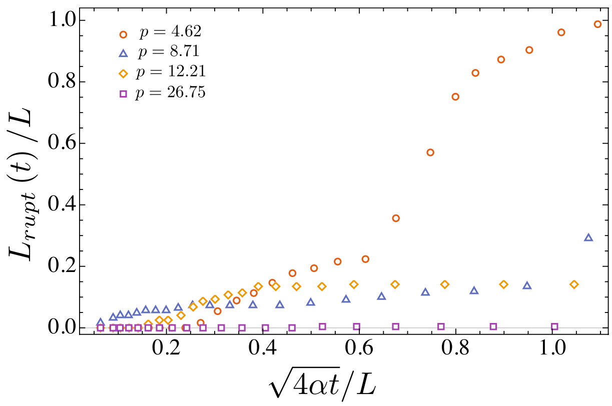

Fig. 8 Time evolution of the normalized total rupture length $L_{\mathrm{rupt}}(t)/L$ for each DFN realization considered (see Appendix 1), in marginally pressurized conditions. p denotes the percolation parameter (25)

ratio set to $\kappa = 3$, representative of critically stressed conditions. This implies that all the pre-existing fractures oriented along the critical angle $\theta_c = \pi/4 + \mathrm{ArcTan}(f)/2 \simeq 60.5°$ are critically stressed and characterized by $\mathcal{T}_c \simeq 0.056$. In other words, they are prompt to fail with little perturbation. Here all the simulations are stopped when the rupture front approached the boundary of the simulation box.

Restricting to the reference case of injection into the DFN with percolation parameter $p = 12.21$, we can observe from Fig. 9a that the fracture in which fluid is injected into is not favourably oriented with respect to far-field stress state: its fracture-stress-injection parameter $\mathcal{T}$ is quite large (albeit the far-field effective stress state is highly critical—see Fig. 9b). Nevertheless, upon fluid injection, pore fluid over-pressure starts to accumulate inside the DFN and activates slip on critically stressed fractures located near injection point (see Fig. 10 at time snapshot $\sqrt{4\alpha t}/L \simeq 0.219$). The activation of these fractures triggers in turn a cascade of other ruptures due to elastic stress interactions between critically stressed pre-existing fractures (denoted by a reddish color in Fig. 9a). The aseismic slipping patch thus propagates outward from injection point significantly faster than the pressurization front. At normalized time $\sqrt{4\alpha t}/L \simeq 1.021$, the pore fluid over-pressure zone is still confined to a surrounding of the injection point, while the slipping patch has propagated almost up to the boundaries of the simulation box. Their relative position, therefore, is reversed with respect to the case of injection in marginally pressurized fractured rock masses. Furthermore, such a fast migration of aseismic slipping patch compared to pore fluid diffusion holds regardless whether the DFN is statistically connected or not.

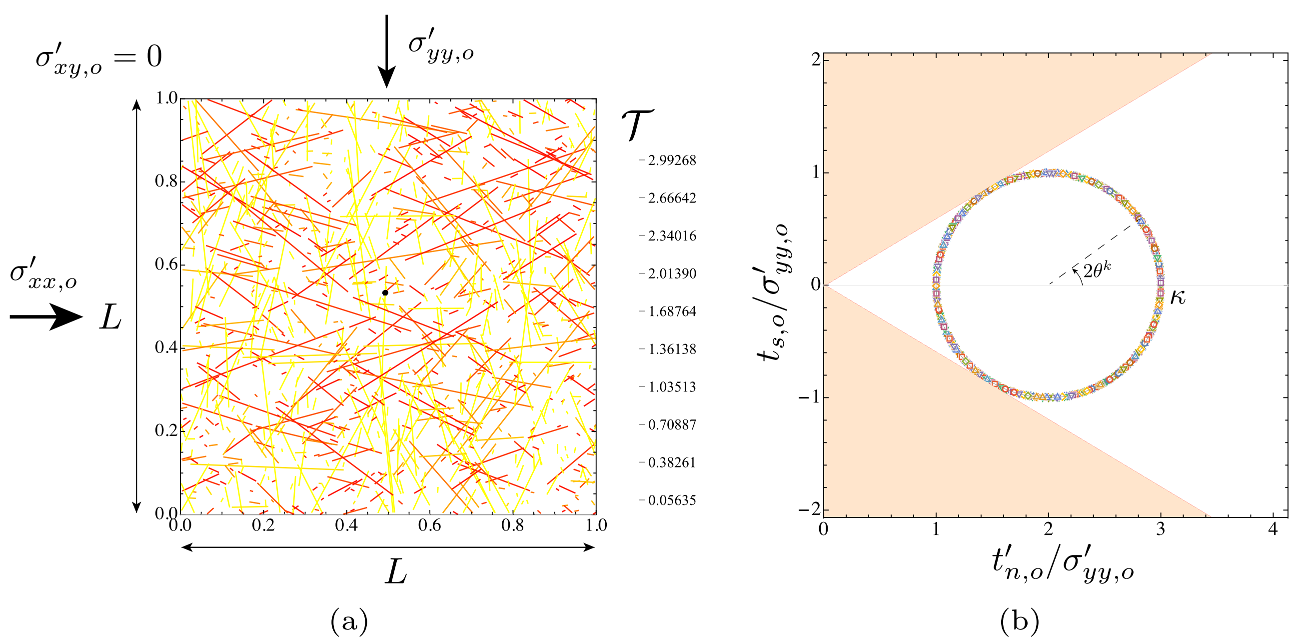

Fig. 9 **a** Critically stressed Discrete Fracture Network with percolation parameter $p = 12.21$, subjected to an in-situ principal effective stress state. The color of each fracture denotes the corresponding magnitude of the fracture-stress-injection parameter $\mathcal{T}$ prior fluid injection. The black dot, instead, denotes the location of injection point. **b** Initial effective stress state in the Mohr–Coulomb plane. Note that the effective tractions are normalized with the minimum far-field principal effective stress $\sigma'_{yy,o}$. Along the Mohr–Coulomb circle, whose diameter equals the value of stress anisotropy ratio considered (i.e. $\kappa = 2$), all the uniform stress states of each pre-existing fracture are reported. Since all the pre-existing fractures are randomly oriented within the region $L \times L$, the whole circle is uniformly "covered" by the fractures' initial stress states

Fig. 10 Evolution of normalized over-pressure $\bar{p}/\Delta P$ (**a**, **c**, **e**) and aseismic rupture extent (denoted by red color—(**b**, **d**, **f**)) along the critically stressed DFN with $p = 12.21$, at different normalized time snapshots $\sqrt{4\alpha t}/L$. Fluid is injected at $\sim (0.493, 0.533)$, in one fracture that is hydraulically connected to many others

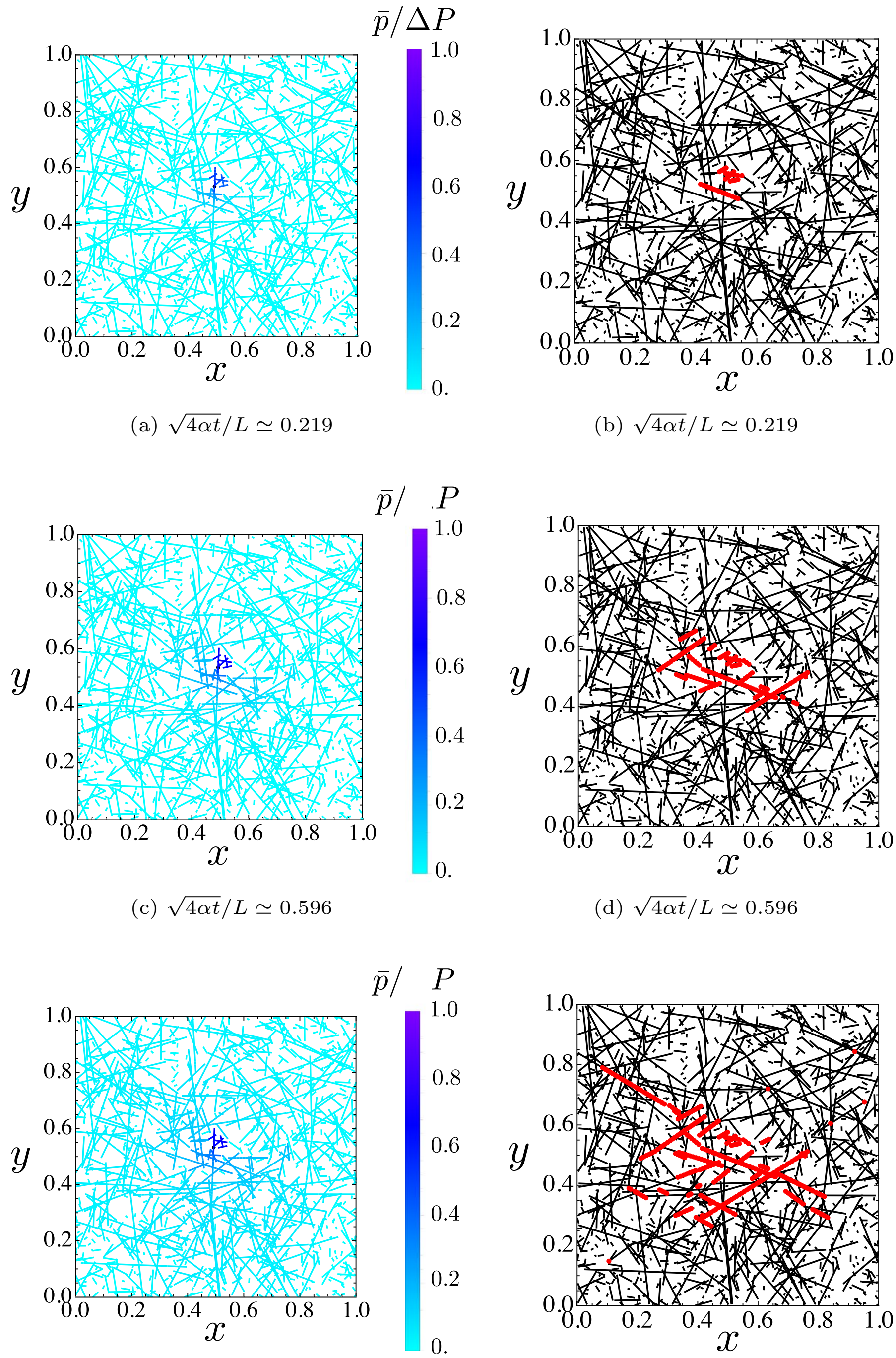

(a) $\sqrt{4\alpha t}/L \simeq 0.219$ (b) $\sqrt{4\alpha t}/L \simeq 0.219$

(c) $\sqrt{4\alpha t}/L \simeq 0.596$ (d) $\sqrt{4\alpha t}/L \simeq 0.596$

(e) $\sqrt{4\alpha t}/L \simeq 1.021$ (f) $\sqrt{4\alpha t}/L \simeq 1.021$

Figure 11 displays the total rupture length as function of pressurization time, for each DFN realization considered. We can notice that, for each value of percolation p, the rupture length increases rapidly and monotonically in time. This suggests that in critically stressed conditions the main driving force for the fast aseismic slip propagation is the elastic stress interactions between favourably oriented fractures (i.e. the fractures oriented approximately at $\theta_c \simeq \pm 60.5°$ with respect to the direction of $\sigma'_{yy,o}$). This is further strengthened by looking at the rose plots reported in Fig. 12, which display the angular histograms of the yielded fractures.[4] For each DFN realization, the majority of yielded fractures are oriented approximately along the critical angle

[4] Note that one pre-existing fracture is considered "yielded" if at least one of its finite element has reached the yielding criterion (1) throughout pressurization and thus has experienced plastic slip.

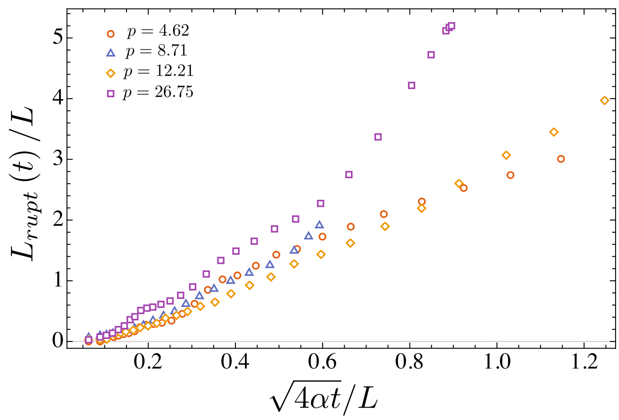

Fig. 11 Time evolution of normalized total rupture length $L_{\text{rupt}}(t)/L$ for each DFN realization considered (see Appendix 1), under critically stressed conditions. p denotes the percolation parameter (25)

θ_c, which, for the value of friction coefficient considered here, is approximately ±60.5° (29).

4.5 Aseismic Moment

Finally, we report how the aseismic moment vary with accumulated injected volume in case fluid is injected in a marginally pressurized or critically stressed DFNs. Referring to the same numerical results presented and discussed in Sects. 4.3 and 4.4, Fig. 13 displays the evolution of scaled $M_o(t)$ as function of normalized $V_{\text{inj}}(t)$ in log-log plots, for all the DFN realizations considered and for the two values of critical $\mathcal{T}$ parameter: $\mathcal{T}_c \simeq 0.528$ (left—marginally pressurized) and $\mathcal{T}_c \simeq 0.056$ (right—critically stressed). Note that the same scaling has been adopted for both plots.

We can readily observe that the aseismic moment scales to the injected volume as $M_o(t) \propto V_{\text{inj}}^2$ in both limiting conditions and regardless the percolation degree of the DFN (see the slopes of each curve that tend to be similar the one of the hypothenuse of the black triangle). In marginally pressurized conditions, however, such a scaling is attained at large injected volumes, with the percolation parameter that affects the factor of proportionality: larger values are obtained at lower percolation degrees due to pore-fluid localization (consistently with the results described in Sect. 4.3). In critically stressed conditions, instead, the aseismic moment tends to scale quadratically with injected volume as soon as slip is activated. Moreover, the subsequent fast migration of aseismic slip due to elastic-stress interactions of favourably oriented fractures tends to result in a constant factor of proportionality, implying that there is a family of solutions that does not depend on the percolation parameter (unlike in marginally pressurized conditions). It is interesting to note that such a factor is lower than the one obtained as if the injection would occur in a single planar fracture, with fracture-stress-injection parameter equal to $\mathcal{T}_c$ (see dark gray line) or equal to the mean value of $\mathcal{T}$ parameters of all the yielded fractures in each realization (see light gray line). This suggests that the cascade of ruptures driven by elastic stress transfer leads to a global "shielding" effect such that the total accumulated slip on a DFN with uniformly distributed and randomly oriented fractures is lower than the corresponding one on a single planar fracture (for the same injection and in-situ conditions).

5 Discussions

5.1 Comparison Between Injection in a Single Fracture and in a Discrete Fracture Network

The problem of injection in a 2-dimensional Discrete Fracture Network with randomly oriented and uniformly distributed fractures described in the previous section shares a lot of similarities with the simpler case of injection in a planar 2D shear fracture (reported in Sect. 3). Here, we describe them and highlight their implications to injection-induced seismicity.

Although the two problems are different, the mechanisms that govern the evolution of aseismic slip driven by pore-fluid diffusion are the same, with a single dimensionless parameter that govern the overall hydro-mechanical response. In the case of injection at constant pressure in a single fracture, we have showed that injection-induced aseismic slip is self-similar in a diffusive manner, with a self-similarity factor that is only function of the fracture-stress-injection parameter $\mathcal{T}$ (12). We have demonstrated that when the $\mathcal{T}$ parameter is large, the aseismic rupture extent lags the pressurization region (marginally pressurized conditions). Vice-versa, when $\mathcal{T}$ parameter is low, slip migrates from injection point much faster than pore-fluid diffusion, with such a quick migration controlled by the stress transfer of the propagating rupture (critically stressed conditions). These scenarios are exactly the same in the case of injection in a marginally pressurized or critically stressed DFN in a global sense, albeit the self-similarity condition is not strictly valid anymore and the governing parameter is the $\mathcal{T}$ parameter evaluated at the critical orientation θ_c (29). This implies that micro-seismicity in deep fractured reservoirs, commonly observed to correlate well with a pore fluid diffusion process and thus thought to migrate away from injection point proportional to the square-root of time (Shapiro et al. 1997, 2002; Parotidis et al. 2003; Hainzl and Ogata 2005; Hainzl et al. 2012; Albaric et al. 2014), might instead be driven by elastic stress interactions between critically stressed fractures. This would notably be the case when $\mathcal{T}_c$ is low in which aseismic slip always outpaces pore pressure front and may trigger micro-seismicity by stress transfer way ahead of the actual location of the pore-pressure disturbance. As a result, the fit of micro-seismicity data (via space-time

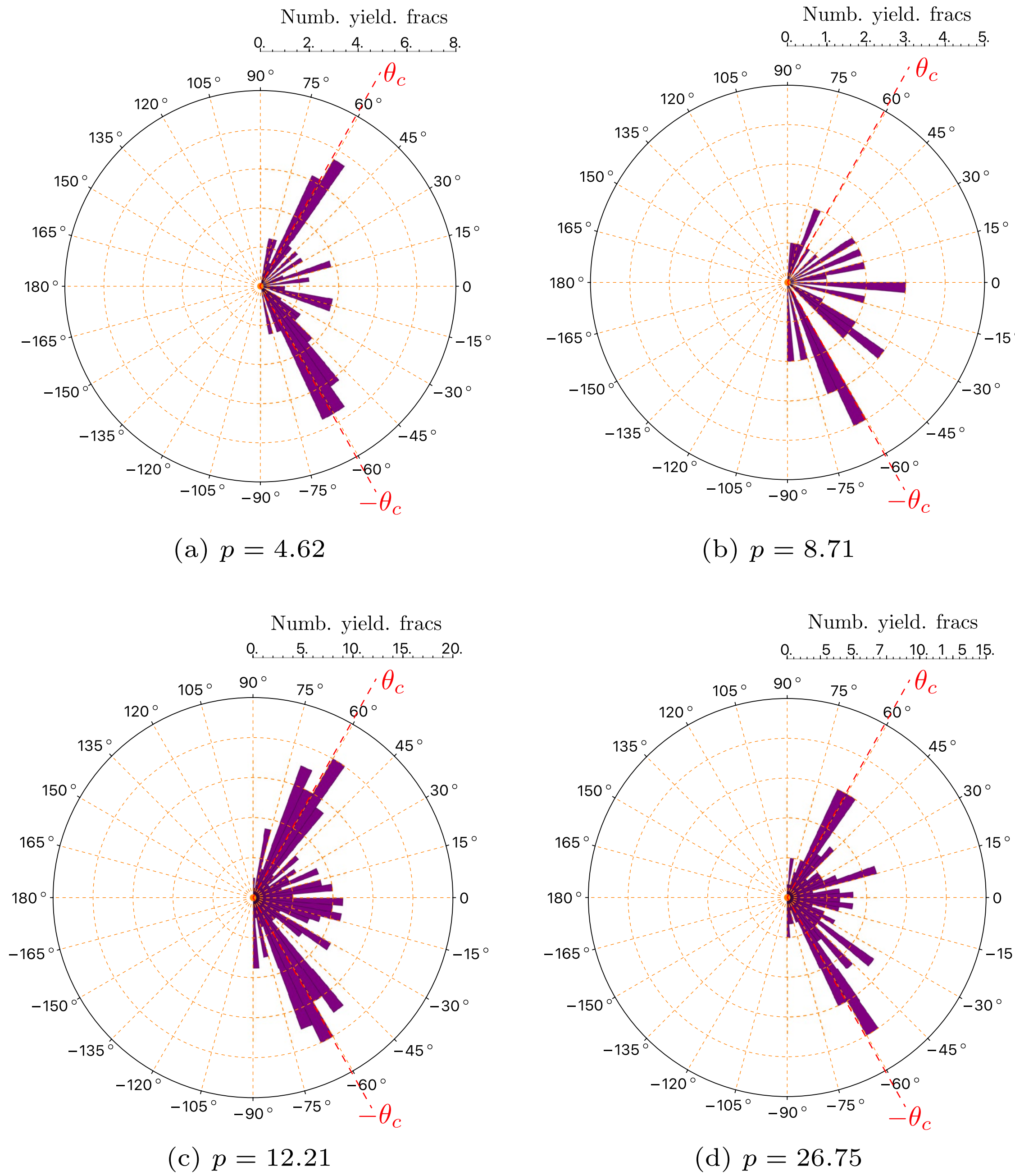

Fig. 12 Angular histograms showing the total number of yielded fractures induced by pressurization, as function of their local orientation θ for each DFN realization considered. A fracture is considered "yielded" when at least one of its element has reached the yielding criterion (1) throughout pressurization and thus has experienced plastic slip. The dashed red lines denote the critical angle $\pm\theta_c$ (29)

migration plots) to infer hydraulic diffusivity α may result in a large over-estimation of the latter.

A number of efforts have been made to understand how the magnitude of induced seismic events vary with operational parameters, such as the total volume of fluid injected (McGarr 2014; Galis et al. 2017) or applied injection conditions: constant injection rate/constant over-pressure (Garagash and Germanovich 2012) or ramp-up of injection rate commonly present in many injection protocols (Ciardo and Rinaldi 2022). These studies are indirectly devoted to understand how to constraint the maximum seismic moment and thus reduce the seismic risk. Although they are of great importance for the design of injection operations, in some cases the relevant contribution to injection-induced moment release in fractured reservoirs may be aseismic (McGarr and Barbour 2018). It is therefore significant to understand how the aseismic moment evolve in function of

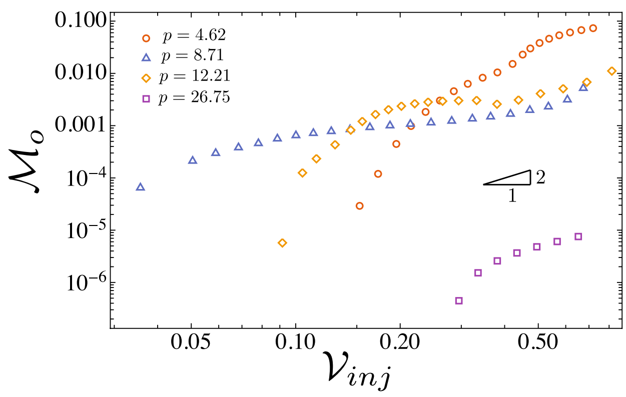

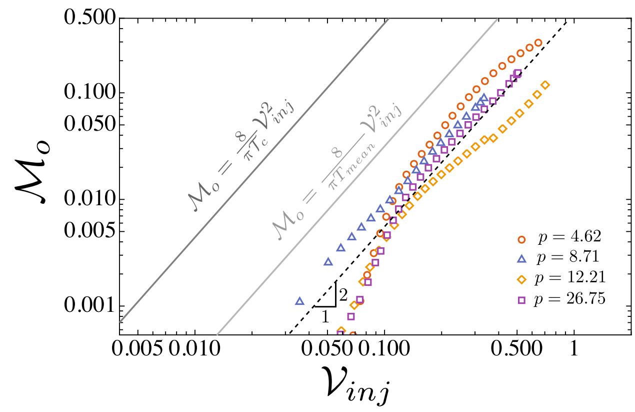

Fig. 13 Log-log plots that display the evolution of normalized aseismic moment with accumulated injected volume, under marginally pressuized conditions (left—$\mathcal{T}_c \simeq 0.528$) and critically stressed conditions (right—$\mathcal{T}_c \simeq 0.056$). The dark gray line represents the analytical solution (22)b valid for a single planar shear fracture with fracture-stress-injection parameter equal to $\mathcal{T}_c \simeq 0.056$, while the light gray line is valid for a single planar shear fracture with fracture-stress-injection parameter equal to the mean value of $\mathcal{T}$ parameters of all the yielded fractures in each realization

operational parameters (such as total volume of fluid injected) when the fractured rock mass is critically stressed or marginally pressurized. Our results show that in both limiting regimes the aseismic moment on a DFN scales quadratically to the injected volume, for an injection at constant over-pressure under plane-strain conditions. The same power-law scaling has been found to be valid for a single planar shear fracture subjected to the same injection condition (see Sect. 3.2). Finally, it is interesting to note that the DFN response in critically stressed conditions is similar to the one of a single planar fracture: the aseismic moment is not significantly affected by geometrical connectivity and scales as $\propto V_{\text{inj}}^2$ with factor of proportionality that is lower than the corresponding one obtained on a single fracture (supposed to be favourably oriented with respect to in-situ stress conditions or supposed to have a fracture-stress-injection parameter $\mathcal{T}$ equal to an average value of all the $\mathcal{T}$ parameters associated with the yielded fractures). A possible explanation for this is the shielding effect between interacting fractures, in a similar way as observed in cases of hydraulic fracturing in naturally fractured rocks [e.g. (Warpinski and Teufel 1987)].

5.2 Modelling Assumptions

Fluid injection in a deep fractured rock mass is a complex hydro-mechanical problem. Large non-linearities arising from the coupling between hydraulic and mechanical deformations make the problem challenging from a computational point of view and, at the same time, difficult to get insight into. In order to properly explore and understand the basic physical mechanisms that take place at depth upon injection, we have made a number of simplifying assumptions which nevertheless provide a first order model. Notably, we have assumed that all the pre-existing fractures in the DFN have a uniform hydraulic transmissivity $w_h k_f$ at ambient conditions, although field observations have shown that critically stressed fractures (low $\mathcal{T}$ parameter) act most likely as high permeable fluid conduits compared to not optimally oriented fractures (Bandis et al. 1983) and that larger apertures are expected on longer fractures (following a sub-linear power law) (Olson 2003). We can certainly say, however, that an initial heterogeneous distribution of hydraulic transmissivities would not change the DFN hydro-mechanical response in critically stressed conditions, as the driving mechanism for the fast slip propagation is the elastic stress interactions of favourably oriented fractures. In marginally pressurized conditions, instead, it may have an impact due to its effect on pore-fluid diffusion (yet still within the rupture extent that lags the pressurization region). This would occur even in the case where shear-induced dilatancy / compaction is included, such that the fracture hydraulic transmissivities are not only heterogeneous at in-situ conditions, but also evolve in space and time in relation to frictional slip.

A more complex response is surely obtained if the friction coefficient weakens during slip propagation, thus allowing the spontaneous nucleation of dynamic (seismic) ruptures. For instance, in the case of slip weakening friction coefficient and shear-induced dilatancy / compaction of pre-existing fractures, we would expect a faster migration of slip front with respect to fluid front on a critically stressed DFN (especially when run-away ruptures take place), even when dilatant hardening effect is able to quench the dynamic events. This is also valid in the limit case of fluid injection into a critically stressed dilatant fracture/fault that is hydraulically disconnected from the other pre-existing fractures (Ciardo and

Lecampion 2019). On a marginally pressurized DFN, instead, the weakening of friction coefficient with shear deformations may lead to finite-sized dynamic events, even along highly dilatant pre-existing fractures (due to the slow rupture front velocity upon fluid injection). At early pressurization time, the pore-pressure front would always be located ahead the slipping patch front, but it may be outpaced by the rupture front after nucleation and arrest of such seismic events (when occurring). Obviously, this scenario strongly depends on the percolation parameter, DFN characteristics and injection condition. Further numerical investigations are therefore needed.

6 Conclusions

We have studied the propagation of stable frictional slip ruptures in fractured rock masses driven by pore-fluid diffusion. Before exploring fluid injection in a Discrete Fracture Network with randomly oriented and uniformly distributed fractures, we revisited the problem of injection in a single isolated frictional shear fracture, first investigated by Bhattacharya and Viesca (2019); Viesca (2021). For constant friction, the stable (aseismic) slip propagates with pore-fluid diffusion in a self-similar manner. The self-similarity factor is function of only one dimensionless parameter $\mathcal{T}$ that identifies two end-member limiting regimes, namely critically stressed ($\mathcal{T} \rightarrow 0$), associated with fast migration of slip compared to pressurization front, and marginally pressurized ($\mathcal{T} \rightarrow 1$) regime (reversed scenario). We have solved numerically the problem and extensively benchmarked our results against the analytical asymptotic solutions of Bhattacharya and Viesca (2019) and Viesca (2021). As demonstrated in Fig. 2, our numerical results are very accurate, with a relative error in terms of crack half-length that is always lower than 2% in both critically stressed and marginally pressurized limiting conditions. Furthermore, we have derived closed form solutions for the aseismic moment evolution with pressurization time and total injected volume in both limiting regimes, and compared them with numerical results obtaining a very good agreement. An interesting finding is that the aseismic moment scales quadratically to the injected volume in both critically stressed and marginally pressurized regime.

Similar considerations and similar limiting regimes have been found to be valid even in the case fluid is injected in one fracture that is hydraulically connected to many others, forming a Discrete Fracture Network (with no preferred orientation). Although the self-similarity between the evolution of rupture extent and pore fluid front does not strictly hold anymore, the hydro-mechanical response is at first order governed by the fracture-stress-injection parameter $\mathcal{T}$ evaluated at the critical orientation $\theta_c = \pm(\pi/4 + \mathrm{ArcTan}(f)/2)$.

In marginally pressurized conditions ($\mathcal{T}_c \gtrsim 1$), the frictional ruptures are solely contained within the region of pore-pressure disturbance. As a result, in that limit, the percolation number of the DFN affects to first order the response of the medium. On the other hand, in critically-stressed conditions ($\mathcal{T}_c \ll 1$), a cascade of ruptures occurs on critically oriented fractures driven by stress transfer at distances largely ahead of the pressurized region. As a result, if aseismic slip is the dominant mechanism for the triggering of micro-seismicity, the estimation of hydraulic diffusivity α from the spatio-temporal pattern of micro-seismicity are grossly over-estimated. The aseismic moment also scales as $\propto V_{\mathrm{inj}}^2$ in both limiting regimes albeit with a different coefficient of proportionality compared to the single fracture case. Indeed, this coefficient of proportionality clearly depends on the DFN characteristics in the marginally pressurized case (as the rupture tracks the flow and is affected by percolation to first order). In the critically stressed case, this pre-factor appears to be only mildly dependent on the DFN properties.

From the results presented in this contribution we can conclude that, on a DFN with randomly oriented and uniformly distributed fractures, stable slip propagation activated by an injection at constant over-pressure and driven by pore fluid diffusion is qualitatively similar as if slip would propagate in a single planar fracture under the same injection condition. Future works should combine scaling analysis with numerical simulations to investigate rock masses with non-random fractures orientation (joint sets), quantify the effect introduced by variation of hydraulic properties with slip and the effect of linkage between fractures via the propagation of wing cracks (Jung 2013).

Appendix: DFN Realizations

We generated different Discrete Fracture Networks using an open source library called ADFNE (Alghalandis 2017). We replaced the original exponential distribution for fracture length with the power law distribution (24). We fixed the total number of pre-existing fractures to be 1000 as well as the minimum fracture length $l_{\min}$ to be $0.01L$, being L the characteristic length of the domain area. We then varied the power law exponent b and the maximum fracture length $l_{\max}$ in order to generate several DFNs, all characterized by different values of percolation p (see Fig. 14). Note, however, that the fracture lengths in each realization cover two orders of magnitude of the power law distribution (see histograms in Fig. 14) and that the b values considered fall between 1.3 and 3.5, as suggested by outcrop data [e.g. (Bonnet et al. 2001)].

For a given value of b and l_{max}, initial and end coordinates of each fracture were obtained. A pre-processing script in Wolfram Mathematica (Wolfram Research Inc 2022) was then used to mesh all the generated fractures, with the possibility of (i) controlling the mesh element size per fracture, (ii) inserting automatically a mesh node at each fracture intersection and finally (iii) set a minimum number of finite straight segments per fracture. In all the realizations, the mean mesh size is $0.005L$ and the minimum number of straight elements per fracture is 5 (Fig. 14).

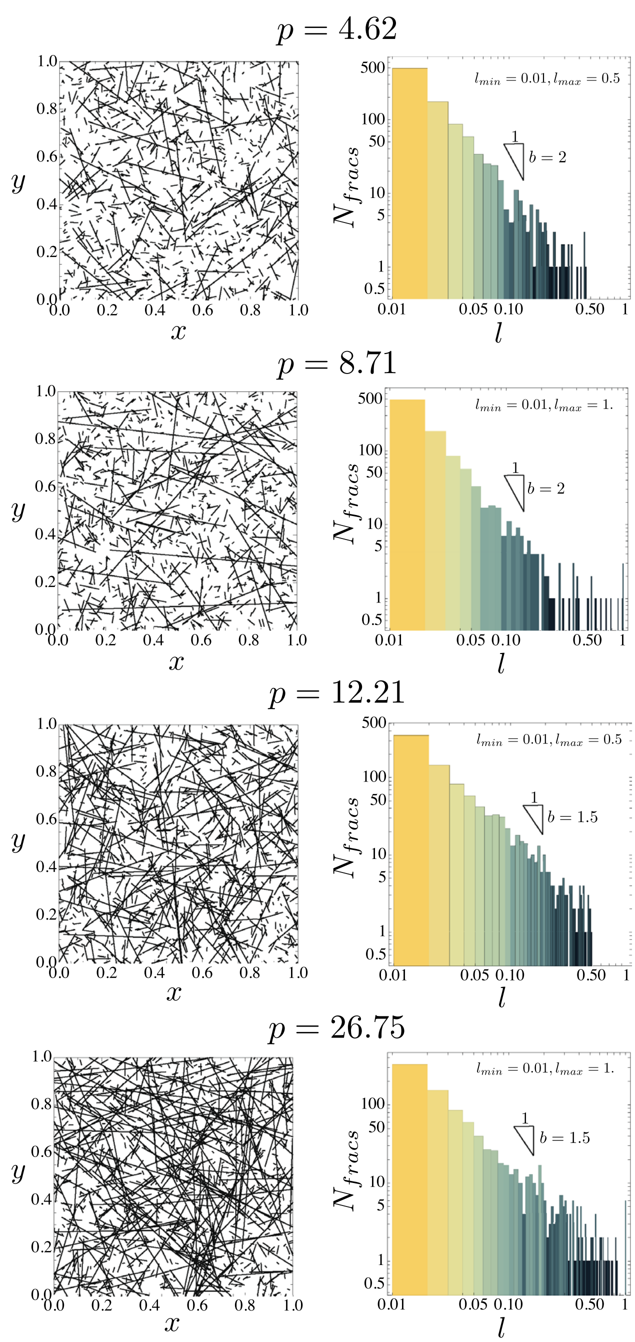

Fig. 14 Discrete fracture networks realizations used in our numerical investigations. The fractures length is sampled from power law distribution (24), with fixed minimum length $l_{min} = 0.01L$ (with L being the characteristic length of the computational domain) and different maximum length l_{max} and power law exponent b in order to obtain different percolation degrees. The left column displays the trace of each DFN, and the right column the histograms of the fractures length

Author contributions FC: conceptualization, methodology, software, validation, formal analysis, writing—original draft, visualization. BL: conceptualization, methodology, software, validation, formal analysis, writing—review and editing.

Funding Open access funding provided by Swiss Federal Institute of Technology Zurich. F. Ciardo was supported by the Swiss Federal Office of Energy (SFOE) through the ERANET Cofund GEOTHERMICA (Project No. 200320-4001), which is supported by the European Union's HORIZON 2020 programme for research, technological development and demonstration. B. Lecampion acknowledges funding for the EMOD project (Engineering model for hydraulic stimulation) via a grant (research contract SI/502081-01) and an exploration subsidy (contract number MF-021-GEO-ERK) of the Swiss federal office of energy for the EGS geothermal project in Haute-Sorne, canton of Jura.

Declarations

Conflict of interest The authors have no competing interests to declare that are relevant to the content of this article.

References

Aki K (1966) Generation and Propagation of G Waves from the Niigata Earthquake of June 16, 1964. Part 2. Estimation of earthquake moment, released energy, and stress-strain drop from the G wave spectrum. Bull Earthq Res Inst 44:73–88

Albaric J, Oye V, Langet N, Hasting M, Lecomte I, Iranpour K, Reid P (2014) Monitoring of induced seismicity during the first geothermal reservoir stimulation at Paralana, Australia. Geothermics 52:120–131

Alghalandis YF (2017) ADFNE: open source software for discrete fracture network engineering, two and three dimensional applications. Comput Geosci 102:1–11

Anders MH, Wiltschko DV (1994) Microfracturing, paleostress and the growth of faults. J Struct Geol 16(6):795–815

Bandis S, Lumsden A, Barton N (1983) Fundamentals of rock joint deformation. Int J Rock Mech Min Sci Geomech Abstr 20:249–268

Bhattacharya P, Viesca RC (2019) Fluid-induced aseismic fault slip outpaces pore-uid migration. Science 364(6439):464–468

Bonnet E, Bour O, Odling NE, Davy P, Main I, Cowie P, Berkowitz B (2001) Scaling of fracture systems in geological media. Rev Geophys 39:347–383
Bour O, Davy P (1997) Connectivity of random fault networks following a power law fault length distribution. Water Resour Res 33(7):1567–1583
Bourouis S, Bernard P (2007) Evidence for coupled seismic and aseismic fault slip during water injection in the geothermal site of Soultz (France), and implications for seismogenic transients. Geophys J Int 169:723–732
Byerlee J (1978) Friction of rocks. Pure Appl Geophys 116:615–626
Cappa F, Scuderi MM, Collettini C, Guglielmi Y, Avouac J-P (2019) Stabilization of fault slip by fluid injection in the laboratory and in situ. Science Adv 5(3)
Carslaw HS, Jaeger JC (1959) Conduction of heat in solids. Oxford University Press, Oxford
Ciardo F, Lecampion B (2019) Effect of dilatancy on the transition from aseismic to seismic slip due to fluid injection in a fault. J Geophys Res Solid Earth 124:3724–3743
Ciardo F, Lecampion B, Fayard F, Chaillat S (2020) A fast boundary element based solver for localized inelastic deformations. Int J Numer Methods Eng 1–23
Ciardo F, Rinaldi AP (2022) Impact of injection rate ramp-up on nucleation and arrest of dynamic fault slip. Geomech Geophys Geo-energy Geo-resour 8(28)
Cornet FH (2016) Seismic and aseismic motions generated by fluid injections. Geomech Energy Environ 5:42–54
Cornet FH (2021) The engineering of safe hydraulic stimulations for EGS development in hot crystalline rock masses. Geomech Energy Environ 26:100151
Cornet FH, Helm J, Poitrenaud H, Etchecopar A (1997) Seismic and aseismic slips induced by large-scale fluid injections. Pure Appl Geophys 150:563–583
Davy P, Bour O, De Dreuzy J-R (2006) Discrete fracture network for the Forsmark site (Tech. Rep.). Itasca Consulting Group
Duboeuf L, De Barros L, Cappa F, Guglielmini Y, Deschamps A, Seguy S (2017) Aseismic motions drive a sparse seismicity during fluid injections into a fractured zone in a carbonate reservoir. J Geophys Res Solid Earth 122:8285–8304
Ellsworth WL (2013) Injection-induced earthquakes. Science 341
Eyre T, Eaton DW, Garagash DI, Zecevic M, Venieri M, Weir R, Lawton DC (2019). The role of aseismic slip in hydraulic fracturing-induced seismicity. Sci Adv 5(8)
Faulkner D, Jackson CAL, Lunn RJ, Schlische RW, Shipton ZK, Wibberley CAJ, Withjack MO (2010) A review of recent developments concerning the structure, mechanics and fluid flow properties of fault zones. J Struct Geol 32:1557–1575
Galis M, Ampuero J-P, Mai PM, Cappa F (2017) Induced seismicity provides insight into why earthquake ruptures stop. Sci Adv 3(12):eaap7528
Garagash DI, Germanovich LN (2012) Nucleation and arrest of dynamic slip on a pressurized fault. J Geophys Res 117(B10310)
Gebbia M (1891) Formule fondamentali della statica dei corpi elastici. Rend Circ Mat di Palermo 5:320–323
Guglielmini Y, Cappa F, Avouac J-P, Henry P, Elsworth D (2015) Seismicity triggered by fluid injection-induced aseismic slip. Science 348
Hainzl S, Fischer T, Dahm T (2012) Seismicity-based estimation of the driving fluid pressure in the case of swarm activity in Western Bohemia. Geophys J Int 191:271–281
Hainzl S, Ogata Y (2005) Detecting fluid signals in seismicity data through statistical earthquake modeling. J Geophys Res Solid Earth 110
Hamilton DH, Meehan RL (1971) Ground rupture in the Baldwin Hills. Science 172(3981):333–344
Hatton CG, Main IG, Meredith PG (1994) Non-universal scaling of fracture length and opening displacement. Nature 367
Healy JH, Rubey WW, Griggs DT, Raleigh CB (1968) The denver earthquakes. Science 161(3848):1301–1310
Hill DA, Kelly PA, Dai DN, Korsunsky AM (1996) Solution of crack problems: the distributed dislocation technique. Kluwer Academic Publishers, New York
Jung R (2013) EGS—goodbye or Back to the Future 95. Effective and sustainable hydraulic fracturing
Keranen KM, Weingarten M (2018) Induced seismicity. Annu Rev Earth Planet Sci 46(1):149–174
Kranz RL (1983) Microcracks in rocks: a review. Tectonophysics 100:449–480
Lei Q, Gao K (2018) Correlation between fracture network properties and stress variability in geological media. Geophys Res Lett 45
Lei Q, Wang X (2016) Tectonic interpretation of the connectivity of a multiscale fracture system in limestone. Geophys Res Lett 43:1551–1558
Lei Q, Latham J-P, Tsang C-F (2017) The use of discrete fracture networks for modelling coupled geomechanical and hydrological behaviour of fractured rocks. Comput Geotech 85:151–176
McGarr A (2014) Maximum magnitude earthquakes induced by uid injection. J Geophys Res Solid Earth 119(2):1008–1019
McGarr A, Barbour AJ (2018) Injection-induced moment release can also be aseismic. Geophys Res Lett 45:5344–5351
Mogilevskaya SG (2014) Lost in translation: crack problems in different languages. Int J Solids Struct 51(25):4492–4503
Olson JE (2003) Sublinear scaling of fracture aperture versus length: an exception or the rule? J Geophys Res 108(B9)
Parotidis M, Rothert E, Shapiro SA (2003) Pore-pressure diffusion: a possible triggering mechanism for the earthquake swarms 2000 in Vogtland/NW-Bohemia, central Europe. Geophys Res Lett 30
Quarteroni A, Sacco R, Saleri F (2000) Numerical mathematics (T. in applied mathematics, Ed.). Springer
Sáez A, Lecampion B, Bhattacharya P, Viesca RC (2022) Three dimensional uid-driven stable frictional ruptures. J Mech Phys Solids 160
Scotti O, Cornet FH (1994) In situ evidence for fluid-induced aseismic slip events along fault zones. Int J Rock Mech Min Sci Geom Abstr 31(4):347–358
Scuderi MM, Collettini C (2016) The role of uid pressure in induced vs. triggered seismicity: insights from rock deformation experiments on carbonates. Sci Rep 6(24852)
Shapiro SA, Huenges E, Borm G (1997) Estimating the crust permeability from fluid-injection-induced seismic emission at the KTB site. Geophys J Int 131:F15–F18
Shapiro SA, Rothert E, Rath V, Rindschwentner J (2002) Characterization of uid transport properties of reservoirs using induced seismicity. Geophysics 67(1):212–220
Söderlind G, Wang L (2003) Adaptive time-stepping and computational stability. J Comput Appl Math 185:225–243
Sornette A, Davy P, Sornette D (1993) Fault growth in brittle-ductile experiments and the mechanics of continental collisions. J Geophys Res 98(N7):12111–12139
Viesca R (2021) Self-similar fault slip in response to fluid injection. J Fluid Mech 928(A29)
Walmann T, Malthe-Sørenssen A, Feder J, Jøssang T, Maekin P (1996) Scaling relations for the lenghts and widths of fractures. Phys Rev Lett 77(27)
Warpinski NR, Teufel LW (1987) In uence of geologic discontinuities on hydraulic fracture propagation. J Pet Technol 39(02):209–220
Wibberley CAJ, Yielding G, Di Toro G (2008) Recent advances in the understanding of fault zone internal structure: a review. Geol Soc Spec Publ 299:5–33
Witherspoon PA, Gale JE (1977) Mechanical and hydraulic properties of rocks related to induced seismicity. Eng Geol 11(1):23–55

Wolfram Research, Inc. (2022) Mathematica, Version 13.1. https://www.wolfram.com/mathematica (Champaign, IL, 2022)

Zoback M, Harjes H-P (1997) Injection-induced earthquakes and crustal stress at 9 km depth at the KTB deep drilling site, Germany. J Geophys Res Solid Earth 102(B8):18477–18491

Supplementary Materials for:

Maximum size and magnitude of injection-induced slow slip events

Alexis Sáez*[a], François Passelègue[b], and Brice Lecampion[a]

[a]Ecole Polytechnique Fédérale de Lausanne (EPFL), Institute of Civil Engineering, Gaznat chair on Geo-Energy, CH-1015 Lausanne, Switzerland
[b]Géoazur, ESEILA, Université Côte d'Azur, CNRS, Observatoire de la Côte d'Azur, IRD, Sophia Antipolis, Nice, France,

*E-mail: saez@caltech.edu

1 Estimates of moment release, rupture run-out distance, and injected fluid volumes

Here, we present the references and calculations behind the dataset of injection-induced aseismic slip events used in this study. For some events, the moment release, rupture run-out distance (maximum distance from the aseismic slip front to the injection point), and injected fluid volume are provided by the original authors. In other cases, we estimated these quantities based on the assumptions we state below. In addition, we include data points from previously unpublished laboratory experiments. The dataset is thus both compiled and produced, and is summarized in Table S1. Note that for some events in the dataset, the moment release and rupture run-out distance are estimated within a range that is represented by a vertical line connecting their maximum and minimum values in Figs. 5 and 6 in the main text. Also, in some cases, the injected fluid volume is estimated within a range that is represented in a similar manner by a horizontal line in the same figures. In Table S1, the corresponding values are denoted by the subscripts *max* and *min* respectively.

1.1 Small-scale laboratory experiments

Passelègue *et al.* [1] conducted fluid injection experiments on a saw-cut sample of andesite exhibiting negligible bulk permeability. Their experimental fault is elliptical, with a maximum length $L_f = 0.08$ m and a maximum width of $w_f = 0.04$ m (Fig. 1a). Fluid injections were carried out at 90 percent of the fault's peak strength, with initial effective confining pressure ($P_{ef} = P_c - P_f$) ranging from 20 to 85 MPa ($P_c = 30$, 60 and 95 MPa, and $P_f = 10$ MPa). As highlighted by the strain gages array along the fault (Figs. 1a and 1c), an aseismic rupture nucleates near the injection borehole and propagates predominantly toward the other side of the sample where the measurement borehole is (see [1] for further details). At the moment in which the rupture reaches this latter edge of the experimental fault, the two sample pieces undergo a rigid-body motion. Due to the assumptions of our model which considers a rupture propagating on a fault embedded in an unbounded domain, we calculate the moment release aseismically only up to the time in which the slip front reaches that edge of the experimental fault. This time is denominated t_n (Figs. 1c and 1d). The initial time of each slow slip event, denominated as t_0, corresponds to the time at which the fault comes back to its elastic behavior after each event. Since the experiments are conducted at a constant injection flow rate Q_0, we estimate the total injected fluid volume for each event as $V_{tot} = Q_0(t_n - t_0)$. The experiments conducted at $Q_0 = 50$ μL/min are the ones reported by Passelègue *et al.* [1]. The experiments conducted at $Q_0 = 10$ μL/min are new, previously unpublished experiments (see Table S1).

We estimated the *macroscopic* aseismic slip induced along the fault between t_0 to t_n using the macroscopic measurement of axial shortening, as given by the formula:

$$\delta = \left(\frac{D_{ax}}{L_s} - \frac{\Delta \sigma_D}{E_{ap}} \right) \frac{L_s}{\cos(\theta)}, \quad (1)$$

where D_{ax} represents the direct measurement of axial shortening monitored using gap sensors (see [1] for further details), L_s is the sample length, $\Delta\sigma_D$ is the change in differential stress measured during each event, E_{ap} is the Young modulus of the experimental apparatus, and θ is the angle between the sample axial direction and the fault plane (equal to 30 degrees).

The aseismic moment release is then computed assuming that at the end of each aseismic slip event, the entire fault interface is sliding. The moment release is thus calculated as $M_0 = \mu\delta S$, where μ = X is the sample shear modulus, and S is the macroscopic fault surface equal to $\pi(L_f/2)(w_f/2)$. This hypothesis holds to the first order, as the estimate of δ is derived from the average strain measured along the entire sample. For the rupture run-out distance, we consider it to be equal to L_f for all events. This is consistent with the fact that each aseismic slip event is considered up to the time at which the rupture reaches the side of the sample where the measurement borehole is. The latter is the maximum possible distance from the slip front to the injection point.

1.2 Large-scale laboratory experiments

Cebry *et al.* [2] reported three meter-scale experiments on a saw-cut granitic fault, denominated Cases A, B, and C in their work. The main quantity they varied throughout their experiments was the initial shear stress, from higher to lower values from Cases A to C respectively. Their experimental fault size is 3.15 m long and $W = 0.3$ m wide. Fluid is injected directly into the fault through a wellbore which is located right in the middle of the shortest side of the sample interface. An aseismic rupture nucleates most likely near the injection point, yet slip measurements start only once the rupture reaches the traction-free face of the shortest side of the sample. From this time on, an 'average' one-dimensional rupture is monitored while propagating along the longest side of the sample. Here, we focus on the aseismic slip phases preceding seismic events in each experiment. For Case A, a maximum aseismic slip of $\delta_A = 46.9$ μm was measured at the sensor that was closest to the injection point within a measured rupture length of approximately L_A = 1.4 m. Assuming a symmetric and linear distribution of slip from the maximum slip δ_A to zero at the rupture front, we estimate the moment release as $M_0 = \mu\delta_A L_A W/2$. Considering a shear modulus of 30 GPa, the estimated moment release is then 2.95×10^5 Nm. For Case B, a maximum aseismic slip of $\delta_B = 92.6$ μm was measured within a rupture extent of approximately $L_B = 1.6$ m. Likewise, we can estimate the moment release in 6.67×10^5 Nm. The experiments were conducted at a constant injection rate equal to 10 mL/min. Cebry *et al.* [2] reported that the time between the injection start and the maximum fluid pressure measured at the well during each experiment varied from 140 to 240 seconds. The instant of maximum pressure was associated with the time at which the injected fluid reached the shortest side of the sample for the first time. Starting from this moment, fluid leaks from the sample interface. In Cases A and B, the aseismic slip phases end shortly upon reaching the instant of maximum pressure, after

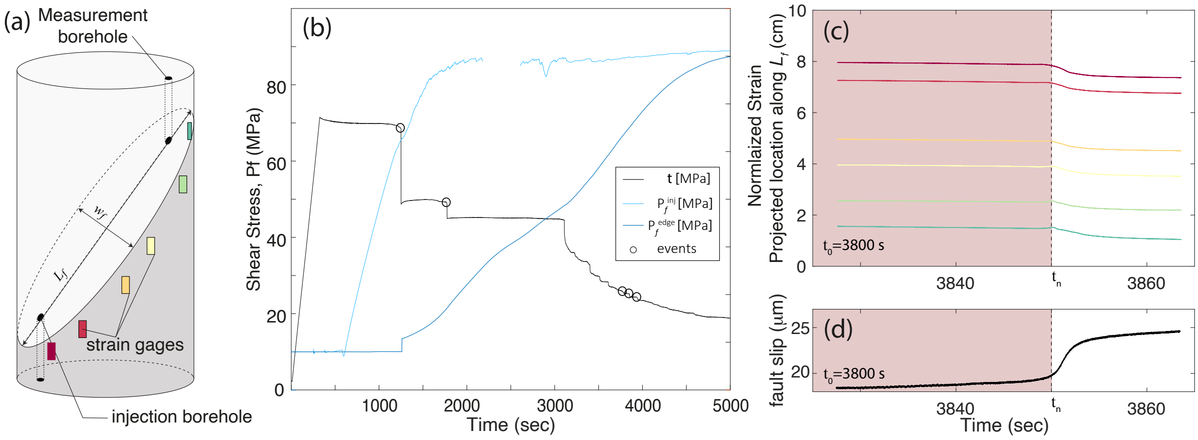

Figure 1: **Description of the centimeter-scale laboratory experiments.** (a) Schematic of the sample assembly. The length of the fault is $L_f = 8$ cm along strike. Injection is conducted in the bottom sample through a borehole reaching the fault interface. The evolution of the fluid pressure is measured both at the injection borehole and at the opposite edge of the fault through a measurement borehole. Strain gages are located along one side of the fault. See Passelègue *et al.* [1] for further details. (b) Evolution of the macroscopic shear stress (black solid line) and fluid pressure measured in the injection (cyan solid line) and measurement (blue solid line) boreholes during the experiments conducted at 95 MPa of confining pressure. Black circles correspond to aseismic slip events. (c) Evolution of the strain on each strain gage during the propagation of the slip front along the fault interface. The color code corresponds to the one used in panel (a) for the strain gages. t_n is the moment at which the slipping front reaches the edge of the sample and rigid block motion initiates, highlighted by the simultaneous release of stress on all strain gages. (d) Evolution of macroscopic fault slip during the propagation of an aseismic slip event.

approximately 3 seconds and 15 seconds respectively. Since these periods are short compared to the total injection time and the pressure drop associated with fluid leakage is small relative to the maximum pressure, we neglect the fluid losses in Cases A and B. For the aforementioned periods (140 to 240 seconds), the injected fluid volumes are 2.4×10^{-5} m^3 and 3.6×10^{-5} m^3 respectively. This provides a possible range of volumes for Cases A and B, which are the ones included in Table S1. For Case C, the aseismic slip phase ended around 500 seconds after reaching the maximum pressure. In principle, we think it is not possible to neglect the fluid loss here. Hence, we do not consider this case in the dataset. Finally, The maximum rupture run-out distance is calculated as $L_A/2 = 0.7$ m and $L_B/2 = 0.8$ m for Cases A and B respectively. This is because the ruptures are nearly symmetric with regard to the injection point so half of the rupture length corresponds to the rupture run-out distance from the injection well.

1.3 In-situ experiments on natural shallow faults

The 2015 Guglielmi et al's experiment in Southeastern France

In 2015, Guglielmi *et al.* [3] conducted an experiment of fault reactivation by fluid injection in a shallow carbonate fault system in Southeastern France, by injecting 0.95 m^3 of water at a depth of about 280 m. They monitored micro-seismicity, injection-well fluid pressure, volume rate history, and the history of induced fracture slip and opening at the injection interval. Guglielmi *et al.* concluded that most of the induced fracture slip was aseismic, with a maximum value of about 1.2 cm at the injection interval. By fitting part of the data through a simplified hydro-mechanical model including a circular rupture with complete stress drop, they estimated the associated aseismic moment release in 6.5×10^{10} Nm. For this same experiment, another estimate of the aseismic moment release may be obtained from the inverse modeling results of Bhattacharya and Viesca [4]. They estimated the rupture radius at the moment the injection stops in approximately $R = 6.5$ m and a shear modulus of about 12 GPa. Considering a triangular distribution of slip from the measured maximum slip at the injection interval $\delta_{\text{well}} = 1.2$ cm to zero at the rupture front which we approximate as being circular, we estimate the moment release in $(\pi/3)\mu\delta_{\text{well}}R^2 \approx 6.4 \times 10^8$ Nm. This value is two orders of magnitude lower than the one estimated by Guglielmi *et al.* [3]. The difference is essentially due to the dissimilar estimates for the rupture radius. Guglielmi *et al.* [3] estimated the rupture radius to be approximately 35 m, which is more than five times larger than the one estimated by Bhattacharya and Viesca [4]. We therefore consider the estimates of moment release and rupture radius coming from these two previous studies as maximum and minimum values, respectively.

The 2014 De Barros et al's experiments in Tournemire, France

In 2014, a set of in-situ experiments reported by De Barros *et al.* [5] took place in an underground laboratory (IRSN) in Tournemire, France. Fluids were injected into a low-permeability shale fault zone at a depth of approximately 200 m. The acquired datasets are similar to the ones obtained by Guglielmi *et al.* [3]. Here, we consider two events for which the injected fluid volume, aseismic moment release, and rupture run-out distance are reported by De Barros *et al.* [6]. The estimates of aseismic moment release, denominated as deformation moment in [6], are several orders of magnitude greater than the cumulative moment released by the monitored micro-seismicity. De Barros *et al.* [6] provided an uncertainty range for both aseismic moment release and rupture radius of each event that we incorporate directly in our compiled dataset, Table S1 (see supplementary materials in [6] for further details).

The 2015 Duboeuf et al's experiments in Rustrel, France

In 2015, a set of in-situ experiments reported by Duboeuf *et al.* [7] was conducted in an underground laboratory (LSBB) in Rustrel, France. Fluid injections were performed, in this case, into a fault damage zone in limestone, at a depth of about 300 m. Here, we consider six events for which the injected fluid volume, aseismic moment release, and rupture radius are also reported by De Barros *et al.* [6]. To provide an uncertainty range for the aseismic moment release and rupture radius of each event, they considered the same kind of uncertainties as for the experiments in IRSN, Tournemire, France (see supplementary materials in [6] for further details). We incorporate those uncertainty ranges directly in our compilation of events, Table S1.

1.4 Large-scale fluid injections in the field

The 1993 hydraulic stimulation at the Soultz geothermal site, France

A hydraulic stimulation was conducted in two stages in 1993 at the Soultz geothermal site in France, where a total water volume of 44600 m^3 was injected into granite through a 550 m open-hole section located at depths between 2850 m and 3400 m [8]. Cornet *et al.* [8] estimated fracture slips along the open-hole section of the well from ultrasonic imaging logs in up to 4.7 cm, as a result of the two hydraulic-stimulation stages. Based on two scenarios of stress drop (equal to 9 and 19 MPa), they estimated the moment release associated with the inferred fracture slips in 3.6×10^{13} and 8.9×10^{12} Nm, respectively. Because the moment release by the largest seismic event recorded during the operation was estimated to be about two orders of magnitude lower than the moment release estimated from fracture slip, they concluded that the moment release during this experiment was mainly due to aseismic motions [8]. On the other hand, by analyzing repeating earthquakes (multiplets) in one of the faults with the greatest slip, Bourouis and Bernard [9] provided further support to the mostly aseismic nature of the reservoir deformation during this hydraulic-stimulation experiment. From the analysis of Bourouis and Bernard, we constrain the aseismic moment release as $\sim \mu\delta_{\text{avg}}L_*^2$, where $\mu = 20$ GPa [8], δ_{avg} is the average slip on the fault estimated from the repeaters analysis in 4 cm [9] which is remarkably consistent with the estimates by Cornet *et al.* [8] from ultrasonic imaging logs, and L_* is the characteristic size of the slipped fault patch. An upper bound for L_* of approximately 500 m can be considered if one assumes that all the micro-seismicity (including repeaters and non-repeaters) delineating the examined fault (see Figure 5 in [9]) has been triggered by shear loading due to aseismic slip surrounding nominally locked asperities where the micro-seismic events are hosted. On the other hand, if we consider that micro-seismicity could be also triggered ahead of the aseismic slip front due to quasi-static stress transfer and assume repeaters as evidence for aseismic slip around the repeaters source, one can estimate a lower bound for L_* corresponding to the minimum fault patch size that contains all the repeaters (see Figure 5 in [9]), in approximately 350 m. This yields an aseismic moment release of 9.8×10^{13} and 2.0×10^{14} Nm for the lower and upper bounds of the slipped patch size, respectively. Taking together the estimates from the studies by Cornet *et al.* [8] and Bourouis and Bernard [9], we obtain a minimum and maximum value of M_0 as 8.9×10^{12} Nm and 2.0×10^{14} Nm respectively, which are the two values reported in Table S1. For the rupture run-out distance, we consider a minimum value of 68 m from the rupture radius estimated by Cornet *et al.* [8] at their highest stress drop scenario, and a maximum value of 500 m from the scenario in which the aseismic slip patch wraps all the micro-seismicity in Bourouis and Bernard's analysis [9].

The 2017-2018 hydraulic-fracturing-induced slow slip events in Northwestern Canada

Eyre *et al.* [10] have recently reported the two largest injection-induced slow slip events detected thus far. The first event of magnitude M_w 5.0 occurred in September 2017, whereas the second event of magnitude M_w 4.2 occurred approximately one year later, in October 2018. Both events were attributed to hydraulic fracturing operations into a low-permeability hydrocarbon reservoir (the so-called Montney Formation, a fine-grained siltstone) that were conducted through two horizontal wells at a depth of approximately 2 km. The total injected fluid volume associated with each of these events is 88473 m^3 and 98193 m^3, respectively [10]. The moment release was estimated from kinematic inversions of fault slip using InSAR surface deformation measurements, resulting in shallowly-dipping (8°) thrust events that are consistent with known bedding planes within the Montney Formation [10]. The inferred aseismic slip events were corroborated independently against large well-case deformations reported at the same depths as the events, just above the horizontal wells. The moment release was estimated in 4.24×10^{16} Nm for the largest event in 2017, and 2.09×10^{15} Nm for the smaller event in 2018. The associated maximum slips for each event are 24 cm and 11 cm, respectively. We consider their rupture run-out distances as half of the rupture size in the most elongated direction of the slipped fault patch (see Figure 3a in [10]), namely, ≈2.5 km and ≈1.75 km respectively. This assumes that the equivalent injection point for each event would be approximately in the centroid of the rupture surface. The slow slip events were likely produced by hydraulic fractures intersecting and activating the bedding planes in shear. We do not attempt to determine an equivalent injection point from the multiple hydraulic fracturing stages. Finally, it is important to note that no seismic events were detected by the regional network (with a detection threshold of ∼M1.5 [10]). Hence, the geodetically inferred moment releases can be reasonably assumed to correspond to virtually pure aseismic ruptures.

The 2016 hydraulic-fracturing-induced slow slip transient triggering the M_w 4.1 earthquake in Alberta, Canada

In 2016, an earthquake of magnitude M_w 4.1 was triggered by hydraulic-fracturing operations in an unconventional hydrocarbon reservoir in Alberta, Canada [11]. Eyre *et al.* [11] investigated the triggering mechanism of this earthquake. They provided evidence for an aseismic slip event induced by hydraulic fractures that intersected (and pressurized) at the reservoir level (shales at around 3.4 km depth), frictionally stable segments of a nearby sub-vertical strike-slip fault. They suggested that this fluid-driven aseismic slip event propagated and transmitted solid stresses to distal (upward) segments of the same fault but in frictionally unstable carbonate units where the hypocenter of the M_w 4.1 earthquake was located (at about 3 km depth). Our focus here is the aseismic slip transient which developed mostly on unconditionally stable fault segments and presumably triggered the earthquake. Eyre *et al.* [11] estimated via numerical modeling an aseismic moment release for this event of about 0.9×10^{14} Nm (see Figure 5d in [11]). The total injected volume concerning all the hydraulic fracturing stages before the earthquake happened, that is, until stage 23, is 28408 m^3 (Table S1 in [11]). It is important to note that, unlike all the other previous cases, here fault slip has not been measured nor observationally inferred. Although the numerical model from which we extract the moment release assimilates a significant body of geological, geophysical, and experimental data, besides reproducing the timing and magnitude of the mainshock, we believe the degree of uncertainty for the moment release in this case is higher than in other cases were observational constraints of fault slip are available. For this reason, the data point corresponding to this event is differentiated in the main text in Figs. 5 and 6 with respect to other data points by using a dashed symbol instead of a solid one. For the rupture run-out distance, we consider an uncertainty range between 200 m and 400 m. The maximum value is taken as the distance between the mainshock hypocenter and the hydraulic fracturing depth where the fractures presumably intersected the fault (see Fig. 4 in [11]). The minimum value is taken as the distance between the hydraulic fracturing depth and the end of the frictionally stable fault segment upward from the hydraulically stimulated reservoir (see Fig. S3 in [11]).

The 2013 hydraulic stimulation at the Rittershoffen geothermal site, France

In 2013, a hydraulic stimulation for the development of a deep geothermal reservoir was performed in the Rittershoffen geothermal field, in Northeastern France [12]. A total volume of approximately 2600 m^3 of water was injected into the crystalline basement through the so-called GRT-1 well with a 640 m open-hole section located at depths between 1920 m and 2560 m [13]. The hydraulic stimulation lasted for approximately 18 hours. The seismicity taking place during the injection operation illuminated a fault whose location and orientation are consistent with a major structure that experienced a significant permeability enhancement as a result of the stimulation [12]. The fault plane that fits well the micro-seismicity is a patch of about $W = 200$ m $\times$ $L = 300$ m. Upon stopping the injection, seismicity ceased immediately. However, after 4 seismically quiescent days, a second swarm episode occurred in a nearby fault. Lengliné *et al.* [12] found that an aseismic slip of $\delta = 1$ cm (estimated via empirical scaling relations) in the first reactivated fault patch of 200 m $\times$ 300 m could explain via quasi-static stress transfer the triggering of the second swarm. Following their analysis, the corresponding aseismic moment release could be estimated as $\sim \mu\delta LW$. Considering $\mu = 20$ GPa [12], we obtain $1.2{\times}10^{13}$ Nm. In their study, Lengliné *et al.* [12] attributed the delay of the second swarm to the so-called clock-advance effect in earthquake nucleation produced in this case by the aseismic-slip stress jump. Recently, we discussed an alternative scenario [14] in which this delay could be associated with the continuous propagation of aseismic slip during the shut-in stage, without the need for any clock-advance effect. To give an uncertainty range for this event, we consider the results from the simplifying modeling analysis in [14], which gives an estimate of slip at the injection point of about 0.28 cm. Assuming a triangular distribution of slip over a circular patch of radius $R \approx 250$ m [14], we estimate the moment release as $(\pi/3)\mu\delta R^2 \approx 3.67 \times 10^{12}$ Nm. Finally, the rupture run-out distance is simply considered as 300 m which is approximately the furthest distance of the seismicity cloud from the injection point [12]. This assumes that all the seismicity is induced by aseismic slip surrounding the unstable patches hosting the micro-seismic events. Therefore, this may be regarded as a maximum. It is important to mention that similarly to the previous case, fault slip here has not been measured nor observationally inferred. Neither a compelling geomechanical model that assimilates the available data has been built. We should thus consider this poorly-constrained case with caution. As for the previous case, we highlight the large uncertainty for this event in the main text by using a dashed symbol instead of a solid one.

References

1. Passelègue, F. X. *et al.* Initial effective stress controls the nature of earthquakes. *Nature Communications* **11,** 5132 (2020).

2. Cebry, S. B. L., Ke, C.-Y. & McLaskey, G. C. The Role of Background Stress State in Fluid-Induced Aseismic Slip and Dynamic Rupture on a 3-m Laboratory Fault. *Journal of Geophysical Research: Solid Earth* **127,** e2022JB024371 (2022).

3. Guglielmi, Y., Cappa, F., Avouac, J., Henry, P. & Elsworth, D. Seismicity triggered by fluid injection-induced aseismic slip. *Science* **348,** 1224–1226 (2015).

4. Bhattacharya, P. & Viesca, R. Fluid-induced aseismic fault slip outpaces pore-fluid migration. *Science* **364,** 464–468 (2019).

5. De Barros, L. *et al.* Fault structure, stress, or pressure control of the seismicity in shale? Insights from a controlled experiment of fluid-induced fault reactivation. *Journal of Geophysical Research: Solid Earth* **121,** 4506–4522 (2016).

6. De Barros, L., Cappa, F., Guglielmi, Y., Duboeuf, L. & Grasso, J.-R. Energy of injection-induced seismicity predicted from in-situ experiments. *Scientific Reports* **9,** 4999 (2019).

7. Duboeuf, L. *et al.* Aseismic Motions Drive a Sparse Seismicity During Fluid Injections Into a Fractured Zone in a Carbonate Reservoir. *Journal of Geophysical Research: Solid Earth* **122,** 8285–8304 (2017).

8. Cornet, F., Helm, J., Poitrenaud, H. & Etchecopar, A. Seismic and aseismic slips induced by large-scale fluid injections. *Pure and Applied Geophysics* **150,** 563–583 (1997).

9. Bourouis, S. & Bernard, P. Evidence for coupled seismic and aseismic fault slip during water injection in the geothermal site of Soultz (France), and implications for seismogenic transients. *Geophysical Journal International* **169,** 723–732 (2007).

10. Eyre, T., Samsonov, S., Feng, W., Kao, H. & Eaton, D. W. InSAR data reveal that the largest hydraulic fracturing-induced earthquake in Canada, to date, is a slow-slip event. *Scientific Reports* **12,** 2043 (2022).

11. Eyre, T. *et al.* The role of aseismic slip in hydraulic fracturing-induced seismicity. *Science Advances* **5** (2019).

12. Lengliné, O., Boubacar, M. & Schmittbuhl, J. Seismicity related to the hydraulic stimulation of GRT1, Rittershoffen, France. *Geophysical Journal International* **208,** 1704–1715 (2017).

13. Baujard, C. *et al.* Hydrothermal characterization of wells GRT-1 and GRT-2 in Rittershoffen, France: Implications on the understanding of natural flow systems in the rhine graben. *Geothermics* **65,** 255–268 (2017).

14. Sáez, A. & Lecampion, B. Post-injection aseismic slip as a mechanism for the delayed triggering of seismicity. *Proceedings of the Royal Society A: Mathematical, Physical and Engineering Sciences* **479,** 20220810 (2023).

Maximum size and magnitude of injection-induced slow slip events

Alexis Sáez[1*a], François Passelègue[b], and Brice Lecampion[a]

[a]Ecole Polytechnique Fédérale de Lausanne (EPFL), Institute of Civil Engineering, Gaznat chair on Geo-Energy, CH-1015 Lausanne, Switzerland
[b]Géoazur, Université Côte d'Azur, CNRS, Observatoire de la Côte d'Azur, IRD, Sophia Antipolis, Nice, France,

[1]E-mail: saez@caltech.edu

Abstract

Fluid injections can induce aseismic slip, resulting in stress changes that may propagate faster than pore pressure diffusion, potentially triggering seismicity at significant distances from injection wells. Constraining the maximum extent of these aseismic ruptures is thus important for better delineating the influence zone of injections concerning their seismic hazard. Here we derive a scaling relation based on rupture physics for the maximum size of aseismic ruptures, accounting for fluid injections with arbitrary flow rate histories. Moreover, based on mounting evidence that the moment release during these operations is often predominantly aseismic, we derive a scaling relation for the maximum magnitude of aseismic slip events. Our theoretical predictions are consistent with observations over a broad spectrum of event sizes, from laboratory to real-world cases, indicating that fault-zone storativity, background stress state, and injected fluid volume are key determinants of the maximum size and magnitude of injection-induced slow slip events.

1 Introduction

A growing body of observations suggests that a significant part of the deformation induced by subsurface fluid injections is due to aseismic fault motions [1–11]. This phenomenon, known as injection-induced aseismic slip, has been known since at least the 1960s when a slow surface fault rupture was causally linked to fluid injection operations of an oil field in Los Angeles [1]. Since then, an increasing number of observational studies have inferred the occurrence of slow slip events as a result of industrial fluid injections. For example, in the Brawley geothermal field, California, ground- and satellite-based geodetic techniques allowed for the detection of an injection-induced aseismic slip event [7, 9]. This event was found to precede and likely trigger a seismic sequence in 2012 [12]. In western Canada, two of the largest aseismic slip events observed thus far (magnitudes 5.0 and 4.2) occurred in 2017-2018 and were detected using InSAR measurements of surface deformation [10]. These events were attributed to hydraulic fractures possibly intersecting glide planes during the stimulation of an unconventional

*Present address: Division of Geological and Planetary Sciences, California Institute of Technology, Pasadena, California 91125, USA

hydrocarbon reservoir [10]. Similarly, InSAR-derived surface deformations allowed for the recent detection of aseismic ruptures in the southern Delaware Basin, Texas [11], likely induced by wastewater injection operations [13]. These recent geodetic observations, in combination with mounting evidence for aseismic slip from fluid-injection field experiments [2–6, 8], suggest that injection-induced slow slip events might be a ubiquitous phenomenon, largely underdetected over the past decades only due to the lack of geodetic monitoring.

There is increasing recognition of the importance of injection-induced aseismic slip in the geo-energy industry. For instance, in the development of deep geothermal reservoirs, hydraulic stimulation techniques are commonly used to reactivate pre-existing fractures in shear. This process aims to enhance reservoir permeability through the permanent dilation of pre-existing fractures or the creation of new ones. The occurrence of predominantly aseismic rather than seismic slip is desirable, as earthquakes of significant magnitude can pose a substantial hazard to the success of these projects [14, 15]. Injection-induced aseismic slip can be, however, detrimental in several ways. For example, aseismic slip on fractures intersecting wells can cause casing shearing [3, 10] and adversely impact well stability [16, 17]. Additionally, in CO_2 storage operations, injection-induced aseismic slip could affect the integrity of low–permeability caprocks, as fault slip may be accompanied by permeability enhancements, increasing the risk of CO_2 leakage [18, 19]. Similar concerns may arise in other underground operations such as the storage of hydrogen and gas. Furthermore, it is well-established that quasi-static stress changes due to aseismic slip may induce seismic failures on nearby unstable fault patches [2–4, 6, 7]. Moreover, since aseismic slip can propagate faster than pore pressure diffusion [6, 20, 21], aseismic-slip stress changes can potentially reach regions much further than the zones affected by the direct increase in pore pressure due to injection, thereby increasing the likelihood of triggering earthquakes of undesirably large magnitude by perturbing a larger rock volume [12, 21, 22].

Understanding the physical factors controlling the spatial extent of aseismic slip is thus of great importance to better constrain the influence zone of injection operations concerning seismic hazards. Recent theoretical and numerical modeling studies have provided, within certain simplifying assumptions, a fundamental mechanistic understanding of how injection-induced aseismic slip grows in a realistic three-dimensional context and through all its stages, from nucleation to arrest [23–25]. Estimating the rupture run-out distance of aseismic slip transients remains, despite these efforts, an unresolved issue, particularly as these prior investigations have focused only on specific injection protocols [23–25]. Yet the spatiotemporal patterns of injection-induced aseismic slip growth are anticipated to be strongly influenced by the history of injection flow rate [23]. On the other hand, a related issue is estimating the maximum magnitude of injection-induced earthquakes. This quantity plays a crucial role in earthquake hazard assessment and has been the focus of significant research efforts in recent times [26–36]. A common limitation of prior research in this area is neglecting the portion of moment release due to aseismic slip, despite substantial evidence suggesting that aseismic motions may contribute significantly to the total moment release [1–11], potentially surpassing seismic contributions in some cases [1–6, 8, 10, 37]. Understanding the factors governing aseismic moment release is thus important, and would constitute a first step toward understanding the physical controls on slip partitioning, that is, the relative contributions of aseismic and seismic motions to the release of elastic strain energy, which is crucial for a better understanding of the seismic hazard posed by these operations.

Building upon our previous works [23–25], we develop here an upper-bound model for the spatial extent and moment release of injection-induced aseismic slip events. Our model notably accounts for fluid injections that are conducted with an arbitrary history of injection flow rate including the shut-in stage, thus effectively reproducing aseismic slip events during their entire life cycle, from nucleation to arrest. Using fracture mechanics theory, scaling analysis, and numerical simulations, we propose scaling relations for the maximum size and magnitude of aseismic ruptures which are shown to be consistent with a global compilation of events that vary

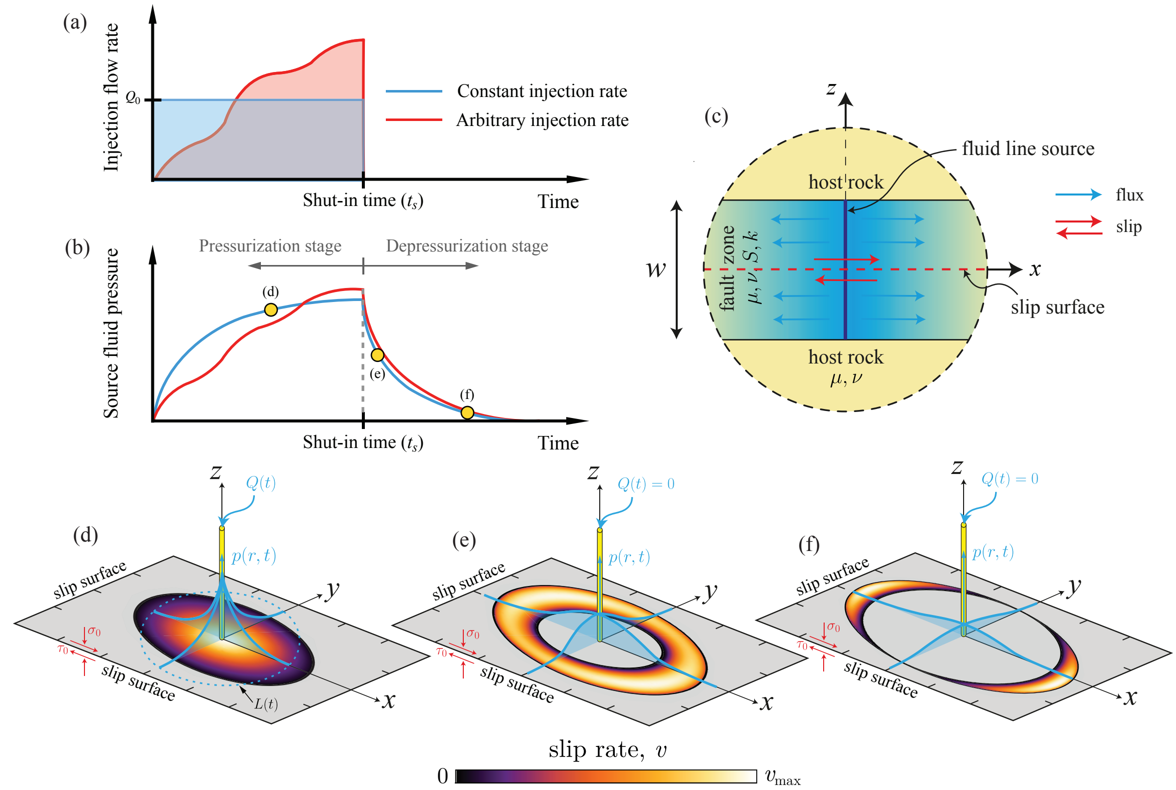

Figure 1: **Model schematics.** (a) Fluid is injected at a constant or arbitrary volumetric rate until the shut-in time t_s at which the injection is instantaneously stopped. (b) This results in two distinct stages: a pressurization stage and a depressurization (or shut-in) stage. (c) Details of the porous fault zone near the fluid source. (d,e,f) Distinct stages of rupture propagation in our upper-bound model (see panel (b) indicating the corresponding times as yellow circles). (d) Crack-like rupture phase during the pressurization stage. (e,f) Pulse-like rupture phase during the depressurization stage: first as a ring-like pulse (panel (e)), after as two moon-shaped pulses (panel (f)). See the main text for a detailed description of the stages.

in size from cm-scale slip transients monitored in the laboratory to km-scale, geodetically inferred slow slip events induced by industrial injections. Our results suggest that fault-zone hydro-mechanical storativity, background stress state, and injected fluid volume are crucial quantities in determining upper limits for the size and magnitude of aseismic ruptures. Moreover, the total fluid volume injected by a given operation is shown to be the only operational parameter that matters in determining the upper bounds in our model, regardless of any other characteristic of the injection protocol.

2 Results

2.1 Physical model and upper bound rationale

We consider purely aseismic ruptures nucleated by a localized increase of pore-fluid pressure due to the direct injection of fluids into a porous fault zone of width w (Fig. 1c). For simplicity, we begin by examining a fluid injection conducted at a constant volumetric rate Q_0 over a finite time t_s, followed by a sudden injection stop (Fig. 1a). This results in two distinct stages: a continuous injection or pressurization stage, in which pore pressure increases everywhere within the permeable fault zone; and a shut-in or depressurization stage, in which pore pressure decays near the injection point (Fig. 1b) while transiently increasing away from it (Fig. 1e). Incorporating these two stages into the model allows for examining aseismic ruptures throughout their entire lifetime, from nucleation to arrest. We consider a planar infinite fault obeying a slip-weakening friction law with a static (peak) friction coefficient f_p, dynamic (residual) friction coefficient f_r, and characteristic slip-weakening distance δ_c. The decay of friction from the peak to the residual value can be either linear or exponential [25]. The host rock is considered purely elastic with the same elastic constants as the fault zone (Fig. 1c). We assume the host rock to be impermeable at the relevant time scales of the injection. This configuration is motivated by the permeability structure of fault zones in which a highly-permeable damage zone is commonly surrounded by a less permeable host rock [38, 39]. Under these assumptions and, particularly at large times compared to the characteristic time for diffusion of pore pressure in the direction perpendicular to the fault, w^2/α, with α the fault-zone hydraulic diffusivity, the deformation rate in the fault zone is essentially oedometric (uniaxial along the z-axis) [40]. Fluid flow within the fault zone is then governed by an axisymmetric linear diffusion equation for the pore pressure field p, $\partial p/\partial t = \alpha\nabla^2 p$ [41], where the hydraulic diffusivity $\alpha = k/S\eta$, with k and η the fault permeability and fluid dynamic viscosity respectively, and S is the so-called oedometric storage coefficient representing the variation of fluid content caused by a unit pore pressure change under uniaxial strain and constant stress normal to the fault plane [41, 42]. By neglecting any poroelastic coupling within the fault zone upon the activation of slip, deformation in the medium is governed by linear elasticity which by virtue of the slow nature of the slip we are concerned with, is regarded in its quasi-static approximation. Moreover, we assume that fault slip is concentrated in a principal slip zone modeled as a mathematical plane located at $z = 0$ (Fig. 1c). We presented an investigation of this physical model, which can be regarded as an extension to three dimensions of the two-dimensional plane-strain model of Garagash and Germanovich [43], in a recent study [25]. Here, our main focus is on the case of ruptures that are unconditionally stable according to the terminology and regimes presented in [25]. This condition requires that the background shear stress τ_0, which is assumed to be uniform, must be lower than the in-situ residual fault strength $f_r\sigma'_0$, where $\sigma'_0 = \sigma_0 - p_0$, with σ_0 and p_0 the uniform background normal stress and pore pressure respectively. τ_0 and σ'_0 are thought to be the result of long-term tectonic processes and thus considered to be constant during the times scales associated with the injection operation.

In our model, unconditionally stable ruptures evolve always between two similarity solutions (Fig. 2a and see [25] for further details), one at early times where the fault interface operates with a constant friction coefficient equal to the peak value f_p, and the other one at late times where the fault interface behaves as if it were governed by a constant friction coefficient equal to the residual value f_r. As shown in Fig. 2a, the constant residual friction solution, which is the ultimate asymptotic regime of any unconditionally stable rupture, is an upper bound for the rupture size at any given time during the pressurization stage. In this asymptotic regime, rupture growth is dictated by a fracture-mechanics energy balance, where the interplay between driving and resisting forces leads to a scenario in which the fracture energy can be effectively neglected [25]. For this reason, this upper-bound limiting regime is also referred to as the zero-fracture-energy solution [25]. During the shut-in stage, a similar upper-bound rationale can be applied to the case of unconditionally stable ruptures. Assuming the fault slides with a constant residual friction value across the slipping region (equivalent to neglecting the fracture energy in the rupture-tip energy balance), this limiting solution would consistently yield a maximum for the rupture size, as the effect of the fracture energy is always to slow down rupture advancement. The limiting scenario of constant residual friction serves, therefore, as an effective upper-bound model for unconditionally stable ruptures from nucleation to arrest. In the following sections, we explore the consequences of such a limiting condition to provide an upper bound for the evolution of the rupture size and moment release during and after fluid injection, as well as a theoretical estimate for the final, maximum size and magnitude of injection-induced slow slip events. While

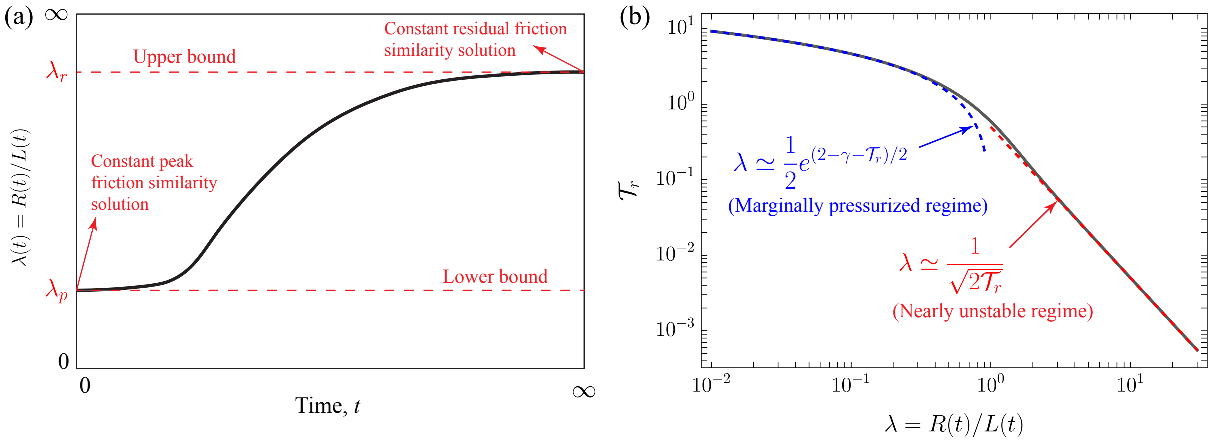

Figure 2: **Upper bound rationale and amplification factor.** (a) Evolution of the amplification factor $\lambda(t) = R(t)/L(t)$ for unconditionally stable ruptures in the slip-weakening fault model (adapted from figure 9 in [25]). $R(t)$ is the rupture radius and $L(t) = \sqrt{4\alpha t}$ is the position of the overpressure front. λ_r (time-independent) hereafter denoted simply λ, is an upper bound for the rupture size at any time during continuous injection. (b) Analytical solution (solid black line) for the amplification factor λ in our upper-bound model. λ depends uniquely on the residual stress-injection parameter $\mathcal{T}_r$. Blue and red dashed lines correspond to asymptotic limiting behaviors for marginally pressurized ($\lambda \ll 1$) and nearly unstable ($\lambda \gg 1$) ruptures.

the canonical example of injection at a constant flow rate is used to examine injection-induced aseismic slip in a relatively comprehensive manner which includes different stages and regimes, we emphasize in advance that our estimates for the maximum size and magnitude will account for fluid injections conducted with an arbitrary volumetric rate history (Fig. 1a).

2.2 Dynamics of unconditionally stable ruptures and maximum rupture size

During and after fluid injection, our upper-bound model is governed by a single dimensionless number (see Methods), the so-called residual stress-injection parameter:

$$\mathcal{T}_r = \frac{\Delta\tau_{r-0}}{f_r \Delta p_*}, \quad \text{with} \quad \Delta\tau_{r-0} = f_r\sigma_0' - \tau_0 \quad \text{and} \quad \Delta p_* = Q_0\eta/4\pi k w. \tag{1}$$

This dimensionless number systematically emerges in physics-based models of injection-induced fault slip [20, 23–25, 44]. It quantifies the competition between the two opposite *forces* that determine the dynamics of unconditionally-stable ruptures in our upper-bound model. One is a driving force associated with the sole effect of pore pressure increase due to fluid injection which continuously reduces fault shear strength, thereby releasing elastic strain energy that becomes available for rupture growth. Its stress scale is $f_r\Delta p_*$, where Δp_* is the injection intensity. Injections with faster pressurization are associated with increasing values of Δp_* which can occur, for example, due to a higher injection flow rate (Q_0) or a lower hydraulic transmissivity (kw). The other force is of a resisting kind, which in the absence of a local energy dissipation mechanism such as the fracture energy, corresponds to a non-local *consumption* of elastic strain energy associated with the background stress change, $\Delta\tau_{r-0}$. The latter is defined as the difference between the in-situ residual fault strength ($f_r\sigma_0'$) and the initial shear stress (τ_0). The former quantity can be also interpreted as the final shear stress that would act on the slipped fault patch after the termination of the injection operation and the subsequent dissipation of overpressure due to the injection. Hence, $\Delta\tau_{r-0}$ quantifies a change of shear stress between a final and initial state. The background stress change is strictly positive. This is an essential feature of unconditionally stable ruptures. Specifically, the ultimate stability condition: $\tau_0 < f_r\sigma_0'$, ensures the fault stability and the development of quasi-static slip unconditionally in this regime [25, 43]. Intuitively one expects that as the intensity of the injection (Δp_*) increases, the rupture would propagate faster. Conversely, when the background stress change ($\Delta\tau_{r-0}$) is higher, it presents greater resistance to rupture growth, consequently slowing down the slip propagation. Hence, decreasing $\mathcal{T}_r$ values will always result in faster aseismic ruptures. This behavior can be clearly observed in Fig. 2b, where the solution (see Methods) during the pressurization stage for a circular rupture of radius $R(t)$ is shown. Here, $R(t) = \lambda L(t)$, where λ is the so-called amplification factor [20], and $L(t) = \sqrt{4\alpha t}$ is the classical diffusion length scale, also considered as the nominal position of the overpressure front (Fig. 1d). λ therefore relates the position of the overpressure and slip fronts. This analytical circular-rupture solution is strictly valid only when $\nu = 0$ [23]. Throughout this work, we generally adopt the circular rupture approximation to derive purely analytical insights. We, nevertheless, quantify the effect of rupture non-circularity numerically via a boundary-element-based numerical solver (see Methods).

The analytical solution in Fig. 2b provides important insights into the response of our upper-bound model. During the pressurization stage, the fault response is characterized by two distinct regimes. When $\mathcal{T}_r \sim 10$, aseismic ruptures are confined well within the overpressurized region ($\lambda \ll 1$), a regime known as marginally pressurized because it relates to a scenario in which the fluid injection provides just the minimum amount of overpressure that is necessary to activate fault slip [25, 43]. Conversely, when $\mathcal{T}_r \ll 1$, aseismic ruptures break regions much further away than the pressurized fault zone ($\lambda \gg 1$). This is the so-called nearly unstable regime [25] as when $\Delta\tau_{r-0} \to 0$ the rupture approaches the condition under which it becomes ultimately unstable. From a practical standpoint and in an upper-bound sense, this is indeed the most relevant regime as it produces the largest ruptures for a given injection. While operators in geo-energy applications typically maintain good control over the parameters of the fluid injection, in-situ conditions such as the stress state acting upon fractures and faults within a reservoir are subject to significant uncertainties. Given that in-situ conditions largely control the response of aseismic slip in our model, it seems reasonable to assume under rather generic, generally uncertain conditions in the rock mass surrounding a given operation, that the nearly unstable regime provides an upper limit for the size and magnitude of aseismic slip events. Consequently, our emphasis in this work will predominantly be on exploring this regime. In fact, when $\lambda \gg 1$, one can derive a relation linking the evolution of the rupture radius to the accumulated injected fluid volume ($V(t)$) and in-situ conditions as follows (see Methods):

$$R(t) = A_{\text{situ}}\sqrt{V(t)}, \quad \text{with} \quad A_{\text{situ}} = \left(\frac{f_r}{2\pi w S \Delta\tau_{r-0}}\right)^{1/2}. \tag{2}$$

This equation is valid not only for injection at a constant flow rate but also for any arbitrary fluid injection as long as the rupture propagates in crack-like mode during the pressurization stage (see Methods), so that the fracture-mechanics energy balance, equation (10), remains valid. A crack-like propagation mode will certainly hold at least in one relevant scenario, wherein overpressure due to fluid injection increases monotonically everywhere within the sliding region. Hereafter, to put the term arbitrary in a more specific but still sufficiently general scope, we refer to injection with monotonically increasing fluid pressure as *arbitrary.* However, we emphasize that in our model, a monotonically increasing fluid pressure is only a sufficient (not a necessary and sufficient) condition for crack-like propagation. Moreover, equation (2) implies that, during the pressurization stage, the cumulative injected fluid volume $V(t)$ is the only operational parameter of the injection that matters to estimate an upper bound for the rupture size at a given time t. Furthermore, the prefactor is exclusively related to in-situ conditions (A_{situ}).

Upon the stop of the fluid injection ($t > t_s$), our upper-bound model produces ruptures that transition from crack-like to pulse-like propagation mode (Fig. 1d-f). Indeed, since we have reduced the upper-bound problem to a fault responding with a constant friction coefficient

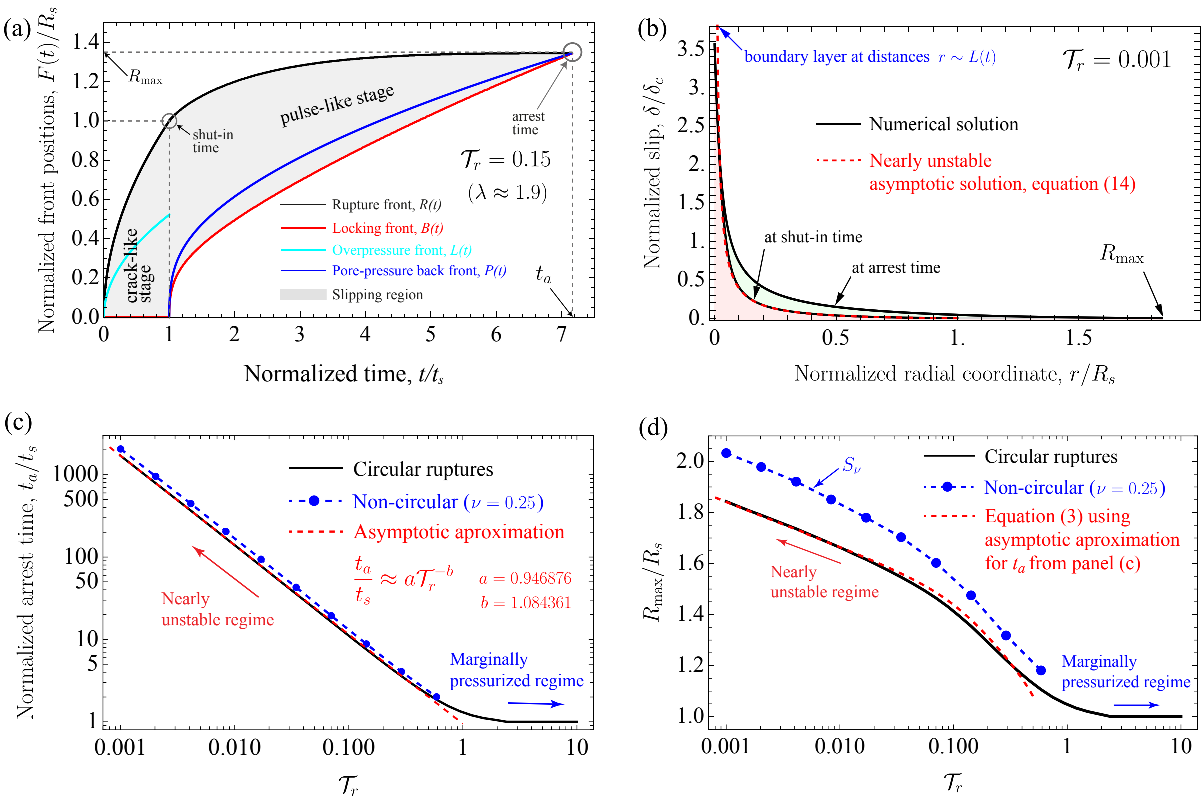

Figure 3: **Dynamics of unconditionally stable ruptures, arrest time, and maximum rupture size.** (a) Evolution of fluid- and slip-related fronts, during the entire lifetime of an injection-induced aseismic slip event, for a case with $\mathcal{T}_r = 0.15$. Front positions $F(t) = R(t), B(t), L(t), P(t)$ are normalized by the rupture radius at the shut-in time, R_s (see the main text for a description of the different fronts). (b) Slip distribution for a very nearly unstable rupture ($\mathcal{T}_r \ll 1$) at the shut-in and arrest times. $\delta_c(t) = f_r \Delta p_* L(t)/\mu$ is the characteristic slip scale in this regime (see Methods). Slip is further accumulated during the shut-in stage due to the slip pulse that travels along the fault upon the shut-in of the injection. (c) Upper bound for the arrest time and (d) maximum rupture run-out distance as a function of the dimensionless parameter $\mathcal{T}_r$.

equal to the residual value f_r, we inherit essentially all the results obtained recently by Sáez and Lecampion [24] who extensively investigated the propagation and arrest of post-injection aseismic slip on a fault with constant friction. In particular, the overpressure drops quickly near the fluid source upon the stop of the injection while it keeps increasing transiently away from it (Fig. 1d-e). This latter increase of pore pressure is what further drives the propagation of aseismic ruptures after shut-in. As shown in Fig. 1e, slip propagates first as a ring-shaped pulse with a locking front that propagates always faster than the rupture front (Fig. 3a). The locking front is driven by the continuous depressurization of pore fluids which re-strengthens the fault. After, and for the more general case of non-circular ruptures, the pulse splits into two 'moon-shaped' pulses (Fig. 1f). This ultimate stage is due to the locking front catching up with the rupture front first in the less elongated side of the slipping region. For the idealized case of circular ruptures, the moon-shaped pulses are absent due to the axisymmetry property of both the fluid flow and shear rupture problems. Fig. 3a displays the evolution of the locking front $B(t)$ and rupture front $R(t)$ for a circular rupture for an exemplifying case with $\mathcal{T}_r = 0.15$. Slip arrests when the locking front catches the rupture front at the time t_a (arrest time or duration of the slow slip event), resulting in the maximum rupture run-out distance $R_{\max}$. Although perhaps more insightfully, the rupture front stops when it is caught by the so-called pore-pressure back front $P(t)$ [24] introduced by Parotidis *et al.* [45]. This latter means that there is no further increase of pore pressure within the rupture pulse that is available to sustain the propagation of slip. Moreover, this arrest condition leads to the following analytical relation between the maximum rupture radius $R_{\max}$ and the arrest time t_a:

$$R_{\max} = \left[4\alpha t_a \left(\frac{t_a}{t_s} - 1\right) \ln\left(\frac{t_a}{t_a - t_s}\right)\right]^{1/2}. \tag{3}$$

In the more practically relevant, nearly unstable regime ($\mathcal{T}_r \ll 1$), the normalized arrest time (Fig. 3c) can be estimated via the following numerically-derived asymptotic approximation, $t_a/t_s \approx a\mathcal{T}_r^{-b}$, with $a = 0.946876$ and $b = 1.084361$. Moreover, Fig. 3c shows that when ruptures are marginally pressurized ($\mathcal{T}_r \sim 10$), the slip pulses arrest almost immediately after the injection stops. Conversely, when ruptures are nearly unstable ($\mathcal{T}_r \ll 1$), the upper bound for the arrest time (t_a) is predicted to be several orders of magnitude the injection duration (t_s). Rupture non-circularity has the effect of slightly increasing both the arrest time and maximum rupture run-out distance $R_{\max}$ (Figs. 3c-d). Furthermore, the contribution of the shut-in stage to $R_{\max}$ is approximately a factor of two at most when ruptures are very nearly unstable ($\mathcal{T}_r \sim 0.001$, Fig. 3d). Hence, the order of magnitude of $R_{\max}$ comes directly from evaluating $R(t)$ in the analytical solution displayed in Fig 2b at the shut-in time, which in the regime $\lambda \gg 1$ takes a more insightful expression given by equation (2), which is valid for arbitrary fluid injections. Using this latter expression, we can calculate the maximum run-out distance when $\lambda \gg 1$ as:

$$R_{\max} = S_\nu A_{\text{situ}} \sqrt{V_{\text{tot}}}, \tag{4}$$

where $V_{\text{tot}} = V(t_s)$ is the total volume of fluid injected during a given operation, and the coefficient S_ν accounts for the further growth of the rupture during the shut-in stage and the effect of rupture non-circularity. S_ν is a function of $\mathcal{T}_r$ and ν and can be simply approximated by the blue dashed line in Fig. 3d for $\nu = 0.25$.

2.3 Maximum moment release and magnitude

To calculate the moment release, we derive analytical upper bounds for the spatiotemporal evolution of fault slip during the pressurization stage, for both nearly unstable ($\lambda \gg 1$) and marginally pressurized ($\lambda \ll 1$) ruptures (see Methods). Notably, the slip distribution of nearly unstable ruptures is highly concentrated around the injection point due to a boundary layer associated with the fluid-injection force at distances $r \sim L(t)$ (Fig. 3b). Upon integrating the analytical slip distributions over the rupture surface, the temporal evolution of moment release is:

$$M_0 \simeq \begin{cases} \frac{16}{3}\Delta\tau_{r-0}R^3 & \text{for nearly unstable ruptures, } \lambda \gg 1, \\ \frac{16}{9}f_r\Delta p_* R^3 & \text{for marginally pressurized ruptures, } \lambda \ll 1, \end{cases} \tag{5}$$

with the temporal dependence of M_0 embedded implicitly in $R(t) = \lambda L(t)$ which is known analytically (Fig. 2b). As expected, the previous asymptotic solutions for M_0 match very closely the full numerical solution (Fig. 4a). The numerical solution helps us to describe the precise transition between the two end members. We emphasize that the structure of the scaling for M_0 is evidently the one expected for a circular crack ($M_0 \propto R^3$). Yet the pre-factors and relevant stress scales are specific to the characteristic loading of each regime. For instance, in the nearly unstable regime ($\lambda \gg 1$), the proper stress scale is the background stress change ($\Delta\tau_{r-0}$), as opposed to the injection intensity ($f_r\Delta p_*$) which is the adequate stress scale when $\lambda \ll 1$. This is because, in the nearly unstable regime, most of the slipping region experiences a uniform stress variation $\Delta\tau_{r-0}$ except for a very small region of size $\sim L(t)$ near the fluid source which undergoes an additional non-uniform stress change due to the fluid injection. The effect of the fluid-injection force is indeed in the pre-factor 16/3, which is about two times bigger than the one of a circular crack with purely uniform stress drop (16/7 when $\nu = 0.25$ [46], and 8/3 when $\nu = 0$ [47]). Moreover, in this regime, we obtain the following expression for the moment release which is valid for arbitrary fluid injections (see Methods):

$$M_0(t) = I_{\text{situ}} \cdot V(t)^{3/2}, \quad \text{with} \quad I_{\text{situ}} = \frac{16}{3(2\pi)^{3/2}} \frac{1}{\sqrt{\Delta\tau_{r-0}}} \left(\frac{f_r}{wS}\right)^{3/2}. \tag{6}$$

Equation (6) has the same property as equation (2), that is, the only operational parameter of the injection controlling the upper bound for the moment release during the pressurization stage is the cumulative injected fluid volume $V(t)$. Furthermore, the prefactor corresponds as well to in-situ conditions (I_{situ}), thus effectively separating contributions to the moment release that are controllable during an operation (V) and those that are not (I_{situ}). Such kind of relation for the moment release has been previously reported in the literature for the case of regular, fast earthquakes [27, 28, 30, 32, 35].

Equation (6) shows that a decrease in background stress change ($\Delta\tau_{r-0}$) leads to an increase in moment release. The reason behind such behavior is simple, lower background stress variations result in less opposition for the rupture to grow and thus in a higher moment release. For the same reason, higher values of the residual friction coefficient (f_r) also augment M_0. On the other hand, decreasing the product between the fault-zone width and oedometric storage coefficient (wS), hereafter denominated as fault-zone storativity, also leads to a larger moment release. The explanation, in this case, is that wS controls the pressurization intensity due to fluid injection that is experienced on average over the fault pressurized region. A lower storativity in the fault zone naturally implies a higher fluid pressure to accommodate a fixed amount of injected volume (see equation (18)). A higher fluid overpressure decreases fault shear strength therefore increasing the mechanical energy available for rupture growth and the corresponding moment release. It is important to note that in the marginally pressurized regime ($\lambda \ll 1$), M_0 does not follow an expression as in (6). Indeed, by substituting the expressions $\Delta p_* = Q_0\eta/4\pi kw$, $R(t) = \lambda\sqrt{4\alpha t}$, and $V(t) = Q_0 t$ into equation (5), one can readily show that the moment release for an injection at a constant flow rate is given by $M_0(t) = B \cdot V(t)^{3/2}$, with $B = (32/9\pi)(f_r\eta/kw)(\lambda^3\alpha^{3/2}/Q_0^{1/2})$. This implies that in this regime, the moment release depends on both the current injected volume $V(t)$ (or injection time t) and the injection rate Q_0 (which is also implicitly in λ). More importantly, the in-situ and operational factors cannot be separated as in (6). This separation is a unique characteristic of nearly unstable ruptures, associated with the fact that when $\lambda \gg 1$, the effect of the fluid source on rupture propagation is

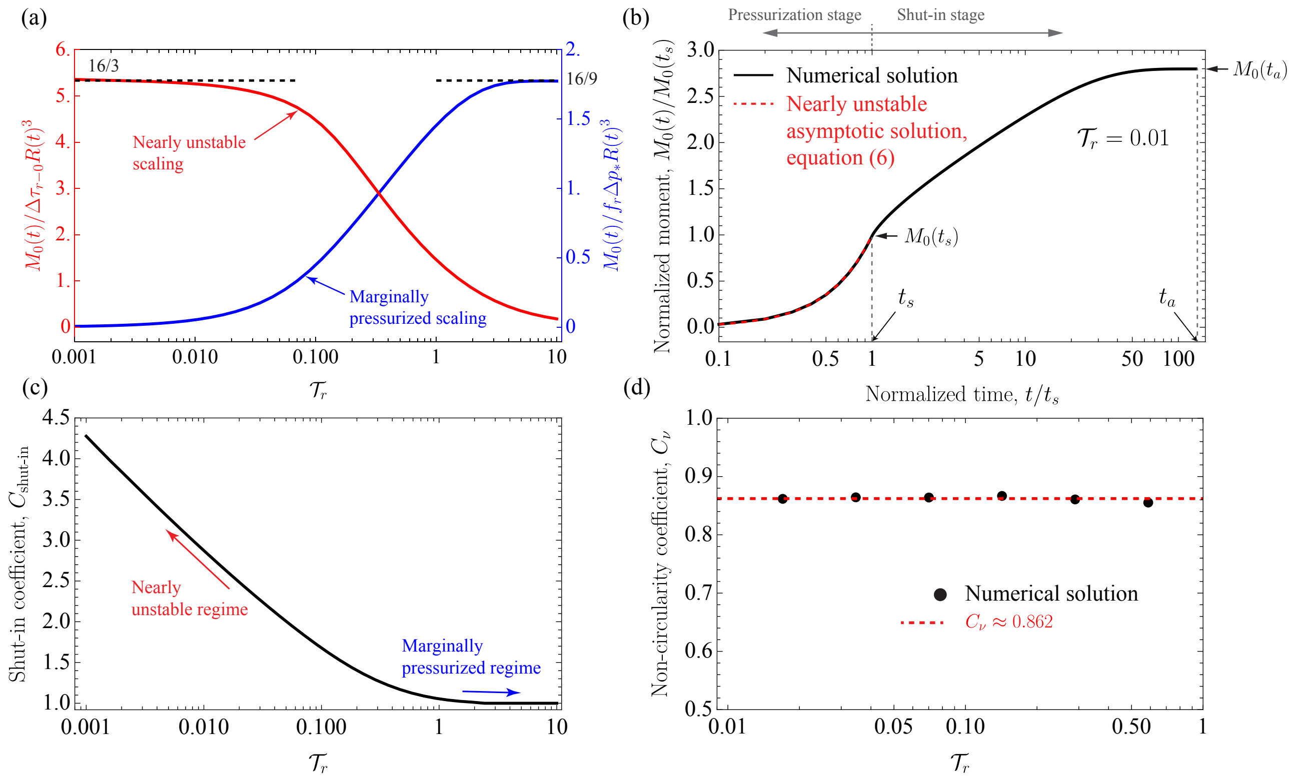

Figure 4: **Upper-bound model for the moment release.** (a) Normalized moment release during the pressurization stage as a function of the residual stress-injection parameter $\mathcal{T}_r$ using the nearly unstable (red, left axis) and marginally pressurized (blue, right axis) scalings. Black dashed lines correspond to asymptotic analytical solutions provided in the main text. Solid lines correspond to numerical solutions. (b) Evolution of the moment release for a nearly unstable circular rupture ($\mathcal{T}_r \ll 1$) during and after fluid injection. The moment release increases up to ≈ 3 times the moment release at the shut-in time in this particular case. (c) Shut-in coefficient $C_{\text{shut-in}} = M_0(t_a)/M_0(t_s)$ for a circular rupture as a function of the dimensionless parameter $\mathcal{T}_r$. Nearly unstable ruptures can experience a moment release increment of up to ≈ 4 times during the shut-in stage. Conversely, marginally pressurized ruptures ($\mathcal{T}_r \sim 10$) are characterized by no increment at all. (d) Non-circularity coefficient C_ν as a function of $\mathcal{T}_r$ for $\nu = 0.25$. The numerical simulations suggest that over a wide range of practically relevant cases ($0.01 \leq \mathcal{T}_r \leq 1$), the moment release of a non-circular rupture is about 13.8 percent smaller than the moment release of a circular rupture ($\nu = 0$) at same $\mathcal{T}_r$.

entirely described by its equivalent force at distances $r \gg L(t)$. The magnitude of this equivalent force is determined only by the injected fluid volume, irrespective of any other detail of the fluid injection (see Methods, equation (21)).

During the shut-in stage ($t > t_s$), the propagation and ultimate arrest of the aseismic slip pulses result in a further accumulation of fault slip (Fig. 3b). The depressurization stage thus increases the final, maximum moment release of the events. Fig. 4b displays the evolution of this increase for an exemplifying case with $\mathcal{T}_r = 0.01$. We observe that the moment release keeps growing after shut-in very slowly (over a timescale that is about 100 times the injection duration) up to reaching (at arrest) nearly three times the moment release at the time the injection stops ($M_0(t_s)$). We quantify this effect in the most general form by defining the shut-in coefficient $C_{\text{shut-in}}$, equal to the ratio between the maximum moment release at the time in which a circular rupture arrest, $M_0(t_a)$, and the moment release at the shut-in time, $M_0(t_s)$. By dimensional analysis, the shut-in coefficient depends only on the residual stress-injection parameter $\mathcal{T}_r$, whose relation is calculated numerically and displayed in Fig. 4c. We observe that $M_0(t_a)$ is at most around 4 times the moment release at the time the injection stops in the more nearly unstable cases (smallest values of $\mathcal{T}_r$). Conversely, there is virtually no further accumulation of moment release for marginally pressurized ruptures. We quantify the effect of rupture non-circularity in a similar way by introducing the coefficient C_ν equal to the ratio between the moment release at the time of arrest for non-circular ruptures ($\nu \neq 0$), and the same quantity for the circular case ($\nu = 0$). Again, by dimensional considerations, C_ν depends only on $\mathcal{T}_r$ for a given ν. This is shown in Fig. 4d for the particular case of a Poisson's solid ($\nu = 0.25$, a common approximation for rocks). We observe that the effect of the Poisson's ratio is to reduce in about 13.8 percent the moment release of a non-circular rupture with respect to the one of a circular rupture, for the same $\mathcal{T}_r$. We find this to be valid over a wide range of practically relevant cases ($0.01 \leq \mathcal{T}_r \leq 1$). With all the previous definitions and calculations, we can finally estimate the maximum moment release as $M_0^{\max} = C_\nu \cdot C_{\text{shut-in}} \cdot M_0(t_s)$. Notably, in the nearly unstable regime ($\lambda \gg 1$), equation (6) can be evaluated at the shut-in time, which allows us to arrive at the following expression valid for arbitrary fluid injections:

$$M_0^{\max} = C_\nu \cdot C_{\text{shut-in}} \cdot I_{\text{situ}} \cdot V_{\text{tot}}^{3/2}, \tag{7}$$

where $V_{\text{tot}} = V(t_s)$ is the total volume of fluid injected during a given operation. Equation (7) has a multiplicative form, thus effectively factorizing contributions from the injected fluid volume, in-situ conditions, shut-in stage, and rupture non-circularity to the maximum moment release. Note that both $C_{\text{shut-in}}$ and C_ν depend on $\mathcal{T}_r$ and thus also on in-situ conditions and parameters of the injection (equation (1)). However, the in-situ conditions and injection protocol are for the most part contained in I_{situ} and V_{tot}, respectively, which can vary over several orders of magnitude. On the contrary, the dimensionless coefficients $C_{\text{shut-in}}$ and C_ν remain always of order one. Moreover, we shall keep in mind that these latter two coefficients are, strictly speaking, defined only for injection at a constant flow rate. Nevertheless, one could crudely approximate any other kind of injection protocol as $Q_{\text{eq}} = (1/t_s)\int_0^{t_s} Q(t)\mathrm{d}t$ for the purpose of estimating these two coefficients. The previous approximation guarantees that the same amount of fluid volume is injected over the same injection period t_s by both the equivalent constant-rate source Q_{eq} and the time-varying arbitrary source $Q(t)$. Finally, for marginally pressurized ruptures ($\lambda \ll 1$), a similar expression for the maximum moment release can be derived as $M_0^{\max} = C_\nu \cdot B \cdot V_{\text{tot}}^{3/2}$ (since $C_{\text{shut-in}} \approx 1$, Fig. 4c). As already discussed, the in-situ and operational factors cannot be separated in this regime.

To calculate the maximum magnitude, we follow the definition by Hanks and Kanamori [48]: $M_w^{\max} = 2/3 \cdot [\log_{10}(M_0^{\max}) - 9.1]$ (here, in SI units). In the regime that provides the largest rupture size and moment release for a given injection ($\lambda \gg 1$), equation (7) leads to the following estimate for the maximum magnitude:

$$M_w^{\max} = \log_{10}(V_{\text{tot}}) + \frac{2}{3}\left[\log_{10}(I_{\text{situ}}) + \log_{10}(C_{\text{shut-in}}) + \log_{10}(C_\nu) - 9.1\right]. \tag{8}$$

Due to the multiplicative form of equation (7), equation (8) takes an additive form that separates contributions from different factors to the maximum magnitude of injection-induced slow slip events. Among these factors, rupture non-circularity decreases the magnitude only by 0.06. The contribution from the shut-in stage is, on the other hand, slightly larger. Since $C_{\text{shut-in}} \approx 4$ at most when ruptures are very nearly unstable ($\mathcal{T}_r \sim 0.001$), the shut-in stage may contribute to an increase in the moment magnitude of 0.4 at the maximum. The larger contributions to $M_w^{\max}$ are by far the ones associated with in-situ conditions and the total injected fluid volume. For example, a tenfold increase in V_{tot} gives a magnitude increase of 1.0, while a tenfold increase in I_{situ} results in a magnitude growth of approximately 0.67. The relative contributions from the sub-factors composing I_{situ} can be further understood by substituting equation (6) into (8), and then isolating the in-situ term as follows:

$$(2/3)\log_{10}(I_{\text{situ}}) = \log_{10}(f_r) - (1/3)\log_{10}(\Delta\tau_{r-0}) - \log_{10}(wS) - 0.3135. \tag{9}$$

The more significant variations in $M_w^{\max}$ come clearly from the fault-zone storativity (wS) and background stress change ($\Delta\tau_{r-0}$), which could vary over several orders of magnitude. For instance, a variation of three orders of magnitude in $\Delta\tau_{r-0}$ yields a change of magnitude of 1.0, while the same variation in fault-zone storativity results in a magnitude change of 3.0, highlighting the potentially strong effect of wS in $M_w^{\max}$.

2.4 Fault-zone storativity and injected fluid volume: two key parameters

To test our scaling relations, we compiled and produced a new dataset (Supplementary Materials) with estimates of aseismic moment release, rupture size, and injected fluid volumes from events that vary in size from laboratory experiments (centimetric to metric scale ruptures) [49, 50] to industrial applications (hectometric to kilometric scale ruptures) [3, 4, 10, 21, 51], including in-situ experiments in shallow natural faults at intermediate scales (metric to decametric ruptures) [6, 52, 53]. The comparison between this dataset and our expressions for the maximum moment release (7) (or magnitude (8)) and maximum rupture size (3), are displayed in Figs. 5 and 6 respectively. We focus first on the maximum moment release (Fig. 5). To facilitate the comparison against the dataset, we introduce in Fig. 5 the factor $N = C_\nu \cdot C_{\text{shut-in}} \cdot I_{\text{situ}}$ which encapsulates all effects other than the injected fluid volume, so that equation (7) can be simply written as $M_0^{\max} = N \cdot V_{\text{tot}}^{3/2}$. Three different values for N are considered in Fig. 5 which collectively form an upper bound for the data across the different volume and moment release scales characterizing the dataset. Considering that $C_\nu \approx 0.862$ and that plausible values for the coefficient $C_{\text{shut-in}}$ range from 1 to 4, the order of magnitude and units of N are the ones determined by the in-situ factor (I_{situ}). This latter, in turn, depends on three parameters: the residual friction coefficient f_r (with a plausible range of 0.4 to 0.8), the background stress change ($\Delta\tau_{r-0}$), and the fault-zone storativity (wS). The background stress change can be at most equal to the amount of shear stress that is necessary to activate fault slip before the injection starts, $\Delta\tau_{p-0} = f_p\sigma'_0 - \tau_0$, in the limiting case in which the weakening of friction is small ($f_r \approx f_p$). Its minimum value could be, on the other hand, as small (but positive) as possible when the residual fault strength drops close to the initial shear stress ($f_r\sigma'_0 \approx \tau_0$). This is, as already discussed, the case that would promote larger ruptures and moment release. $\Delta\tau_{r-0}$ could therefore reasonably fluctuate between some MPa and a few kPa. The fault-zone storativity (wS) may similarly vary over several or potentially many orders of magnitude [54–57]. Estimating this parameter is quite challenging; however, as anticipated by equation (9), wS could have a strong effect on

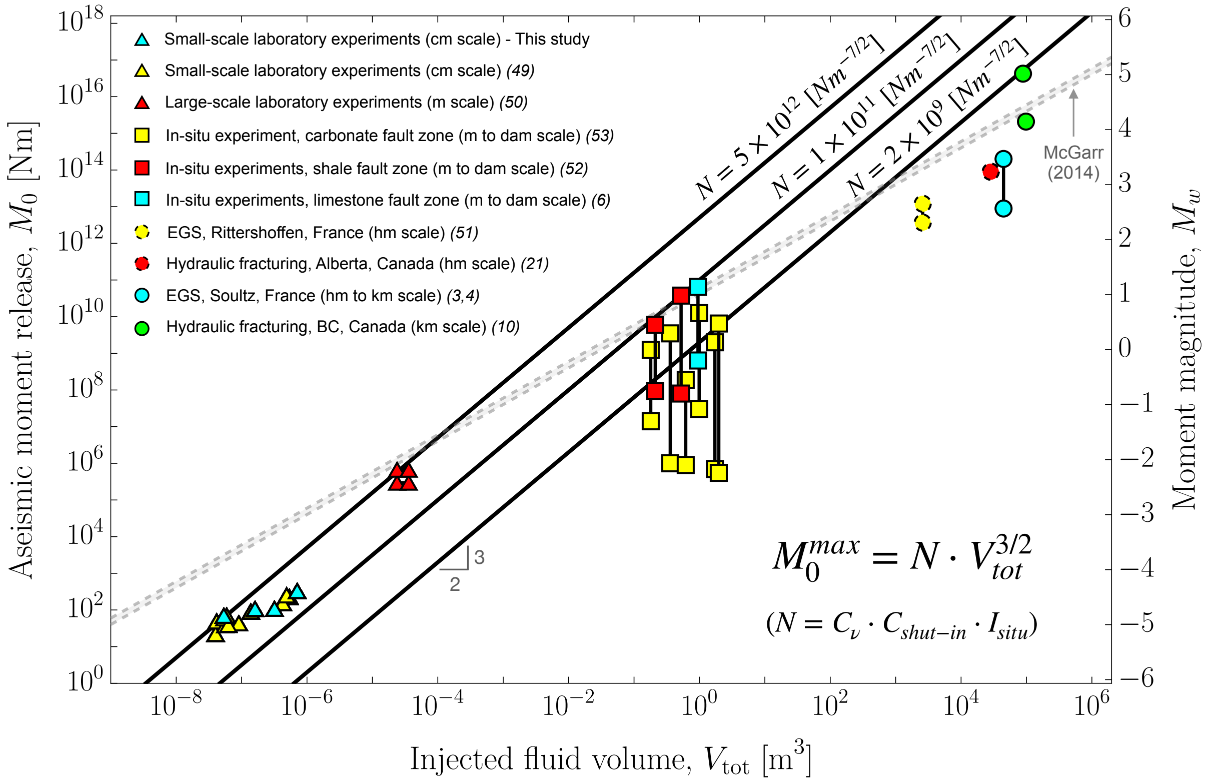

Figure 5: **Comparison of our scaling relation for the maximum magnitude $M_w^{\mathbf{max}}$ with estimates of moment magnitude from injection-induced slow slip events, as a function of the total injected fluid volume.** We consider three values of the factor N (solid black lines) which collectively form an upper bound for the data across different volume and moment release scales. For some events in the dataset, the moment release is estimated within a range that is represented by a vertical line connecting their maximum and minimum values (see Supplementary Materials for further details). Gray dashed lines represent McGarr's relation [28] for shear moduli of 20 and 30 GPa.

the maximum magnitude. Hence, we conduct a more intricate analysis of representative values for wS within our compilation of events.

To do so, we examine the end members of our data points, namely, small-scale laboratory experiments and industrial-scale fluid injections. Let us first note that in our model, wS can be written in terms of generally more accessible quantities as $kw/\alpha\eta$, where kw is the fault-zone hydraulic transmissivity, η is the fluid dynamic viscosity, and α is the fault-zone hydraulic diffusivity. At the centimetric scale composing the smallest aseismic slip events in the dataset, Passelègue *et al.* [49] estimated the hydraulic transmissivity of their saw-cut granitic fault within 10^{-17} and 2×10^{-18} m^3, and a hydraulic diffusivity from 3×10^{-5} m^2/s to 10^{-6} m^2/s [58], at confining pressures ranging from 20 to 100 MPa respectively. Considering a water dynamic viscosity at the room temperature the experiments were conducted, $\eta \sim 10^{-3}$ Pa·s, we estimate wS to be within 3×10^{-10} and 2×10^{-9} m/Pa (assuming that kw and α are positively correlated). Taking into consideration the aforementioned characteristic range of values for f_r and $\Delta\tau_{r-0}$, we estimate the maximum value for the in-situ factor that is representative of these laboratory experiments to be roughly $I_{\text{situ}} \sim 10^{12}$ N·m$^{-7/2}$. Interestingly, the upper bound for the moment release resulting from this value of I_{situ} aligns closely with our estimates of moment release and injected fluid volumes for this very same set of experiments (Fig. 5, yellow triangles). Note that in Fig. 5, the factor N must always be interpreted as being greater than I_{situ} due to the combined effect of the coefficients C_ν and $C_{\text{shut-in}}$. In addition, this upper bound seems to explain relatively well the centimeter-scale laboratory experiments presented in this study (cyan triangles; Supplementary Materials) and the meter-scale laboratory experiments of Cebry *et al.* [50] (red triangles). The former experiments were carried out under almost identical conditions to the ones of Passelègue *et al.* [49], whereas the latter ones were conducted in a similar saw-cut granitic fault with hydraulic properties that are close to the ones of Passelègue *et al.*'s fault at the lower confining pressures of this latter one [49].

At the large scale of industrial fluid injections, we consider one of the best-documented field cases: the 1993 hydraulic stimulation at the Soultz geothermal site in France [3]. The hydraulic transmissivity associated with the 550-m open-hole section stimulated during the test has been estimated to experience a 200-fold increase as a consequence of the two fluid injections conducted, giving us a possible range of approximately 10^{-14} m^3 to 2×10^{-12} m^3 [59]. However, the smallest value of kw represents only the very short, initial part of the injection [59]. Therefore, a possible variation between 5×10^{-14} m^3 and 2×10^{-12} m^3 seems a more reasonable range to be considered within the assumptions of our model which assumes a constant transmissivity. On the other hand, the hydraulic diffusivity possesses significant uncertainties due to the single-well nature of the hydraulic data in contrast to the double-well measurements employed, for instance, by Passelègue *et al.* [49] in the laboratory. We consider a range of values for α from 0.01 m^2/s to 0.1 m^2/s, which is consistent with estimates derived from micro-seismicity migration [45] and aseismic fracture slip [24]. Assuming a water dynamic viscosity of $\eta = 2\times10^{-4}$ Pa·s which is representative of the temperature conditions within the reservoir [60], we estimate wS to fall within the range of 5×10^{-8} m/Pa to 10^{-7} m/Pa. With these estimates, we calculate a representative maximum value for the in-situ factor in this field test to be roughly $I_{\text{situ}} \sim 10^9$ N· m$^{-7/2}$. As shown in Fig. 5, the resulting upper limit aligns very well with the field data (circles), providing an effective upper bound for the hectometric to kilometric rupture cases composing the dataset. Furthermore, this simplified, order-of-magnitude analysis suggests that the behavior of the upper limit we observe from the laboratory to the reservoir scale, namely, the decrease of the factor N with increasingly larger volume and moment release scales, might be primarily controlled by an increase in fault-zone storativity. Moreover, the upper bound for intermediate scales (in-situ experiments, square symbols in Fig. 5) is characterized by a value of N (or I_{situ}) that is approximately in the middle of the values that provide an upper limit for the laboratory and field data, suggesting that the increase in storativity with larger scales could be a general explanation for the trend observed throughout the entire dataset.

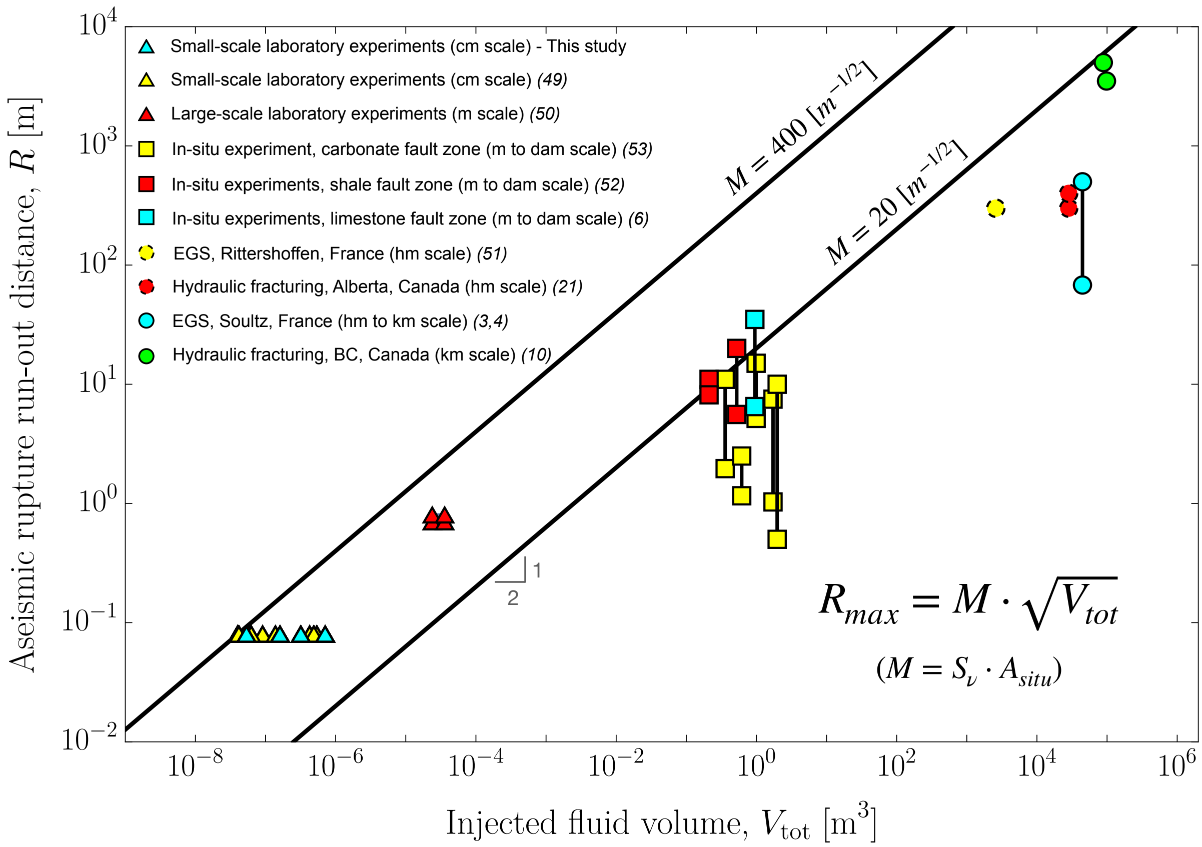

Figure 6: **Comparison of our scaling relation for the maximum rupture run-out distance $R_{\max}$ with estimates of rupture extent for the same injection-induced slow slip events as in Fig. 5, as a function of the total injected fluid volume.** We consider two values of the factor M (solid black lines) which together form an upper bound for the data across different volume and rupture run-out distance scales. Likewise in Fig. 5, for some events the rupture extent is estimated within a range that is represented by a vertical line connecting their maximum and minimum values (see Supplementary Materials for further details)

Finally, Fig. 6 shows the comparison of our scaling relation for the maximum rupture run-out distance, equation (4), with the estimated rupture run-out distances for the same injection-induced aseismic slip events as in Fig. 5. To facilitate the interpretation, we similarly define the factor $M = S_\nu A_{\text{situ}}$ accounting for all effects other than the injected fluid volume, so that equation (4) becomes simply $R_{\max} = M\sqrt{V_{\text{tot}}}$. It is important to note that the effects of $\Delta\tau_{r-0}$ and wS are now of similar order, as $R_{\max}$ scales alike with the background stress change $R_{\max} \propto \Delta\tau_{r-0}^{-1/2}$ and fault-zone storativity $R_{\max} \propto (wS)^{-1/2}$. Considering the same range of values for f_r, $\Delta\tau_{r-0}$ and wS discussed previously, we calculate A_{situ} to be around 200 $\text{m}^{-1/2}$ for Passelègue *et al.*'s experiments, and 15 $\text{m}^{-1/2}$ for the Soultz case. As shown in Fig. 6, the upper limits resulting from these two values of A_{situ} (considering also an amplification due to the factor S_ν) are in remarkably good agreement with the data, providing an effective upper bound for the maximum rupture run-out distance from cm-scale ruptures in the laboratory to km-scale ruptures in industrial applications.

3 Discussion

Our results provide a rupture-mechanics-based estimate for the maximum size, moment release, and magnitude of injection-induced slow slip events. Moreover, the dependence of our scaling relations on in-situ conditions and injected fluid volume allows us to explain variations in rupture sizes and moment releases resulting from fluid injections that span more than 12 orders of magnitude of injected fluid volume. Similar scaling relations for the moment release of regular, fast earthquakes have been previously proposed in the literature [28, 32, 35]. Notably absent in those relations, fault-zone storativity appears here to be a crucial factor influencing the upper-bound behavior we observe with increasing scales of volume and moment release in the data. While our scaling relation for the maximum aseismic rupture run-out distance is the first of its kind, McGarr and Barbour [61] suggested in a prior work that for the moment release, the relation for the cumulative moment $\Sigma M_0 = 2\mu V_{\text{tot}}$ that was originally proposed by McGarr [28] for regular earthquakes, account also for aseismic slips. It is thus pertinent to discuss their scaling relation in light of our findings.

We first note that in testing their relation, McGarr and Barbour [61] incorporated numerous data points of aseismic moment release and injected volume into a dataset characterized by otherwise only regular earthquakes. All of these aseismic slip events come from laboratory experiments of hydraulic fracturing [62], except for one single data point that stems from direct measurements of injection-induced aseismic slip during an in-situ experiment [6]. The mechanics of hydraulic fractures [63], however, differs significantly from its shear rupture counterpart. Indeed, the moment release by hydraulic fractures scales linearly with the injected fluid volume simply because the integral of the fracture width over the crack area is equal to the fracture volume. The latter is approximately equal to the injected volume under common field conditions, namely, negligible fluid leak-off and fluid lag [63]. In our study, we discarded these hydraulic-fracturing data points because they correspond to a different phenomenon. The remaining data point of McGarr and Barbour, which does correspond to a fluid-driven shear rupture [6], is retained in our dataset albeit with a certain degree of uncertainty based on moment release estimates provided by more recent studies (Supplementary Materials).

In terms of modeling assumptions, one of the most significant differences between McGarr's and ours is that we account for the potential for aseismic ruptures to propagate beyond the fluid-pressurized region ($\lambda \gg 1$). This regime, which from an upper-bound perspective is of most practical interest as it produces the largest ruptures for a given injection, is not allowed by construction in McGarr's model due to his assumption that any fault slip induced by the fluid injection must be confined within the region where pore fluids have been effectively pressurized due to the injection [28]. We emphasize that aseismic ruptures breaking non-pressurized fault regions are a possibility that always emerges when incorporating rupture physics in a model [43], even in the absence of frictional weakening owing simply to long-range elastostatic stress transfer effects [20]. Moreover, such a regime has already been directly observed in laboratory experiments [50], and inferred to have occurred during in-situ experiments [6, 20] and industrial fluid injections for reservoir stimulation [21]. Furthermore, as a natural consequence of incorporating rupture physics in our model, we obtain a dependence of the moment release on the background stress state and fault frictional parameters. McGarr's model is, in contrast, insensitive to these physical quantities, which largely control the release of elastic strain energy during rupture propagation. Another important distinction between both models is that McGarr's relies uniquely on the capacity of the rock bulk to elastically deform and volumetrically shrink to accommodate the influx of fluid mass from the injection, unlike our model which accounts for bulk, fluid, and pore compressibilities within the fault zone via the so-called oedometric storage coefficient [42].

Despite the significant differences between both models, it is pertinent to compare McGarr's relation for the moment release with our newly compiled dataset. By doing so, we observe that McGarr's upper bound can explain the majority of the data points, albeit with one very important exception (Fig. 5): the 2017 M_w 5.0 slow slip event in western Canada [10]; the largest event detected thus far. Specifically, McGarr's formula fails by predicting a maximum magnitude of 4.4 (considering $V_{\text{tot}} = 88,473$ m^3 and assuming a shear modulus of 30 GPa [10]). This magnitude is equivalent to predicting an upper limit for the moment release that is 16 times smaller than the actual moment that was inferred geodetically [10]. Such underestimation is somewhat similar to that performed by McGarr's formula in the case of regular earthquakes: for instance, when considering the 2017 M_w 5.5 Pohang earthquake in South Korea [15]. Our scaling relation can, conversely, explain the M_w 5.0 slow slip event in Canada and, more generally, our entire compilation of events by accounting for variations in in-situ conditions such as the background stress change ($\Delta\tau_{r-0}$) and, especially, the fault-zone storativity (wS). Note that from a 'data-fitting' perspective, the dependence of our model on wS and $\Delta\tau_{r-0}$ introduces additional degrees of freedom compared to McGarr's formula, which depends only on the injected fluid volume and the shear modulus; a parameter that has very little variation in practice.

Our estimates of the maximum rupture size and magnitude for slow slip events may be regarded, to some extent, as an aseismic counterpart of the also rupture-mechanics-based scaling relation proposed by Galis *et al.* [32] for regular earthquakes. Although we are describing a fundamentally different process here, the two scaling relations share the same 3/2-power law dependence on the injected fluid volume. This equal exponent arises from the similarities between the competing forces driving both slow slip events and dynamic ruptures in each model, namely, a point-force load due to fluid injection and a uniform stress change behind the cohesive zone and within the ruptured surface. In Galis *et al.*'s model, a point-force-like load is imposed to nucleate an earthquake. In our model, it is the natural asymptotic form that the equivalent force associated with the fluid injection takes in the regime that provides the largest ruptures for a given injection ($\lambda \gg 1$). Note that the two models differ in their storativity-like quantity. As we discussed before, we account for the capacity of the fluid, pore space, and bulk material in the fault zone to store pressurized fluids. In contrast, Galis *et al.*'s model accounts only for the capacity of the bulk material: a property they inherited from McGarr's model [28]. A revision of seismic scaling relations may be required to include the notion of a more general storativity term, particularly considering the significant variability in pore compressibility observed in practice [54–57] which can sometimes dominate over bulk and fluid compressibilities. Another important difference with Galis *et al.*'s model is the uniform variation of background stress which in their model is the so-called stress drop $\Delta\tau_{0-r} = \tau_0 - f_r\sigma_0'$, whereas in our case, it corresponds to the same quantity but of opposite sign, $\Delta\tau_{r-0} = f_r\sigma_0' - \tau_0$. Conceptually, this is indeed a very important difference. In our model, the stress *drop* is negative, which implies that after the termination of the injection operation and the subsequent dissipation of overpressure due to the injection, the residual shear stress acting on the slipped fault patch will be greater than the initial shear stress. This, which is a prominent feature of unconditionally stable ruptures, implies no release of tectonically accumulated pre-stresses on the fault.

The previous point brings us to an important issue: we have considered only one of the two possible modes of aseismic slip, namely, fault ruptures that are unconditionally stable. However, injection-induced aseismic slip can also be the result of conditionally stable slip, that is, the nucleation phase preceding an otherwise dynamic rupture. The principal factor determining whether aseismic slip will develop in one way or the other is the so-called ultimate stability condition [25, 43]. For conditionally stable slip to occur, the initial shear stress must be thus greater than the background residual fault strength ($\tau_0 > f_r\sigma_0'$), resulting in a positive stress drop. This is therefore the mode of aseismic slip that can potentially release tectonically accumulated pre-stresses. In general, we cannot rule out that the points in the datasets of Fig. 5 and 6 correspond to either conditionally stable or unconditionally stable slip, as estimating the background stress state and fault frictional properties that are representative of the reactivated fault remains extremely challenging in practice. There is, nevertheless, at least one case in the dataset in which aseismic slip is as a matter of fact, conditionally stable. These are the two aseismic slip events from the meter-scale laboratory experiments of Cebry *et al.* [50], which preceded seismic ruptures that broke the entire fault interface sample (Supplementary Materials). The scaling relations resulting from this mode of aseismic slip are therefore important. Moreover, considering that the data points from Cebry *et al.*'s experiments align well with the other points in the dataset, we anticipate these scaling relations to be similar in their structure to the ones presented here.

Our model aimed to capture the most essential physical ingredients of unconditionally stable ruptures to provide the desired theoretical insights into the physical mechanisms controlling the maximum size and magnitude of injection-induced slow slip events. To achieve this, we have however adopted several simplifying assumptions that warrant further investigation. In particular, our model does not account for fluid leak-off from the permeable fault zone to the host rock, nor permeability enhancements associated with fault slip and/or the reduction of effective normal stress due to fluid injection. Despite these simplifications, we expect our scaling relations to still provide an effective upper bound with regard to these additional factors. Indeed, we think that incorporating a permeable host rock would notably decrease the injection overpressure in the fault zone compared to the impermeable case, thus decelerating rupture growth. The effect of slip-induced dilatancy, which is relatively well-established [64, 65], would introduce a toughening effect that would similarly slow down slip propagation from a fracture-mechanics perspective. Furthermore, permeability enhancements due to both dilatancy and reduced effective normal stress are expected to be inconsequential in the limit $\lambda \gg 1$, which is the relevant one for establishing an upper bound. This is due to, in this regime, most of the slipping region remains non-pressurized except for a small area near the fluid source. The strength of this small (point-force-like) region remains unchanged in our model, provided that the enhanced hydraulic properties are considered as the constant ones [65]. An additional simplification in our model is the consideration of a single fault zone. Although this might likely be the case for the majority of the events incorporated in our dataset [6, 10, 21, 49–53], in some cases, a network of fractures or faults could be reactivated instead [3, 60]. Recent numerical modeling studies on injection-induced aseismic slip have, however, shown that approximately the same scaling relations for the moment release predicted by a single fracture in two dimensions emerge collectively for a set of reactivated fractures belonging to a two-dimensional discrete fracture network [44]. This is notably the case when the regime $\lambda \gg 1$ is reached in a global, fracture-network sense. Yet the generality and prevalence of this finding in three dimensions remain to be confirmed.

We notably showed that in the nearly unstable regime ($\lambda \gg 1$), the dynamics of the rupture expansion in our upper-bound configuration are controlled uniquely by the history of injected fluid volume, irrespective of any other characteristic of the injection protocol. The implications of this finding may go well beyond the ones explored in this work. For example, in hydraulic stimulation operations for the development of deep geothermal energy, micro-seismicity clouds which often accompany fluid injections are commonly used to constrain the areas of the reservoir that have been effectively stimulated. If aseismic-slip stress transfer is a dominant mechanism in the triggering of micro-seismicity, our model suggests that these seismicity clouds may contain important information about the pre-injection stress state and fault frictional properties which are embedded in the factor A_{situ} (equation (2)). Moreover, if the effect of the fracture energy on rupture propagation can be approximately neglected in comparison to the other two competing forces driving aseismic ruptures in our model, that is, the background stress change and fluid-injection force, our results imply that the spatiotemporal patterns of seismicity migration might be deeply connected to injection protocols via the dependence of the aseismic slip front dynamics on the square root of the cumulative injected fluid volume. This could be used, for instance, to identify from injection-induced seismicity catalogs under what conditions aseismic-slip stress transfer may become a potentially dominant triggering mechanism due to this unique spatiotemporal footprint, which differs notably from the ones emerging from other triggering mechanisms such as pore pressure diffusion and poroelastic stressing [66, 67]. Similarly, our model could be potentially applied to the study of natural seismic swarms where sometimes fluid flow and aseismic slip processes are thought to be the driving forces behind their observed dynamics [68, 69]. Lastly, our model could be also utilized to understand slow slip events occurring at tectonic plate boundaries in many subduction zones worldwide. The fundamental mechanics of slow slip events remains debated [70] yet multiple, recent observations suggest that their onset and arrest might be spatially and temporally correlated with transients of pore-fluid pressure [71–73].

Finally, we emphasize that our investigation has focused on constraining the rupture size and moment release of purely aseismic injection-induced ruptures. However, in some instances, seismic or micro-seismic events may release a substantial portion of the elastic strain energy stored in the medium. In this study, we have incorporated in our compilation of events only cases where the seismic contribution to the moment release is thought to be orders of magnitude smaller than the aseismic part. From a mechanics perspective, this aimed to exclude events where the stress transfer from frictional instabilities could significantly influence the dynamics of the slow rupture under consideration, thereby ensuring a robust comparison between the data and the scaling relations of our model. Future studies should therefore focus on understanding what physical factors govern the partitioning between aseismic and seismic slips during injection operations. Our work, in this sense, contributes to such possibility by providing an upper limit to the previously unexplored aseismic end-member. Together with prior works on purely seismic ruptures, we believe this offers a starting point to examine slip partitioning during injection-induced fault slip sequences: a crucial step toward advancing our physical understanding of the seismogenic behavior of reactivated faults and the associated seismic hazard.

4 Materials and Methods

4.1 Time-dependent upper-bound model for the size of unconditionally stable ruptures

We define the axisymmetric overpressure due to the injection as $\Delta p(r,t) = p(r,t) - p_0$, with p_0 the uniform background pore pressure. During the pressurization stage ($t \leq t_s$), the overpressure is given by $\Delta p(r,t) = \Delta p_* \cdot E_1\left(r^2/4\alpha t\right)$ for an injection at constant flow rate Q_0 [74], where $\Delta p_* = Q_0\eta/4\pi k w$ is the intensity of the injection with units of pressure, α is the fault hydraulic diffusivity, η is the fluid dynamic viscosity, the product kw is the so-called fault hydraulic transmissivity, and E_1 is the exponential integral function. The fracture-mechanics energy balance for a quasi-static circular rupture propagating on a slip-weakening fault was presented in [25]. In our upper-bound configuration here, neglecting the fracture energy spent during rupture propagation leads to the following expression describing the evolution of the rupture radius R with time:

$$\frac{2}{\sqrt{\pi}} \frac{f_r \Delta p_*}{\sqrt{R(t)}} \int_0^{R(t)} \frac{E_1\left(r^2/4\alpha t\right)}{\sqrt{R(t)^2 - r^2}} r \mathrm{d}r = \frac{2}{\sqrt{\pi}} \Delta\tau_{r-0} \sqrt{R(t)}, \tag{10}$$

where $\Delta\tau_{r-0} = f_r \sigma_0' - \tau_0$ is the background stress change. In equation (10), the integral term of the left-hand side is associated with an influx of potential energy towards the rupture front which becomes available for the rupture to grow owing to the sole effect of overpressure due to the injection. Conversely, the term of the right-hand side due to the background stress change is responsible alone for resisting rupture advancement. Nondimensionalization of equation (10) shows that the competition between both *energy* terms is quantified by one single dimensionless number, the so-called residual stress-injection parameter $\mathcal{T}_r = \Delta\tau_{r-0}/f_r \Delta p_*$, introduced first in [25]. Moreover, equation (10) admits analytical solution in the form: $R(t) = \lambda \cdot L(t)$ [23], with the asymptotes $\lambda \simeq 1/\sqrt{2\mathcal{T}_r}$ for nearly unstable ruptures ($\lambda \gg 1, \mathcal{T}_r \ll 1$), and $\lambda \simeq e^{(2-\gamma-\mathcal{T}_r)/2}/2$ for marginally pressurized ruptures ($\lambda \ll 1, \mathcal{T}_r \sim 10$). To highlight how significant is to analyze the end-member cases of nearly unstable ($\lambda \gg 1$) and marginally pressurized ($\lambda \ll 1$) ruptures throughout this work, we refer to their asymptotes for λ plotted in Fig. 2b which nearly overlap and thus quantify together almost any rupture scenario. This analytical solution for λ was first derived by Sáez *et al.* [23] for a fault interface with a constant friction coefficient (equation (21) in [23]). Here, in our upper-bound configuration, the mathematical solution is identical to the one presented in [23] provided that the constant friction coefficient f in [23] is understood as the residual value f_r of the slip-weakening friction law here.

To make the link between the evolution of the rupture radius $R(t)$ and the injected fluid volume $V(t)$ in the most practically relevant, nearly unstable regime ($\lambda \gg 1$), we use the asymptote $R(t) \simeq (1/\sqrt{2\mathcal{T}_r})L(t)$ in combination with the following expressions for the residual stress-injection parameter $\mathcal{T}_r = \Delta\tau_{r-0}/f_r \Delta p_*$, overpressure intensity $\Delta p_* = Q_0 \eta / 4\pi k w$, overpressure front $L(t) = \sqrt{4\alpha t}$, hydraulic diffusivity $\alpha = k/S\eta$, and injected fluid volume $V(t) = Q_0 t$. By doing so, we arrive at equation (2) in the main text. For non-circular ruptures ($\nu \neq 0$), building upon the work of Sáez *et al.* [23] for a constant friction coefficient, we obtain that the rupture front of our upper-bound model is well-approximated by an elliptical shape that becomes more elongated for increasing values of ν and decreasing values of $\mathcal{T}_r$, with a maximum aspect ratio of $1/(1-\nu)$ when $\mathcal{T}_r \ll 1$ and a minimum aspect ratio of $(3-\nu)/(3-2\nu)$ when $\mathcal{T}_r \sim 10$. Other features of Sáez *et al.*'s model [23] such as the invariance of the rupture area with regard to the Poisson's ratio and the numerically-derived asymptotes for the quasi-elliptical fronts are also inherited here in the upper-bound model. In the shut-in stage ($t > t_s$), the overpressure is obtained by superposition simply as $\Delta p(r,t) = \Delta p_* \cdot \left[E_1\left(r^2/4\alpha t\right) - E_1\left(r^2/4\alpha(t-t_s)\right)\right]$. The spatiotemporal evolution of overpressure has been studied in detail in [24]. Moreover, as already discussed in the main text, we reduced the upper-bound problem in the shut-in stage to a fault responding with a constant friction coefficient equal to f_r. Hence, our upper-bound model inherits all the results obtained by Sáez and Lecampion [24] who investigated extensively the propagation and arrest of post-injection aseismic slip on a fault obeying a constant friction coefficient. In particular, we take advantage of their understanding of the propagation and arrest of the slip front that ultimately determines the maximum size of unconditionally stable ruptures in our upper-bound model. Here, we have indeed expanded the work of Sáez and Lecampion [24] to account for an examination of the previously unknown evolution of the moment release during the shut-in stage (Fig. 4).

4.2 Asymptotics of moment release for nearly unstable and marginally pressurized ruptures

The scalar moment release M_0 at a given time t is given by [75],

$$M_0(t) = \mu \iint_{A_r(t)} \delta(x, y, t)\mathrm{d}x\mathrm{d}y, \tag{11}$$

where μ is the bulk shear modulus, δ is the current slip distribution, and A_r is the current rupture surface. To calculate the time-dependent slip distribution in the circular rupture case, we consider the quasi-static relation between fault slip δ and the associated elastic change of shear stress $\Delta\tau$ within an axisymmetric circular shear crack [76]:

$$\delta(r, t) = \frac{4R(t)}{\pi\mu} \int_{\bar{r}}^{1} \frac{\xi \mathrm{d}\xi}{\sqrt{\xi^2 - \bar{r}^2}} \int_0^1 \frac{\Delta\tau(s\xi R(t), t)s\mathrm{d}s}{\sqrt{1 - s^2}}, \tag{12}$$

where $\bar{r} = r/R(t)$ is the normalized radial coordinate. Equation (12) was originally derived for an internally-pressurized tensile circular crack with axisymmetric load [76]. Nevertheless, under the assumptions of uni-directional slip with axisymmetric magnitude and a Poisson's ratio $\nu = 0$, the shear crack problem is mathematically equivalent on the fault plane to its tensile counterpart [20]: crack opening being δ and crack-normal stress change being $\Delta\tau$. In the limiting regime of a rupture propagating with zero fracture energy and at the residual friction level f_r, the change of shear stress is simply

$$\Delta\tau(r, t) = \tau_0 - f_r \left[\sigma'_0 - \Delta p(r, t)\right] = f_r \Delta p(r, t) - \Delta\tau_{r-0}, \tag{13}$$

where $\Delta\tau_{r-0} = f_r\sigma'_0 - \tau_0$ is the background stress change. Hence, for injection at a constant volumetric rate Q_0, the spatio-temporal evolution of slip for the end-member cases of nearly unstable ($\lambda \gg 1$) and marginally pressurized ($\lambda \ll 1$) ruptures turn out to be identical to the ones determined by Sáez *et al.* [23] for their so-called critically stressed regime (equation (26) in [23]) and marginally pressurized regime (equation (25) in [23]) respectively, as long as we interpret their constant friction coefficient f as f_r. The self-similar slip profiles can be written in a more convenient dimensionless form as:

$$\delta(r, t)/\delta_*(t) = D\left(r/R(t)\right), \quad \text{with} \quad \delta_*(t) = \begin{cases} \Delta\tau_{r-0}R(t)/\mu & \text{when } \lambda \gg 1, \\ f_r \Delta p_* R(t)/\mu & \text{when } \lambda \ll 1, \end{cases} \tag{14}$$

and

$$D(x) = \begin{cases} (4/\pi)(\arccos(x)/x - \sqrt{1 - x^2}) & \text{when } \lambda \gg 1, \\ (8/\pi)(\sqrt{1 - x^2} - x \cdot \arccos(x)) & \text{when } \lambda \ll 1. \end{cases} \tag{15}$$

Note that in the nearly unstable regime ($\lambda \gg 1$), we have recast equation (26) in [23] using the expressions $L(t) = R(t)/\lambda$ and $\lambda \simeq 1/\sqrt{2\mathcal{T}_r}$. The nearly unstable asymptote for fault slip is plotted in Fig. 3b and compared to the numerical solution. Integration of the self-similar slip profiles via equation (11) leads to the asymptotes for the moment release during the pressurization stage given in the main text: $M_0(t) = (16/3)\Delta\tau_{r-0}R(t)^3$ when $\lambda \gg 1$, and $M_0(t) = (16/9)f_r\Delta p_* R(t)^3$ when $\lambda \ll 1$. It is worth mentioning that the slip distribution of nearly unstable ruptures has a singularity (of order $1/r$) at $r = 0$. Strictly speaking, this asymptote corresponds to the solution of the so-called outer problem which is defined at distances $r \gg L(t)$. An interior layer must be resolved at distances $r \sim L(t)$ to obtain the finite slip at the injection point, which scales as $\delta_c(t) = f_r \Delta p_* L(t)/\mu$ [23] (see Fig. 3b). Nevertheless, this interior layer has no consequences in estimating the moment release. Indeed, the integrand in equation (11) for such a slip distribution is non-singular so that after taking the limit $L(t)/R(t) \to 0$, one effectively recovers the actual asymptote for the moment release. The details of the interior layer are therefore irrelevant to the calculation of M_0 in this limit.

4.3 Relation between fluid-injection force and injected fluid volume for arbitrary fluid sources

Under the assumptions of our model, the displacement field $\boldsymbol{u}$ induced by the fluid injection into the poroelastic fault zone is irrotational $\nabla \times \boldsymbol{u} = 0$ [40]. Therefore, the variation in fluid content ζ, which corresponds to the change of fluid volume per unit volume of porous material with respect to an initial state (here, $t = 0$), satisfies the following constitutive relation with the pore-fluid overpressure Δp (eq. 96, [41]),

$$\zeta = S\Delta p, \tag{16}$$

where S is the so-called oedometric storage coefficient representing the variation of fluid content caused by a unit pore pressure change under uniaxial strain and constant normal stress in the direction of the strain [42], here, the z-axis (Fig. 1c). S accounts for the effects of fluid, pore, and bulk compressibilities of the fault zone, and is equal to [41]

$$S = \frac{1}{M} + \frac{b^2(1-2\nu)}{2(1-\nu)\mu}, \tag{17}$$

where M is the Biot's modulus and b the Biot's coefficient.

To obtain the cumulative injected fluid volume at a given time, $V(t)$, we just sum up changes in fluid volume all over the spatial domain of interest, say Ω, at a given time t, that is, $V(t) = \int_\Omega \zeta \mathrm{d}\Omega$. In our model, the fluid flow problem is axisymmetric and the fault-zone width w is uniform, such that the differential of the volume is simply $\mathrm{d}\Omega = 2\pi w r \mathrm{d}r$ in cylindrical coordinates. With these definitions, we can now integrate (16) over the entire fault-zone volume to obtain the following expression for the injected fluid volume valid for an arbitrary fluid injection:

$$V(t) = Sw \cdot 2\pi \int_0^\infty \Delta p(r,t) r \mathrm{d}r. \tag{18}$$

By defining the normal force induced by the fluid injection over the slip surface (simply equal to the integral of the overpressure over the fault plane) as:

$$F(t) = 2\pi \int_0^\infty \Delta p(r,t) r \mathrm{d}r, \tag{19}$$

we arrive at the following relation between the fluid-injection force and injected fluid volume:

$$F(t) = \frac{V(t)}{wS}. \tag{20}$$

Expressions of a similar kind to (20) have been reported in previous studies [28, 77, 78]. For example, McGarr [28] considered a similar relation except that his storativity-like term is the inverse of the elastic bulk modulus. Garagash [78] also proposed a similar expression to (20) but accounting only for pore compressibility. Finally, the relation considered by Shapiro *et al.* [77] is the closest to our expression, including the oedometric storage coefficient.

4.4 Scaling relations for nearly unstable ruptures accounting for arbitrary fluid injections

Nearly unstable ruptures ($\lambda \gg 1$) provide the upper bound of most practical interest. Here, we generalize such an upper bound for the rupture size and moment release to account for an arbitrary fluid injection. In the pressurization stage ($t \leq t_s$), the reduction of fault strength due to fluid injection in the so-called outer problem ($r \gg L(t)$) can be effectively approximated as a point force (e.g., [23, 43]),

$$f_r \Delta p(r,t) \approx f_r F(t) \frac{\delta^{\mathrm{dirac}}(r)}{2\pi r} = f_r \frac{V(t)}{wS} \frac{\delta^{\mathrm{dirac}}(r)}{2\pi r}, \tag{21}$$

where $F(t)$ is the fluid-injection normal force, equation (19), which is related to the cumulative injected fluid volume via equation (20). Substituting equation (21) into the stress change (13), and then the latter into the double integral, equation (12), we obtain upon evaluating those integrals an asymptotic upper bound for the spatiotemporal evolution of fault slip as:

$$\delta(r,t) = \frac{4}{\pi} \frac{\Delta\tau_{r-0}}{\mu} R(t) \left[\frac{f_r V(t)}{2\pi w S \Delta\tau_{r-0}} \frac{\arccos\left(r/R(t)\right)}{r/R(t)} - \sqrt{1 - \left(r/R(t)\right)^2} \right], \tag{22}$$

The propagation condition for a rupture with negligible fracture energy, equation (10), can be alternatively written in terms of the slip behavior near the rupture front as [79],

$$\lim_{r \to R(t)^-} \frac{\partial \delta(r,t)}{\partial r} \sqrt{R(t) - r} = 0. \tag{23}$$

This imposes a constraint in the slip distribution (22) that can be also seen, in a limiting sense, as eliminating any stress singularity at the rupture front. By differentiating equation (22) with respect to r, and then applying the propagation condition (23), we obtain the following relation:

$$R(t) = \sqrt{\frac{f_r V(t)}{2\pi w S \Delta\tau_{r-0}}}, \tag{24}$$

which is valid for an arbitrary fluid injection.

Equation (24) is identical to equation (2) in the main text, which was originally derived for injection at constant flow rate. It thus represents a generalization of the insightful relation between the evolution of the rupture radius and the cumulative injected fluid volume, equation (2), for arbitrary fluid injections. Note that alternatively, equation (24) can be derived through the rupture propagation condition imposed over the stress change, equation (10). It only takes to replace the particular overpressure solution for injection at a constant volumetric rate, $\Delta p(r,t) = \Delta p_* E_1\left(r^2/4\alpha t\right)$, by the more general point-force representation, equation (21). We report here the derivation based on the slip distribution because it makes now the calculation of the moment release for arbitrary fluid injections straightforward. Indeed, by substituting (24) into (22), we obtain the slip distribution satisfying the zero-fracture-energy condition of our upper-bound model. Upon integrating the resulting slip profile via equation (11), we obtain the following final expression for the moment release:

$$M_0(t) = \frac{16}{3(2\pi)^{3/2}} \frac{V(t)^{3/2}}{\sqrt{\Delta\tau_{r-0}}} \left(\frac{f_r}{wS}\right)^{3/2}, \tag{25}$$

which is identical to equation (6) in the main text, thus demonstrating that the relation between the moment release, in-situ conditions, and injected fluid volume (6), holds for arbitrary fluid injections.

Finally, we note that some constraints on the fluid source are required to ensure that some important model assumptions are satisfied. For example, the rupture must always propagate in a crack-like mode during the pressurization stage. This is necessary so that equations (10) and (12) (in combination with (13)) remain always valid. Essentially, crack-like propagation allows for substituting the shear stress acting within the ruptured surface directly with the fault shear strength at any time during propagation. This would not be valid, for instance, for the pulse-like ruptures characterizing the shut-in stage [24], where behind the locking front equating the shear stress to the fault strength is no longer valid. As discussed in the main text, crack-like propagation holds at least in one relevant scenario, where the pore pressure increases monotonically everywhere within the fault zone. Another assumption in the upper bound rationale of our model relies on the following property of unconditionally stable ruptures: the effect of the fracture energy in the front-localized energy balance must diminish as the rupture grows and, ultimately, become negligible [25]. Although this is certainly valid even in the case of arbitrary fluid injections, it relies on an implicit assumption of the slip-weakening model, namely, the fracture energy being constant. Our theoretical framework allowed in principle to account for non-constant and non-uniform fracture energy. We do not account for fracture-energy heterogeneity for the same reason that we do not account for stress or other kinds of heterogeneities in our model: we aim to provide fundamental, first-order insights into the problem at hand. Moreover, we also do not consider a possible scale dependence of the fracture energy. The scale-dependency of fracture energy for seismic ruptures is a topic of active research ([80] and references therein). Although we do expect this phenomenon to be also present in aseismic ruptures, to the best of our knowledge, there is no experimental or observational evidence suggesting such behavior for slow frictional ruptures. We therefore refrain from exploring the theoretical implications of this hypothetical physical ingredient at the moment.

4.5 Numerical methods

All the numerical calculations in this study have been conducted via the boundary-element-based method described in [23]. For the general case of non-circular ruptures, we use the fully three-dimensional method presented in [23]. For the particular case of axisymmetric, circular ruptures, we use a more efficient axisymmetric version of the method presented in [24].

Funding

The results were obtained within the EMOD project (Engineering model for hydraulic stimulation). The EMOD project benefits from a grant (research contract no. SI/502081-01) and an exploration subsidy (contract no. MF-021-GEO-ERK) of the Swiss federal office of energy for the EGS geothermal project in Haute-Sorne, canton of Jura, which is gratefully acknowledged. Alexis Sáez was partially funded by the Federal Commission for Scholarships for Foreign Students via the Swiss Government Excellence Scholarship.

References

1. Hamilton, D. & Meehan, R. Ground Rupture in the Baldwin Hills. *Science* **172,** 333–344 (1971).
2. Scotti, O. & Cornet, F. In Situ Evidence for fluid-induced aseismic slip events along fault zones. *International Journal of Rock Mechanics and Mining Sciences and Geomechanics Abstracts* **31,** 347–358 (1994).
3. Cornet, F., Helm, J., Poitrenaud, H. & Etchecopar, A. Seismic and aseismic slips induced by large-scale fluid injections. *Pure and Applied Geophysics* **150,** 563–583 (1997).
4. Bourouis, S. & Bernard, P. Evidence for coupled seismic and aseismic fault slip during water injection in the geothermal site of Soultz (France), and implications for seismogenic transients. *Geophysical Journal International* **169,** 723–732 (2007).
5. Calò, M., Dorbath, C., Cornet, F. & Cuenot, N. Large-scale aseismic motion identified through 4-D P-wave tomography. *Geophysical Journal International* **186,** 1295–1314 (2011).

6. Guglielmi, Y., Cappa, F., Avouac, J., Henry, P. & Elsworth, D. Seismicity triggered by fluid injection-induced aseismic slip. *Science* **348,** 1224–1226 (2015).

7. Wei, S. *et al.* The 2012 Brawley swarm triggered by injection-induced aseismic slip. *Earth and Planetary Science Letters* **422,** 115–125 (2015).

8. Cappa, F., Scuderi, M., Collettini, C., Guglielmi, Y. & Avouac, J. Stabilization of fault slip by fluid injection in the laboratory and in situ. *Science Advances* **5** (2019).

9. Materna, K., Barbour, A., Jiang, J. & Eneva, M. Detection of Aseismic Slip and Poroelastic Reservoir Deformation at the North Brawley Geothermal Field From 2009 to 2019. *Journal of Geophysical Research: Solid Earth* **127,** e2021JB023335 (2022).

10. Eyre, T., Samsonov, S., Feng, W., Kao, H. & Eaton, D. W. InSAR data reveal that the largest hydraulic fracturing-induced earthquake in Canada, to date, is a slow-slip event. *Scientific Reports* **12,** 2043 (2022).

11. Pepin, K. S., Ellsworth, W. L., Sheng, Y. & Zebker, H. A. Shallow Aseismic Slip in the Delaware Basin Determined by Sentinel-1 InSAR. *Journal of Geophysical Research: Solid Earth* **127,** e2021JB023157 (2022).

12. Im, K. & Avouac, J.-P. On the role of thermal stress and fluid pressure in triggering seismic and aseismic faulting at the Brawley Geothermal Field, California. *Geothermics* **97,** 102238 (2021).

13. Dvory, N. Z., Yang, Y. & Dunham, E. M. Models of Injection-Induced Aseismic Slip on Height-Bounded Faults in the Delaware Basin Constrain Fault-Zone Pore Pressure Changes and Permeability. *Geophysical Research Letters* **49,** e2021GL097330 (2022).

14. Deichmann, N. & Giardini, D. Earthquakes induced by the stimulation of an enhanced geothermal system below Basel (Switzerland). *Seismological Research Letters* **80,** 784–798 (2009).

15. Ellsworth, W., Giardini, D., Townend, J., Ge, S. & Shimamoto, T. Triggering of the Pohang, Korea, Earthquake (Mw 5.5) by Enhanced Geothermal System Stimulation. *Seismological Research Letters* **90,** 1844–1858 (2019).

16. Dusseault, M. B., Bruno, M. S. & Barrera, J. Casing Shear: Causes, Cases, Cures. *SPE Drilling and Completion* **16,** 98–107 (June 2001).

17. Li, Y., Liu, W., Yan, W., Deng, J. & Li, H. Mechanism of casing failure during hydraulic fracturing: Lessons learned from a tight-oil reservoir in China. *Engineering Failure Analysis* **98,** 58–71 (2019).

18. Cappa, F. & Rutqvist, J. Modeling of coupled deformation and permeability evolution during fault reactivation induced by deep underground injection of CO2. *International Journal of Greenhouse Gas Control* **5,** 336–346 (2011).

19. Rinaldi, A. P., Vilarrasa, V., Rutqvist, J. & Cappa, F. Fault reactivation during CO2 sequestration: Effects of well orientation on seismicity and leakage. *Greenhouse Gases: Science and Technology* **5,** 645–656 (2015).

20. Bhattacharya, P. & Viesca, R. Fluid-induced aseismic fault slip outpaces pore-fluid migration. *Science* **364,** 464–468 (2019).

21. Eyre, T. *et al.* The role of aseismic slip in hydraulic fracturing-induced seismicity. *Science Advances* **5** (2019).

22. Vilarrasa, V., De Simone, S., Carrera, J. & Villaseñor, A. Unraveling the Causes of the Seismicity Induced by Underground Gas Storage at Castor, Spain. *Geophysical Research Letters* **48,** e2020GL092038 (2021).

23. Sáez, A., Lecampion, B., Bhattacharya, P. & Viesca, R. C. Three-dimensional fluid-driven stable frictional ruptures. *Journal of the Mechanics and Physics of Solids* **160,** 104754 (2022).

24. Sáez, A. & Lecampion, B. Post-injection aseismic slip as a mechanism for the delayed triggering of seismicity. *Proceedings of the Royal Society A: Mathematical, Physical and Engineering Sciences* **479,** 20220810 (2023).

25. Sáez, A. & Lecampion, B. Fluid-driven slow slip and earthquake nucleation on a slip-weakening circular fault. *Journal of the Mechanics and Physics of Solids* **183,** 105506 (2024).

26. Shapiro, S. A., Dinske, C. & Kummerow, J. Probability of a given-magnitude earthquake induced by a fluid injection. *Geophysical Research Letters* **34** (2007).

27. Shapiro, S. A., Krüger, O. S., Dinske, C. & Langenbruch, C. Magnitudes of induced earthquakes and geometric scales of fluid-stimulated rock volumes. *Geophysics* **76,** WC55–WC63 (2011).

28. McGarr, A. Maximum magnitude earthquakes induced by fluid injection. *Journal of Geophysical Research: solid earth* **119,** 1008–1019 (2014).

29. Atkinson, G. M. *et al.* Hydraulic Fracturing and Seismicity in the Western Canada Sedimentary Basin. *Seismological Research Letters* **87,** 631–647 (2016).

30. van der Elst, N., Page, M., Weiser, D., Goebel, T. & Hosseini, S. M. Induced earthquake magnitudes are as large as (statistically) expected. *Journal of Geophysical Research: Solid Earth* **121,** 4575–4590 (2016).

31. McGarr, A. & Barbour, A. J. Wastewater Disposal and the Earthquake Sequences During 2016 Near Fairview, Pawnee, and Cushing, Oklahoma. *Geophysical Research Letters* **44,** 9330–9336 (2017).

32. Galis, M., Ampuero, J., Mai, P. & Cappa, F. Induced seismicity provides insight into why earthquake ruptures stop. *Science Advances* **3** (2017).

33. De Barros, L., Cappa, F., Guglielmi, Y., Duboeuf, L. & Grasso, J.-R. Energy of injection-induced seismicity predicted from in-situ experiments. *Scientific Reports* **9,** 4999 (2019).

34. Bentz, S., Kwiatek, G., Martínez-Garzón, P., Bohnhoff, M. & Dresen, G. Seismic moment evolution during hydraulic stimulations. *Geophysical Research Letters* **n/a,** e2019GL086185 (2020).

35. Li, Z. *et al.* Constraining maximum event magnitude during injection-triggered seismicity. *Nature Communications* **12,** 1528 (2021).

36. Shapiro, S. A., Kim, K.-H. & Ree, J.-H. Magnitude and nucleation time of the 2017 Pohang Earthquake point to its predictable artificial triggering. *Nature Communications* **12,** 6397 (2021).

37. Im, K., Avouac, J.-P., Heimisson, E. R. & Elsworth, D. Ridgecrest aftershocks at Coso suppressed by thermal destressing. *Nature* **595,** 70–74 (2021).

38. J.S. Caine, J. E. & Forster, C. Fault Zone Architecture and Permeability Structure. *Geology* **24,** 1025–1028 (1996).

39. Faulkner, D. *et al.* A review of recent developments concerning the structure, mechanics and fluid flow properties of fault zones. *Journal of Structural Geology* **32,** 1557–1575 (2010).

40. Marck, J., Savitski, A. A. & Detournay, E. Line source in a poroelastic layer bounded by an elastic space. *Int. J. Numer. Anal. Methods Geomech.* **39,** 1484–1505 (2015).

41. Detournay, E. & Cheng, A. in, 113–171 (Elsevier, 1993).

42. Green, D. H. & Wang, H. F. Specific storage as a poroelastic coefficient. *Water Resources Research* **26,** 1631–1637 (1990).

43. Garagash, D. & Germanovich, L. Nucleation and arrest of dynamic slip on a pressurized fault. *Journal of Geophysical Research: Solid Earth* **117** (2012).

44. Ciardo, F. & Lecampion, B. Injection-Induced Aseismic Slip in Tight Fractured Rocks. *Rock Mechanics and Rock Engineering* (2023).

45. Parotidis, M., Shapiro, S. A. & Rothert, E. Back front of seismicity induced after termination of borehole fluid injection. *Geophysical Research Letters* **31** (2004).

46. Kanamori, H. & Anderson, D. L. Theoretical basis of some empirical relations in seismology. *Bulletin of the seismological society of America* **65,** 1073–1095 (1975).

47. Segedin, C. Note on a penny-shaped crack under shear. **47,** 396–400 (1951).

48. Hanks, T. C. & Kanamori, H. A moment magnitude scale. *Journal of Geophysical Research: Solid Earth* **84,** 2348–2350 (1979).

49. Passelègue, F. X. *et al.* Initial effective stress controls the nature of earthquakes. *Nature Communications* **11,** 5132 (2020).

50. Cebry, S. B. L., Ke, C.-Y. & McLaskey, G. C. The Role of Background Stress State in Fluid-Induced Aseismic Slip and Dynamic Rupture on a 3-m Laboratory Fault. *Journal of Geophysical Research: Solid Earth* **127,** e2022JB024371 (2022).

51. Lengliné, O., Boubacar, M. & Schmittbuhl, J. Seismicity related to the hydraulic stimulation of GRT1, Rittershoffen, France. *Geophysical Journal International* **208,** 1704–1715 (2017).

52. De Barros, L. *et al.* Fault structure, stress, or pressure control of the seismicity in shale? Insights from a controlled experiment of fluid-induced fault reactivation. *Journal of Geophysical Research: Solid Earth* **121,** 4506–4522 (2016).

53. Duboeuf, L. *et al.* Aseismic Motions Drive a Sparse Seismicity During Fluid Injections Into a Fractured Zone in a Carbonate Reservoir. *Journal of Geophysical Research: Solid Earth* **122,** 8285–8304 (2017).

54. Kuang, X., Jiao, J. J., Zheng, C., Cherry, J. A. & Li, H. A review of specific storage in aquifers. *Journal of Hydrology* **581,** 124383 (2020).

55. Doan, M. L., Brodsky, E. E., Kano, Y. & Ma, K. F. In situ measurement of the hydraulic diffusivity of the active Chelungpu Fault, Taiwan. *Geophysical Research Letters* **33** (2006).

56. Xue, L. *et al.* Continuous Permeability Measurements Record Healing Inside the Wenchuan Earthquake Fault Zone. *Science* **340,** 1555–1559 (2013).

57. Rutqvist, J., Noorishad, J., Tsang, C.-F. & Stephansson, O. Determination of fracture storativity in hard rocks using high-pressure injection testing. *Water Resources Research* **34,** 2551–2560 (1998).

58. Almakari, M., Chauris, H., Passelègue, F., Dublanchet, P. & Gesret, A. Fault's hydraulic diffusivity enhancement during injection induced fault reactivation: application of pore pressure diffusion inversions to laboratory injection experiments. *Geophysical Journal International* **223,** 2117–2132 (2020).

59. Evans, K. F., Genter, A. & Sausse, J. Permeability creation and damage due to massive fluid injections into granite at 3.5 km at Soultz: 1. Borehole observations. *Journal of Geophysical Research: Solid Earth* **110** (2005).

60. Evans, K. F. *et al.* Microseismicity and permeability enhancement of hydrogeologic structures during massive fluid injections into granite at 3 km depth at the Soultz HDR site. *Geophysical Journal International* **160,** 388–412 (Jan. 2005).

61. McGarr, A. & Barbour, A. Injection-Induced Moment Release Can Also Be Aseismic. *Geophysical Research Letters* **45,** 5344–5351 (2018).

62. Goodfellow, S. D., Nasseri, M. H. B., Maxwell, S. C. & Young, R. P. Hydraulic fracture energy budget: Insights from the laboratory. *Geophysical Research Letters* **42,** 3179–3187 (2015).

63. Detournay, E. Mechanics of Hydraulic Fractures. *Annual Review of Fluid Mechanics* **48,** 311–339 (2016).

64. Ciardo, F. & Lecampion, B. Effect of Dilatancy on the Transition From Aseismic to Seismic Slip Due to Fluid Injection in a Fault. *Journal of Geophysical Research: Solid Earth* **124,** 3724–3743 (2019).

65. Dunham, E. M. Fluid-driven aseismic fault slip with permeability enhancement and dilatancy. *Philosophical Transactions of the Royal Society A: Mathematical, Physical and Engineering Sciences* **382,** 20230255 (2024).

66. Shapiro, S. A. *Fluid-Induced Seismicity* (Cambridge University Press, 2015).

67. Goebel, T. & Brodsky, E. The spatial footprint of injection wells in a global compilation of induced earthquake sequences. *Science* **361,** 899–904 (2018).

68. Sirorattanakul, K. *et al.* The 2020 Westmorland, California Earthquake Swarm as Aftershocks of a Slow Slip Event Sustained by Fluid Flow. *Journal of Geophysical Research: Solid Earth* **127,** e2022JB024693 (2022).

69. Yukutake, Y., Yoshida, K. & Honda, R. Interaction between aseismic slip and fluid invasion in earthquake swarms revealed by dense geodetic and seismic observations. *Journal of Geophysical Research: Solid Earth,* e2021JB022933 (2022).

70. Bürgmann, R. The geophysics, geology and mechanics of slow fault slip. *Earth and Planetary Science Letters* **495,** 112–134 (2018).

71. Tanaka, Y. *et al.* Gravity changes observed between 2004 and 2009 near the Tokai slow-slip area and prospects for detecting fluid flow during future slow-slip events. *Earth, Planets and Space* **62,** 905–913 (2010).

72. Nakajima, J. & Uchida, N. Repeated drainage from megathrusts during episodic slow slip. *Nature Geoscience* **11,** 351–356 (2018).

73. Warren-Smith, E. *et al.* Episodic stress and fluid pressure cycling in subducting oceanic crust during slow slip. *Nature Geoscience* **12,** 475–481 (2019).

74. Carslaw, H. & Jaeger, J. *Conduction of heat in solids* 2nd edition (Oxford: Clarendon Press, 1959).

75. Aki, K. & Richards, P. *Quantitative Seismology* 2nd edition (2002).

76. Sneddon, I. *Fourier transforms* (McGraw-Hill, New York, 1951).

77. Shapiro, S. A., Dinske, C., Langenbruch, C. & Wenzel, F. Seismogenic index and magnitude probability of earthquakes induced during reservoir fluid stimulations. *The Leading Edge* **29,** 304–309 (2010).

78. Garagash, D. Fracture mechanics of rate-and-state faults and fluid injection induced slip. *Philosophical Transactions of the Royal Society A: Mathematical, Physical and Engineering Sciences* **379,** 20200129 (2021).

79. Barenblatt, G. The mathematical theory of equilibrium cracks in brittle fracture. *Advances in Applied Mechanics* **7,** 55–129 (1962).

80. Cocco, M. *et al.* Fracture Energy and Breakdown Work During Earthquakes. *Annual Review of Earth and Planetary Sciences* **51,** 217–252 (2023).